Aeroservoelasticity of Wind Turbines

Kallesøe, Bjarne Skovmose

Publication date:
2007

Document Version
Publisher's PDF, also known as Version of record

Aeroservoelasticity of Wind Turbines

by

Bjarne Skovmose Kallesøe

DEPT. OF MECHANICAL ENGINEERING
Solid Mechanics

TECHNICAL UNIVERSITY OF DENMARK

Preface

This thesis is submitted in partial fulfillment of the requirements for obtaining the degree of PhD in mechanical engineering. The work was carried out at the Department of Mechanical Engineering, Solid Mechanics, Technical University of Denmark and at the Wind Energy Department, Risø National Laboratory in the period February 2004 to January 2007. The PhD-study was founded by a scholarship from the Technical University of Denmark (50%) and Risø National Laboratory (50%).

I would like to thank my supervisor Associate Professor Jon Juel Thomsen, Technical University of Denmark and co-supervisors Senior Scientists Morten Hartvig Hansen and Thomas Buhl, Risø National Laboratory for their help, support and inspiration.

During my PhD work I visited National Wind Technology Center, The National Renewable Energy Laboratory, Colorado, USA for a period of four month from September 2005 to December 2005. I would like to thank Chief Engineer, Sandy Butterfield for making the visit possible with such a short notice and for the friendly and inspiring atmosphere during my stay.

Finally, thanks to my fellow PhD-students at the department for the inspiring, encouraging and humorous working environment.

Kgs. Lyngby, 31. January 2007

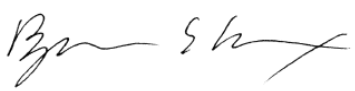

Bjarne Skovmose Kallesøe

Resumé

Denne afhandling omhandler det grundlæggende samspil mellem aerodynamisk kræfter, pitch-aktivitet, regulering og bevægelser af en vindmøllevinge. I takt med at vindmøller er blevet større er det aeroelastiske samspil mellem pitch-aktivitet, vingebevægelser og regulator blevet tilsvarende vigtigt at forstå og tage hensyn til.

Hovedbidraget i denne afhandling er udviklingen af en aeroelastisk model af en vindmøllevinge, der på den ene side medtager påvirkninger fra stationær vingeudbøjning, tyngdekraft, og pitch-aktivitet, og på den anden side er gennemskuelig, egnet til analytisk analyse og parameter studier. Modellen er desuden lineær og derfor velegnet til analyse og udvikling af regulatorer.

Udviklingen af den aeroelastiske vingemodel er opdelt i fire trin: 1) Udledning af ikke-lineær partielle differentialligninger (PDer) for strukturelle vingebevægelser, samt ligninger for pitch-aktivitet og rotorhastighed. Hvert led i ligningerne er diskuteret og givet en fysisk fortolkning, 2) Den stationære udbøjning af vingen er fundet ved at kombinere PDerne med en stationær aerodynamisk model, 3) De aeroelastiske svingningsformer er beregnet med en lineariseret version af PDerne, kombineret med en lineær, ikke-stationær aerodynamisk model. Svingningsformer for en deformeret og en udeformeret vinge er sammenlignet, 4) Den aeroelastiske vingemodel er udledt ved at modal udvikle den lineær version af PDerne kombineret, med den lineær, ikke-stationære aerodynamiske model.

Den aeroelastiske vingemodel har mange ligheder med en 2D model af en vingesektion, og kan i mange situationer bruges i stedet for en sådan. Herved gives en mere klar forbindelse til en vindmøllevinge.

I dette arbejde er den aeroelastiske vingemodel brugt til at analysere samspillet mellem pitch-aktivitet, vindhastigheds-variationer og vingebevægelser. Endvidere er modellen brugt til at konstruere en tilstandsestimator, som estimerer vindhastighed og vindgradient, samt til at konstruere en lastreducerende regulator. Tilstandsestimatoren estimerer vindhastighed og vindgradient godt, og den lastreducerende regulator reducerer svingninger af vingen med 75 % under ideelle betingelser.

Der er altså udviklet en ny aeroelastisk vingemodel, som medtager vigtige egenskaber for store vindmøller, men stadigvæk er simpel nok til at være velegnet til analytisk analyse og regulator-design.

Abstract

This thesis deals with the fundamental aeroelastic interaction between structural motion, Pitch action and control for a wind turbine blade.

As wind turbines become larger, the interaction between pitch action, blade motion, aerodynamic forces, and control become even more important to understand and address.

The main contribution of this thesis is the development of an aeroelastic blade model which on the one hand includes the important effects of steady state blade deformation, gravity and pitch action, and on the other it is transparent, suitable for analytical analysis and parameter studies, and furthermore linear and therefore suitable for control design.

The development of the primary aeroelastic blade model is divided into four steps: 1) Nonlinear partial differential equations (PDEs) of structural blade motion are derived together with equations of pitch action and rotor speed; the individual terms in these equations are discussed and given physical interpretations; 2) Steady state blade deformation and induced velocities are computed by combining the PDEs with a steady state aerodynamic model; 3) Aeroelastic modes of motion are computed by combining the linearized PDEs with a linear unsteady aerodynamic model; this model is used to analyze how blade deformation effects the modes of motion; and 4) the linear aeroelastic blade model is derived by a modal expansion of the linearized PDEs combined with a linear unsteady aerodynamic model.

The aeroelastic blade model has many similarities to a 2D blade section model, and it can be used instead of this in many applications, giving a transparent connection to a real wind turbine blade.

In this work the aeroelastic blade model is used to analyze interaction between pitch action, blade motion and wind speed variations. Furthermore the model is used to develop a state estimator for estimating the wind speed and wind shear, and to suggest a load reducing controller. The state estimator estimates the wind shear very well and the load reducing controller is capable of reducing flapwise blade motion caused by wind shear with 75 % under ideal conditions.

So, a new aeroelastic blade model has been derived, which includes important features of large wind turbines, yet simple enough to be suitable for analytical analysis and control design.

Publications

[P1] B. S. Kallesøe, A low-order model for analyzing effects of blade fatigue load control, *Wind Energy* **9(5)**:421-436, 2006.

[P2] B. S. Kallesøe, Equations of Motion for a Rotor Blade, Including Gravity and Pitch Action, *European Wind Energy Conference*, Athens, Greece, 27 February - 2 March, 2006

[P3] B. S. Kallesøe, Equations of Motion for a Rotor Blade, Including Gravity, Pitch Action and Rotor Speed Variations, *Wind Energy* (in press)

Contents

Chapter 1
Introduction

This thesis deals with fundamental interactions between structural motion, aerodynamic forces and control action for a wind turbine blade. The main contribution is the development of a linear aeroelastic[1] model of a wind turbine blade, which includes the effect of large blade deformations and pitch action, and which can be used for developing wind turbine controllers.

Fatigue caused by aerodynamic driven structural motion is a major constrain in the design of modern wind turbines. Active control can reduce the fatigue loads. An analysis of the interaction between blade motion, aerodynamic forces and control action can help in the design of blades, pitch actuators, and controllers for fatigue load reduction. The model developed in this thesis is used to analyze the dynamic interaction and to suggest a controller to reduce the fatigue loads.

This introduction gives a short historical background for wind power, introduces the most common type of wind turbines in use today and regions of operation conditions for a wind turbine. An overview of current aeroelastic modelling is followed by a review of wind turbine controllers, focusing on the possibilities to reduce fatigue loads.

1.1 Wind Turbine Primer

The energy crisis in the 1970th lead to an increased interest in alternative energy, including wind energy. Wind energy has since turned into a major contributor to the energy market, e.g. Denmark gets 20% of its electric energy from wind energy [1]. Different concepts of wind turbines have been developed; vertical axis wind turbines, such as the Darrieus wind turbine [2], and two and three bladed horizontal axis turbines, etc. The most successful concept has been the three bladed horizontal axis wind turbine with a gearbox and an asynchronous generator (The Danish concept). Because the three bladed horizontal axis wind turbine with a gearbox is the most common turbine today, this type will be used as example in this thesis.

Wind Turbine Architecture

A three blade horizontal axis wind turbine consists of three blades connected to the hub, which drives the generator through the gearbox. The low speed shaft from hub to gearbox, the gearbox and the high speed shaft from gearbox to

[1] Interaction between inertial, elastic, and aerodynamic forces.

generator are often referred to as the drivetrain. On pitch regulated turbines the blades can be turned (called pitch) around a longitudinal axis (pitch axis) to change the angle of attack and thereby the aerodynamic forces on the blades. The gearbox and generator are housed in the nacelle, placed on top of the tower. The nacelle and thereby the rotor is aligned with the wind by the yaw drive, which rotates the nacelle around the tower axis. The blades have an airfoil shaped cross section, much like the wings of an airplane, and the airflow that passes the blades results in aerodynamic forces on the blade. These forces are transferred to the hub and result in a torque on the gearbox. The gearbox raises the rotation speed and lowers the torque from the rotor to meet the requirements of the generator, which finally converts the mechanical energy into electric energy.

Up-Scaling

The hunt for cost efficiency has lead to a continually up-scaling of the state of the art wind turbine. The energy capture increases approximately with the square of the length of the blades. However by simple up-scaling of the blade the weight of the blade increases approximately with the cube of the length of the blade. To counteract the weight increase the development of blades goes towards long and relatively flexible structures. The increased flexibility of the wind turbine structure gives an increase in the fatigue of components, and since the expected lifetime for a wind turbine is about 20 years, fatigue becomes a major design concern.

Operation

The state of the art concept for operating a wind turbine is the pitch regulated variable speed wind turbine, and it is this concept that will be analyzed in this work. The operation objective depends on the wind speed and can be divided into four regions: Region 1: The wind speed is too low for profitable operation of the wind turbine, and the rotor is parked. Region 2: The wind speed is above the cut-in wind speed, at which there is enough energy in the wind for profitable operation of the turbine, but still less than the maximum capacity of the generator. In this region the turbine should extract as much energy from the wind as possible. To optimize the aerodynamic efficiency of the turbine the rotation speed of the rotor is below the rated rotor speed, approaching the rated rotor speed as the wind speed approach the rated wind speed. The pitch is constant. Region 3: The wind speed is above the rated wind speed, at which there is enough energy in the wind for the wind turbine to run at maximum electric energy production. The pitch controller turns the blades towards less aerodynamic torque such that the energy extracted from the wind fits the capacity of the generator. The rotation speed of the rotor is constant. It is this region of operation that will be the topic of the control design in this work. Region 4: The wind speed is too high for safe

operation of the wind turbine, cut-out wind speed, and the rotor is parked.

1.2 Aeroelastic Modelling of Wind Turbines

The main contribution of this work is the development of an aeroelastic model of a wind turbine blade including gravity, pitch action, and rotor speed variation. The model can be configured such that it describes a three blade wind turbine with drivetrain and generator.

Aeroelastic models are e.g. used to compute ultimate and fatigue loads, to analyze fundamental wind turbine behavior and to design and test wind turbine controllers. When aeroelastic models are combined with control it is referred to as aeroservoelastic models. This section contains a review of some existing aeroelastic models, their applications and limitations.

Full Wind Turbine Models

One approach to wind turbine modelling is to model the full wind turbine structure with general purpose commercial finite element or multi-body codes coupled to an aerodynamic model. Ref. [3] combines the commercial general purpose multi-body code from MSC.ADAMS® with the aerodynamic code AeroDyn [4] to obtain the aerodynamic forces. The AeroDyn code is based on Blade Element Momentum theory (BEM) combined with a dynamic stall model. The combined MSC.ADAMS and AeroDyn model can be used to achieve almost any requested degree of accuracy in the structural modelling, but it results in large models without any transparency and with long computation times.

The aeroelastic research code HAWC2 [5, 6] is developed to model wind turbines. In HAWC2 the structural model is based on a combined multi-body and beam element formulation and the aerodynamic model is based on BEM and unsteady aerodynamic modelling. Large structural deformations are handled by the multi-body formulation. Since the model is dedicated to a specific purpose it is more efficient than the MSC.ADAMS® approach discussed above, resulting in faster simulations, on the other hand the code is less versatile.

Another approach to aeroelastic modelling of the full wind turbine is used in the research code FAST [7]. In FAST, the structural motion is described by a finite series expansion of structural mode shapes. The aerodynamic forces are obtained by coupling to the AeroDyn code. This approach leads to a model with relatively small computation cost, but the accuracy highly depends on the modes chosen to describe the wind turbine.

In aeroservoelastic application a common way of simplifying the aeroelastic models is to model the wind turbine structure with rigid bodies connected by springs and dampers. The research code SymDyn [8] adopt such an approach. SymDyn is coupled to AeroDyn to get the aerodynamic forces.

The full wind turbine aeroelastic models above can be used for fatigue analysis and can be coupled to controllers for control design and analysis. The detailed models, such as the MSC.ADAMS® model and HAWC2, are especially valuable for evaluating control performance. The less comprehensive models, such as FAST and SymDyn, are useful for design and tests of controllers and for fatigue analysis. All the full wind turbine models are too comprehensive for analytical analysis and direct interpretation of terms in the models.

Eigenvalue Approach Based on Linear Wind Turbine Models

The aeroelastic behavior of the full wind turbine structure can also be analyzed by an eigenvalue approach [9, 10]. The aeroelastic research code HAWCStab [10] compute the coupled mode shapes, frequencies and aerodynamic dampings of the main flexible components of a wind turbine (tower, drivetrain, blades). The code is based on finite beam element theory and the aerodynamic loads are described by BEM and a Beddoes-Leishman [11] like dynamic stall model. The code reveals information about aeroelastic stability of the wind turbine and modes of motion.

Blade Models

Another approach to simplify aeroelastic models, often used in aeronautics, is to model a single component or part of the aeroelastic structure [12, 13, 14]. Since this type of models embraces less of the wind turbine, the degree of details of a particular phenomenon or the transparency of the model can be increased. The most important aeroelastic components of a wind turbine are the blades. The purpose of the blades is to extract aerodynamic forces from the passing airflow, therefore they are highly affected by aerodynamic forces. Furthermore the development of larger wind turbines has resulted in long slender blades with high flexibility.

An example of blade modelling is given by the frequently cited paper by Hodges and Dowell [12], which develops the nonlinear partial differential equations of motion for a twisted helicopter rotor blade. Wendell [13] develops similar partial differential equations of motion focusing on wind turbine applications. Both works can handle pre-twisted isotropic blades, but they do not take the interaction with gravity, pitch action and rotor speed variations into account. Their formulation as partial differential equations makes them suitable for analytical analysis.

Real wind turbine blades are made of composite materials, making them anisotropic, leading to internal elastic coupling between different forms of blade motion, which cannot be described by the equations discussed above. The problem by modelling composite materials can be solved by detailed 3D finite element modelling [15]. This approach however leads to relatively large models with considerable computation time. Cesnik, Hodges and Sutyrin [16] present the varia-

tional asymptotic beam section analysis (VABS). A method for relating the 3D elastic energy of a composite blade with initial twist and curvature to the strain energy of a 1-D beam description. In [17] the method is refined to produce a Timoshenko-like model for the 1-D strain energy based on the 3D properties of a blade. Ref [18] shows that using this method to describe a composite blade with a beam model produces accurate results comparable to full 3D finite element code, but with much less computation time. A turbine blade can also be modelled as a beam, as in the reaches code HAWC2, discussed above. By combining a beam model with a multi-body formulation large deflections and rigid body motion such as pitch action can be included.

Blade Section Model

The blade model is even more simplified in the 2D blade section model [19, 20]. A 2D blade section is a plane model of a cross section of the blade combined with a 2D aerodynamic model. The relatively simple structure of a blade section model allows more analytical analysis and much faster numerical simulations. Especially the aerodynamics becomes much less complex in plane 2D models compare to 3D models. Chaviaropoulos et al. [21] uses 2D blade section to analyze combined flapwise torsional blade motions, stall induced vibrations and classical flutter of wind turbine blade section. Block and Strganac [22] study flutter suppression with a full-state feedback controller and a Kalman state estimator, using a trailing edge flap as control actuator. The main drawback of the 2D blade section model is that there is no transparent connection between the blade section model and the real rotating wind turbine blade.

1.3 Control of Wind Turbines

The scope of the control analysis in this thesis is to extend the basic wind turbine controller to include fatigue load reduction. This section reviews classic control of wind turbines and possible ways to extend the controller to reduce the fatigue loads.

Classic Control

A classical control strategy for pitch regulated variable speed wind turbines is to use two proportional-integral-derivative (PID) [23] controllers: One to control the generator torque below rated wind speed, and one to control pitch angle above rated wind speed. Below rated wind speed the PID controller regulates the generator torque to track the optimal power coefficient curve using rotational speed as input. The pitch of the blades are at its minimum position, maximizing the energy extracted from the wind. Above rated wind speed the other PID controller regulates the pitch of the blades to keep rotation speed constant, using

the error in rotation speed as input. The generator power is constant at its maximum working limit.

The pitch of the blade changes the aerodynamic forces on the blade, thus affecting the blade motion. The pitch controller can both excite and damp structural vibrations of e.g. the tower and the blades. Structural vibrations are undesirable since they contribute to fatigue of the wind turbine components. As a minimum, a controller has to avoid exciting any structural vibration modes.

A step further is to use the pitch control actively, to introduce additional damping to lightly damped structural vibration modes, hereby reducing the fatigue loads. This can be achieved by additional PID controllers and additional sensors, like a tower accelerometer. The amplitude of tower vibrations was reduced by an extra PID control loop based on a measure of the tower acceleration in real scale experiments [24]. The pitch activity was increased but power and speed regulation are almost unaffected.

Modern Control

Having more than one control objective, such as rotational speed regulation and fatigue load reduction, and more than one measured control input, such as rotor speed and tower acceleration, as in the example above, motivates the use of modern control theory [25, 26].

Classic control theory, such as PID control, is developed to handle single input and single output (SISO) control systems. There is not a methodical way to expand it to multiple input and multiple output (MIMO) systems. The advantage of the PID controller is its simplicity and functionality. It has shown to be capable of handling a variety of different control tasks. Modern control theory is on the other hand developed to handle MIMO systems, and controllers for MIMO systems and multiple control objectives are derived methodically. The disadvantage is that they rely on a model of the system and the performance of the controller is highly dependent on the quality of this model. The implementation of modern controllers is also more complex than the implementation of classical PID controllers. The complexity and the model dependency can, if not carefully designed lead to a lack of robustness.

In [24] two collective pitch controllers are compared; a classical proportional-integral (PI) controller and a modern Linear-Quadratic-Gaussian controller (LQG). The feedback components are rotation speed and tower acceleration. The LQG controller gives a reduction in pitch activity and power excursions compared to the existing PI controller in a real scale experiment.

A robust controller was found to obtain the same performance with less pitch action and to reduce the fatigue loads compared to the turbine manufactures PI controller in real scale experiments [27]. The robust controller was based on a turbine model obtained through system identification [28]. The PI controller consists of two loops; one controlling the pitch angle and one controlling the

generator torque. The robust controller was basically a proportional controller followed by a nonlinear tranformation that linearizes the pitch action.

Individual Pitch Control

During operation the individual turbine blades experience different loading, e.g. when they rotate through wind shear and the effect of gravity. The effect and the resulting fatigue from these individual loads can be reduced by controlling the blades pitch individually. Switching from collective to individual pitch control increase the number of control actuators, hence the motivation for using modern MIMO controllers increase.

Computer simulations [24] show that the fatigue loads near the rotation frequency of the rotor can be considerably reduced by the use of individual pitch control compared to collective pitch control.

The use of different sensors is discussed in [29] where the fatigue at four different spots on a wind turbine are simulated with five different control and sensor configurations. Again it is found that there is a gain by switching from collective to individual pitch control, but there is only a minor difference between the different individual blade controllers and the different sensor configurations. The author states that a controller based on a series of classical PID controllers can be easier to design than a LQG controller, and that the resulting PID control algorithm is less complex than the LQG controller.

In [30] a nonlinear controller is used to reduce the effects of gravity and wind shear on the fatigue loads. The nonlinear control algorithm adds a modulation signal to the individual blades pitch signal based on the rotor position. Two different control objectives are examined; one focused on minimizing flapwise blade fatigue loads, and one focused on minimizing edgewise blade fatigue loads. The controller's performance is evaluated by computer simulations using the MSC.ADAMS aeroelastic model. The first controller, designed to minimize edgewise blade fatigue loads, is seen to demand excessively high control action and the controller excites the blades flapwise. The second controller, designed to minimize flapwise blade fatigue loads, shows good results in the simulations, significantly reducing the tip deflection with only a small effect on the power output.

Disturbance Accommodating Control

Disturbance Accommodating Control (DAC) [31] is a modern control theory that have had a special attention in the field of fatigue load reducing control on wind turbines [32, 33, 34, 35]. The principle in DAC is that disturbances are described by a series of basic functions in state space form. The states of the disturbances can then be estimated using known estimator theory, e.g. Kalman filters [25]. The estimate of the disturbances can be used in the controller to minimize the

effect of the disturbances.

One of the first application of DAC on wind turbines is seen in [36] where a PI controller and a DAC are compared. The control objective is to keep rotor speed constant in a turbulent wind field. The DAC is shown to estimate the wind speed with reasonable results. The wind turbine model is a simple first order model of the generator/rotor. The PI controller and the DAC perform equally on this task, but the author states that the design of the DAC is more methodical and less dependent of the individual wind turbine.

In [37] DAC is applied to the SymDyn model. Two different control objectives are examined; rotational speed regulation and fatigue load reduction. The rotational speed controller shows no improvement compared to a conventional controller. Compared to the conventional controller the fatigue load reducing controller shows a considerable reduction in fatigue loads of tower fort-aft loads and tower side to side loads. The cost is a reduction in power capture and a slightly increased pitch activity. The DAC is seen to estimate the fluctuations of the wind very well.

The DAC can also be used to design periodic controllers. Ref. [32] compares a periodic DAC, a time-invariant DAC and a PID controller. The controllers are based on the SymDyn model. The control objectives for the DAC are to keep constant rotor speed and to reduce blade fatigue loads. The control objective for the PID controller it is to keep constant rotor speed. The DAC is based on measuring the rotor position and speed and designed by LQG theory. The PID controller is based on measuring the rotor speed. Simulations show that there are no benefits of the time invariant DAC compared to the PID controller, whereas the periodic DAC shows a considerably reduction in blade fatigue loads. Both DACs have a higher pitch action than the PID controller. The authors conclude that the reason for the time invariant DAC not to perform better than the PID controller, is that the information from measuring the rotor position and speed is insufficient to estimate the blade loads, even though the system is theoretically observable.

Yaw Control

The yaw angle affects the structural dynamic of a wind turbine. Ref. [38] examine the possibility of reducing the tower bending with the use of active yaw control. A PID and a Linear-Quadratic-Regulator (LQR) for the yaw angle are compared to a case with fixed yaw angle. It is found that the LQR results in less fatigue loads using less control action compared to the PID controller. Both active controllers result in less fatigue than the fixed yaw angle, but higher yaw activity and thereby wear of the yaw system.

1.4 This Thesis

As wind turbines have become larger, interactions between blade deformation, blade motion, pitch action, wind shear, gravity and control have become even more important to understand and address in the design of wind turbines. The aeroelastic models [3, 5, 6] presented above, that include these effects, are too complex for most analytical analysis, direct parameter studies and control design. On the other hand, the simpler models [12, 13], which are suitable for analytical analysis and direct parameter studies, miss the effects of pitch action and gravity. Furthermore they are nonlinear, and therefore not suitable for control design.

The main contribution of this thesis is to develop an aeroelastic model which on one hand includes the important effects of large steady state blade deformation, gravity and pitch action, and on the other hand is transparent, suitable for analytical analysis and parameter studies, and furthermore linear and therefore highly suitable for control design.

1.4.1 Scope

The scope of this work is to derive a linear aeroelastic model of a wind turbine blade, which includes the effects of larger deformation, pitch action, gravity and rotor speed variations. The model is suitable for analysis and design of pitch actuators, controllers and interactions between blade motion, pitch action, gravity and wind shear. In this thesis the model is used to analyze fundamental interactions between wind, pitch action and blade motion, and to design a fatigue load reducing controller.

The aeroelastic blade model is developed in four steps: First, nonlinear partial differential equations of blade motion are derived, like those derived by [12] extended to include gravity, pitch action and rotor speed variations. Second, the steady state deformation is found by a finite difference discretization of the partial differential equations of motion combined with a BEM aerodynamic model to determine the aerodynamic forces. Third, the mode shapes, frequencies and damping of aeroelastic vibrations of the steady state deformed blade are derived by a finite difference discretization of a linearized version of the partial differential equations of motion combined with a linear unsteady aerodynamic model. Finally, the combined linear version of the partial differential equations of motion and linear unsteady aerodynamic model are approximated by an assumed mode method. This model has almost the same simplicity as the 2D blade section model, but with a transparent connection to the real wind turbine blade. The model also describes the pitch moment and rotor speed. Results that are restricted by the limitations of HAWCStab are compare with results from HAWCStab, showing good agreement.

The assumed mode model is used to analyze fundamental blade motion and pitch blade interaction. The analysis is based on frequency response results. It

shows how the blade modes interact creating zeros and peaks in the response. The analysis shows that three modes are enough for describing fundamental blade motion and pitch interaction.

The assumed mode model is also used to construct a state estimator for a three blade horizontal axis turbine. In addition to the states of the model, the estimator is also used to estimate the wind speed and wind shear. The information about the wind shear is used in an individual pitch controller for reducing the fatigue loads on the blades. The state estimator estimates the wind speed well and the wind shear very well. The load reducing controller reduces the flapwise blade motion, caused by wind shear, considerably. However, the performance of the load reducing controller decreases with increased turbulence. The controller is not capable of reducing the edgewise blade motion caused by gravity, since the aerodynamic effects on edgewise blade motion are small.

1.4.2 Outline

Chapter 2 concerns the development of the blade model and results that compare each step in the model development with results from HAWCStab. Chapter 3 is devoted to the analysis of fundamental blade motion and pitch blade interaction. Chapter 4 concerns the development of a state estimator and a fatigue load reduction controller.

Chapter 2
Model Development

This chapter concerns the development of a model describing the main aeroelasticity characteristic of a wind turbine blade, including the effect of pitch action and rotor speed variations. The development of the primary model is divided into three sub-models, where each sub-model provides information about the coupling phenomena between the blade, pitch action and rotor speed variations. In this chapter each of the sub-models are derived, tested and discussed.

First, the partial differential equations (PDEs) of structural motion of a wind turbine blade are derived. The derivation follows the work by Hodges and Dowell [12], extending this by including the effects of pitch action, gravity and rotor speed variations. Furthermore, models for pitch action and rotor speed are derived. Since the primary model is intended to be used in first hand analysis of interaction between pitch action, gravity and blade motion, it neglects features important for a full wind turbine description such as tower motion and yaw error and motion. As a first approach and to keep the equations transparent and simple, the elastic energy of the blade is described by Bernoulli-Euler theory [39] and not including anisotropic and warping effects. A more detailed description of the elastic energy is given by the formulation suggested by [16, 17], but this leads to a more complex and less transparent equations of motion.

The detailed formulation of the PDEs adopted here leads to relatively long notation, compared to e.g. [18]. However the detailed formulation makes direct interpretation and analysis of individual terms in the equations possible. The equations are fully written out, and all terms are given a physical interpretation and discussed.

Next, the PDEs are approximated by a finite difference formulation and combined with a steady state aerodynamic model based on BEM. This model is used to compute the induced velocities and the steady state deformation of the blade at given operational conditions (wind speed and pitch angle). The induced velocities and the steady state deformation of the blade are compared to results from HAWCStab [10], showing an excellent agreement.

The PDEs are linearized about the steady state deformed blade, approximated by a finite difference formulation and combined with a linear unsteady aerodynamic model, leading to an eigenvalue problem. Since the blade equations are linearized about the deformed blade, the main effects of the nonlinear coupling terms in the PDEs are preserved. This can be illustrated by the term uv which is zero when linearized about the undeformed blade and $u_1u_0+v_0v_1$ when linearized about the deformed blade, where (u_0, v_0) is the position of the deformed blade

and (u_1, v_1) the additional linear deformation. The eigenvalues of this eigenvalue problem give the frequencies and aerodynamic damping of natural vibrations of the blade. The eigenvectors give the shape of the corresponding vibrations. The frequencies, damping and shapes are compared with the result from HAWCStab.

Finally, the linearized PDEs are approximate by the method of assumed modes [40, 41], which leads to a set of approximating ordinary differential equations (ODEs). The assumed modes are based on the true modes from the eigenvalue problem above. The approximating ODEs are combined with an assumed mode approximated version of the linear aerodynamic model. The spatial dependencies of the pitch action and rotor speed models are also approximated by the assumed modes. This leads to a set of approximating ODEs describing the blade motion, pitch action and rotor speed, including unsteady aerodynamic forces. The set of ODEs are extended by a model of the drivetrain flexibility and a simple generator torque model. The assumed mode model is compared to the finite difference model and to HAWCstab results.

The following section presents the structural model. In Section 2.2, the PDEs are derived and discussed. In Section 2.3, the connection between blade motion and aerodynamic forces is derived and the aerodynamic models are presented. In Section 2.4, a nonlinear steady state version of the PDEs is approximated by a finite difference formulation, used to compute the steady state deformation and induced velocities. In Section 2.5 a linearized version of the PDEs is approximated by a finite difference formulation leading to an eigenvalue problem, used to compute natural modes of aeroelastic vibrations of the blade. In Section 2.6, the assumed mode description is derived and discussed. Sections 2.1 and 2.2 are an extension of the work presented by the author in [P3].

2.1 Structural Model

The structural model consists of a rotating inextensible blade with flapwise, edgewise and torsional degrees of freedom. The blade is exposed to pitch action, varying rotor speed and non-conservative forces (e.g. aerodynamic forces). The rotor speed is associated with a torque and a rotational moment of inertia, describing the generator and drivetrain without gearing and drivetrain flexibility. The pitch action is associated with a pitch moment, describing the torque from the pitch actuator on the blade, or from the blade on the pitch actuator.

The system does not include the influence from tower and yaw motion, drivetrain flexibility, precone blade, shaft tilt and warping. The shear center[1] and the tension center[2] of the blade are assumed to coincide. Since, the focus of this

[1]The point on the blade cross section where a force in the cross section plane causes bending only, no twist.

[2]The point on the blade cross section where a tension force does not cause any bending.

thesis is blade modelling, not a complete description of a wind turbine, these simplifications are justified.

Figure 2.1(a) shows the blade rotating in the rotor plane. The Y-axis of the (X, Y, Z)-frame points downwind and the (X, Z)-axes span the rotor plane, with the Z-axis pointing upwards. Since the tower-top and yaw position are assumed fixed the (X, Y, Z)-frame becomes an inertial frame. The $(\hat{x}, \hat{y}, \hat{z})$-frame rotates with the hub, allowing the $\hat{z}$-axis to be aligned with the pitch axis pi of the blade and the $\hat{y}$-axis is aligned with the Y-axis. The angle between the two frames is denoted ϕ (the azimuth angle of the rotor).

Figure 2.1(b) shows a cross section of the blade looking outwards along the $\hat{z}$-axis. The position of the blade is described in the (x, y, z)-frame, which is rotated β (the pitch angle) around the $\hat{z}$-axis. The elastic principal (η, ξ)-axes of each blade section are rotated the angle $\tilde{\theta} + \theta$ relative to the (x, z)-plane, where $\tilde{\theta} = \tilde{\theta}(s)$ is the pre-twist of the elastic properties and $\theta = \theta(s, t)$ is the time dependent twist of this section of the blade.

The position of the elastic axis ea in the (x, y, z)-frame is given by $(u+l_{pi}, v, w)$, where $u = u(s, t)$ and $v = v(s, t)$ are the deflection from the undeformed position in the x and y-directions, respectively. The undeformed position of ea on the x-axis is given by $l_{pi} = l_{pi}(s)$. The position in the z-direction is given by $w = \int_r^s \sqrt{(1 - (l'_{pi} + u')^2 - v'^2)}\mathrm{d}s$, based on the inextensibility of the blade. The w coordinate is divided into a static part $w_0 = \int_r^s \sqrt{1 - l'^2_{pi}}\mathrm{d}s$ and an approximation to the time dependent part $w_1 = -\frac{1}{2}\int_r^s \sqrt{u'^2 + v'^2 + 2l'_{pi}u'}\mathrm{d}s$. The independent variable t is the time and s is the distance from the root of the blade to this cross section of the blade measured along ea. The radius of the hub is r and the radius of the rotor is R, also measured along the ea. The radius of the rotor plane is $w(R)$.

The sum of rotational inertia of the hub, gearbox and generator is described by J_{gen}. The inertia of the blade is described by a concentrated mass $m = m(s)$ and a moment of rotational inertia $I_{cg} = I_{cg}(s)$ (associated to rotation in the cross section plane) for each blade section. Both are related to the center of gravity cg which is assumed to be located on the chord at the distance $l_{cg} = l_{cg}(s)$ from ea. The chord is rotated the angle $\bar{\theta} + \theta$ relative to the (x, z)-plane, where $\bar{\theta} = \bar{\theta}(s)$ is the pre-twist of the chord.

The external forces, such as aerodynamic forces, on the blade are described by four components; three forces $(f_u,\ f_v,\ f_w) = (f_u(s, t),\ f_v(s, t),\ f_w(s, t))$ in the (x, y, z)-directions, respectively, and a twisting moment $M = M(s, t)$. The forces act at the elastic axis of the blade.

The pitch moment M_{pitch} is associated with the pitch angle rotation and the generator torque is given by T_{gen}.

In summary, the state of the system is given by $(u, v, \theta, \beta, \phi)$ where (ϕ, β) can be prescribed, given by external models or described by the derived equations.

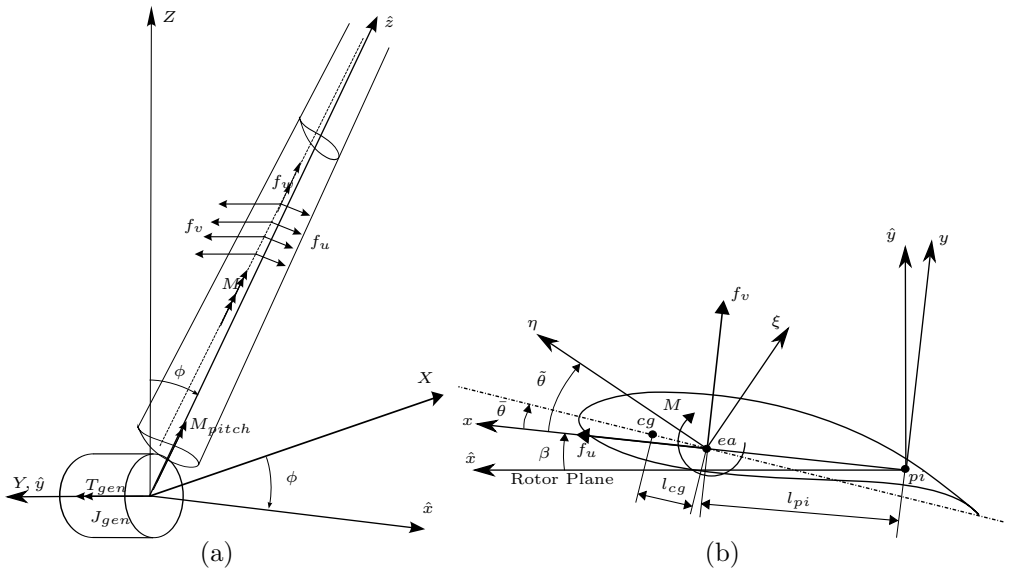

Figure 2.1: a) The inertial (X, Y, Z)-frame and the rotating $(\hat{x}, \hat{y}, \hat{z})$-frame with the $\hat{z}$-axis aligned with the pitch axis of the blade. The external forces (f_u, f_v, f_w) acts at the elastic axis in the $(\hat{x}, \hat{y}, \hat{z})$ directions, respectively. b) Cross section of the blade looking outwards along the $\hat{z}$-axis

The system is exposed to the external forces $(f_u, f_v, f_w, M, T_{gen}, M_{pitch})$, where (T_{gen}, M_{pitch}) only affects the (ϕ, β) equations, respectively.

2.2 Derivation of the Equations of Motion

The derivation of the equations of motion follows the method used in [12]. First, the potential and kinetic energies for the system is set-up. Second, the equations of motion and boundary condition equations are derived from these energy expressions using the extended Hamilton's principle [41].

2.2.1 Method

Order Scheme

To avoid unnecessary complications of the equations of motion, relatively small terms are neglected. This is done in a consistent manner by introducing an ordering scheme, assuming $(\frac{u}{R}, \frac{v}{R}, \frac{l_{pi}}{R}, \frac{l_{cg}}{R}, \theta, c\tilde{\theta}', c\bar{\theta}', \frac{m' l_{cg}}{m l'_{cg}})$ to be of order ϵ, where $c = c(s)$ is the local chord, $\epsilon \ll 1$ is used as a bookkeeping parameter denoting the smallness of terms, $\dot{(\,)} \equiv \frac{\mathrm{d}}{\mathrm{d}t}$ and $(\,)' \equiv \frac{\mathrm{d}}{\mathrm{d}s}$. Furthermore, the angular acceleration of the rotor is assumed to be $\ddot{\phi} R \sim \ddot{u}$. A second order scheme is applied such that terms of order ϵ^{n+2} or higher are neglected, where n is the lowest order of a term in the expression.

Transformations

Before deriving the equations of motion a transformation between the rotating (x, y, z)-frame, in which the blade deflection is described, and the inertial (X, Y, Z)-frame is found

$$\left[\mathbf{i}, \mathbf{j}, \mathbf{k}\right]^{\mathrm{T}} = \mathbf{T}_\beta \mathbf{T}_\phi \left[\mathbf{I}, \mathbf{J}, \mathbf{K}\right]^T \tag{2.1}$$

where $[\mathbf{i}, \mathbf{j}, \mathbf{k}]^T$ and $[\mathbf{I}, \mathbf{J}, \mathbf{K}]^T$ are the unit vectors in the (x, y, z) and (X, Y, Z)-frames, respectively. The matrices $\mathbf{T}_\beta$ and $\mathbf{T}_\phi$ are the transformations from the $(\hat{x}, \hat{y}, \hat{z})$-frame to the (x, y, z)-frame, and from the (X, Y, Z)-frame to the $(\hat{x}, \hat{y}, \hat{z})$-frame, respectively. Both matrices can be found in Appendix A.

The transformation between the principle axis and the (x, y, z)-frame is given by $\mathbf{T}_e$ and the transformation between the chord and the (x, y, z)-frame is given by $\mathbf{T}_c$. Both matrices can be found in Appendix A.

Potential Energy

The strain in the blade is measured by Green's strain tensor

$$2[\mathrm{d}s, \mathrm{d}\eta, \mathrm{d}\xi][\epsilon_{ij}][\mathrm{d}s, \mathrm{d}\eta, \mathrm{d}\xi]^{\mathrm{T}} = \mathrm{d}\mathbf{r}_1 \cdot \mathrm{d}\mathbf{r}_1 - \mathrm{d}\mathbf{r}_0 \cdot \mathrm{d}\mathbf{r}_0 \tag{2.2}$$

where d denotes the differential, ϵ_{ij} is the strain tensor and

$$\mathbf{r}_0 = \left[\mathbf{I}, \mathbf{J}, \mathbf{K}\right] \mathbf{T}_\phi^{\mathrm{T}} \mathbf{T}_\beta^{\mathrm{T}} \left[\left[l_{pi}, 0, w_0\right]^{\mathrm{T}} + (\mathbf{T}_e\big|_{u=v=\theta=0})^{\mathrm{T}} \left[\eta_0, \xi_0, 0\right]^{\mathrm{T}}\right] \tag{2.3}$$

is a position vector defining a point in the undeformed blade, where (η_0, ξ_0) is the position of the point in the undeformed blade cross section. The same point in the deformed blade is defined by

$$\mathbf{r}_1 = \left[\mathbf{I}, \mathbf{J}, \mathbf{K}\right] \mathbf{T}_\phi^{\mathrm{T}} \mathbf{T}_\beta^{\mathrm{T}} \left[\left[l_{pi} + u, v, w_0 + w_1\right]^{\mathrm{T}} + \mathbf{T}_e^{\mathrm{T}} \left[\eta_1, \xi_1, 0\right]^{\mathrm{T}}\right] \tag{2.4}$$

where (η_1, ξ_1) is the position of the point in the deformed blade cross section.

Assuming uniaxial stress $\sigma_{22} = \sigma_{33} = \sigma_{23} = 0$, where σ_{ij} is the stress tensor and applying Hooke's law [39] gives $\epsilon_{22} = \epsilon_{33} = -\nu\epsilon_{11}$, where ν is Poisson's ratio [39]. Expanding these relations to second order of the bookkeeping parameter ϵ it can be shown that $\eta_1 = \eta_0$ and $\xi_1 = \xi_0$ to second order. Expanding the remanding strain tensor components to second order of ϵ gives:

$$\begin{aligned} \epsilon_{11} &= -u'' \left(\eta \cos(\tilde{\theta}) - \xi \sin(\tilde{\theta})\right) - v'' \left(\eta \sin(\tilde{\theta}) + \xi \cos(\tilde{\theta})\right) \\ \epsilon_{12} &= -\tfrac{1}{2}\xi\theta' \,, \qquad \epsilon_{13} = \tfrac{1}{2}\eta\theta' \end{aligned} \tag{2.5}$$

Using engineering strain $\epsilon_{ss} = \epsilon_{11}$, $\epsilon_{s\eta} = 2\epsilon_{12}$, $\epsilon_{s\xi} = 2\epsilon_{13}$ and stresses $\sigma_{ss} = E\epsilon_{ss}$, $\sigma_{s\eta} = G\epsilon_{s\eta}$, $\sigma_{s\xi} = G\epsilon_{s\xi}$ where E is the tensile modulus of elasticity (Young's modulus [39]) and G is the shear modulus of elasticity, the elastic energy becomes:

$$\delta V_{ela} = \int_r^R \iint_A \left(\sigma_{ss}\delta\epsilon_{ss} + \sigma_{s\eta}\delta\epsilon_{s\eta} + \sigma_{s\xi}\delta\epsilon_{s\xi}\right) \mathrm{d}\eta\mathrm{d}\xi\mathrm{d}s \tag{2.6}$$

The potential energy associated with the gravity field defined in the inertial frame (X, Y, Z) is given by

$$V_{gra} = \int_r^R \mathbf{r}_{cg}^{\mathrm{T}} \cdot \mathbf{g} \mathrm{d}s \tag{2.7}$$

where $\mathbf{g} = [0, 0, -g]^{\mathrm{T}}$ is the gravity field and

$$\mathbf{r}_{cg} = \left[\mathbf{I}, \mathbf{J}, \mathbf{K}\right] \mathbf{T}_{\phi}^{\mathrm{T}} \mathbf{T}_{\beta}^{\mathrm{T}} \left[\left[l_{pi} + u, v, w_0 + w_1\right]^{\mathrm{T}} + \mathbf{T}_{c}^{\mathrm{T}} \left[l_{cg}, 0, 0\right]^{\mathrm{T}} \right] \tag{2.8}$$

is a position vector describing the center of gravity.

Kinetic Energy

The inertia of this system is described by the following parameters: mass pr. length m, moment of rotational inertia pr. length I_{cg} of the blade and moment of rotational inertia J_{gen} of the hub, gear box and generator. The use of a concentrated mass description of the blade inertia, instead of a more general description integrating over the cross-section, leads to less complexity in the derivation. A general description leads to extra terms, such as rotational inertia about x and y-axis, but these are small and therefore neglected. The kinetic energy of the system is given by

$$T = \frac{1}{2} J_{gen} \dot{\phi}^2 + \int_r^R \left(\frac{1}{2} m \dot{\mathbf{r}}_{cg}^{\mathrm{T}} \cdot \dot{\mathbf{r}}_{cg} + \frac{1}{2} I_{cg} (\dot{\beta} + \dot{\theta})^2 \right) \mathrm{d}s \tag{2.9}$$

where $\dot{\beta} + \dot{\theta}$ is the angular velocity of the blade section about the elastic axis.

Non-conservative forces

The non-conservative forces are included by describing the variational work done by them for any admissible variation

$$\delta Q = T_{gen} \delta\phi + M_{pitch} \delta\beta + \int_r^R \left(\mathbf{f}^{\mathrm{T}} \cdot \delta \mathbf{r}_{ea} + M \delta(\theta + \beta) \right) \mathrm{d}s \tag{2.10}$$

where $\mathbf{f} = \mathbf{T}_{\phi}^{\mathrm{T}} \mathbf{T}_{\beta}^{\mathrm{T}} [f_u, f_v, f_w]^{\mathrm{T}}$ and

$$\mathbf{r}_{ea} = \left[\mathbf{I}, \mathbf{J}, \mathbf{K}\right] \mathbf{T}_{\phi}^{\mathrm{T}} \mathbf{T}_{\beta}^{\mathrm{T}} \left[l_{pi} + u, v, w_0 + w_1\right]^{\mathrm{T}} \tag{2.11}$$

is a position vector describing the elastic axis.

2.2.2 Equations of motion

By demanding that any admissible variation of the action integral $\delta H \equiv \int_{t_1}^{t_2}(\delta T - \delta u_{ela} - \delta u_{gra} + \delta Q)\mathrm{d}t$ is zero, a set of partial differential equations of motion and a set of boundary condition equations are derived (extended Hamilton's principle [41]). The variation of the w_1 term leads to integral terms in the equations of motion, while the w_1 itself does not appear as it is relatively small. First, the partial differential equations of the blades bending and torsional motion are presented, followed by the corresponding boundary conditions. Secondly, the equations of motion for the rotor azimuth angle and the pitch angle are presented.

Blade Bending Motion

The equation of motion of the x and y-directions becomes:

$$\begin{aligned} &m(\ddot{u} - \ddot{\theta} l_{cg}\sin(\bar{\theta})) + F_{u,1}(\ddot{\beta},\dot{\beta},\dot{\phi},\dot{v},\dot{\theta},u',u,v,\theta,\beta) + F_{u,2}(\dot{\phi},\dot{u},\dot{v},u',v,\theta,\beta) \\ &\quad + F_{u,3}(\phi,\beta,\theta,u',v') + F_{u,4}(u'',v'',\theta) + F_{u,5}(\ddot{\phi},\beta) \\ &\quad = f_u + \left((u' + l'_{pi})\int_s^R f_w \mathrm{d}\rho\right)' \end{aligned} \tag{2.12a}$$

$$\begin{aligned} &m(\ddot{v} + \ddot{\theta} l_{cg}\cos(\bar{\theta})) + F_{v,1}(\ddot{\beta},\dot{\beta},\dot{\phi},\dot{v},\dot{;}u',u,v,\theta,\beta) + F_{v,2}(\dot{\phi},\dot{u},\dot{v},u',v,\theta,\beta) \\ &+F_{v,3}(\phi,\beta,\theta,u',v') + F_{v,4}(u'',v'',\theta) + F_{v,5}(\ddot{\phi},\beta) = f_v + \left(v'\int_s^R f_w \mathrm{d}\rho\right)' \end{aligned} \tag{2.12b}$$

The direction of the x-axis can be turned into the direction of the y-axis by changing the β angle 90 deg and the y-axis can be turned into the direction of the x-axis by changing the β angle -90 deg. Therefore the only differences between the terms in (2.12a) and (2.12b) are the directions of projection of the forces. In the following the individual terms in (2.12) are shown and the physical interpretation of terms is discussed. Because of the similarity between the terms in (2.12a) and (2.12b) only the terms in (2.12a) will be discussed.

The influence of pitch action is described by

$$\begin{aligned} F_{u,1} =& -\ddot{\beta} m v_{cg} - \dot{\beta}^2 m u_{cg} - 2\dot{\beta} m \dot{v}_{cg} \\ &+ (T_1 l_{cg}\cos(\bar{\theta}))' + \left((u' + l'_{pi})\int_s^R T_1 \mathrm{d}\rho\right)' \end{aligned} \tag{2.13a}$$

$$F_{v,1} = \ddot{\beta} m u_{cg} - \dot{\beta}^2 m v_{cg} + 2\dot{\beta} m \dot{u}_{cg} + (T_1 l_{cg}\sin(\bar{\theta}))' + \left(v'\int_s^R T_1 \mathrm{d}\rho\right)' \tag{2.13b}$$

where $u_{cg} = u + l_{pi} + l_{cg}\cos(\bar{\theta}) - l_{cg}\theta\sin(\bar{\theta})$ and $v_{cg} = v + l_{cg}\sin(\bar{\theta}) + l_{cg}\theta\cos(\bar{\theta})$ are the x and y coordinates, respectively, of the center of gravity in the (x, y, z)-frame, $T_1 = 2m\dot{\beta}\dot{\phi}((u + l_{pi})\sin(\beta) + v\cos(\beta) + l_{cg}\sin(\bar{\theta} + \beta))$ is the Coriolis force in

the z-direction, associated with the angular velocity of the (x, y, z)-frame about the z-axis and about the $\hat{y}$-axis. The first term in (2.13a) is the fictitious force[3] in the x-direction associated with the angular acceleration of the (x, y, z)-frame about the z-axis. The second term is the centrifugal force associated with the angular velocity of the (x, y, z)-frame about the z-axis and the offset of cg in the x-direction due to the edgewise deflection. The third term is the Coriolis force associated with the angular velocity of the (x, y, z)-frame about the z-axis and the velocity of cg in the y-direction. The fourth term in (2.13a) is the spatial derivative of the moment caused by the offset of cg and the Coriolis force T_1. The last term is the bending moment caused by the Coriolis force T_1 on the remaining part of the blade, from this point to the tip.

The influence from the rotor speed is described by

$$\begin{aligned} F_{u,2} =& -\dot{\phi}^2 m\hat{u}_{cg}\cos(\beta) - \dot{\phi}^2\big(ml_{cg}w_0(\cos(\bar{\theta}) - \theta\sin(\bar{\theta}))\big)' - (l_{cg}T_2)'\cos(\bar{\theta}) \\ & - 2\dot{\phi}ml_{cg}(\dot{u}'\cos(\bar{\theta}) + \dot{v}'\sin(\bar{\theta}))\cos(\beta) \\ & - \left((u' + l'_{pi})\int_s^R \left(\dot{\phi}^2 m w_0 + T_2\right)\mathrm{d}\rho\right)' \end{aligned} \tag{2.14a}$$

$$\begin{aligned} F_{v,2} =& \dot{\phi}^2 m\hat{u}_{cg}\sin(\beta) - \dot{\phi}^2\big(ml_{cg}w_0(\sin(\bar{\theta}) + \theta\cos(\bar{\theta}))\big)' - (l_{cg}T_2)'\sin(\bar{\theta}) \\ & + 2\dot{\phi}ml_{cg}(\dot{u}'\cos(\bar{\theta}) + \dot{v}'\sin(\bar{\theta}))\sin(\beta) \\ & - \left(v'\int_s^R \left(\dot{\phi}^2 m w_0 + T_2\right)\mathrm{d}\rho\right)' \end{aligned} \tag{2.14b}$$

where $\hat{u}_{cg} = (u + l_{pi})\cos(\beta) - v\sin(\beta) + l_{cg}\cos(\bar{\theta} + \beta) - l_{cg}\theta\sin(\bar{\theta} + \beta)$ is the $\hat{x}$ coordinate of the center of gravity in the $(\hat{x}, \hat{y}, \hat{z})$-frame, $T_2 = 2m\dot{\phi}(\dot{u}\cos(\beta) - \dot{v}\sin(\beta))$ is the Coriolis force in the z-direction which is associated with the rotation in the rotor plane and the velocity of cg in the $\hat{x}$-direction. The first term in (2.14a) is the centrifugal force associated with the rotation in the rotor plane and the offset of cg in the x-direction projected onto the x-direction. The second term in (2.14a) is the spatial derivative of the moments caused by the fictitious centrifugal force associated with the rotation in the rotor plane and the offset of cg from the center of rotation. The third is the spatial derivative of the moments caused by the Coriolis force T_2. The fourth term is the Coriolis force associated with the rotation of the blade in the rotor plane and the velocity of cg in the $\hat{z}$-direction. The last term in (2.14a) is the bending moment from the centrifugal and the Coriolis forces T_2 on the remaining part of the blade from this point to the tip.

[3]Fictitious force refers to a force which occurs because the system is described in a moving frame.

The influence from gravity is described by

$$\begin{aligned} F_{u,3} = & mg\sin(\phi)\cos(\beta) \\ & + \big((l_{cg}(u' + l'_{pi}))'\cos(\bar{\theta})\cos(\beta) + (l_{cg}v')'\sin(\bar{\theta})\cos(\beta)\big)mg\sin(\phi) \\ & - \big(ml_{cg}(\cos(\bar{\theta}) - \theta\sin(\bar{\theta}))\big)'g\cos(\phi) + \left((u' + l'_{pi})\int_s^R mg\cos(\phi)\mathrm{d}\rho\right)' \end{aligned} \tag{2.15a}$$

$$\begin{aligned} F_{v,3} = & -mg\sin(\phi)\sin(\beta) \\ & + \big((l_{cg}(u' + l'_{pi}))'\sin(\bar{\theta})\cos(\beta) - (l_{cg}v')'\sin(\bar{\theta})\sin(\beta)\big)mg\sin(\phi) \\ & - \big(ml_{cg}(\sin(\bar{\theta}) + \theta\cos(\bar{\theta}))\big)'g\cos(\phi) + \left(v'\int_s^R mg\cos(\phi)\mathrm{d}\rho\right)' \end{aligned} \tag{2.15b}$$

where the first term in (2.15a) is the x-component of the gravity force. The second term is the spatial derivative of the moment caused by the $\hat{x}$-component of the gravity force and the offset of cg in the z-direction. The third term is the spatial derivative of the moment caused by the distance between cg and ea in the x-direction and the z-component of the gravity force. The last term in (2.15a) is the bending moment from the z-component of the gravity force on the remaining part of the blade, from this point to the tip.

The restoring force caused by the bending stiffness of the blade is described by

$$\begin{aligned} F_{u,4} = & \big(E(I_\xi\cos^2(\tilde{\theta}) + I_\eta\sin^2(\tilde{\theta}))u''\big)'' + \big(E(I_\xi - I_\eta)\cos(\tilde{\theta})\sin(\tilde{\theta})v''\big)'' \\ & - \big(E(I_\xi - I_\eta)\theta(u''\sin(2\tilde{\theta}) - v''\cos(2\tilde{\theta}) + l''_{pi}\sin(\tilde{\theta})\cos(\tilde{\theta}))\big)'' \end{aligned} \tag{2.16a}$$

$$\begin{aligned} F_{v,4} = & \big(E(I_\xi\sin^2(\tilde{\theta}) + I_\eta\cos^2(\tilde{\theta}))v''\big)'' + \big(E(I_\xi - I_\eta)\cos(\tilde{\theta})\sin(\tilde{\theta})u''\big)'' \\ & + \big(E(I_\xi - I_\eta)\theta(u''\cos(2\tilde{\theta}) + v''\sin(2\tilde{\theta}))\big)'' \\ & - \big(l''_{pi}\theta E(I_\xi\sin^2(\theta) + I_\eta\cos^2(\theta))\big)'' \end{aligned} \tag{2.16b}$$

where the first term is the bending stiffness in the x-direction and the second term is the coupling to the y-direction. The last term is the coupling to the twist. The principle moments of inertia are given by $I_\xi = \iint_A \eta^2\mathrm{d}\eta\mathrm{d}\xi$ and $I_\eta = \iint_A \xi^2\mathrm{d}\eta\mathrm{d}\xi$.

The effect of an angular acceleration of the rotor is described by

$$F_{u,5} = m\ddot{\phi}w_0\cos(\beta)\ , \quad F_{v,5} = -m\ddot{\phi}w_0\sin(\beta) \tag{2.17}$$

which is the fictitious angular acceleration of cg associated with the angular acceleration of the (x, y, z)-frame about the Y-axis.

The right hand sides of (2.12) describes the external forces, f_u and f_v are the forces in the x and y-direction, respectively. The last term is the bending moment from the external force in the z-direction on the the blade, from this point s to the tip R.

Blade Torsional Motion

The equation of torsional motion is:

$$\begin{aligned}(I_{cg}+ml_{cg}^2)\ddot{\theta}-ml_{cg}(\ddot{u}\sin(\bar{\theta})-\ddot{v}\cos(\bar{\theta}))+F_{\theta,1}(\ddot{\beta},\dot{\beta},\dot{u},\dot{v},u,v)+F_{\theta,2}(\dot{\phi},u',v',u,v,\beta)\\ + F_{\theta,3}(\ddot{\phi},\beta) + F_{\theta,4}(\phi,u',v',\theta,\beta) + F_{\theta,5}(u'',v'',\theta') + F_{\theta,6}(\theta') = M\end{aligned} \quad (2.18)$$

The influence from the pitch action is described by

$$\begin{aligned}F_{\theta,1} =&(I_{cg} + ml_{cg}^2)\ddot{\beta} - \ddot{\beta}ml_{cg}(u\cos(\bar{\theta}) + v\sin(\bar{\theta}))\\ &+ ml_{cg}\dot{\beta}^2((u + l_{pi})\sin(\bar{\theta}) - v\cos(\bar{\theta})) + 2ml_{cg}\dot{\beta}(\dot{u}\cos(\bar{\theta}) + \dot{v}\sin(\bar{\theta}))\end{aligned} \quad (2.19)$$

where the first term is the fictitious angular acceleration associated with the angular acceleration of the (x, y, z)-frame about the z-axis. The second term is the centrifugal force associated with the rotation of the (x, y, z)-frame about the z-axis. The last term is the Coriolis force associated with the rotation of the (x, y, z)-frame about the z-axis and the velocity of cg in the chord direction.

The rotor speed leads to the centrifugal forces

$$F_{\theta,2} = ml_{cg}\dot{\phi}^2\hat{u}_{cg}\sin(\bar{\theta} + \beta) + ml_{cg}w_0\dot{\phi}^2(v'\cos(\bar{\theta}) - (u' + l'_{pi})\sin(\bar{\theta})) \quad (2.20)$$

where the first term is associated with the offset of cg in the $\hat{x}$-direction and the second is associated with the distance from center of rotation to cg.

The acceleration of the rotor leads to the following term

$$F_{\theta,3} = -m\ddot{\phi}w_0l_{cg}\sin(\bar{\theta} + \beta) \quad (2.21)$$

which is the fictitious angular acceleration of cg associated with the angular acceleration of the (x, y, z) frame about the Y-axis.

The effect of gravity is described by

$$\begin{aligned}F_{\theta,4} =& - l_{cg}(\sin(\beta + \bar{\theta}) + \theta\cos(\beta + \bar{\theta}))mg\sin(\phi)\\ &+ l_{cg}(v'\cos(\bar{\theta}) - (u' + l'_{pi})\sin(\bar{\theta}))mg\cos(\phi)\end{aligned} \quad (2.22)$$

where the first term is the twisting moment caused by the $\hat{x}$-component of the gravity force and the distance between cg and ea in the $\hat{y}$-direction. The last term is the twisting moment caused by the distance between cg and ea and the z-component of the gravity force projected onto the cross section of the deformed blade.

The elastic coupling between the bending and twisting of the blade is described by

$$\begin{aligned}F_{\theta,5} =& -\big(EI_{\eta\eta\xi}(\tilde{\theta} + \theta)'(u''\sin(\tilde{\theta}) - v''\cos(\tilde{\theta}))\big)'\\ &+ \big(EI_{\eta\xi\xi}(\tilde{\theta} + \theta)'(u''\cos(\tilde{\theta}) + v''\sin(\tilde{\theta}))\big)'\\ &- (EI_{\xi} - EI_{\eta})\big((u''^2 - v''^2)\cos(\tilde{\theta})\sin(\tilde{\theta}) - u''v''\cos(2\tilde{\theta})\big)\\ &- EI_{\xi}l''_{pi}(u''\cos(\tilde{\theta}) + v''\sin(\tilde{\theta}))\sin(\tilde{\theta})\\ &+ EI_{\eta}l''_{pi}(u''\sin(\tilde{\theta}) - v''\cos(\tilde{\theta}))\cos(\tilde{\theta})\end{aligned} \quad (2.23)$$

where $I_{\eta\eta\xi} = \iint_A \eta(\eta^2 + \xi^2)\mathrm{d}\eta\mathrm{d}\xi$ and $I_{\eta\xi\xi} = \iint_A \xi(\eta^2 + \xi^2)\mathrm{d}\eta\mathrm{d}\xi$. The restoring force caused by torsional stiffness is given by

$$F_{\theta,6} = -\left(GJ\left(\theta' + v'(u'' + l''_{pi})\right)\right)' \tag{2.24}$$

where the polar moment of inertia is $J = \iint_A (\eta^2 + \xi^2)\,\mathrm{d}\eta\mathrm{d}\xi$. The right hand side of (2.18) describes the external moment on the blade M.

Boundary Conditions

The boundary conditions for the root of the blade is given by the geometric constraints

$$u(0,t) = u'(0,t) = v(0,t) = v'(0,t) = \theta(0,t) = 0 \tag{2.25}$$

because the coordinate frame used to describe the blade follows the root of the blade.

The boundary conditions for the tip of the blade are determined by the boundary condition equations which are derived by demanding any admissible variation of the action integral to be zero. The boundary conditions become:

$$\begin{aligned}
u''(R,t) &= v''(R,t) = \theta'(R,t) = 0 \\
u'''(R,t) &= \frac{ml_{cg}}{EI_\xi I_\eta}(\dot{\phi}^2 w_0 - g\cos(\phi))\left(I_\eta \sin(\tilde{\theta} - \bar{\theta})\sin(\tilde{\theta}) + I_\xi \cos(\tilde{\theta} - \bar{\theta})\cos(\tilde{\theta})\right) \\
v'''(R,t) &= \frac{ml_{cg}}{EI_\xi I_\eta}(\dot{\phi}^2 w_0 - g\cos(\phi))\left(I_\eta \cos(\tilde{\theta} - \bar{\theta})\sin(\tilde{\theta}) - I_\xi \sin(\tilde{\theta} - \bar{\theta})\cos(\tilde{\theta})\right)
\end{aligned} \tag{2.26}$$

In the case $l_{cg}(R) \neq 0$ the boundary conditions for the tip are functions of rotor speed $\dot{\phi}$ and rotor position ϕ and therefore time-varying. Since an offset of the center of gravity from the elastic axis at the blade tip leads to a bending moment at the tip caused by the gravity and centrifugal force. Most modern wind turbine blades however are tapered at the tip $l_{cg}(s) \underset{s\to R}{\longrightarrow} 0$, making the time-variation of the boundary conditions negligible.

Pitch Action

The equation of motion for the pitch angle is

$$\begin{aligned}
&\int_r^R \Big((I_{cg} + ml_{cg}^2)(\ddot{\theta} + \ddot{\bar{\beta}}) + m(l_{pi}^2 + 2l_{cg}l_{pi}\cos(\bar{\theta}))\ddot{\beta}\Big)\,\mathrm{d}s \\
&+ \int_r^R \big(-m\ddot{u}l_{cg}\sin(\bar{\theta}) + m\ddot{v}(l_{pi} + l_{cg}\cos(\bar{\theta}))\big)\,\mathrm{d}s \\
&+ F_{\beta,1}(\dot{\beta}, \dot{u}, u) + F_{\beta,2}(\dot{\beta}, \dot{v}, v) + F_{\beta,3}(\dot{\phi}, u, v, \beta) + F_{\beta,4}(\ddot{\phi}, u, v, \beta) \\
&+ F_{\beta,5}(u, v, \theta, \beta, \phi) + F_{\beta,6}(\ddot{\beta}, \ddot{u}, \ddot{v}, u, v) \\
&= M_{pitch} + \int_r^R \big(M + f_v(u + l_{pi}) - f_u v\big)\mathrm{d}s
\end{aligned} \tag{2.27}$$

where

$$F_{\beta,1}(\dot{\beta}, \dot{v}, u) = 2\dot{\beta}\int_r^R m\dot{u}u_{cg}\mathrm{d}s\ , \quad F_{\beta,2}(\dot{\beta}, \dot{v}, v) = 2\dot{\beta}\int_r^R m\dot{v}v_{cg}\mathrm{d}s \tag{2.28}$$

are the moments caused by the Coriolis force associated with the relative velocity of the blade and rotation of the (x, y, z)-frame about the z-axis.

The effect of the centrifugal force associated with the rotation of the (x, y, z)-frame about the $\hat{y}$-axis is described by

$$F_{\beta,3}(\dot{\phi}, u, v, \beta) = \dot{\phi}^2\int_r^R m\hat{u}_{cg}\hat{v}_{cg}\mathrm{d}s \tag{2.29}$$

where $\hat{v}_{cg} = (u + l_{pi})\sin(\beta) + v\cos(\beta) + l_{cg}\sin(\bar{\theta} + \beta)$ is the $\hat{y}$ coordinate of the center of gravity in the $(\hat{x}, \hat{y}, \hat{z})$-frame.

The effect of an angular acceleration of the (x, y, z)-frame about the $\hat{y}$-axis is described by:

$$F_{\beta,4}(\ddot{\phi}, u, v, \beta) = -\ddot{\phi}\int_r^R mw_0\hat{v}_{cg}\mathrm{d}s \tag{2.30}$$

The gravity force is described by

$$F_{\beta,5}(u, v, \beta, \phi) = g\sin(\phi)\int_r^R m\hat{v}_{cg}\mathrm{d}s \tag{2.31}$$

and

$$\begin{aligned}
F_{\beta,6}(\ddot{\beta}, \ddot{u}, \ddot{v}, u, v) =& \ddot{\beta}\int_r^R m\big(u^2 + v^2 + 2l_{cg}(u\cos(\bar{\theta}) + v\sin(\bar{\theta})) + 2l_{pi}u\big)\mathrm{d}s \\
&+ \int_r^R m\big(\ddot{v}u - \ddot{u}v\big)\mathrm{d}s
\end{aligned} \tag{2.32}$$

is nonlinear inertia.

If the pitch angle is prescribed or given by an external model (2.27) can be used to compute the pitch moment, by solving for M_{pitch} and feed in the blade motion and pitch action.

Rotor Position

Assuming a rigid drivetrain and no gearing the rotor position is described by

$$\begin{aligned} &J_{gen}\ddot{\phi} + \int_r^R mw_0 \left(w_0\ddot{\phi} + \ddot{u}\cos(\beta) - \ddot{v}\sin(\beta) \right) \mathrm{d}s \\ &+F_{\phi,1}(\dot{\beta}, u, v, \beta) + F_{\phi,2}(\dot{\beta}, \dot{u}, \dot{v}, \dot{\theta}, \beta) + F_{\phi,3}(u, \phi)) + F_{\phi,4}(\ddot{\beta}, u, v, \beta) \\ &=T_{gen} \\ &\quad + \int_r^R \left(\left(f_u\cos(\beta) - f_v\sin(\beta) \right) w_0 + f_w \left(v\sin(\beta) - (u + l_{pi})\cos(\beta) \right) \right) \mathrm{d}s \end{aligned} \tag{2.33}$$

where T_{gen} is the generator torque and J_{gen} is the sum of inertia of the rotor, gearbox, and generator. The effect of the centrifugal force associated with pitch rotation of the (x, y, z)-frame about the z-axis is described by

$$F_{\phi,1}(\dot{\beta}, u, v, \beta) = -\dot{\beta}^2 \int_r^R mw_0\hat{u}_{cg}\mathrm{d}s \tag{2.34}$$

and

$$F_{\phi,2}(\dot{\beta}, \dot{u}, \dot{v}, \dot{\theta}, \beta) = -2\dot{\beta} \int_r^R mw_0 \left(\dot{u}\sin(\beta) + \dot{v}\cos(\beta) \right) \mathrm{d}s \tag{2.35}$$

describes the Coriolis force associated with the rotation of the (x, y, z)-frame about the z-axis and the relative velocity of the blade. The effect of gravity is described by

$$F_{\phi,3}(u, \phi) = g\sin(\phi) \int_r^R mw_0\mathrm{d}s + g\cos(\phi) \int_r^R m\hat{u}_{cg}\mathrm{d}s \tag{2.36}$$

and

$$F_{\phi,4}(\ddot{\beta}, u, v, \beta) = -\ddot{\beta} \int_r^R mw_0\hat{v}_{cg}\mathrm{d}s \tag{2.37}$$

describes the fictitious acceleration associated with an angular pitch acceleration of the (x, y, z)-frame about the z-axis.

The effect of the forces on the blade is described by the integral term on the right hand side of (2.33).

The rotor speed equation (2.33) only includes the effects from one blade, but it can be extended to include the effects from more blades by adding two integral terms in (2.33) and one of (2.34) to (2.37) for each extra blade.

Discussion

Comparing the partial differential equations of motion (2.12) and (2.18) with [12] it is noted that the gravity terms (2.15) (2.22), the pitch action terms (2.13)

(2.19) and the terms involving varying rotor speed (2.17) (2.24) are new, on the other hand the terms involving warp effects in [12] are not included here.

In the following discussion, the x and y-direction will be denoted edgewise and flapwise, respectively, to help the physical interpretation. The inertia terms in (2.12) is seen to couple the edgewise and flapwise motions to the torsional motion of the blade. The degree of coupling is seen to depend on the pre-twist of the chord. The first term in (2.13) shows that an acceleration of the pitch angle excites the edgewise and flapwise motion depending on the flapwise and edgewise deflection, respectively. That is, an acceleration of the pitch angle of a flapwise deflected blade excites the edgewise motion of the blade. The first term in the integral in (2.14) is a restoring force dependent on the rotation speed of the rotor, known as centrifugal stiffness. The effect of gravity (2.15) and (2.22) is seen to vary with the ϕ-angle as expected. The restoring force (2.16) couples the bending motion to the torsional motion. The degree of coupling is dependent on the edgewise and flapwise deflection of the blade. An acceleration of the rotor excites the edgewise and flapwise motion (2.17), the excitation is dependent on the pitch angle.

The inertia term from (2.18) couples the torsional motion to the edgewise and flapwise motion. The degree of coupling to the edgewise and the flapwise motion is dependent on the pre-twist of the chord. The first term in (2.19) shows a strong coupling between pitch acceleration and torsional motion. The effect of rotor acceleration (2.21) on the torsional motion is dependent on the pitch setting and the pre-twist of the blade. The torsional motion is coupled to the bending motion through the bending stiffness (2.23).

The first term in (2.27) shows the strong coupling between torsional motion and pitch motion. The first term in (2.32) shows the effect of blade deflection on the pitch inertia, and the second term in (2.32) shows how the motion of a deflected blade affects the pitch equation.

To avoid unnecessary complications structural damping is not included in the derivation of the equations of motion, but a damping term e.g. viscus damping could easily be added to the equations describing the structural damping.

Extra degrees of freedom like tower, yaw motion or tilt can be included by introducing a new inertial frame, defining a transformation from the new inertial frame to the present inertial frame, and using this new transformation in the description of the energies before applying Hamilton's method. This will give two extra equations for each extra degree of freedom and periodic coefficients (like the gravity term).

Implementations of the partial differential equations of structural motion are tested against HAWC2 [5, 6] in P1 and P2, showing a good agreement.

2.3 Aerodynamic Model

Since the purpose of wind turbines is to convert the kinetic energy in the wind into mechanical energy (and further to electric energy) they are highly affected by aerodynamic forces. On horizontal axis wind turbines the apparent wind (sum of the incoming free wind and the relative wind caused by the rotation of the rotor) flows over an airfoil shaped blade resulting in aerodynamic forces causing a torque on the rotor. The flow around a wind turbine is highly complex and troublesome to describe in details, but many engineering models have been developed, which describe the important aspects of the flow field. The flow around the turbine is divided into a far flow field and a description of the unsteady flow at the blade.

The far flow field around a wind turbine is affected by the turbine: The wind speed decreases, and rotation increases in the downwind flow field. The decrease in wind speed can be explained by the withdrawing of kinetic energy from the wind. The rotational motion of the downwind flow field can be explained by considering the balance of rotational momentum between the wind field and the rotational momentum of the rotor, converted into electric energy. The decrease in wind speed normal to the rotor plan and the increase in rotational wind speed in the rotor plane can be described by the Blade Element Momentum theory (BEM) [42]. In BEM, the aerodynamic forces on the blade are balanced with the loss of momentum in the flow field described by the induced velocities. The induced velocities describe the decrease in wind speed normal to the rotor plane and the increase tangential to the rotor plane. BEM is a 2D theory assuming that each spanwise section of the blade are independent of each other, neglecting any 3D effects. Different correction methods to include 3D effects and tip loss exist. The focus of this work however, is on the fundamental dynamic behavior of the turbine rather than production and exact quantities, therefore these corrections are neglected. The changes in the induced velocities are assumed to happen on a time scale corresponding to two times the rotor diameter divided by the wind speed, which is slower than the time scale for the blade dynamic and control action. Therefore the induced velocities can be assumed constant at each operation condition.

The coupling between blade motion and aerodynamic on a time scale faster than assumed in BEM is handled by an unsteady 2D aerodynamic model [43]. Again, using 2D theory neglects numerous aerodynamic effects, but it still captures the essential aerodynamic effects and fairly accurate values with a relatively low complexity of the equations.

Fundamentally; a 2D aerodynamic model is independent of the spanwise position on the blade, giving the aerodynamic forces for each cross section of blade independent of the neighbor cross sections. However, the model inherit a spanwise dependency through airfoil profile, the apparent wind speed and angle of attack, which are all functions of spanwise position on the blade.

2.3.1 Relations Between Structural and Aerodynamic Models

The aerodynamic model is coupled to the structural model through the apparent wind speed and angle of attack, both depending on the deformation and the motion of the blade. The structural model is dependent on the aerodynamic model through the aerodynamic forces acting on the blade.

Apparent wind Velocity

The apparent wind velocity at the three-quarter point is used in the aerodynamic model. Formulated in the coordinates along the chord, normal to the chord and along the blade the apparent wind velocity at the three-quarter point is

$$\mathbf{U}_{3/4} = \mathbf{T}_c \mathbf{T}_\beta \left(\begin{bmatrix} -(U_t + w\dot{\phi})(1+a') \\ U_n(1-a) \\ 0 \end{bmatrix} - \dot{\mathbf{r}}_{3/4} \right) \tag{2.38}$$

where $U_t = U_t(s,t)$ is the wind in the rotor plane normal to the blade (caused by e.g. turbulence), $w\dot{\phi}$ is the relative wind in the rotor plane caused by rotation of the rotor and $a' = a'(s,t)$ is the induced velocity in the rotor plane. The free inflow is given by $U_n = U_n(s,t)$ and $a = a(s,t)$ is the induced velocity in the free wind direction. The induced velocities are determined by BEM in Section 2.4. The position vector

$$\mathbf{r}_{3/4} = \mathbf{T}_\beta^{\mathrm{T}} \left(\begin{bmatrix} u + l_{pi} & v & w \end{bmatrix}^{\mathrm{T}} + \mathbf{T}_c^{\mathrm{T}} \begin{bmatrix} l_{3/4} & 0 & 0 \end{bmatrix}^{\mathrm{T}} \right) \tag{2.39}$$

defines the position of the three quarter point of the blade in the $(\hat{x}, \hat{y}, \hat{z})$-frame. The apparent wind velocity without pitch rate of the blade section is also used for determine the aerodynamic forces:

$$\mathbf{U} = \mathbf{U}_{3/4}\big|_{\ddot{\beta}=\dot{\beta}=\ddot{\theta}=\dot{\theta}=0} \tag{2.40}$$

Angle of Attack

The angle of attack is the angle between the direction of the apparent wind and the chord, which is given by[4]

$$\alpha = -\arctan\left(\frac{\mathbf{U}[2]}{\mathbf{U}[1]}\right) \text{ and } \alpha_{3/4} = -\arctan\left(\frac{\mathbf{U}_{3/4}[2]}{\mathbf{U}_{3/4}[1]}\right) \tag{2.41}$$

without and with pitch rate of the blade section, respectively.

[4]The notation $\mathbf{U}[i]$ denotes the i'th component of the vector $\mathbf{U}$. Informally known as Matlab notation.

Aerodynamic Forces

The aerodynamic models describe the aerodynamic forces and moment by the aerodynamic lift, drag and moment coefficients. The aerodynamic forces are given by multiplying the aerodynamic coefficients by $\frac{1}{2}c\rho U^2$ where $U = \sqrt{\mathbf{U}[1]^2 + \mathbf{U}[2]^2}$ is the apparent wind speed. Combining this with a projection of the forces onto the (x, y, z)-directions the aerodynamic forces become

$$\mathbf{f}_{aero} = \mathbf{T}_c^{\mathrm{T}} \frac{1}{2}\rho c U \begin{bmatrix} C_D\mathbf{U}[1] + C_L\mathbf{U}[2] \\ C_D\mathbf{U}[2] - C_L\mathbf{U}[1] \\ 0 \end{bmatrix} \tag{2.42a}$$

$$M = \frac{1}{2}\rho c^2 U^2 C_M + \left(\mathbf{f}_{aero}[2] l_{ac}\cos(\theta + \bar{\theta}) - \mathbf{f}_{aero}[1] l_{ac}\sin(\theta + \bar{\theta})\right) \tag{2.42b}$$

where (C_L, C_D, C_M) are lift, drag and moment coefficients, respectively, given by airfoil data $(C_L^{st}(\alpha), C_D^{st}(\alpha), C_M^{st}(\alpha))$ for steady state conditions, or by the aerodynamic model (presented below) for unsteady conditions.

2.3.2 Unsteady Aerodynamic Model

In the unsteady case the aerodynamic forces on the blade are described by a 2D unsteady aerodynamic state space model, suggested by Hansen et al. [43]. The model is based on the Beddoes-Leishman dynamic stall model [11], it uses airfoil data and time constants to compute the unsteady aerodynamic coefficients. A brief description of the model will be given here. The aerodynamic state equations are [43]

$$\dot{z}_1 + T_u^{-1}\left(b_1 + c\tfrac{\dot{U}}{2U^2}\right) z_1 = b_1 A_1 T_u^{-1}\alpha_{3/4} \tag{2.43a}$$

$$\dot{z}_2 + T_u^{-1}\left(b_2 + c\tfrac{\dot{U}}{2U^2}\right) z_2 = b_2 A_2 T_u^{-1}\alpha_{3/4} \tag{2.43b}$$

$$\dot{z}_3 + T_p^{-1} z_3 = T_p^{-1} C_{L,\alpha}(\alpha_E - \alpha^0) + T_p^{-1} T_u \pi \dot{\alpha} \tag{2.43c}$$

$$\dot{z}_4 + T_f^{-1} z_4 = T_f^{-1} f^{st}(z_3/C_{L,\alpha} + \alpha^0) \tag{2.43d}$$

where the first two states (z_1, z_2) are 2. order approximations to Theodorsen's function [20], describing the shed vorticity. The last two states (z_3, z_4) describe the dynamics of the trailing edge separation point, having $z_4 = 1$ for fully attached flow and $z_4 = 0$ for fully separated flow, $T_u = \frac{c}{2U}$ is a normalized time constant, $T_p = 1.7T_u$ and $T_f = 6T_u$ are time lags for the pressure built up and the dynamic of the boundary layer separation point, respectively, $b_1 = 0.0455$, $b_2 = 0.3$, $A_1 = 0.165$ and $A_2 = 0.335$ are time lags and magnitudes, suggested by Jones [44]. The apparent wind speed is U. The effective angle of attack is $\alpha_E = \alpha_{3/4}(1 - A_1 - A_2) + z_1 + z_2$, α^0 is the angle of attack where the static lift coefficient is zero, and $C_{L,\alpha}$ is the slope of the linear part of the static lift curve. The $f^{st}(\alpha)$

function describes the static position of the trailing edge separation point [43]. The unsteady aerodynamic coefficients are [43]

$$\begin{aligned} C_L^{dyn} =& C_{L,\alpha}(\alpha_E - \alpha^0)z_4 + C_L^{fs}(\alpha_E)(1 - z_4) + T_u \pi \dot{\alpha} && \text{(2.44a)} \\ C_D^{dyn} =& C_D^{st}(\alpha_E) + (\alpha - \alpha_E)C_L^{dyn} \\ & + \tfrac{1}{2}(C_D^{st}(\alpha_E) - C_D^0)\left(\sqrt{f^{st}(\alpha_E)} - \sqrt{z_4} - f^{st}(\alpha_E) + z_4\right) && \text{(2.44b)} \\ C_M^{dyn} =& C_M^{st}(\alpha_E) - \tfrac{\pi}{2} T_u \dot{\alpha} && \text{(2.44c)} \end{aligned}$$

where $C_D^0 = C_D^{st}(\alpha^0)$ is the static drag coefficient at the angle of attack with zero lift. The $C_L^{fs}(\alpha)$ function is the lift curve for full separated flow [43]. The last terms in (2.44a) and (2.44c) are apparent mass terms.

The aerodynamic model is linearized [43] by dividing the aerodynamic states into a static, and an oscillating part $z_i(t) = z_{i,0} + \epsilon z_{i,1}(t)$ for $i = \{1, 2, 3, 4\}$, Taylor expanding all nonlinear terms, assuming $\epsilon \ll 1$, and balancing terms of order ϵ^0 to get the equilibrium states [43]

$$z_{1,0} = A_1 \alpha^0 \,, \quad z_{2,0} = A_2 \alpha^0 \,, \quad z_{3,0} = C_{L,\alpha}(\alpha_0 - \alpha^0) \,, \quad z_{4,0} = f^{st}(\alpha^0) \tag{2.45}$$

where α_0 is the static angle of attack. Balancing terms of order ϵ^1 gives the linear approximations

$$\begin{aligned} \dot{z}_{1,1} + T_1^{-1} z_{1,1} &= A_1 T_1^{-1} \alpha_{3/4}^1 - \tfrac{A_1 \alpha_0}{U_0} \dot{U}_1 \\ \dot{z}_{2,1} + T_2^{-1} z_{2,1} &= A_2 T_2^{-1} \alpha_{3/4}^1 - \tfrac{A_2 \alpha_0}{U_0} \dot{U}_1 \\ \dot{z}_{3,1} + T_p^{-1} z_{3,1} &= T_p^{-1} \left(C_{L,\alpha} \alpha_E^1 + \pi T_0 \dot{\alpha}_1 \right) \\ \dot{z}_{4,1} + T_f^{-1} z_{4,1} &= T_f^{-1} \tfrac{\mathrm{d}f^{st}}{\mathrm{d}\alpha}\big|_{\alpha=\alpha_0} \tfrac{z_{3,1}}{C_{L,\alpha}} \end{aligned} \tag{2.46}$$

where $T_1 = \frac{c}{2U_0 b_1}$ and $T_2 = \frac{c}{2U_0 b_2}$. The unsteady aerodynamic coefficients (2.44) are linearized, by inserting $C_i^{dyn}(t) = C_i^{st}(\alpha_0) + \epsilon C_{i,1}(t)$ for $i = \{L, D, M\}$ and the expansions used above into (2.44), and Taylor expanding the coefficients, assuming $\epsilon \ll 1$. The static aerodynamic coefficient C_i^{st} are given by airfoil data. Balance terms of order ϵ^1 give these linear approximations

$$\begin{aligned} C_{L,1} =& c_{l,\alpha} \alpha_{E,1} + c_{l,f} z_{4,1} + \pi T_0 \dot{\alpha}_1 \\ C_{D,1} =& c_{d,\alpha} \alpha_{E,1} + c_{d,f} z_{4,1} + C_L^{st} \left(\alpha_1 - \alpha_{E,1} \right) \\ C_{M,1} =& c_{m,\alpha} \alpha_{E,1} - \tfrac{\pi}{2} T_0 \dot{\alpha}_1 \end{aligned} \tag{2.47}$$

where

$$
\begin{aligned}
c_{l,\alpha} &= C_{L,\alpha} f_0 + \left.\frac{\mathrm{d}C_L^{fs}}{\mathrm{d}\alpha}\right|_{\alpha=\alpha_0} (1 - f_0) \\
c_{l,f} &= C_{L,\alpha}(\alpha_0 - \alpha^0) - C_L^{fs}(\alpha_0) \\
c_{d,\alpha} &= \left.\frac{\mathrm{d}C_D^{st}}{\mathrm{d}\alpha}\right|_{\alpha=\alpha_0} - \left.\frac{\mathrm{d}f^{fs}}{\mathrm{d}\alpha}\right|_{\alpha=\alpha_0} (C_D^{st} - C_{D,0}) \frac{1 - \sqrt{f_0}}{4\sqrt{f0}} \\
c_{d,f} &= (C_D^0 - C_D^{st}) \frac{1 - \sqrt{f_0}}{4\sqrt{f0}} \\
c_{m,\alpha} &= \left.\frac{\mathrm{d}C_M^{st}}{\mathrm{d}\alpha}\right|_{\alpha=\alpha_0}
\end{aligned}
\tag{2.48}
$$

are terms from the Taylor expansions.

2.4 Steady State Aeroelastic Model

This section concerns the description of a wind turbine blade under steady state conditions. The steady state model is used to compute the steady state deformation of the blade and the induced velocities for each set of operation conditions. The steady state conditions are: Uniform inflow ($\dot{U}_n = 0$ and $U_t = 0$), gravity is neglected $g = 0$, constant rotor speed and pitch angle $\ddot{\phi} = \dot{\beta} = 0$, and all time derivatives in the structural equations of motion are zero $\ddot{u} = \ddot{v} = \ddot{\theta} = \dot{u} = \dot{v} = \dot{\theta} = 0$. The spatial dependencies in the equations of motion are approximated by a finite difference formulation giving a set of algebraic equations for the equilibriums between aerodynamic forces and blade deformation.

The steady state model is used to compute steady state deformation and induced velocities of the test blade (Appendix C) for all operation conditions. The results are compared with results from HAWCStab [10] showing a very good agreement.

2.4.1 Method

First the PDEs (2.12) and (2.18) are discretized, next the boundary conditions are derived. The steady state equations are set-up and a scheme for solving them is presented.

Discretization of Structural Model

The blade is discretized with an equidistance grid along the *ea* with step size h and N computation points, with point number 1 near the blade root at $s = h$ and point number N at the blade tip $s = R$. The spatial derivatives of the partial

Table 2.1: Second order finite difference formulation of uniform step size

$f'(s,t)$	$\frac{\partial f(s,t)}{\partial s}$	$\frac{f_{i+1}(t)-f_{i-1}(t)}{2h}$
$f''(s,t)$	$\frac{\partial^2 f(s,t)}{\partial s^2}$	$\frac{f_{i+1}(t)-2f_i(t)+f_{i-1}(t)}{h^2}$
$f'''(s,t)$	$\frac{\partial^3 f(s,t)}{\partial s^3}$	$\frac{-f_{i-2}(t)+2f_{i-1}(t)-2f_{i+1}(t)+f_{i+2}(t)}{2h^3}$
$f''''(s,t)$	$\frac{\partial^4 f(s,t)}{\partial s^4}$	$\frac{f_{i-2}(t)-4f_{i-1}(t)+6f_i(t)-4f_{i+1}(t)+f_{i+2}(t)}{h^4}$

differential equations of motion (2.12) and (2.18) are approximated by the finite difference formulation given i Table 2.1. The derivatives of parameters (such as mass, stiffness, etc.) are approximated by the same finite difference scheme. The differential of integral terms in the equations of motion is rewritten using Leibnitz rule

$$\left(f(s)'\int_s^R g(\zeta)\mathrm{d}\zeta\right)' = f(s)''\int_s^R g(\zeta)\mathrm{d}\zeta - f(s)'g(s) \tag{2.49}$$

where the integrals are approximated by sums using the trapezoid rule.

Implementation of Boundary Conditions

The blade root boundary conditions (2.25) give

$$u(0,t) = v(0,t) = \theta(0,t) = 0 \Rightarrow u_0(t) = v_0(t) = \theta_0(t) = 0 \tag{2.50a}$$

$$u'(0,t) = \frac{u_1(t) - u_{-1}(t)}{2h} = 0 \Rightarrow u_{-1}(t) = u_1(t) \tag{2.50b}$$

$$v'(0,t) = \frac{v_1(t) - v_{-1}(t)}{2h} = 0 \Rightarrow v_{-1}(t) = v_1(t) \tag{2.50c}$$

where $(u_0(t), v_0(t), \theta_0(t))$ are the deformation at the root of the blade $s = 0$. The tip boundary conditions lead to

$$\theta'(R,t) = \frac{\theta_{N+1}(t) - \theta_{N-1}(t)}{2h} = 0 \Rightarrow \theta_{N+1}(t) = \theta_{N-1}(t) \tag{2.51a}$$

$$u''(R,t) = \frac{u_{N+1}(t) - 2u_N(t) + u_{N-1}(t)}{h^2} = 0$$
$$\Rightarrow u_{N+1}(t) = 2u_N(t) - u_{N-1}(t) \tag{2.51b}$$

$$v''(R,t) = \frac{v_{N+1}(t) - 2v_N(t) + v_{N-1}(t)}{h^2} = 0$$
$$\Rightarrow v_{N+1}(t) = 2v_N(t) - v_{N-1}(t) \tag{2.51c}$$

$$u'''(R,t) = \frac{-u_{N-2}(t) + 2u_{N-1}(t) - 2u_{N+1}(t) + u_{N+2}(t)}{2h^3} = f_{u,bc}(t)$$
$$\Rightarrow u_{N+2}(t) = 2h^3 f_{u,bc}(t) + 4u_N(t) - 4u_{N-1}(t) \tag{2.51d}$$

$$v'''(R,t) = \frac{-v_{N-2}(t) + 2v_{N-1}(t) - 2v_{N+1}(t) + v_{N+2}(t)}{2h^3} = f_{v,bc}(t)$$
$$\Rightarrow v_{N+2}(t) = 2h^3 f_{v,bc}(t) + 4v_N(t) - 4v_{N-1}(t) \tag{2.51e}$$

where $(u_N(t), v_N(t), \theta_N(t))$ are the deformation at the tip of the blade $s = R$ and $(f_{u,bc}(t), f_{v,bc}(t))$ are the time-varying part of the boundary conditions at the blade tip, which can be neglected if $l_{cg}(R)$ is sufficiently small.

Steady State Equations

Equations (2.50) and (2.51) holds sufficient information to implement the partial differential equations of motion (2.12) and (2.18) on all discretization points from 1 to N leading to a set of nonlinear algebraic equations

$$\mathbf{F}_{st}(\mathbf{u}, \dot{\phi}, \beta) = \mathbf{f} \tag{2.52}$$

where $\mathbf{F}_{st}(\mathbf{u}, \dot{\phi}, \beta)$ holds the terms from the discretization of the structural equations, $\mathbf{u} = [u_1, v_1, \theta_1, ..., u_N, v_N, \theta_N]^{\mathrm{T}}$ holds the deformation at the discretization points and $\mathbf{f}$ holds the right hand sides of (2.12) and (2.18) with the forces given by the aerodynamic forces (2.42) computed at each discretization points with the aerodynamic coefficients from airfoil data.

The induced velocities for the i'th computation point are given by [42]

$$a_i = \left(\frac{4\sin(\psi_i)^2}{\sigma_i C_{y,i}} + 1 \right)^{-1}, \quad a'_i = \left(\frac{4\sin(\psi_i)\cos(\psi_i)}{\sigma_i C_{x,i}} - 1 \right)^{-1} \tag{2.53}$$

where $\psi_i = \alpha_i - \beta - \bar{\theta}_i - \theta_i$ is the angle between apparent wind and the rotor plane ($(\hat{x}, \hat{z})$-plane), α_i is the angle of attack (2.41) at the i'th computation point, $\bar{\theta}_i$ the local pretwist of the chord. The solidity is $\sigma_i = \frac{c_i B}{2\pi s}$, where B is the number of blades on a given rotor, c_i is the local chord and s is the radius to the i'th computation point. The aerodynamic coefficients projected onto the $\hat{x}$ and $\hat{y}$-axes are given by $C_{x,i} = C^{st}_{L,i}\sin(\psi_i) - C^{st}_{D,i}\cos(\psi_i)$ and $C_{y,i} = C^{st}_{L,i}\cos(\psi_i) + C^{st}_{D,i}\sin(\psi_i)$, respectively, where $C^{st}_{L,i}$ and $C^{st}_{D,i}$ are the aerodynamic lift and drag coefficients, respectively, given by airfoil data for the i'th computation point. It is noted that no 3D or tip corrections are included in this formulation.

Solution Scheme

The $3N + 2N$ nonlinear equations (2.52) and (2.53) have $3N$ unknown deformations and $2N$ unknown induced velocities. The system of nonlinear equations are solved using the following iterative scheme:

1. Choose operations conditions: U_n, $\dot{\phi}_0 = \dot{\phi}_0(U_n)$ and $\beta_0 = \beta_0(U_n)$
2. Compute apparent wind velocity and angle of attack using (2.40) and (2.41), respectively
3. Compute the aerodynamic forces using (2.42), with (C_L, C_D, C_M) from the airfoil data

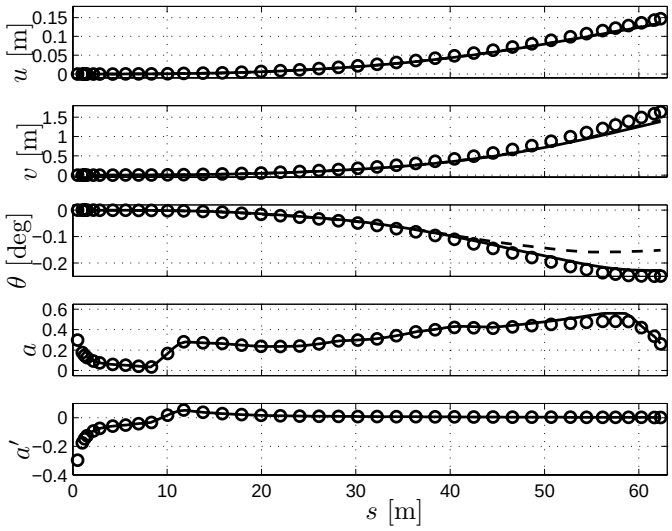

Figure 2.2: Steady state deformation of test blade at $U_n = 5$ m/s. '–' result from nonlinear finite difference formulation (2.52), '- -' linear finite difference formulation, '∘' HAWCStab results.

4. Solve (2.52) for the deformations $\mathbf{u}$

5. Compute new induced velocities parameters $\mathbf{a} = [a_1, a_2, \ldots, a_N]^{\mathrm{T}}$ and $\mathbf{a}' = [a'_1, a'_2, \ldots, a'_N]^{\mathrm{T}}$ using (2.53)

6. If not converged return to 2

leading to the steady state deformations $\mathbf{u}_0 = \mathbf{u}_0(U_n, \dot{\phi}, \beta)$ and the induced velocities $(\mathbf{a}, \mathbf{a}')$ for the given operations conditions $(U_n, \dot{\phi}, \beta)$.

2.4.2 Test and Discussion

The steady state deformation and induced velocities of the test blade are computed for all operation conditions (Table C.1). Figure 2.2 shows the results for $U_n = 5$ m/s (corresponding to $\dot{\phi} = 7.55$ rpm and $\beta = 0$ deg). The results are shown for both the nonlinear finite difference formulation, a linearized version of this and from HAWCStab. It is seen that all three results are in good agreement except for twist of the blade. The reason for the disagreement between the linear and nonlinear twist is the nonlinear contribution from the double curvature of the deformed blade (2.23).

Figure 2.3 shows the tip deformation at different wind speeds. It is seen that the present nonlinear model and HAWCStab agree well for all operation conditions.

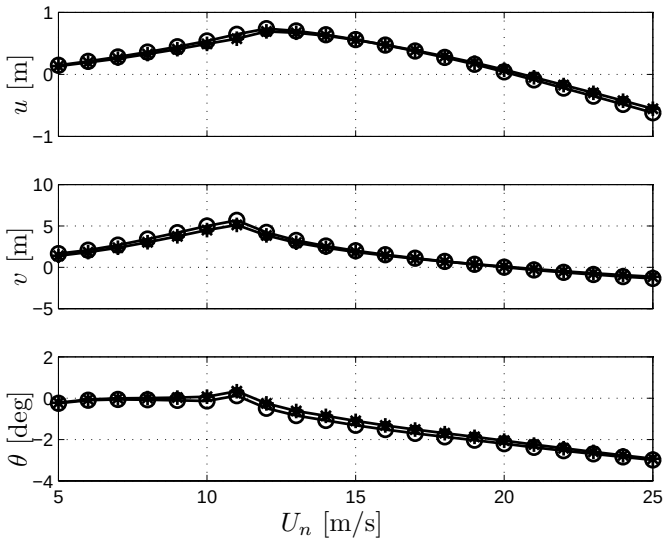

Figure 2.3: Tip deflection versus wind speed for present nonlinear finite difference model (2.52) '$*$' and HAWCStab '$\circ$'. The deflection is measured in the $(\hat{x}, \hat{y}, \hat{z})$-frame.

2.5 Modes of Aeroelastic Blade Motion

In this section the shapes, frequencies and damping ratios of natural vibrations (modes of motion) of a wind turbine blade are derived. The partial differential equations of motion of the wind turbine blade are linearized and combined with the linear unsteady aerodynamic model. The spatial dependencies of the model are approximated by a finite difference formulation, leading to a differential eigenvalue problem. The solution to this eigenvalue problem gives the frequency, damping and shape of natural vibrations for the wind turbine blade.

The model is used to compute modes of natural vibrations of the test blade. Results for the undeformed blade are compared with results from HAWCStab, showing good agreement. Only results for the undeformed blade are compared to HAWCStab, since HAWCStab is not capable of including steady state blade deformation.

2.5.1 Method

First the PDEs 2.12) and (2.18) are linearized and combined with the linear aerodynamic model, next the spatial dependencies of the linear model are approximated by the finite difference formulation (2.1), forming an eigenvalue problem.

Linearization

The PDE (2.12) and (2.18) are linearized about the deformed blade position $\mathbf{u}_0$ and combined with the linear aerodynamic model (2.46) through linearized version of the apparent wind speed (2.40), angle of attack (2.41) etc.. The equations are linearized by inserting:

$$\begin{aligned}
&u(s,t) = u_0(s) + \epsilon u_1(s,t),\ v(s,t) = v_0(s) + \epsilon v_1(s,t)\\
&\theta(s,t) = \theta_0(s) + \epsilon\theta_1(s,t),\ \beta(t) = \beta_0 + \epsilon\beta_1(t),\ \dot{\phi}(t) = \dot{\phi}_0 + \epsilon\dot{\phi}_1(t)\\
&\sin(\phi(t)) = \epsilon\sin(\phi_1(t) + t\dot{\phi}_0)\ ,\quad \cos(\phi(t)) = \epsilon\cos(\phi_1(t) + t\dot{\phi}_0)\\
&U_n(s,t) = U_{n,0}(s) + \epsilon U_{n,1}(s,t)\ ,\quad U_t(s,t) = U_{t,0}(s) + \epsilon U_{t,1}(s,t)
\end{aligned} \tag{2.54}$$

Taylor expand all equations assuming $\epsilon \ll 1$ and balancing terms of order ϵ^1 to give the linear approximations. Periodic effects, such as gravity, are included in the linear model by considering $\sin(\phi_1 + t\dot{\phi}_0)$ and $\cos(\phi_1 + t\dot{\phi}_0)$ as independent variables, which then can be obtained by a nonlinear transformation. The set of linear partial differential equations of motion can be written as

$$\tilde{\mathbf{M}}\dot{\mathbf{u}} + \left(\tilde{\mathbf{K}}_{ss}\mathbf{u}''\right)'' + \left(\tilde{\mathbf{K}}_{s}\mathbf{u}'\right)' + \tilde{\mathbf{K}}\mathbf{u} = \tilde{\mathbf{F}}\tilde{\mathbf{f}} \tag{2.55}$$

where $\mathbf{u} = \mathbf{u}(s,t) = [u_1(s,t), v_1(s,t), \theta_1(s,t), \dot{u}_1(s,t), \dot{v}_1(s,t), \dot{\theta}_1(s,t), z_{1,1}(s,t), z_{2,1}(s,t), z_{3,1}(s,t), z_{4,1}(s,t)]^{\mathrm{T}}$ are the linearized states and $\tilde{\mathbf{M}} = \tilde{\mathbf{M}}(\dot{\phi}_0, \beta_0, u_{n,0})$, $\tilde{\mathbf{K}}_{ss} = \tilde{\mathbf{K}}_{ss}(\dot{\phi}_0, \beta_0)$, $\tilde{\mathbf{K}}_{s} = \tilde{\mathbf{K}}_{s}(\dot{\phi}_0, \beta_0)$, $\tilde{\mathbf{K}} = \tilde{\mathbf{K}}(\dot{\phi}_0, \beta_0, u_{n,0})$ are collections of the linear coefficients. The coupling to external effects such as pitch action and wind speed variations are described by the right hand side, where $\tilde{\mathbf{F}} = \tilde{\mathbf{F}}(\dot{\phi}_0, \beta_0, u_{n,0})$ holds the linear gains on the external effects, given by $\tilde{\mathbf{f}} = [\beta(t), \dot{\beta}(t), \ddot{\beta}(t), \sin(\phi_1(t) + t\dot{\phi}_0), \cos(\phi_1(t) + t\dot{\phi}_0), \dot{\phi}_1(t),\ \ddot{\phi}_1(t),\ U_{n,1}(s,t),\ U_{t,1}(s,t),\ \dot{U}_{n,1}(s,t)\ , \dot{U}_{t,1}(s,t)]^{\mathrm{T}}$. All matrices are shown in Appendix B. When linearized about the deformed position the main effect from the geometric nonlinearities are preserved since terms like uv, which are zero when linearized about the undeformed blade, becomes $u_1 v_0 + u_0 v_1$ when linearized about the deformed blade.

Discretization

To formulate an eigenvalue problem the external effects are set to zero $\tilde{\mathbf{f}} = \mathbf{0}$ and the spatial dependencies in (2.55) are approximated by the finite difference formulation (2.1), which leads to a system of ordinary differential equations:

$$\bar{\mathbf{M}}\dot{\bar{\mathbf{u}}} + \bar{\mathbf{K}}\bar{\mathbf{u}} = \mathbf{0} \tag{2.56}$$

where $\bar{\mathbf{M}} = \bar{\mathbf{M}}(U_{n,0}, \dot{\phi}_0, \beta_0)$ and $\bar{\mathbf{K}} = \bar{\mathbf{K}}(U_{n,0}, \dot{\phi}_0, \beta_0)$ hold the coefficients from the finite difference approximation of (2.55) and $\bar{\mathbf{u}}$ holds the deformations, velocities and aerodynamic states at each discretization point.

The set of ordinary differential equations (2.56) is recognized as a differential eigenvalue problem. The eigenvalues and corresponding eigenvectors can be grouped in two sets: Real valued eigenvalues and complex valued eigenvectors. The real valued eigenvalues are related to the aerodynamic states, and corresponds to the time lags that they describe. Complex valued eigenvalues from a real valued eigenvalue problem will always come in pairs of complex conjugated, with corresponding complex conjugated eigenvectors. Each of these pairs of complex conjugated eigenvalue and eigenvectors describe one mode of under-damped natural vibrations of the blade. The imaginary part of the eigenvalue gives the frequency of the particular mode of vibration and the real part the aerodynamic damping. The magnitude of the complex valued eigenvector is the amplitude of the ten states at each computation point and the phase of the complex valued eigenvector is the phase between the states. The natural modes of motion are enumerated such that first mode is the one with the lowest frequency.

It is noted that since aerodynamic forces are included the eigenvalue problem (2.56) is not self-adjoint and therefore the eigenvectors are not orthogonal.

2.5.2 Test and Discussion

The model (2.56) is used to compute modes of motion for the test blade (Appendix C). The modes of the undeformed blade are compared to results from HAWCStab. Since HAWCStab is only capable of computing modes of a undeformed blade, it is only these results that are compared.

Frequencies and Damping ratios

Table 2.2 shows the frequencies for the first three blade modes dominated by edgewise and flapwise motion, respectively, and the first two blade modes dominated by torsional motion. The frequencies are computed by the present finite difference formulation based on Bernoulli-Euler beam theory, HAWCStab based on Bernoulli-Euler beam theory and HAWCStab based on Timoshenko beam theory [39]. All results are without aerodynamic forces and steady state deformation of the blade. It is seen that the present finite difference formulation based on Bernoulli-Euler beam theory differs less than 6 % compared to results from HAWCstab based on Bernoulli-Euler beam theory. For the second and third edgewise modes and the third flapwise mode there are considerable differences between the results based on Timoshenko beam theory and the results based on Bernoulli-Euler theory. These differences are caused by the slenderness ratio of these modes violates the Bernoulli-Euler assumption about slender beams. The focus of this work is however on fundamental blade dynamic, which is dominated by low order blade motion, for which the Bernoulli-Euler formulation is well suited. The torsional degree of freedom is seen to agree well for all three formulations.

Table 2.2: Natural frequencies for the test blade (Appendix C) without aerodynamic forces and steady state deformation. First row shows results from present finite difference formulation, second row shows results from HAWCStab with Bernoulli-Euler beam theory, and third row shows results from HAWCStab with Timoshenko beam theory. First three columns are the first three edgewise dominated vibrations, column fourth to sixth are the first three flapwise dominated vibrations and the last two columns are the first two torsional dominated vibrations.

	Edgewise			Flapwise			Torsional	
	1.	2.	3.	1.	2.	3.	1.	2.
Present Model	1.16	4.10	9.47	0.73	2.02	4.58	8.39	13.61
HAWC (Bernoulli)	1.09	3.99	9.30	0.72	2.00	4.54	8.31	13.57
HAWC (Timoshenko)	0.98	2.85	4.80	0.70	1.81	3.60	8.19	13.48

Figure 2.4 shows the frequencies and damping ratio for the first, second, third and seventh modes of motion of the undeformed blade. The results from the present finite difference formulation are compared to results from HAWCStab. The frequencies from the two programs are seen to agree reasonable well, especially for the first, second and seventh modes, which corresponds to first flapwise, first edgewise and first torsional dominated modes, respectively. The damping are also seen to agree reasonable well. There is a high relative error for the second mode, corresponding to first edgewise mode. This is because the damping is close to zero, hence a small absolute difference results in a high relative difference. Anyway the structural damping, which is not yet included, is of the same magnitude, making the aerodynamic damping less important.

Mode Shapes

Figure 2.5 compares four different modes of motion for the test blade without steady state deformation with results from HAWCStab. For the first three modes all results are seen to agree very well. For the torsional mode (Figure 2.5(d)) the torsion part is seen to agree very well. The edgewise and flapwise motion are seen not to agree that well, but they are relatively small so the disagreements do not affect the later results. Anyway the results from the HAWCStab version with Bernoulli-Euler beam theory is seen to be closer to the present results than the HAWCStab version with Timoshenko beam theory. The disagreement between the two versions is caused by the high order edgewise and flapwise motion that the torsional motion couples to.

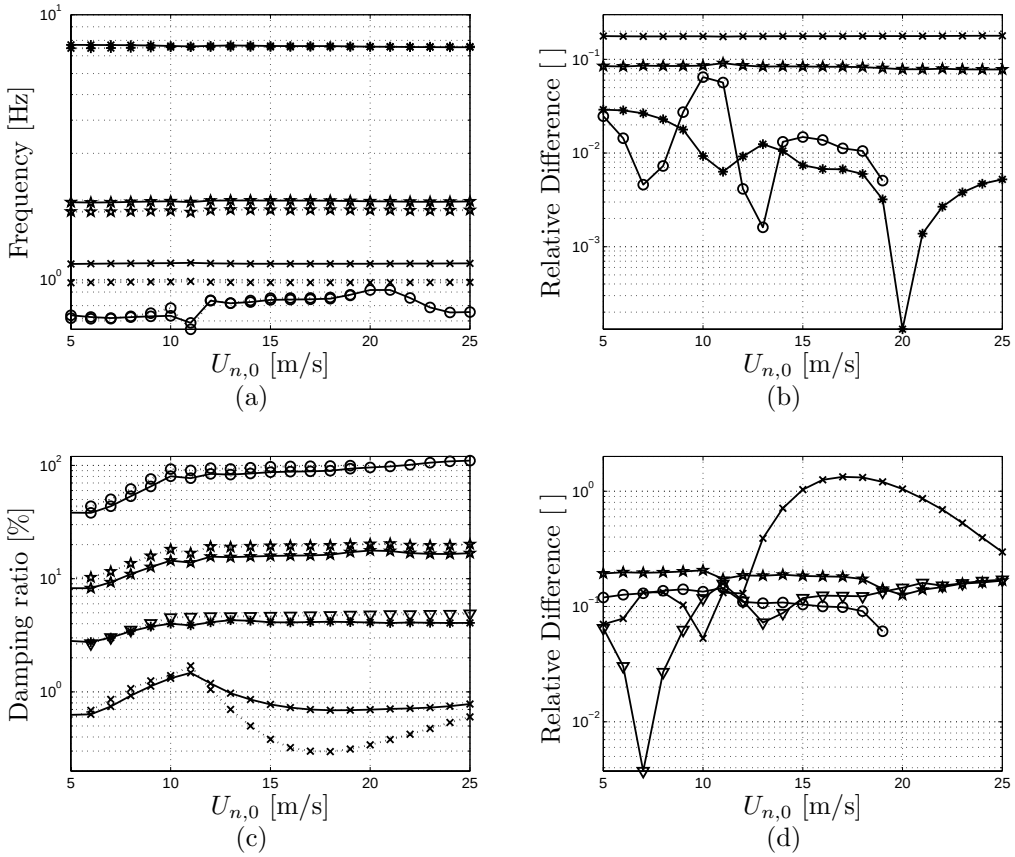

Figure 2.4: Frequencies and damping for the first, second, third and seventh modes of motion for the undeformed test blade. "–" results from the present finite difference model, "$\cdots$" results from HAWCStab. "$\circ$" first mode, "$\times$" second mode, , "$\star$" fourth mode, "$*$" seventh mode. a) The frequencies of modes of blade motion, b) Relative differences between frequencies computed by the present finite difference model and by HAWCStab, c) Damping ratio of modes of blade motion d) Relative differences between damping computed by the present finite difference model and by HAWCStab. It is noted that results from HAWCStab for first mode are only available up to $U_{n,0} = 19$ m/s.

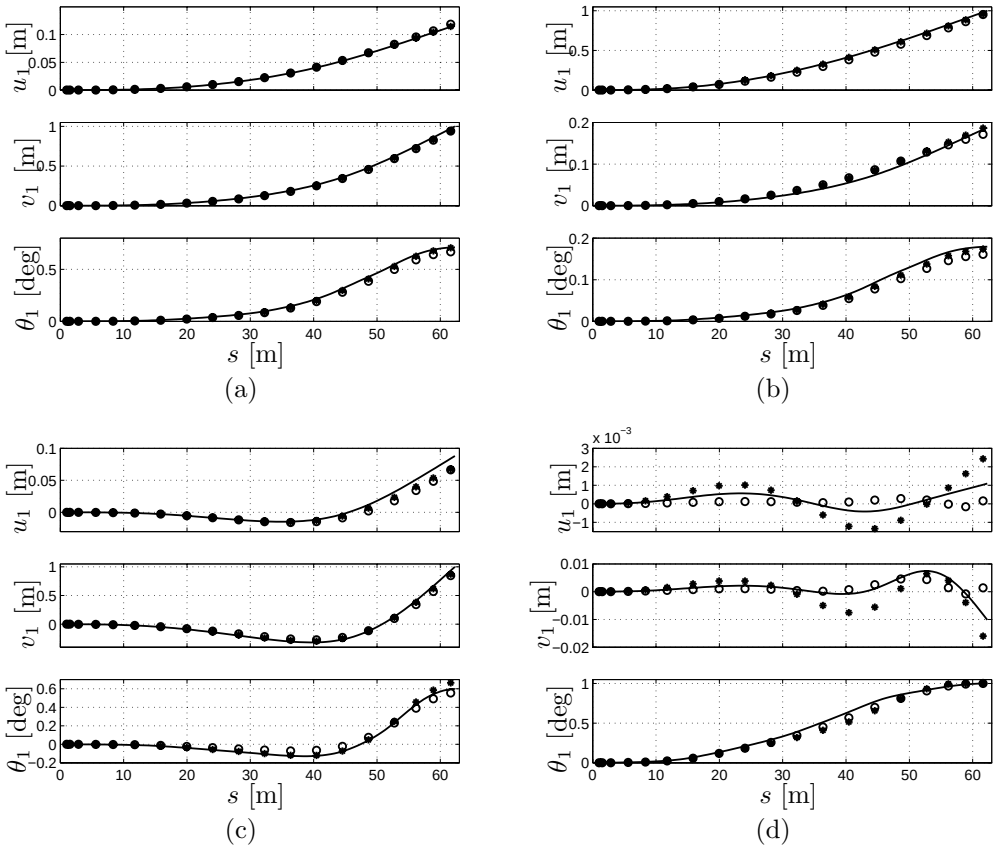

Figure 2.5: The mode shapes from (2.56) compared to results from HAWC-Stab. a) first mode, b) second mode, c) third mode and d) seventh mode. Top graphs shows the amplitude of deformation in x, middle graphs the deformation in y directions and bottom graphs the torsional deformation. '–' present finite difference formulation without steady state deformation, '$\circ$' HAWCStab with Timoshenko, '$*$' HAWCStab with Bernoulli-Euler.

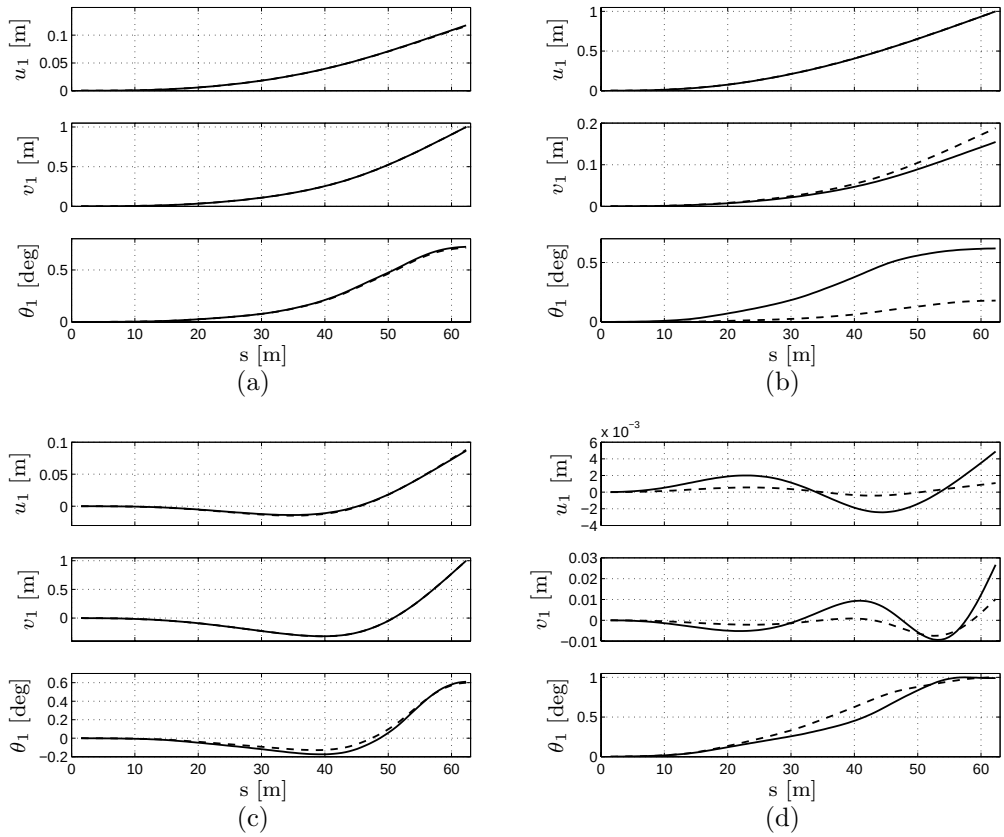

Figure 2.6: First, second, third and seventh mode shapes for the model linearized about the deformed blade $\mathbf{u}_0 \neq \mathbf{0}$ '–' and about the undeformed blade $\mathbf{u}_0 = \mathbf{0}$ '- -' for operation conditions corresponding to $U_{n,0} = 5$ m/s.

Effect of Steady State Deformation on Mode Shapes

Figure 2.6 shows the first, second, third and seventh mode shapes of the test blade. The mode shapes are computed both by a model linearized about the deformed blade $\mathbf{u}_0 \neq \mathbf{0}$, and by one linearized about the undeformed blade $\mathbf{u}_0 = \mathbf{0}$. It is seen that especially the coupling between edgewise and torsional blade motion are much stronger for the model linearized about the deformed blade compared to the model linearized about the undeformed blade. The reason for this strong coupling is that the flapwise deformation acts as a moment arm for the edgewise blade motion, leading to a considerable twisting moment on the blade. The coupling between flapwise and torsional blade motion is not as strong, since the steady state edgewise deformation is much smaller, hence the moment arm for flapwise blade motion is small.

2.6 Modal Discretized Aeroelastic Model

In this section the linearized version of the partial differential equations of motion for the wind turbine blade are approximated by an assumed mode method leading to a relative smaller set of ordinary differential equations to describe the fundamental blade motion. The equations for pitch action and rotor speed are also approximated by the assumed mode method.

The derived model is applied to the test blade (Appendix C). Results from the model are compared to results from HAWCStab and to results from the finite difference formulation above, showing a reasonable agreement.

2.6.1 Method

The linearized version of the PDEs (2.55) are approximated by ordinary differential equations of motion using an assumed mode method [40, 41]. That is, the states variables $\mathbf{u}$ are approximated by a sum of assumed mode shapes weighted by unknown time dependent functions

$$\mathbf{u}(s,t) = \mathbf{\Phi}(s)\mathbf{q}(t) \tag{2.57}$$

where

$$\mathbf{\Phi}(s) = \begin{bmatrix} \Phi_1(s) & \Phi_2(s) & \dots & \Phi_n(s) \end{bmatrix} \tag{2.58}$$

is the modal matrix, which holds the assumed mode shapes, where

$$\begin{aligned} \Phi_i(s) = [&\Phi_{u_1,i}(s), \Phi_{v_1,i}(s), \Phi_{\theta_1,i}(s), \Phi_{\dot{u}_1,i}(s), \Phi_{\dot{v}_1,i}(s), \Phi_{\dot{\theta}_1,i}(s), \\ &\Phi_{z_1,i}(s), \Phi_{z_2,i}(s), \Phi_{z_3,i}(s), \Phi_{z_4,i}(s)]^{\mathrm{T}} \end{aligned} \tag{2.59}$$

are the assumed relative amplitude of each states variable in the i'th mode, and $\mathbf{q}(t) = [q_1(t), q_2(t), \dots, q_n(t)]^{\mathrm{T}}$ are the corresponding time dependent weight functions, which are the new state variables.

Insert (2.57) into (2.55) multiply with the transpose of the modal matrix (2.59) and integrate over the spatial dependent variable

$$\begin{aligned} \int_r^R \mathbf{\Phi}^{\mathrm{T}}\tilde{\mathbf{M}}\mathbf{\Phi}\mathrm{d}s\dot{\mathbf{q}} + \int_r^R \mathbf{\Phi}^{\mathrm{T}}\left(\tilde{\mathbf{K}}_{ss}\mathbf{\Phi}''\right)''\mathrm{d}s\mathbf{q} + \int_r^R \mathbf{\Phi}^{\mathrm{T}}\left(\tilde{\mathbf{K}}_{s}\mathbf{\Phi}'\right)'\mathrm{d}s\mathbf{q} \\ + \int_r^R \mathbf{\Phi}^{\mathrm{T}}\tilde{\mathbf{K}}\mathbf{\Phi}\mathrm{d}s\mathbf{q} = \int_r^R \mathbf{\Phi}^{\mathrm{T}}\tilde{\mathbf{F}}\bar{\mathbf{F}}\mathbf{f}\mathrm{d}s \end{aligned} \tag{2.60}$$

removes the spatial dependency and results in n ordinary differential equations which describes each of the n assumed modes. The external effects are approximated by $\tilde{\mathbf{f}} = \bar{\mathbf{F}}\mathbf{f}$, where $\bar{\mathbf{F}} = \bar{\mathbf{F}}(s)$ is the assumed spatial shape of the external effects and $\mathbf{f} = \mathbf{f}(t)$ is the time dependent description of the effects.

Using partial integration and the fact that the assumed mode shapes fulfill the geometric boundary conditions (2.60) can be rewritten into:

$$\int_r^R \mathbf{\Phi}^{\mathrm{T}}\tilde{\mathbf{M}}\mathbf{\Phi}\mathrm{d}s\dot{\mathbf{q}} + \int_r^R \left((\mathbf{\Phi}^{\mathrm{T}})''\tilde{\mathbf{K}}_{ss}\mathbf{\Phi}'' - (\mathbf{\Phi}^{\mathrm{T}})'\tilde{\mathbf{K}}_s\mathbf{\Phi}' + \mathbf{\Phi}^{\mathrm{T}}\tilde{\mathbf{K}}\mathbf{\Phi}\right)\mathrm{d}s\mathbf{q} = \int_r^R \mathbf{\Phi}^{\mathrm{T}}\tilde{\mathbf{F}}\bar{\mathbf{F}}\mathrm{d}s\mathbf{f} \quad (2.61)$$

The inclusion of aerodynamic forces in the equations for motion (2.61) leads to a non-self-adjoint system. For a non-self-adjoint system the expansion theorem [40] does not hold and an eigenfunction expansion will not uncouple the equations of motion. That is, the resulting equations of motion will be coupled for any set of true or assumed mode shapes ϕ_i. Since the resulting equations of motion will be coupled for any choice of mode shapes, the mode shapes are chosen such that interpretation of the equations and the results are straightforward. This is achieved by using uncoupled assumed mode shapes instead of the true coupled mode shapes found in Section 2.5. When uncoupled mode shapes are used, the coupling will instead appear in the resulting equations. An eigenvalue analysis of the resulting set of equations will reveal a coupling between the uncoupled mode shapes, such that coupled modes of motion of the uncoupled mode shapes approximate the true coupled mode shapes fairly well.

In this work two assumed mode models are derived: One version where the structural states are approximated by three assumed modes (AMM1) and one version where the structural states are approximated by four assumed modes (AMM2). In the first version (AMM1), the structural states are approximated by one mode each, corresponding to the first flapwise mode, the first edgewise mode and the first torsional mode. The assumed modes are chosen as the edgewise, flapwise and torsional contents of the true coupled modes dominated by edgewise, flapwise and torsional blade motion, respectively. This is the first, second and seventh modes found in the finite difference analysis above (Figure 2.5). Figure 2.7(a) shows the assumed structural mode shapes used in the expansion (2.57). This choice leads to a set of equations, which have many similarities with the equations of motion of a 2D blade section model (As the one presented by the author in [P1]).

In the second version (AMM2), an additional flapwise mode is included. This assumed mode is chosen as the flapwise contents of the third mode found in the finite difference analysis (Figure 2.5), corresponding to the second flapwise mode.

In AMM1 the aerodynamic states are approximated by four expansion functions each. The aerodynamic expansion functions are chosen as; a constant function to capture uniform variations in the apparent wind, the contents of the aerodynamic mode corresponding to flapwise motion, the contents of the aerodynamic mode corresponding to torsional motion and a linear decreasing function (from one at the blade tip to zero at the hub) to capture first order approximation

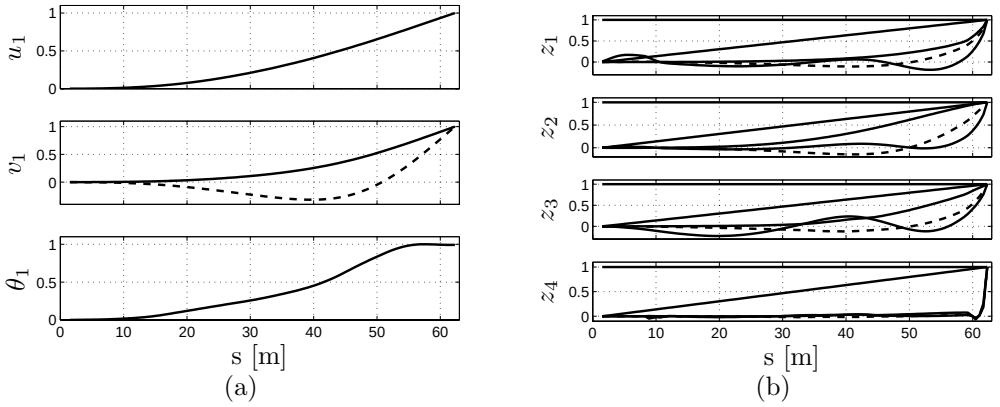

Figure 2.7: Expansion functions used in the assumed mode model. a) the structural expansion functions. b) the aerodynamic expansion functions. '–' denote the expansion functions from the AMM1, and '- -' denote the additional expansion functions in the AMM2.

of wind shear. The aerodynamic mode corresponding to the edgewise blade mode is very similar to the aerodynamic mode corresponding to the first flapwise mode, therefore it is not included in the model. In AMM2, one additional aerodynamic expansion function of each aerodynamic state is included; the contents of the aerodynamic modes corresponding to the second flapwise mode. Figure 2.7(b) shows the aerodynamic expansion functions.

The wind is modelled as

$$U_{n,0}(s) = u_{n,0}\ , \quad U_{n,1}(s,t) = u_{n,1}(t) + \phi_{u_{n,2}}(s)u_{n,2}(t) \tag{2.62}$$

$$U_{t,0}(s) = 0 \quad , \quad U_{t,1}(s,t) = u_{t,1}(t) \tag{2.63}$$

where $u_{n,0}$ is the uniform distributed steady state incoming wind, $u_{n,1}(t)$ is a uniform distributed time varying contribution, modelling variations in the incoming mean wind speed, $\phi_{u_{n,2}}(s)$ is a linear varying function (zero at the rotor center and one at the blade tip) and $u_{n,2}(t)$ is the time varying magnitude of this wind contribution. The linear varying wind contribution is a first order approximation of wind shear. It is assumed that there is no steady state wind component in the rotor plan, and $u_{t,1}(t)$ models the time varying uniform distributed mean wind contribution in the rotor plane, which could be caused by e.g. turbulence.

The structural and aerodynamic equations of motion reduce to a set of linear ordinary differential equations of motion

$$\mathbf{M}\dot{\mathbf{q}} + \mathbf{K}\mathbf{q} = \mathbf{F}\mathbf{f} \tag{2.64}$$

where:

$$\begin{aligned}
\mathbf{M} &= \int_r^R \mathbf{\Phi}^{\mathrm{T}} \tilde{\mathbf{M}} \mathbf{\Phi} \mathrm{d}s \\
\mathbf{K} &= \int_r^R \left((\mathbf{\Phi}^{\mathrm{T}})'' \tilde{\mathbf{K}}_{ss} \mathbf{\Phi}'' - (\mathbf{\Phi}^{\mathrm{T}})' \tilde{\mathbf{K}}_s \mathbf{\Phi}' + \mathbf{\Phi}^{\mathrm{T}} \tilde{\mathbf{K}} \mathbf{\Phi} \right) \mathrm{d}s \\
\mathbf{F} &= \int_r^R \mathbf{\Phi}^{\mathrm{T}} \tilde{\mathbf{F}} \bar{\mathbf{F}} \\
\mathbf{f} &= [\beta_1, \dot{\beta}_1, \ddot{\beta}_1, \sin(\phi_1 + \dot{\phi}_0 t), \cos(\phi_1 + \dot{\phi}_0 t), \dot{\phi}_1, \ddot{\phi}_1, \\
&\quad u_{n,1}, u_{n,2}, u_{t,1}, \dot{u}_{n,1}, \dot{u}_{n,2}, \dot{u}_{t,1}]^{\mathrm{T}}
\end{aligned} \tag{2.65}$$

Structural damping of the blade is included by adding a damping value $2\zeta_i \sqrt{K[i,i]M[i,i]}$ to the $\mathbf{K}[i,i]$ element for $i = \{4,5,6\}$ (or $i = \{5,6,7,8\}$ for AMM2), where ζ_i is the damping ratio of the i'th mode.

Pitch Action

The expansions (2.54) are introduced in the pitch action equation (2.27) whereby terms of order ϵ^0 gives the steady state pitch moment:

$$M_{pitch,0} = \int_r^R \tilde{f}_{\beta,ss}(\mathbf{u}_0, \dot{\phi}_0, \beta_0) \mathrm{d}s \tag{2.66}$$

where $\mathbf{u}_0$ is the steady state deformation found in Section (2.4). Balancing terms of order ϵ^1 leads to the linear approximation of the pitch action equation (2.27)

$$\begin{aligned}
&\int_r^R \tilde{M}_\beta \mathrm{d}s \ddot{\beta}_1 + \int_r^R \tilde{D}_\beta \mathrm{d}s \dot{\beta}_1 + \int_r^R \tilde{K}_\beta \mathrm{d}s \beta_1 \\
&\qquad + \int_r^R \tilde{\mathbf{M}}_\beta \dot{\mathbf{u}} \mathrm{d}s + \int_r^R \tilde{\mathbf{K}}_\beta \mathbf{u} \mathrm{d}s = M_{pitch,1} + \int_r^R \tilde{\mathbf{f}}_\beta \tilde{\mathbf{F}}_\beta \mathrm{d}s \bar{\mathbf{f}}_\beta
\end{aligned} \tag{2.67}$$

where $\tilde{\mathbf{F}}_\beta = \bar{\mathbf{F}}[4:13, 4:13]$ [5] and the rest of the matrices are shown in appendix B.

Inserting the assumed modes (2.57), (2.62) and computing the integrals the pitch action are described by

$$M_\beta \ddot{\beta}_1 + D_\beta \dot{\beta}_1 + K_\beta \beta_1 + \mathbf{M}_\beta \dot{\mathbf{q}} + \mathbf{K}_\beta \mathbf{q} = \mathbf{f}_\beta \bar{\mathbf{f}}_\beta + M_{pitch,1} \tag{2.68}$$

[5] The notation $\mathbf{F}[i:j, k:l]$ denotes the sub-matrix of $\mathbf{F}$ with the upper left corner at $\mathbf{F}[i,k]$ and lower right corner at $\mathbf{F}[j,l]$, and $\mathbf{F}[:,i]$ denote the i'th column of $\mathbf{F}$. Informally known as Matlab notation.

where:

$$
\begin{aligned}
M_\beta &= \int_r^R \tilde{M}_\beta \mathrm{d}s,\ D_\beta = \int_r^R \tilde{D}_\beta \mathrm{d}s,\ K_\beta = \int_r^R \tilde{K}_\beta \mathrm{d}s \\
\mathbf{M}_\beta &= \int_r^R \tilde{\mathbf{M}}_\beta \mathbf{\Phi} \mathrm{d}s,\ \mathbf{K}_\beta = \int_r^R \tilde{\mathbf{K}}_\beta \mathbf{\Phi} \mathrm{d}s,\ \mathbf{f}_\beta = \int_r^R \tilde{\mathbf{f}}_\beta \tilde{\mathbf{F}}_\beta \mathrm{d}s \\
\bar{\mathbf{f}}_\beta &= [\sin(\phi_1 + \dot{\phi}_0 t), \cos(\phi_1 + \dot{\phi}_0 t), \dot{\phi}_1, \ddot{\phi}_1, u_{n,1}, u_{n,2}, u_{t,1}, \dot{u}_{n,1}, \dot{u}_{n,2}, \dot{u}_{t,1}]^{\mathrm{T}}
\end{aligned}
\tag{2.69}
$$

Rotor Speed

Linearizing the rotor speed equations (2.33) using (2.54) and balancing terms of order ϵ^0 gives the steady state rotor torque

$$
T_{gen,0} = \int_r^R \tilde{f}_{\phi,ss}(\mathbf{u}_0, \dot{\phi}_0, \beta_0) \mathrm{d}s \tag{2.70}
$$

and balancing terms of order ϵ^1 gives the linear approximation

$$
\begin{aligned}
\int_r^R \tilde{M}_\phi \mathrm{d}s \ddot{\phi} + \int_r^R \tilde{D}_\phi \mathrm{d}s \dot{\phi} + \int_r^R \tilde{K}_{\phi,\sin} \mathrm{d}s \sin(\phi_1 + \dot{\phi}_0 t) + \int_r^R \tilde{K}_{\phi,\cos} \mathrm{d}s \cos(\phi_1 + \dot{\phi}_0 t) \\
+ \int_r^R \tilde{\mathbf{M}}_\phi \dot{\mathbf{u}} \mathrm{d}s + \int_r^R \tilde{\mathbf{K}}_\phi \mathbf{u} \mathrm{d}s = \int_r^R \tilde{\mathbf{f}}_\phi \tilde{\mathbf{F}}_\phi \mathrm{d}s \bar{\mathbf{f}}_\phi + T_{gen,1}
\end{aligned}
\tag{2.71}
$$

where

$$
\tilde{\mathbf{F}}_\phi = \begin{bmatrix} \tilde{\mathbf{F}}[1:3, 1:3] & \tilde{\mathbf{F}}[1:3, 8:13] \\ \tilde{\mathbf{F}}[8:13, 1:3] & \tilde{\mathbf{F}}[8:13, 8:13] \end{bmatrix} \tag{2.72}
$$

and the rest of the matrices are shown in Appendix B. Inserting the assumed mode (2.57), (2.62) and compute the integrals give

$$
M_\phi \ddot{\phi} + D_\phi \dot{\phi} + \mathbf{K}_\phi^f \begin{bmatrix} \sin(\phi_1 + \dot{\phi}_0 t) \\ \cos(\phi_1 + \dot{\phi}_0 t) \end{bmatrix} + \mathbf{M}_\phi \dot{\mathbf{q}} + \mathbf{K}_\phi \mathbf{q} = \mathbf{f}_\phi \bar{\mathbf{f}}_\phi + T_{gen,1} \tag{2.73}
$$

where:

$$
\begin{aligned}
M_\phi &= \int_r^R \tilde{M}_\phi \mathrm{d}s,\ D_\phi = \int_r^R \tilde{D}_\phi \mathrm{d}s \\
\mathbf{K}_\phi^f &= \int_r^R \begin{bmatrix} \tilde{K}_{\phi,\sin} & \tilde{K}_{\phi,\cos} \end{bmatrix} \mathrm{d}s \\
\mathbf{M}_\phi &= \int_r^R \tilde{\mathbf{M}}_\phi \mathbf{\Phi} \mathrm{d}s,\ \mathbf{K}_\phi = \int_r^R \tilde{\mathbf{K}}_\phi \mathbf{\Phi} \mathrm{d}s,\ \mathbf{f}_\beta = \int_r^R \tilde{\mathbf{f}}_\beta \tilde{\mathbf{F}}_\beta \mathrm{d}s \\
\bar{\mathbf{f}}_\phi &= [\beta_1, \dot{\beta}_1, \ddot{\beta}_1, u_{n,1}, u_{n,2}, u_{t,1}, \dot{u}_{n,1}, \dot{u}_{n,2}, \dot{u}_{t,1}]^{\mathrm{T}}
\end{aligned}
\tag{2.74}
$$

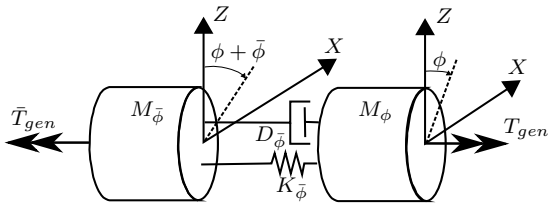

Figure 2.8: The drivetrain model.

Drivetrain Model

Even as drivetrain flexibility has been neglected until now, the rotor speed model can be extended to include a model of the drivetrain flexibility (Figure 2.8). The equation of motion for the drivetrain model is

$$M_{\bar{\phi}}(\ddot{\bar{\phi}} + \ddot{\phi}) + D_{\bar{\phi}}\dot{\bar{\phi}} + K_{\bar{\phi}}\bar{\phi} = \bar{T}_{gen} \tag{2.75}$$

where $\bar{\phi}$ is the twist of the drivetrain, $M_{\bar{\phi}}$ is the inertia of the generator and part of the drivetrain, $D_{\bar{\phi}}$ and $K_{\bar{\phi}}$ are the damping and stiffness of the drivetrain, respectively, and $\bar{T}_{gen}$ is the generator torque. The torque T_{gen} in the rotor speed equation (2.73) is then given by torque from the drivetrain $T_{gen} = D_{\bar{\phi}}\dot{\bar{\phi}} + K_{\bar{\phi}}\bar{\phi}$.

Above rated wind speed the generator works at maximum power and the generator controller regulates the generator torque to keep the power constant. It is assumed that the control of the generator torque is much faster than any time constants of the present model, whereby the generator torque is given by

$$\bar{T}_{gen} = -\frac{P_{gen}}{\dot{\phi} + \dot{\bar{\phi}}} \tag{2.76}$$

where P_{gen} is the constant generator power and $\bar{T}_{gen}$ is the generator torque, both related to the rotation speed of the generator $\dot{\phi} + \dot{\bar{\phi}}$. That is, the generator power and moment incorporates the effect of the increased of rotation speed, caused by the gearbox. Inserting (2.54) and $\bar{\phi}(t) = \bar{\phi}_0 + \epsilon\bar{\phi}_1(t)$ into (2.76) and balancing terms of order ϵ^0 yields the steady state generator torque and balancing to order ϵ^1 yields the linear generator torque:

$$\bar{T}_{gen,0} = -\frac{P_{gen}}{\dot{\phi}_0}\ , \quad \bar{T}_{gen,1} = \frac{P_{gen}}{\dot{\phi}_0}\left(\dot{\phi}_1 + \dot{\bar{\phi}}_1\right) \tag{2.77}$$

The drivetrain equation (2.75) is linearized by the same procedure giving the steady state deformation of the drivetrain

$$K_{\bar{\phi}}\bar{\phi}_0 = \bar{T}_{gen,0} = -\frac{P_{gen}}{\dot{\phi}_0} \tag{2.78}$$

and the linear drivetrain equation:

$$M_{\bar{\phi}}(\ddot{\bar{\phi}}_1 + \ddot{\phi}_1) + D_{\bar{\phi}}\dot{\bar{\phi}}_1 + K_{\bar{\phi}}\bar{\phi}_1 = \bar{T}_{gen,1} \tag{2.79}$$

Combining the linear drivetrain model (2.79) with the linear generator model (2.77) gives the linear generator and drive train model:

$$M_{\bar{\phi}}(\ddot{\bar{\phi}}_1 + \ddot{\phi}_1) + \left(D_{\bar{\phi}} - \frac{P_{gen}}{\dot{\phi}_0}\right)\dot{\bar{\phi}}_1 + K_{\bar{\phi}}\bar{\phi}_1 = \frac{P_{gen}}{\dot{\phi}_0}\dot{\phi}_1 \tag{2.80}$$

The generator model is seen to impose a negative damping of the drivetrain, making the equilibriums point unstable.

When using the drivetrain model (2.79) the generator torque in the rotor speed model (2.73) becomes:

$$T_{gen,1} = D_{\bar{\phi}}\dot{\bar{\phi}}_1 + K_{\bar{\phi}}\bar{\phi}_1 \tag{2.81}$$

Three Bladed Rotor

The motion of the individual blades on a wind turbine is coupled to each other through the coupling to the rotor speed, among other factors. The coupling through the rotor speed can be included in this model by expanding the rotor speed model to include more blades. As an example, a three blade wind turbine with the flexible drivetrain and the generator model described above (2.79) is described by

$$\begin{bmatrix} \mathbf{M} & \mathbf{0} & \mathbf{0} & -\mathbf{F}[:,7] & \mathbf{0} & \mathbf{0} \\ \mathbf{0} & \mathbf{M} & \mathbf{0} & -\mathbf{F}[:,7] & \mathbf{0} & \mathbf{0} \\ \mathbf{0} & \mathbf{0} & \mathbf{M} & -\mathbf{F}[:,7] & \mathbf{0} & \mathbf{0} \\ \mathbf{M}_\phi & \mathbf{M}_\phi & \mathbf{M}_\phi & 3M_\phi & 0 & 0 \\ \mathbf{0} & \mathbf{0} & \mathbf{0} & 0 & -1 & 0 \\ \mathbf{0} & \mathbf{0} & \mathbf{0} & M_{\bar{\phi}} & 0 & M_{\bar{\phi}} \end{bmatrix} \begin{bmatrix} \dot{\mathbf{q}}_1 \\ \dot{\mathbf{q}}_2 \\ \dot{\mathbf{q}}_3 \\ \ddot{\phi}_1 \\ \dot{\bar{\phi}}_1 \\ \ddot{\bar{\phi}}_1 \end{bmatrix}$$

$$+ \begin{bmatrix} \mathbf{K} & \mathbf{0} & \mathbf{0} & -\mathbf{F}[:,6] & \mathbf{0} & \mathbf{0} \\ \mathbf{0} & \mathbf{K} & \mathbf{0} & -\mathbf{F}[:,6] & \mathbf{0} & \mathbf{0} \\ \mathbf{0} & \mathbf{0} & \mathbf{K} & -\mathbf{F}[:,6] & \mathbf{0} & \mathbf{0} \\ \mathbf{K}_\phi & \mathbf{K}_\phi & \mathbf{K}_\phi & 3D_\phi & -K_{\bar{\phi}} & -D_{\bar{\phi}} \\ \mathbf{0} & \mathbf{0} & \mathbf{0} & 0 & 0 & 1 \\ \mathbf{0} & \mathbf{0} & \mathbf{0} & -E_{gen} & K_{\bar{\phi}} & -E_{gen} + D_{\bar{\phi}} \end{bmatrix} \begin{bmatrix} \mathbf{q}_1 \\ \mathbf{q}_2 \\ \mathbf{q}_3 \\ \dot{\phi}_1 \\ \dot{\bar{\phi}}_1 \\ \dot{\bar{\phi}}_1 \end{bmatrix}$$

$$= \begin{bmatrix} \mathbf{f}[:,1:3] & \mathbf{f}[:,8:13] \\ \mathbf{f}[:,1:3] & \mathbf{f}[:,8:13] \\ \mathbf{f}[:,1:3] & \mathbf{f}[:,8:13] \\ \mathbf{f}_\phi & \\ \mathbf{0} & \\ \mathbf{0} & \end{bmatrix} \begin{bmatrix} \beta_1 \\ \dot{\beta}_1 \\ \ddot{\beta}_1 \\ u_{n,1} \\ u_{n,2} \\ u_{t,1} \\ \dot{u}_{n,1} \\ \dot{u}_{n,2} \\ \dot{u}_{t,1} \end{bmatrix} \tag{2.82}$$

where the subscript on the **q** refer to the specific blade. Setting the right hand side to zero, this system forms an eigenvalue problem, which can be solved to reveal coupled modes of vibrations.

2.6.2 Test and Discussion

An assumed mode model of the test blade (Appendix C) is derived. Results from the model are compared to results from the finite difference formulation and from HAWCStab. Similarities between the present assumed mode model and a 2D blade section model are discussed.

Frequencies and Damping

Figure 2.9 shows the frequencies and damping for the first, second, third and seventh mode of motion of the test blade. The frequencies and damping of each mode are computed by three different models: The AMM1, AMM2 and the finite difference formulation. The third mode is not computed by the AMM1 as it is not included in that model. The relative differences between the results from the different models are also shown. The frequencies and the damping from all three models are seen to agree reasonable well. Large relative differences between the different models are seen for the damping of the second and the seventh modes. Despite this fact, the aerodynamic damping of these modes are small and therefore the absolute differences in damping of these modes are small, and become negligible when structural damping is introduced.

Steady State Properties

Figure 2.10 shows the steady state power production versus wind speed computed by (2.70) and HAWCStab for operation conditions given in Table C.1. The results are seen to agree reasonably well.

Modes of Motion

Figure 2.11 shows the coupling between modes of motion for the steady state deformed blade in the assumed mode formulations compared to the coupled modes found by the finite difference formulation. For the edgewise and flapwise dominated blade modes the assumed mode model capture the true coupling reasonable well. The edgewise and flapwise contents of blade motion in the torsional dominated mode of blade motion are not very well described, as the true torsional blade motion couples to higher order flapwise and edgewise modes of blade motion, which are not included in the assumed mode model. Anyway the amplitude on the flapwise and edgewise contents are small, so the error is small. For the first, second and seventh mode the AMM1 and AMM2 are seen to perform equally well. For the third mode, only results from the AMM2 are available. Again the

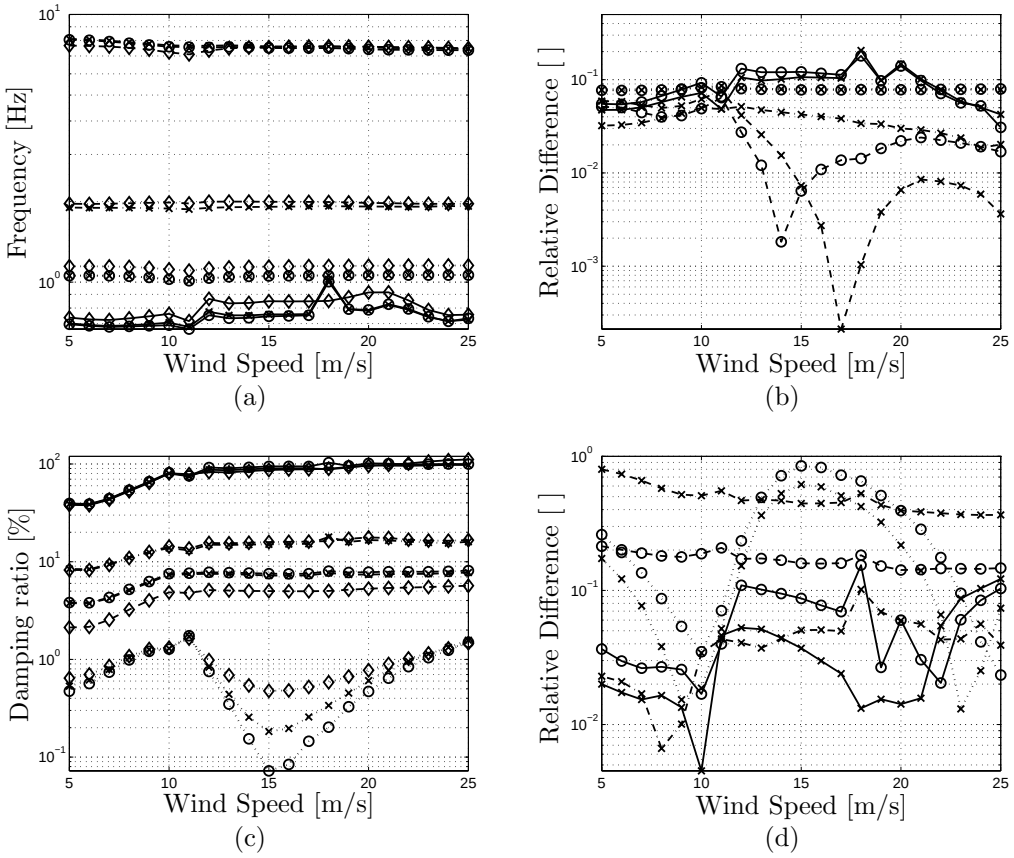

Figure 2.9: Frequencies (a) and damping ratio (c) of natural modes of blade motion computed by the AMM1 '$\circ$', by the AMM2 'x' and by the finite difference model '$\diamond$'. '–' first mode, '$\cdots$' second mode, '$- \cdot -$' third mode and '- -' seventh mode. Sub-figures (b) and (d) shows the relative difference between the results: Relative difference between the AMM1 and the finite difference model '$\circ$'. The relative difference between the AMM2 and the finite difference model 'x'.

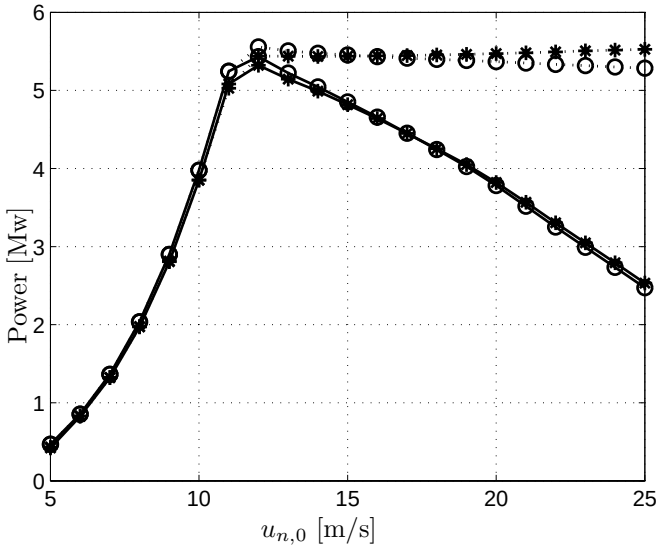

Figure 2.10: Steady state power production for a blade without steady state deformation '–' and with steady state torsional deformation '$\cdots$'. Result from assumed mode approximated model '$*$' and results from HAWCStab '$\circ$'.

edgewise and torsional contents are not very well approximated, since the second flapwise mode couples to higher order edgewise and torsional blade modes, which are not included in the model.

Three Bladed Wind Turbine Model

Table 2.3 shows the main results from an eigenvalue analysis of the three bladed wind turbine model (2.82). The results from the present aeroelastic model and HAWCStab are not directly comparable, since tower and yaw flexibility is not included. The asymmetric modes in the present formulation become whirling modes when tower and yaw flexibility is included, as in HAWCStab. However the modes which are comparable with HAWCStab agree reasonable well. It is seen that both AMM1 and AMM2 describe the symmetric second edgewise mode, even though it is not included in the blade model. The reason for this is that the second edgewise mode is interacting with the drivetrain, which is included. This point will be discussed further in Chapter 3.

Comparison with 2D Blade Section Model

Comparing the present AMM2 with a 2D blade section model, as the one presented by the author in [P1], a great deal of similarity is found.

Comparing the integral terms in the mass matrix of the assumed mode model

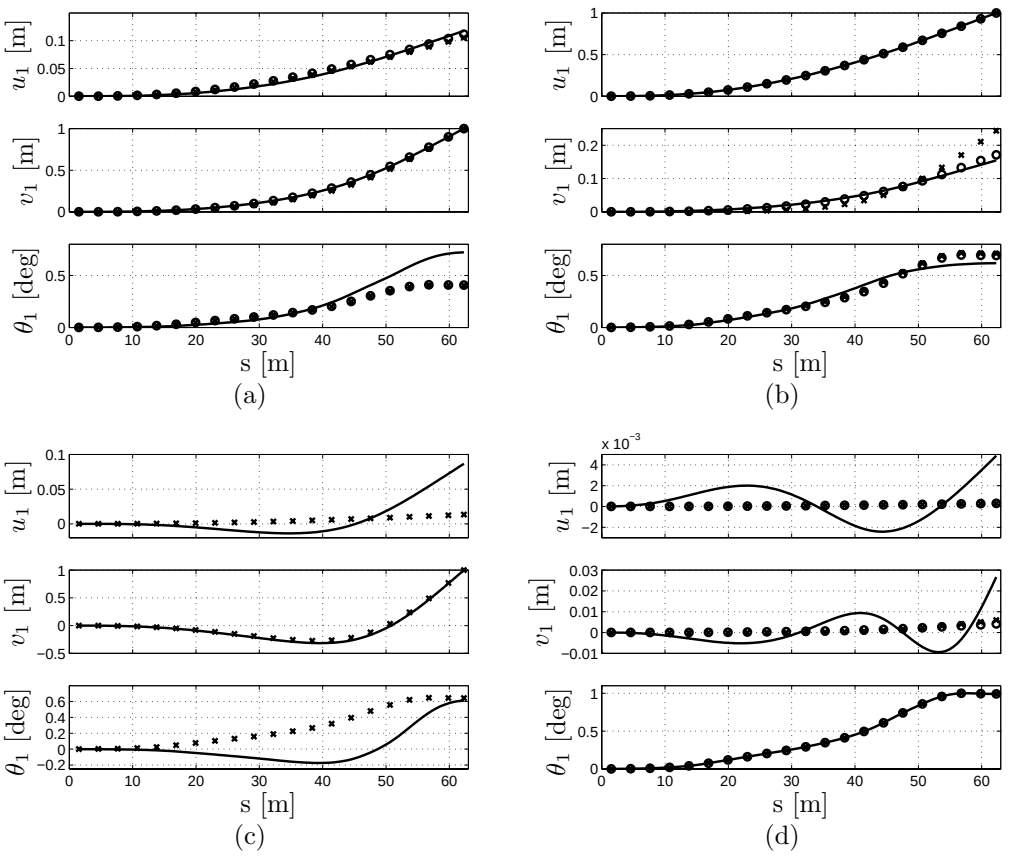

Figure 2.11: Modes of blade motion computed by the AMM1 '$\circ$' and by the AMM2 '$\times$' compared to the coupled modes computed by the finite difference mode '–'. a) first mode, b) second mode, c) third mode and d) seventh mode. For operation conditions corresponding to $u_{n,0} = 5$ m/s.

Table 2.3: Frequencies, damping and descriptions of modes for three bladed model (2.82) at operation conditions corresponding to $u_{n,0} = 5$ m/s. The results are shown from AMM2 and AMM1, and the results from HAWCstab which are comparable.

Frequency [Hz]			damping ratio [%]			Description
AMM2	AMM1	HAWCS.	AMM2	AMM1	HAWCS.	
0.70	0.70	-	38.7	39.3	-	1. flap asym. tilt
0.70	0.70	-	38.7	39.3	-	1. flap asym. yaw
0.71	0.70	0.75	38.8	39.5	40.9	1. flap sym.
1.06	1.06	-	0.5	0.5	-	1. edge asym. tilt
1.06	1.06	-	0.5	0.5	-	1. edge asym. yaw
1.60	1.60	-	-0.4	-0.4	-	Drivtrain
1.90	-	2.00	8.4	-	8.8	2. flap sym.
1.90	-	-	8.4	-	-	2. flap asym. tilt
1.90	-	-	8.4	-	-	2. flap asym. yaw
3.45	3.5	3.85	0.2	0.2	0.2	2. edge sym.
8.14	8.1	-	3.7	3.8	-	1. twist sym.
8.15	8.1	7.8	3.8	3.8	2.7	1. twist asym.
8.15	8.1	-	3.8	3.8	-	1. twist asym.

$\tilde{\mathbf{M}}_{st}$ with the structural part of blade section model gives a perfect match. There are more terms in the aerodynamic part of the mass matrix $\tilde{\mathbf{M}}_{aero}$, but this is caused by extra apparent mass terms which are included in the aerodynamic equations in [P1].

The structural part of the stiffness of the blade section model is seen to miss all the off diagonal terms which are present in the assumed mode model $\tilde{\mathbf{K}}_{st}$. This is because the springs in the blade section model are uncoupled. The diagonal centrifugal stiffness terms can be incorporated in the stiffness terms in the blade section mode.

The aerodynamic stiffness and damping $\tilde{\mathbf{K}}_{aero,1,1}$ are similar to the aerodynamic stiffness and damping of the blade section model, again with the difference caused by the difference in apparent mass formulation.

Only the acceleration of the pitch angle $\ddot{\beta}$ is seen to effect the structural part of the blade section mode, whereas both position and velocity affect the assumed mode model. This is because the position effects the direction of centrifugal stiffness, which is not present in the blade section mode, and the velocity causes Coriolis forces, which can not occur in the linear moving blade section model. The effect from gravity, and the change in centrifugal stiffness caused by change in rotor speed are also not included in the blade section model. The effect of an acceleration of the rotor is the same for the two models.

All in all, the assumed mode model is close to the blade section model, including more effects and only introduces a small increasing in the complexity of the equations of motion. Using the assumed modes model instead of a blade section model, the task of choosing parameters (such as stiffness, mass etc.) is turned

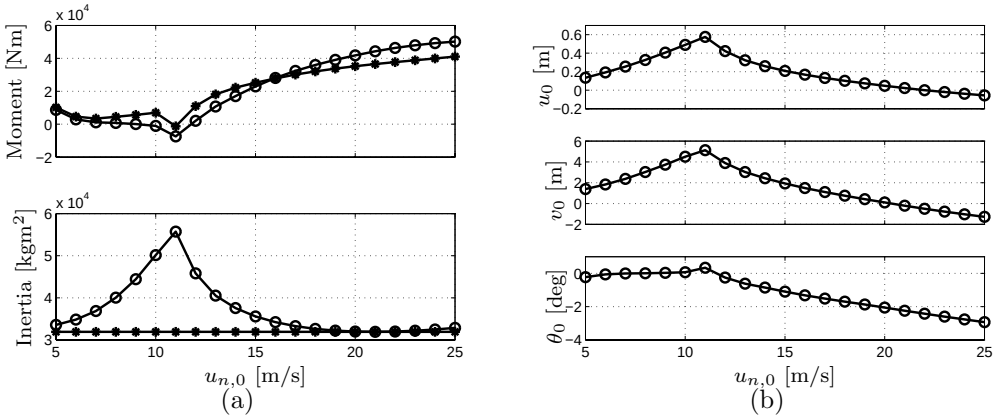

Figure 2.12: a) Steady state pitch torque and inertia vs. wind speed for model linearized about deformed blade 'o' and about undeformed blade '*'. b) Steady state blade tip deformation vs. wind speed measured in the (x, y, z)-frame.

into a formalized integration of real blade parameters.

Steady State Deformations Effect on Pitch Properties

Figure 2.12(a) shows the steady state pitch moment and inertia. The top figure shows the steady state pitch torque necessary to keep the pitch angle constant at different wind speeds and the bottom figure shows the pitch inertia at the different wind speeds. Results are given both from the model linearized about the deformed blade $\mathbf{u}_0 \neq \mathbf{0}$ and from the model linearized about the undeformed blade $\mathbf{u}_0 = \mathbf{0}$. The pitch torque vary strongly with the wind speed caused by the change in aerodynamic forces on the blade. A peak in the torque curve is seen at $u_{n,0} = 11$ m/s, where the operations of the turbine shift from having constant pitch angle with varying rotor speed to constant rotor speed with varying pitch angle. For wind speeds below 11 m/s the operation conditions ensure an almost constant tip speed ratio, and thereby almost constant angle of attack. For wind speeds above 11 m/s the pitch angle changes, whereby the angle of attack changes, which leads to changes in the ratio between aerodynamic lift and moment. The change in ratio between aerodynamic lift and moment leads to the considerably changes in pitch torque. The pitch torque is less affected by the deformation of the blade.

For the undeformed blade the pitch inertia is seen to be constant, whereas the pitch inertia varies strongly with the wind speed for the deformed blade. The reason for this is that the blade deformation varies with wind speed (Figure 2.12(b)). Since deformation of the blade moves the mass of the blade away from the pitch axis, and thereby increase the pitch inertia.

2.7 Summary

In summary the procedure for using the model proposed in this chapter is:

1. Compute steady state deformation and induced velocities using the procedure given on page 31
2. Compute modes of blade motion about the deformed blade position by solving the eigenvalue problem (2.56)
3. Compute assumed mode model integrals (2.65), (2.69) and (2.74)
4. Collect the system to fit the specific problem, e.g. as one blade with given rotor speed and pitch action (2.64) or as the three blade rotor (2.82)

The model is suitable for: Analyze of fundamental aspects of coupling between blade motions, pitch action and control, analyze aspects of load reducing control and analyze and design of pitch actuators.

In the next chapters the assumed mode approximated model will be used for analyzing fundamental blade motion. In Chapter 4 the model will be used for discussing load reducing control potentials and to develop and test a load reducing controller.

Chapter 3
Blade Response Analysis

In this chapter, the effects of wind speed and pitch angle variations on blade motion and pitch moment are analyzed. An analysis of the interaction between disturbances, blade motion and pitch action gives fundamental information about the system's behavior. Furthermore the analysis reveals information about the potential for using pitch control to reduce the fatigue loads on the blade.

The blade response to uniform wind speed and to pitch angle oscillations are analysis by frequency response plots (Bode plots [23]). The Bode plots shows the gain of the response of a linear system to a harmonic oscillating input, and the phase between the input and the response. All the Bode plots in this chapter are computed by the standard MATLAB® function *bode*, which evaluate the transfer function for the given model on the imaginary axis.

First, the effect of uniform wind speed and pitch angle oscillations on one blade are analyzed by the frequency response of the assumed mode aeroelastic model based on four structural modes (AMM2). Next, the response of the assumed mode aeroelastic model based on three structural modes (AMM1) and AMM2 in an one blade configuration and in a three bladed configuration are compared. Finally, the potential for using pitch control to reduced the fatigue loads on the blade is discussed based on the previously frequency response analysis and an quasi steady analysis.

It should be noticed that even through excitation frequencies up to 20 Hz are shown, not all modes of vibration with natural frequencies below 20 Hz are included in the model, therefore the results should be taken with some caution. The results however shows that the three basic modes; first flapwise, first edgewise and first torsional mode, are not considerably affected by including the second flapwise mode into the analysis, indicating that the three basic modes capture the fundamental blade motion.

The one blade configuration differs considerably from the tree bladed configuration, indicating that analysis based on the one blade configurations should be used with care. For excitations below 1 Hz however the one blade and three bladed configurations shows a reasonable agreement. The results from the AMM2 agree well with results from the AMM1 indicating that three structural modes is enough for analyze of basic blade motion and pitch moment response. All results are shown and discussed for operation conditions corresponding to $u_{n,0} = 5$ m/s and $u_{n,0} = 15$ m/s to illustrate differences between low and high wind speeds.

The quasi steady analysis of the effect of disturbances and pitch angle shows that there is a high potential for using pitch control to reduce flapwise blade

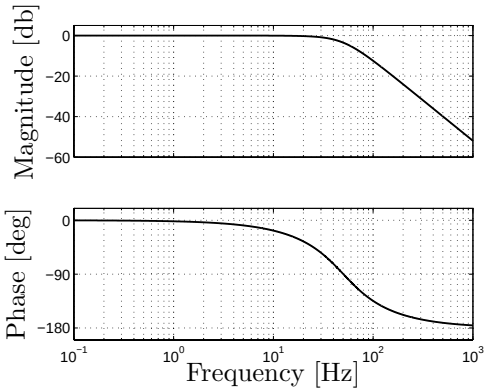

Figure 3.1: Frequency response plot for the model used to impose wind speed and pitch angle oscillations (3.1).

motion caused by uniform wind speed variations and wind shear. It is also found that the potential for using pitch control to reduce the edgewise blade motion caused by gravity is low.

3.1 Wind Speed and Pitch Action Model

The input to the frequency response function is a single value, the wind speed or the pitch angle, while the AMM1 and AMM2 needs both the wind speed and wind speed variations, or the pitch angle, pitch rate and pitch acceleration. The missing states (wind speed variations or pitch rate and acceleration) are achieved by imposing the wind speed or the pitch angle variations through a second order model

$$\begin{bmatrix} \dot{\Lambda} \\ \ddot{\Lambda} \end{bmatrix} + \begin{bmatrix} 0 & -1 \\ G & D \end{bmatrix} \begin{bmatrix} \Lambda \\ \dot{\Lambda} \end{bmatrix} = \begin{bmatrix} 0 \\ G \end{bmatrix} \Lambda_{step} \tag{3.1}$$

where Λ is replaced by $u_{n,1}$ or β_1 to model wind speed or pitch action, respectively, and Λ_{step} is the reference value. The gain is $G = 10^5$ and $D = 2\sqrt{G}$ is the critical damping of the step system. Figure 3.1 shows the frequency response plot of (3.1). The top graph shows the gain and the bottom graph shows the phase between input and response. It is seen that the output follows the input closely both in phase and magnitude up to 20 Hz, which is the highes excitation frequency used in this chapter, and therefore sufficient.

3.2 One Blade Configuration

The one blade configuration consists of the AMM2 combined with (3.1) to impose wind speed and pitch angle oscillations. The blade response to uniform wind speed and pitch angle oscillations is shown and discussed. The pitch moment

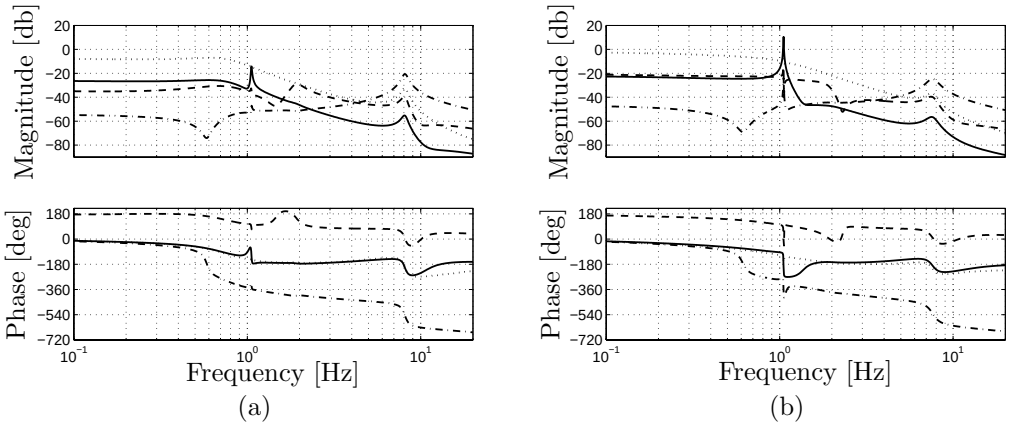

Figure 3.2: Bode plots for blade response to uniform wind speed $u_{n,1}$ oscillations, with fixed rotor speed and pitch angle. '–' the first edgewise mode $\mathbf{q}[1]$, '$\cdots$' the first flapwise mode $\mathbf{q}[2]$, '- -' the second flapwise mode $\mathbf{q}[3]$ and '$-\cdot-$' the first torsional mode $\mathbf{q}[4]$. a) $u_{n,0} = 5$ m/s and b) $u_{n,0} = 15$ m/s. The magnitude is given in [m/(m/s)].

response is also shown and discussed. The pitch moment is computed by the assumed mode pitch model (2.68).

3.2.1 Blade Response to Uniform Wind Speed Oscillations

The AMM2 (2.64) is combined with (3.1) to impose uniform wind speed oscillations, the rotor speed and pitch angle are kept constant

$$\begin{bmatrix} \mathbf{M} & \mathbf{0} & \mathbf{0} \\ \mathbf{0} & 1 & 0 \\ \mathbf{0} & 0 & 1 \end{bmatrix} \begin{bmatrix} \dot{\mathbf{q}} \\ \dot{u}_{n,1} \\ \ddot{u}_{n,1} \end{bmatrix} + \begin{bmatrix} \mathbf{K} & -\mathbf{F}[:,8] & -\mathbf{F}[:,11] \\ \mathbf{0} & 0 & -1 \\ \mathbf{0} & G & D \end{bmatrix} \begin{bmatrix} \mathbf{q} \\ u_{n,1} \\ \dot{u}_{n,1} \end{bmatrix} = \begin{bmatrix} \mathbf{0} \\ 0 \\ G \end{bmatrix} u_n \tag{3.2}$$

where u_n is the input in the Bode plot analysis and $\mathbf{q}[i]$ for $i = 1, 2, 3, 4$ are the states corresponding to the first edgewise, first and second flapwise and first torsional modes of blade motion, respectively.

Figure 3.2 shows the Bode plots for uniform wind speed oscillations to blade motion based on (3.2). Below 1 Hz the first flapwise blade motion dominates the blade response. At the first edgewise natural frequency (≈ 1.1 Hz) there is a strong edgewise response peak. After the edgewise resonance peak the first and second flapwise blade motion are of similar size for 5 m/s, while the first flapwise blade motion dominates for 15 m/s. A strong influence of the torsional mode is seen on all modes at the torsional natural frequency (≈ 7.9 Hz).

The response of the individual modes will be discussed in details below. The response of each mode is shown together with the particular contributions form structural couplings to the most important of the other blade modes, and the

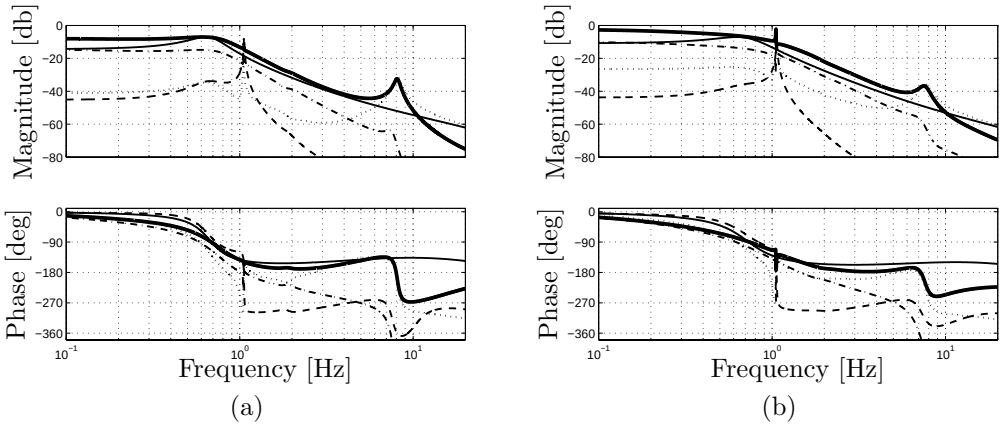

Figure 3.3: Bode plots for first flapwise blade mode $\mathbf{q}[2]$ response to uniform wind speed $u_{n,1}$ oscillations, with fixed rotor speed and pitch angle. The total response '**—**' and the contributions from structural coupling to first edgewise blade motion '- -', first torsional blade motion '$\cdots$', and from UAF '$-\cdot-$' and DEW '–'. a) $u_{n,0} = 5$ m/s and b) $u_{n,0} = 15$ m/s. The magnitude is given in [m/(m/s)].

contribution form unsteady aerodynamic forces (UAF) and the direct effect of the wind (DEW). The DEW is described by $\mathbf{F}[:, 8]$ and $\mathbf{F}[:, 11]$ in (3.2). The individual contributions are computed by removing all other couplings elements in the rows of $\mathbf{M}$, $\mathbf{K}$ and $\mathbf{F}$ that describes the particular mode.

First Flapwise Dominated Blade Mode

The first flapwise response is seen on Figure 3.3, together with the particular contribution from structural coupling to first edgewise and first torsional blade motion, and from UAF and DEW.

For low excitation frequencies the response is dominated by DEW and UAF and all contributions are in phase. Around the first flapwise natural frequency ($\approx$0.7 Hz) the DEW increases, but also the phase between the different contributions increases, such that the total response stays almost constant.

At the first edgewise natural frequency ($\approx$1 Hz) the strong edgewise resonance peak dominate the response through the structural coupling between the two modes. After the edgewise natural frequency the response is dominated by DEW, and the phase follows the phase of this contribution.

Approaching the torsional natural frequency ($\approx$7.9 Hz) the contribution from the structural coupling to the torsional blade motion starts to dominate the response. The phase follows the dominating torsional contribution and loses 180 deg at the torsional resonance peak, as expected at a resonance peak. After the torsional natural frequency the torsional contribution decreases, and the DEW

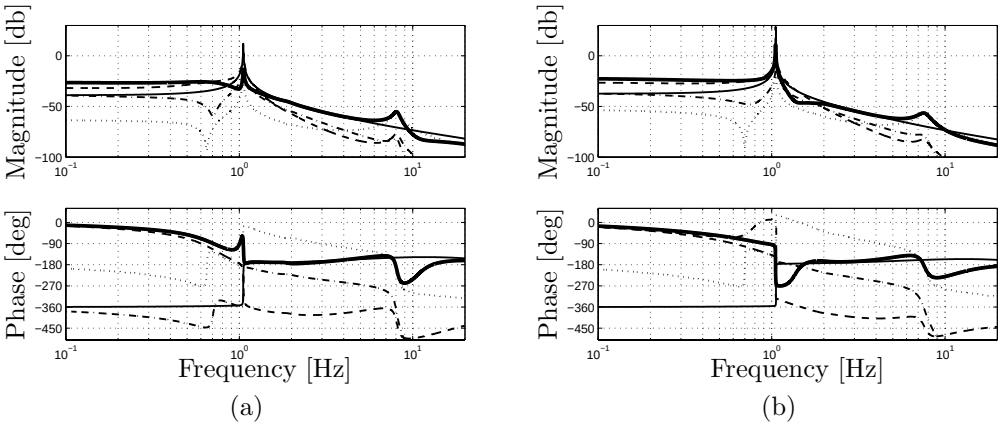

Figure 3.4: Bode plots for first edgewise blade mode $\mathbf{q}[1]$ response to uniform wind speed $u_{n,1}$ oscillations, with fixed rotor speed and pitch angle. The total response '**—**' and the contributions from structural coupling to first flapwise blade motion '- -', torsional blade motion '$\cdots$', and from UAF '-·-' and DEW '–'. a) $u_{n,0} = 5$ m/s and b) $u_{n,0} = 15$ m/s. The magnitude is given in [m/(m/s)].

starts to dominated the response again. The phase of the total response shifts to follow the phase of the dominating DEW.

The frequency response for 5 m/s and 15 m/s are seen to be qualitative similar.

First Edgewise Dominated Blade Mode

Figure 3.3 shows the first edgewise blade response together with the particular contribution from structural coupling to first flapwise and first torsional blade motion, and the contribution from UAF and DEW.

For low excitation frequencies the edgewise response is dominated by the structural coupling to the first flapwise blade motion with considerably contributions from UAF and DEW. The contributions from DEW and UAF are in phase with the contribution from the first flapwise blade motion whereby the total response is increased.

After the first flapwise natural frequency (≈ 0.7 Hz) the contribution from the first flapwise blade motion slightly increases. The phase of this contribution however loses 180 deg of phase, approaching counter phase with the contribution from DEW. At 5 m/s the first flapwise blade motion reach counter phase before the strong effect from the edgewise resonance peak, resulting in a dip in total response before the edgewise resonance peak. At 15 m/s the first flapwise blade motion loses phase slower, and the phase between the flapwise and the DEW contributions is not large enough to make the total response decrease before the edgewise resonance peak.

At the edgewise natural frequency ($\approx$ 1 Hz) a sharp response peak is seen. The edgewise response at the edgewise natural frequency is much more pronounced than the first flapwise response at the first flapwise natural frequency (Figure 3.2). This is because the edgewise blade motion is much less aerodynamic damped than the first flapwise blade motion (Figure 2.9). At 5 m/s the peak is dominated by the contribution from DEW, but the total response is reduced because of the counter phase contribution from the flapwise blade motion. The phase follows the phase of DEW. For 15 m/s the response peak of the contribution from first flapwise blade motion is shifted to the left, such that it appears before the resonance peak of the contribution from DEW. First, the response is dominated by the contribution from flapwise blade motion and the phase follows the phase of this, losing 180 deg at the resonance peak. Next, the contribution from DEW takes over and the phase shifts to follow this new dominating contribution.

For both wind speeds the contribution from DEW dominates the response until the torsional resonance peak appears around the torsional natural frequency ($\approx$ 7.9 Hz). The contribution from torsional blade motion starts to dominate the response and the phase shifts to follow the phase of this contribution again losing 180 deg at the resonance peak.

After the torsional natural frequency ($\approx$ 7.9 Hz) the torsional contribution decrease, the contribution from DEW dominates again and the phase shifts back to follow this contribution.

Second Flapwise Dominated Blade Mode

Figure 3.5 shows the response of the second flapwise mode (with a natural frequency on $\approx$ 1.8 Hz) to uniform wind speed oscillations. The particular contributions to the response from structural coupling to first flapwise and first torsional blade motion, and the contributions from UAF and UAF are also shown.

At 5 m/s and low frequency excitation the contributions from first flapwise blade motion, DEW and UAF are of similar size and phase. The total response is the sum of these contributions, and it increase slightly at the first flapwise natural frequency, since the contribution from first flapwise blade motion and UAF increase. At the first flapwise natural frequency ($\approx$ 0.7 Hz) the contribution from flapwise blade motion and UAF loses 180 deg phase. The phase of the total response follows the phase of the contribution from first flapwise blade motion and UAF since the sum of these contributions dominates the response. Approaching the second flapwise natural frequency ($\approx$ 1.8 Hz) the contribution from DEW increase and since it is in counter phase with the other contributions the total response decrease. At some point the DEW overtakes and the phase of the total response shifts to follow the phase of the this contribution.

For 15 m/s the contribution from first flapwise blade motion dominates the response until the first edgewise natural frequency ($\approx$ 1 Hz). The strong coupling between first and second flapwise blade motion is caused by the extra steady state

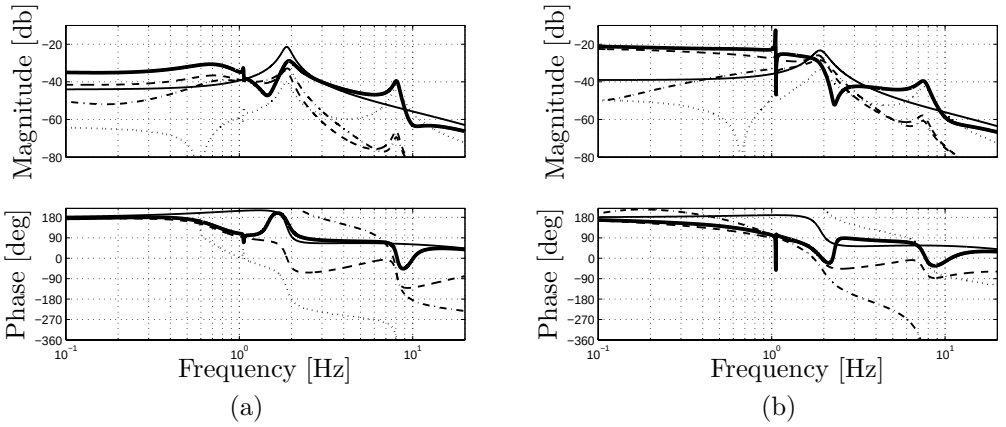

Figure 3.5: Bode plots for second flapwise blade mode $\mathbf{q}[3]$ response to uniform wind speed $u_{n,1}$ oscillations, with fixed rotor speed and pitch angle. The total response '**—**' and the contributions from structural coupling to first flapwise blade motion '- -', torsional blade motion '$\cdots$', and from UAF '$-\cdot-$' and DEW '–'. a) $u_{n,0} = 5$ m/s and b) $u_{n,0} = 15$ m/s. The magnitude is given in [m/(m/s)].

deformation of the blade at the higher wind speed (Figure 2.3). Approaching the first edgewise natural frequency the contributions from UAF and DEW increase and contribute considerably to the total response. At the first edgewise natural frequency the strong edgewise resonance peak affects all contributions leading to a peak in the second flapwise response. After the first edgewise natural frequency the contributions from first flapwise blade motion, UAF and DEW are of similar size. The contributions from UAF and flapwise blade motion are in phase and in counter phase with the DEW, which therefore reduce the total response. At the second flapwise natural frequency the DEW makes a resonance peak, but because it is in counter phase with the dominating contributions form UAF and first flapwise blade motion the total response is reduced.

For both operation conditions the DEW dominates until the torsional natural frequency (≈ 7.9 Hz), where the contribution from torsional blade motion starts to dominate. Around the first torsional natural frequency the phase follows the phase of the torsional contribution, and loses 180 deg at the torsional resonance peak. After the torsional resonance, DEW dominates again and the phase shifts to follow this contribution.

First Torsional Dominated Blade Mode

Figure 3.6 shows the torsional blade response and the particular contributions from the structural coupling to first flapwise and first edgewise blade motion, and from UAF and DEW.

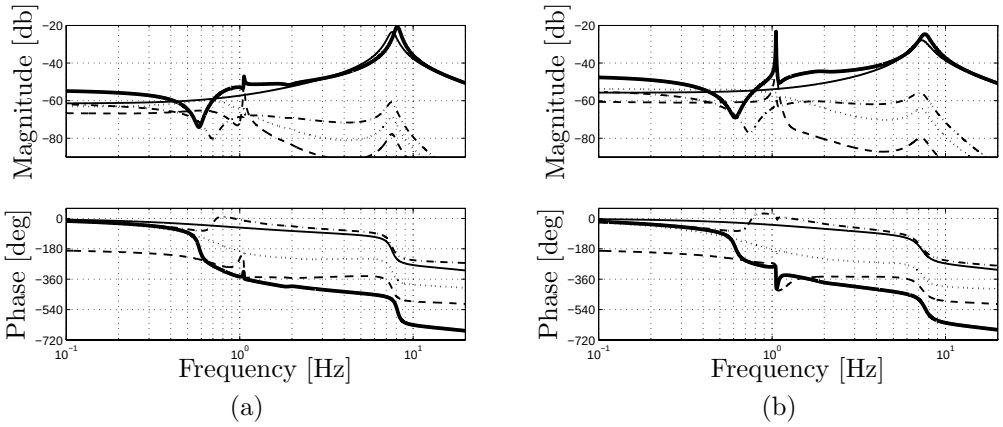

Figure 3.6: Bode plots for first torsional blade mode $\mathbf{q}[4]$ response to uniform wind speed $u_{n,1}$ oscillations, with fixed rotor speed and pitch angle. The total response '**—**' and the contributions from structural coupling to first flapwise blade motion '$\cdots$', edgewise blade motion '- -', and from UAF '$-\cdot-$' and DEW '–'. a) $u_{n,0} = 5$ m/s and b) $u_{n,0} = 15$ m/s. The magnitude is given in [m/(m/s)].

For low excitations frequencies the contributions from first flapwise blade motion, DEW and UAF are of similar size and in phase and their sum gives the total response.

Approaching the first flapwise resonance (≈ 0.7 Hz) frequency the contributions from flapwise blade motion and UAF lose 180 deg of phase, whereby it turns into counter phase with the contribution from DEW, leading to a drop in the total response. The phase of the total response is seen to lose 180 deg at the drop, which shows that it is a right half plane (RHP) zero in the transfer function.

A RHP zero in the transfer function indicates that the initial response of the system to a step input is in the opposite direction of the final response [23]. Numerical simulations show however that this RHP zero do not influence the response noticeably. The RHP zero is caused by small differences in the interaction between the acceleration of the two flapwise modes. Flapwise blade motion gives a twisting moment on the blade because of the offset of the center of gravity from the elastic axis. Using the AMM1 (witch only has one flapwise mode) the RHP zero is shifts to the left half plane, verifying that the RHP zero is caused by interaction between the two flapwise modes.

At the edgewise natural frequency (≈ 1 Hz) the response is dominated by the strong edgewise resonance peak for 15 m/s. After the edgewise natural frequency, the response is dominated by the DEW and the phase follows the phase of this contribution. A resonance peak is seen at the torsional natural frequency (≈ 7.9 Hz), where the phase loses 180 deg.

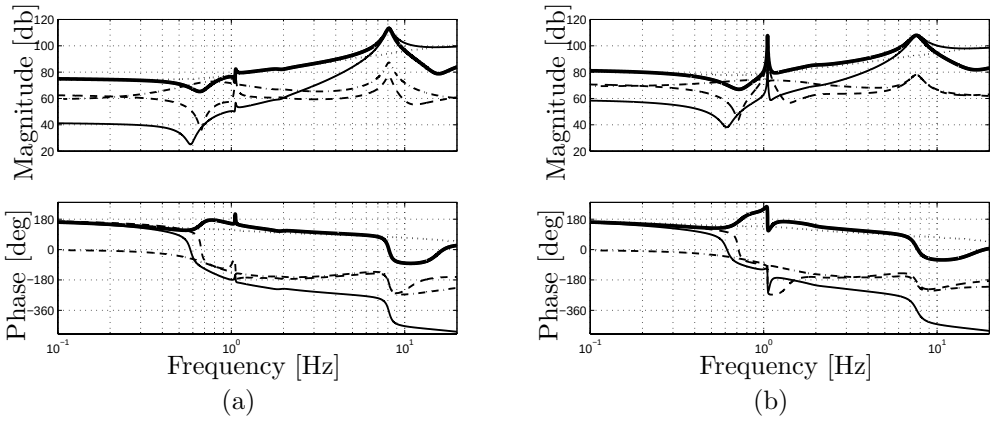

Figure 3.7: Bode plots for pitch moment $M_{pitch,1}$ response to uniform wind speed $u_{n,1}$ oscillations. The total response '**—**' and the contributions from structural coupling to first flapwise blade motion'$-\cdot-$', edgewise blade motion '- -', torsional blade motion '–' and from aerodynamic forces '$\cdots$'. a) $u_{n,0} = 5$ m/s and b) $u_{n,0} = 15$ m/s. The magnitude is given in [Nm/(m/s)].

Pitch Moment Response to Uniform Wind Speed Oscillations

The variations in pitch moment $M_{pitch,1}$ caused by uniform wind speed oscillations is computed by rearranging the assumed mode pitch model (2.68)

$$M_{phitch,1} = \begin{bmatrix}\mathbf{M}_\beta & 0 & 0\end{bmatrix} \begin{bmatrix}\dot{\mathbf{q}} \\ \dot{u}_{n,1} \\ \ddot{u}_{n,1}\end{bmatrix} + \begin{bmatrix}\mathbf{K}_\beta & -\mathbf{f}_\beta[5] & -\mathbf{f}_\beta[8]\end{bmatrix} \begin{bmatrix}\mathbf{q} \\ u_{n,1} \\ \dot{u}_{n,1}\end{bmatrix} \tag{3.3}$$

where the blade motion and wind speed are given by the blade model (3.2).

Figure 3.7 shows the Bode plot for pitch moment $M_{pitch,1}$ response to uniform wind speed $u_{n,1}$ oscillations. The total response is shown together with the particular contributions from structural coupling to first flapwise, first edgewise, and first torsional blade motion, and from aerodynamic forces (the contribution from UAF and DEW).

The aerodynamic forces dominate the response for almost any excitation frequency. For excitation around the first flapwise natural frequency (≈ 0.7 Hz), the structural coupling to the first flapwise mode become considerably, and since it is in counter phase with the effect from aerodynamic forces, it reduces the total response.

Around the first edgewise natural frequency (≈ 1 Hz) the structural coupling to edgewise blade motion affects the pitch moment strongly, especially for 15 m/s. The coupling between edgewise blade motion and pitch moment is strongest at 15 m/s because the blade is more flapwise deformed (Figure 2.3). Because of the flapwise deflection edgewise blade motion directly excite the pitch moment.

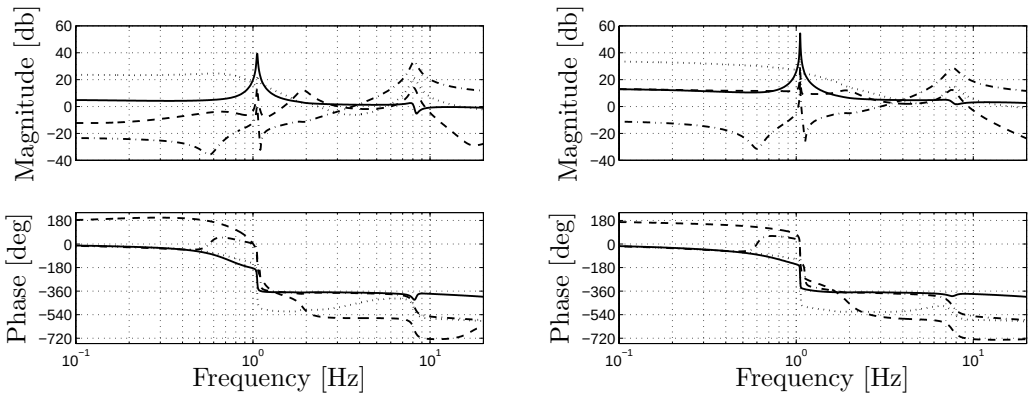

Figure 3.8: Bode plots for blade response to pitch angle β_1 oscillations, with fixed rotor and wind speed. '–' the edgewise mode $\mathbf{q}[1]$, '$\cdots$' the first flapwise mode $\mathbf{q}[2]$, '- -' the second flapwise mode $\mathbf{q}[3]$ and '$-\cdot-$ the torsional mode $\mathbf{q}[4]$. a) $u_{n,0} = 5$ m/s and b) $u_{n,0} = 15$ m/s. The magnitude is given in [m/rad].

The torsional resonance is clearly seen in the pitch moment response. The torsional blade motion is strongly coupled to the pitch moment because it almost acts directly at this degree of freedom.

After the torsional natural frequency (≈ 7.9 Hz) the contributions from torsional blade motion and aerodynamic forces are seen to be of similar size and in counter phase, leading to a drop in the total response.

3.2.2 Blade Response to Pitch Angle Oscillations

The AMM2 is combined with (3.1) to impose pitch angle oscillations, and the rotor and wind speed are constant

$$\begin{bmatrix} \mathbf{M} & \mathbf{0} & -\mathbf{F}[:,3] \\ \mathbf{0} & 1 & 0 \\ \mathbf{0} & 0 & 1 \end{bmatrix} \begin{bmatrix} \dot{\mathbf{q}} \\ \dot{\beta}_1 \\ \ddot{\beta}_1 \end{bmatrix} + \begin{bmatrix} \mathbf{K} & -\mathbf{F}[:,1] & -\mathbf{F}[:,2] \\ \mathbf{0} & 0 & -1 \\ \mathbf{0} & G & D \end{bmatrix} \begin{bmatrix} \mathbf{q} \\ \beta_1 \\ \dot{\beta}_1 \end{bmatrix} = \begin{bmatrix} \mathbf{0} \\ 0 \\ G \end{bmatrix} \beta_{ref} \tag{3.4}$$

where β_{ref} is the input to the Bode plot analysis and $\mathbf{q}[i]$ for $i = 1, 2, 3, 4$ are the states corresponding to the edgewise, first and second flapwise and first torsional mode of blade motion, respectively. Figure 3.8 shows the Bode plots for the blade response to pitch angle oscillations based on (3.4).

For low excitation frequencies the first flapwise blade motion dominates the response, as in the previously case with wind speed oscillations (Figure 3.2). The first edgewise resonance peak (≈ 1 Hz) is more pronounced and the edgewise response after the resonance peak is relatively strong compared to the previously case with wind speed oscillations. The strong coupling between pitch action and

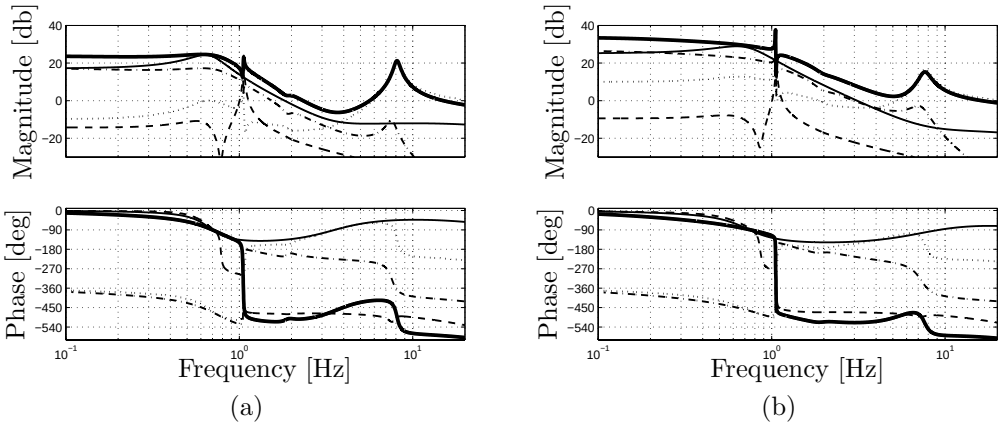

Figure 3.9: Bode plots for first flapwise blade mode $\mathbf{q}[2]$ response to pitch angle β_1 oscillations, with fixed rotor and wind speed. The total response '**—**' and the contributions from structural coupling to edgewise blade motion '- -', torsional blade motion '$\cdots$', and from aerodynamic forces '$- \cdot -$' and DEP '–'. a) $u_{n,0} = 5$ m/s and b) $u_{n,0} = 15$ m/s. The magnitude is given in [m/rad].

edgewise blade motion is caused by the relative large flapwise blade deformation. Because of the flapwise deflection the pitch angle oscillations directly excite the edgewise blade motion.

First Flapwise Dominated Blade Response

Figure 3.9 shows the first flapwise response together with the particular contribution from structural coupling to first edgewise and first torsional blade motion, and the contribution from aerodynamic forces and direct effect from pitch action (DEP), given by $\mathbf{F}[:, 1:3]$ in (3.4).

For low excitation frequencies the total response is dominated by aerodynamic forces and DEP, which are in phase. Approaching the first flapwise natural frequency (≈ 0.7 Hz) the contribution from DEP increase. However the phase between the aerodynamic forces and the DEP increase, resulting in an almost constant total response.

Approaching the first edgewise natural frequency (≈ 1 Hz) the phase between the aerodynamic forces and the DEP continues to increase, reducing the total response.

At 5 m/s there is a zero in the response just before the first edgewise resonance peak and at 15 m/s the is a zero in the response just after the resonance peak. The Phase lose 180 deg at both zeros, which indicates that it are RHP zeros. The zeros are caused by the built up of the edgewise resonance peak, which before it starts to dominate the response is in counter phase with the dominating

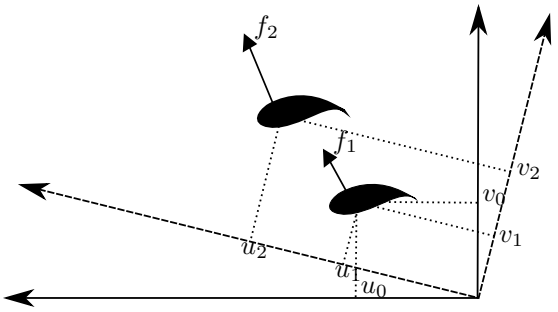

Figure 3.10: Sketch of pitch to blade effect

contributions.

The existence of a RHP zeros indicates that the initial response of the flapwise mode to a changes in pitch angle is in the opposite direction than the final response. Figure 3.10 illustrates the reason for this behavior. Initially the blade cross section is located at (u_0, v_0), the changes of pitch angle rotates the root of the blade and the frame in which the blade deformation is measured. Because of the inertia of the blade the cross section does not instantaneously follow the root of the blade. The new position of the cross section in the rotated frame is (u_1, v_1), hence the u-coordinate increase and the v-coordinate decrease. Eventually the stiffness of the blade makes the cross section follow the rotation of the blade root, increasing the angle of attack, and thereby the aerodynamic forces from f_1 to f_2. The increased aerodynamic forces pull the blade to the new deformed position (u_2, v_2), increasing both the u and v-coordinates. In summary the u-coordinate increase monotonous during the pitch action while the v-coordinate initially decrease before it increase, as predicted by the RHP zero.

After the first edgewise natural frequency all the contributions are in phase and the total response is dominated by the contributions from aerodynamic forces and DEP. Approaching the torsional natural frequency (≈ 7.9 Hz) the contribution from torsional blade motion starts to dominate, and the phase of the total response shift to follow this contribution.

First Edgewise Dominated Response

Figure 3.11 shows the edgewise response together with the particular contribution from structural coupling to first flapwise and first torsional blade motion, and the contribution from aerodynamic forces and DEP.

The edgewise response is dominated by the flapwise blade motion for excitation frequencies below the edgewise natural frequency (≈ 1 Hz), and by the DEP above the edgewise natural frequency. The torsional blade motion has a slight effect on the response at the torsional natural frequency (≈ 7.9 Hz).

The strong coupling between the DEP and the edgewise blade motion is caused by the flapwise blade deformation, as discussed previously. The effect

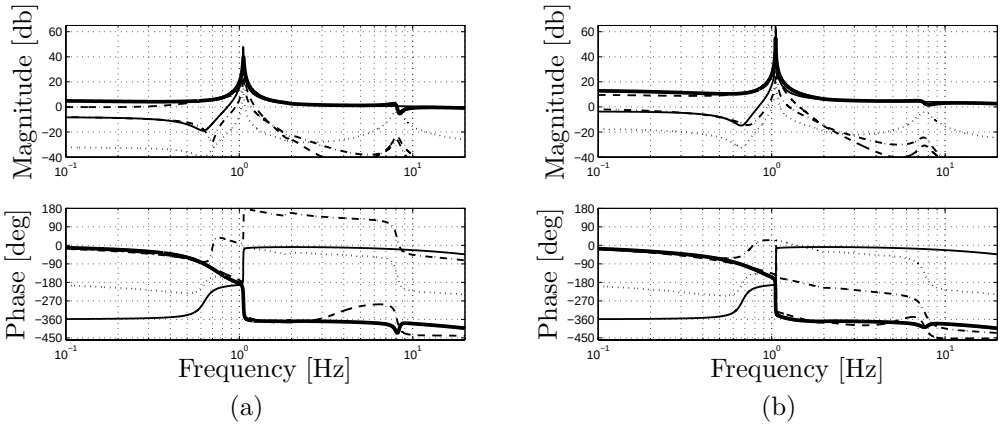

Figure 3.11: Bode plots for first edgewise blade mode $\mathbf{q}[1]$ response to pitch angle β_1 oscillations with fixed rotor and wind speed. The total response '**—**' and the contributions from structural coupling to first flapwise blade motion '- -', torsional blade motion '$\cdots$', and from aerodynamic forces '$- \cdot -$' and DEP '–'. a) $u_{n,0} = 5$ m/s and b) $u_{n,0} = 15$ m/s. The magnitude is given in [m/rad].

is especial pronounced at high frequency excitation because the coupling term in the mass matrix gives an excitation proportional to the pitch acceleration.

Second Flapwise Dominated Blade Mode

Figure 3.12 shows the response of the second flapwise mode to pitch angle oscillations together with the particular contributions from the structural coupling to first flapwise and first torsional blade motion, and from DEP and aerodynamic forces.

For excitations below the edgewise natural frequency ($\approx$ 1 Hz) the second flapwise response is dominated by the first flapwise blade motion. After the edgewise natural peak the response is dominated by the first flapwise blade motion for 5 m/s and by the DEP for 15 m/s. The reason for this difference in dominating contribution is that the flapwise response is larger for 5 m/s than for 15 m/s (Figure 3.8).

Around the torsional natural frequency ($\approx$ 7.9 Hz) the torsional contribution dominates, and at higher frequencies the DEP dominates. As for the first flapwise response there is a zero in the response close to the edgewise resonance peak. The phase at this zero lose 180 deg, hence it is a RHP zero. The physical interpretation of this RHP zero is the same as described under the discussion of first flapwise response.

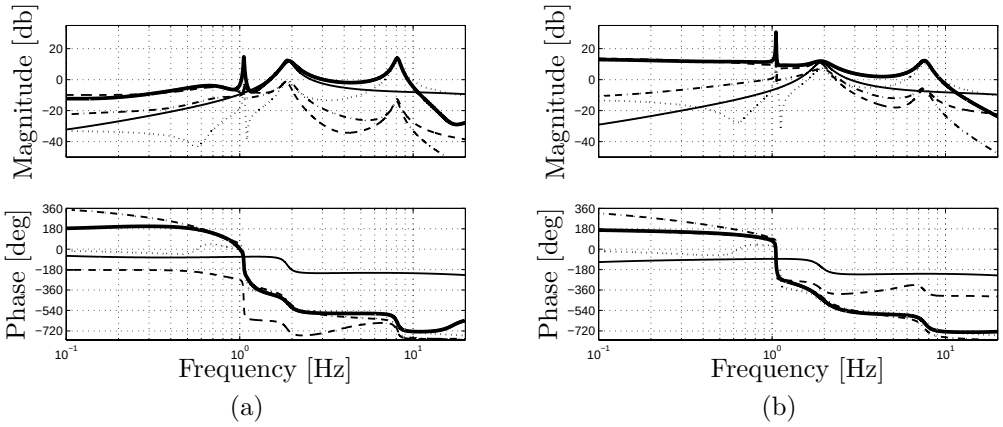

Figure 3.12: Bode plots for second flapwise blade mode $\mathbf{q}[3]$ response to pitch angle β_1 oscillations, with fixed rotor and wind speed. The total response '**—**' and the contributions from structural coupling to first flapwise blade motion '- -', torsional blade motion '$\cdots$', and from aerodynamic forces '$- \cdot -$' and DEP '–'. a) $u_{n,0} = 5$ m/s and b) $u_{n,0} = 15$ m/s. The magnitude is given in [m/rad].

First Torsional Dominated Blade Response

Figure 3.13 shows the torsional response and the particular contributions from the structural coupling to first flapwise and first edgewise blade motion, from aerodynamic forces and DEP.

For low excitations frequencies the contributions from DEP, aerodynamic forces and first flapwise blade motion are in phase and of similar size. The contribution from edgewise blade motion is in counter phase, reducing the total response. Approaching the first flapwise natural frequency (≈ 0.7 Hz) the contributions from flapwise blade motion and unsteady aerodynamic forces lose phase, leading to a decrease in total response.

Approaching the edgewise natural frequency (≈ 1 Hz) the contribution from edgewise blade motion starts to dominate and the phase shifts to follow the phase of this contribution. The edgewise contribution loses 180 deg of phase at the resonance peak, whereby it gets in counter phase with the contribution from the DEP. Just after the edgewise resonance peak the contribution from edgewise blade motion become of similar size as the contribution from DEP, and since they are in counter phase, this leads to a drop in the total response. After this the DEP dominates and the phase of the total response shift to follow this contribution, losing additional 180 deg.

Again the phase lose at the zero just after the edgewise resonance peak indicates a RHP zero in the transfer function. The physical explanation of this RHP zero is as described under the discussion of first flapwise response (Figure 3.10).

For excitations above the edgewise natural frequency the DEP dominates

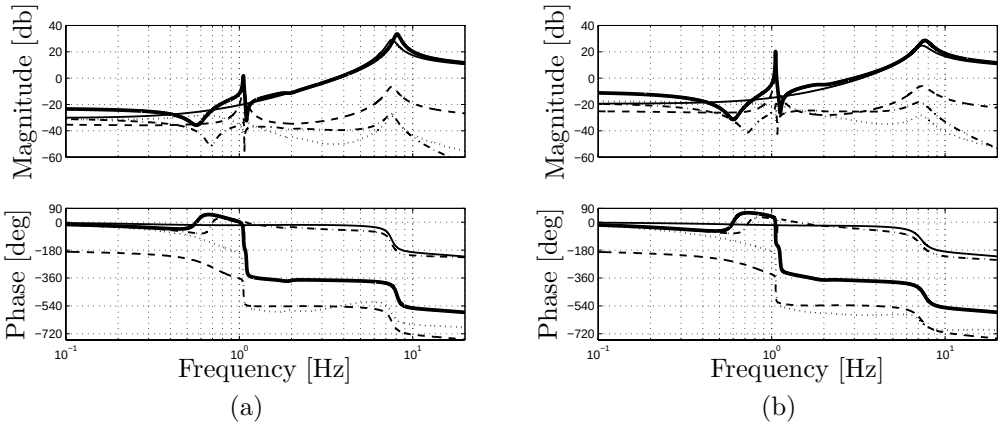

Figure 3.13: Bode plots for first torsional blade mode $\mathbf{q}[4]$ response to pitch angle β_1 oscillations, with fixed rotor and wind speed. The total response '**—**' and the contributions from structural coupling to first flapwise blade motion '$\cdots$', edgewise blade motion '- -', and from aerodynamic forces '$- \cdot -$' and DEP '–'. a) $u_{n,0} = 5$ m/s and b) $u_{n,0} = 15$ m/s. The magnitude is given in [m/rad].

the total response and a large resonance peak is seen at the torsional natural frequency (≈ 7.9 Hz).

Pitch Moment Response to Pitch Angle Oscillations

The variations in pitch moment $M_{pitch,1}$ caused by pitch angle oscillations are computed by the rearranged assumed mode pitch model (2.68)

$$M_{pitch,1} = \begin{bmatrix}\mathbf{M}_\beta & 0 & M_\beta\end{bmatrix} \begin{bmatrix}\ddot{\mathbf{q}} \\ \ddot{\beta}_1 \\ \ddot{\beta}_1\end{bmatrix} + \begin{bmatrix}\mathbf{K}_\beta & K_\beta & D_\beta\end{bmatrix} \begin{bmatrix}\mathbf{q} \\ \beta_1 \\ \dot{\beta}_1\end{bmatrix} \tag{3.5}$$

where the blade motion and pitch action are given by the blade model (3.4).

Figure 3.14 shows the Bode plot for the pitch moment variations $M_{pitch,1}$ response to pitch angle β_1 oscillations. The total response is shown together with the particular contributions from structural coupling to first flapwise, first edgewise and first torsional blade motion, and from DEP.

The pitch moment is dominated by DEP for almost all frequencies. Around the first edgewise natural frequency (≈ 1 Hz) the edgewise contribution dominates the total response, first being in phase with the DEP, increasing the total response. At the edgewise resonance frequency the edgewise contribution loses 180 deg of phase, and becomes in counter phase with the contribution from DEP, witch results in a drop in the total response. As the edgewise response decreases the DEP becomes dominating again, and the phase of the total response follows the phase of this contribution.

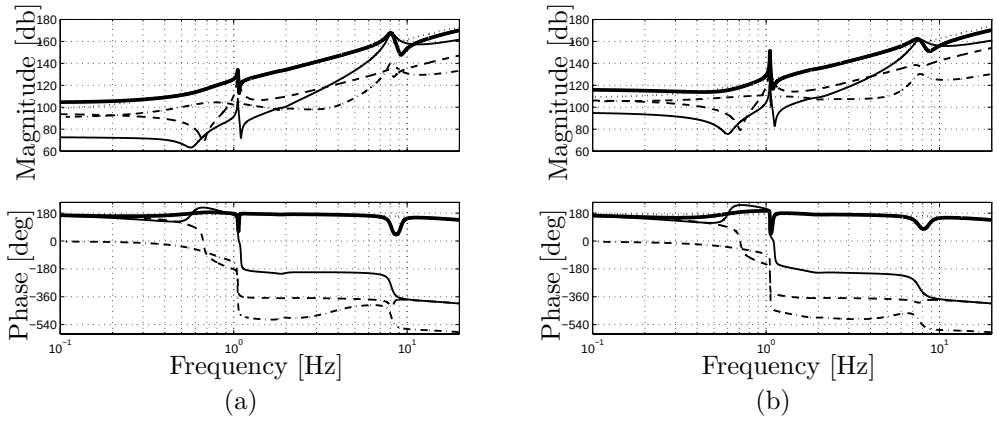

Figure 3.14: Bode plots for pitch moment $M_{pitch,1}$ response to pitch angle β_1 oscillations. The total response '**—**' and the contributions from structural coupling to first flapwise blade motion '$-\cdot-$', edgewise blade motion '- -', torsional blade motion '–', and from DEP '$\cdots$'. a) $u_{n,0} = 5$ m/s and b) $u_{n,0} = 15$ m/s. The magnitude is given in [Nm/rad].

At the torsional natural frequency (≈ 7.9 Hz) the torsional contribution becomes of similar size as the DEP, and is in phase, leading to an increase in the total response. After the torsional resonance peak, the torsional contribution loses 180 deg of phase and becomes in counter phase with the DEP, reducing the total response. The phase follows the phase of the torsional contribution until the DEP becomes dominating again.

3.3 Three Bladed Configuration

The three bladed configuration consists of a system with three of the assumed mode blade models combined with the drivetrain model and (3.1) to impose wind speed and pitch angle oscillations. The response of one blade in the three bladed configuration is compared to the response of the one blade configuration and discussed. The drivetrain and pitch moment responses are shown and the effect of the inclusion of the drivetrain on the edgewise blade response is discussed. The pitch moment is computed by the assumed mode approximated pitch model.

3.3.1 Blade Response to Uniform Wind Speed Oscillations

Three AMM2s are combined with the drivetrain model (2.80) and (3.1) to impose uniform wind speed oscillations, the rotor speed and pitch angle are constant. The

governing equation becomes

$$\begin{bmatrix} \mathbf{M} & \mathbf{0} & \mathbf{0} & \mathbf{0} & -\mathbf{F}[:,7] & \mathbf{0} & \mathbf{0} & \mathbf{0} & \mathbf{0} \\ \mathbf{0} & \mathbf{M} & \mathbf{0} & \mathbf{0} & -\mathbf{F}[:,7] & \mathbf{0} & \mathbf{0} & \mathbf{0} & \mathbf{0} \\ \mathbf{0} & \mathbf{0} & \mathbf{M} & \mathbf{0} & -\mathbf{F}[:,7] & \mathbf{0} & \mathbf{0} & \mathbf{0} & \mathbf{0} \\ \mathbf{0} & \mathbf{0} & \mathbf{0} & 1 & 0 & 0 & 0 & 0 & 0 \\ \mathbf{M}_\phi & \mathbf{M}_\phi & \mathbf{M}_\phi & \mathbf{0} & 3M_\phi & 0 & 0 & 0 & 0 \\ \mathbf{0} & \mathbf{0} & \mathbf{0} & \mathbf{0} & 0 & 1 & 0 & 0 & 0 \\ \mathbf{0} & \mathbf{0} & \mathbf{0} & \mathbf{0} & M_{\bar{\phi}} & 0 & M_{\bar{\phi}} & 0 & 0 \\ \mathbf{0} & \mathbf{0} & \mathbf{0} & \mathbf{0} & 0 & 0 & 0 & 1 & 0 \\ \mathbf{0} & \mathbf{0} & \mathbf{0} & \mathbf{0} & 0 & 0 & 0 & 0 & 1 \end{bmatrix} \begin{bmatrix} \dot{\mathbf{q}}_1 \\ \dot{\mathbf{q}}_2 \\ \dot{\mathbf{q}}_3 \\ \dot{\phi}_1 \\ \ddot{\phi}_1 \\ \dot{\bar{\phi}}_1 \\ \ddot{\bar{\phi}}_1 \\ \dot{u}_{n,1} \\ \ddot{u}_{n,1} \end{bmatrix} +$$

$$\begin{bmatrix} \mathbf{K} & \mathbf{0} & \mathbf{0} & \mathbf{0} & -\mathbf{F}[:,6] & \mathbf{0} & \mathbf{0} & -\mathbf{F}[:,8] & -\mathbf{F}[:,11] \\ \mathbf{0} & \mathbf{K} & \mathbf{0} & \mathbf{0} & -\mathbf{F}[:,6] & \mathbf{0} & \mathbf{0} & -\mathbf{F}[:,8] & -\mathbf{F}[:,11] \\ \mathbf{0} & \mathbf{0} & \mathbf{K} & \mathbf{0} & -\mathbf{F}[:,6] & \mathbf{0} & \mathbf{0} & -\mathbf{F}[:,8] & -\mathbf{F}[:,11] \\ \mathbf{0} & \mathbf{0} & \mathbf{0} & 0 & -1 & 0 & 0 & 1 & 0 \\ \mathbf{K}_\phi & \mathbf{K}_\phi & \mathbf{K}_\phi & \mathbf{0} & 3D_\phi & -K_{\bar{\phi}} & -D_{\bar{\phi}} & -3\mathbf{f}_\phi[4] & -3\mathbf{f}_\phi[7] \\ \mathbf{0} & \mathbf{0} & \mathbf{0} & \mathbf{0} & 0 & K_{\bar{\phi}} & -1 & 0 & 0 \\ \mathbf{0} & \mathbf{0} & \mathbf{0} & \mathbf{0} & -E_{gen} & 0 & D_{\bar{\phi}} - E_{gen} & 0 & 0 \\ \mathbf{0} & \mathbf{0} & \mathbf{0} & \mathbf{0} & 0 & 0 & 0 & 0 & -1 \\ \mathbf{0} & \mathbf{0} & \mathbf{0} & \mathbf{0} & 0 & 0 & 0 & G & D \end{bmatrix} \begin{bmatrix} \mathbf{q}_1 \\ \mathbf{q}_2 \\ \mathbf{q}_3 \\ \phi_1 \\ \dot{\phi}_1 \\ \bar{\phi}_1 \\ \dot{\bar{\phi}}_1 \\ u_{n,1} \\ \dot{u}_{n,1} \end{bmatrix} = \begin{bmatrix} \mathbf{0} \\ \mathbf{0} \\ \mathbf{0} \\ 0 \\ 0 \\ 0 \\ 0 \\ 0 \\ G \end{bmatrix} u_n \tag{3.6}$$

where u_n is the input to the Bode plot analysis and $\mathbf{q}_i$ for $i = 1, 2, 3$ are the outputs corresponding to the ith blade and $\mathbf{q}[j]_i$ $j = 1, 2, 3, 4$ are the first edgewise, first and second flapwise and first torsional mode of blade motion of the ith blade.

Figure 3.15 shows the bode plots for the response of one blade in the three bladed configuration (3.6) to uniform wind speed $u_{n,1}$ oscillations. The response for low excitation frequencies is dominated by the first flapwise mode, this corresponds to the results from the one blade configuration (Figure 3.2). The edgewise blade motion has three resonance peaks compare to two for the one blade configuration. The extra edgewise resonance is caused by interaction with the drivetrain (further discussed below). Between the first two edgewise resonance peaks the first and second flapwise mode are of similar size for 5 m/s while the first flapwise dominates for 15 m/s. Above the second edgewise natural frequency the torsional blade motion dominates the response.

Three Bladed Configuration Versus One Blade Configuration

Figure 3.16 and 3.17 compare the responses from the three bladed configuration (3.6) and the one blade configuration (3.2). The edgewise response has three peaks for the three bladed configuration compared to the two for the one blade configuration. The first edgewise natural frequency ($\approx$ 1.5 Hz) is higher for the three bladed configurations than for the one blade configuration ($\approx$ 1 Hz). This is caused by the interaction with the drivetrain which changes the boundary condition for edgewise blade motion. In the one blade configuration, the hub acts

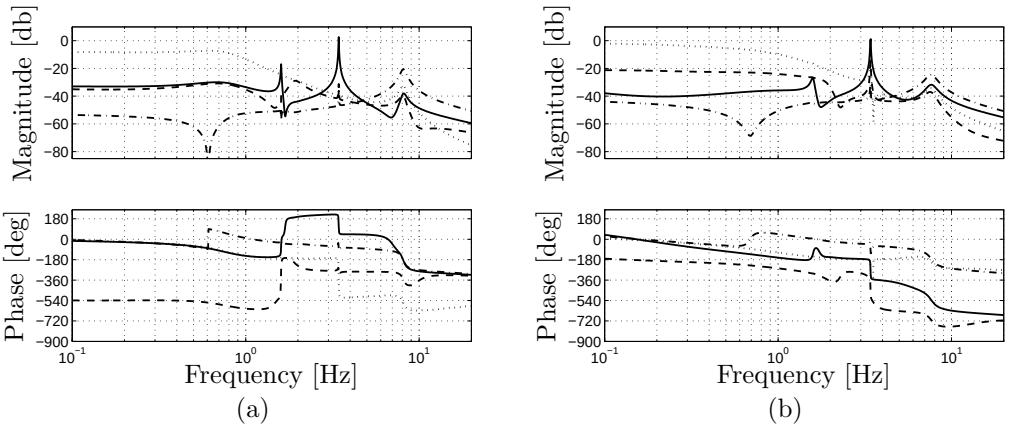

Figure 3.15: Bode plots for the response of one blade in the the three bladed configuration (3.6) to wind speed $u_{n,1}$ oscillations. '–' edgewise response $\mathbf{q}[1]_1$, '$\cdots$' first flapwise response $\mathbf{q}[2]_1$, '- -' second flapwise response $\mathbf{q}[3]_1$ and '$- \cdot -$'' torsional response $\mathbf{q}[4]_1$. a) $u_{n,0} = 5$ m/s and b) $u_{n,0} = 15$ m/s. The magnitude is given in [m/(m/s)].

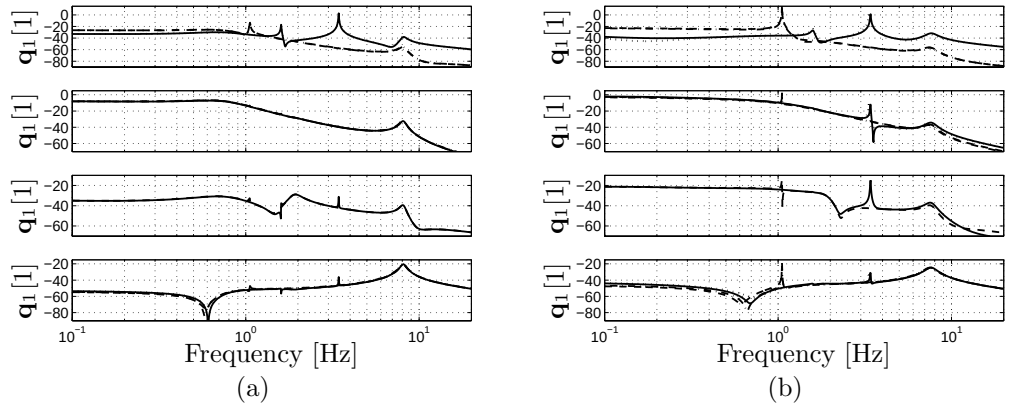

Figure 3.16: Magnitude of blade response to uniform wind speed $u_{n,1}$ oscillations. Three bladed '–' and one blade '- -' configurations of AMM2, three bladed '$\cdots$' and one blade '$- \cdot -$' configurations of AMM1. a) $u_{n,0} = 5$ m/s and b) $u_{n,0} = 15$ m/s. The magnitude is given in [m/(m/s)] on a db scale.

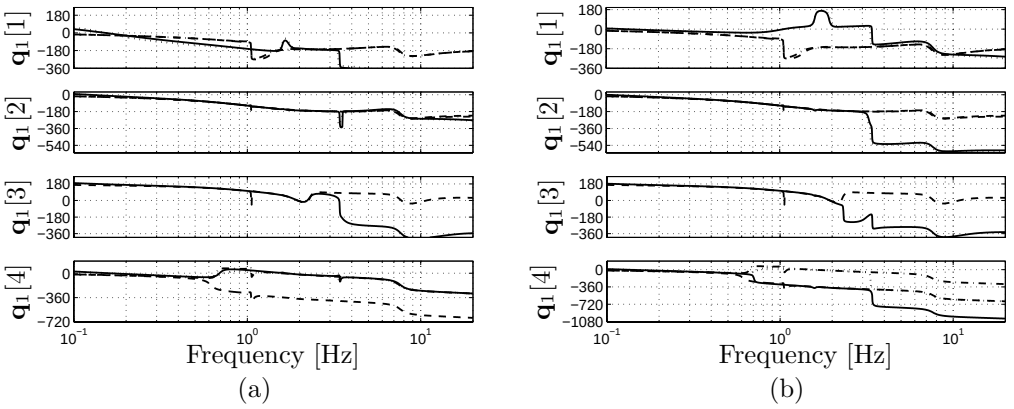

Figure 3.17: Phase between blade response and uniform wind speed $u_{n,1}$ oscillations. Three bladed '–' and one blade '- -' configurations of AMM2, three bladed'$\cdots$' and one blade '$-\cdot-$' configurations of AMM1. a) $u_{n,0} = 5$ m/s and b) $u_{n,0} = 15$ m/s. The phase is given in [deg].

almost as a clamped boundary condition, because the rotor speed is constant. Whereas in the three bladed configuration the hub acts as a simple supported boundary condition with a moment, because the flexible drivetrain and the generator react to the blade motion.

The first flapwise response is very similar for the two cases, except from the effect of the second edgewise resonance peak in the three bladed configuration, which is not present in the one blade configuration. The second flapwise mode is very similar for the two configurations. The flapwise modes are not considerably effected by the introduction of the drive train because the drivetrain contribution is in the rotor plane, almost orthogonal to the flapwise modes.

The torsional response is also very similar for the two configurations, except for the effect of the extra edgewise resonance peak in the three bladed configuration.

Drivetrain Response

Figure 3.18 shows the Bode plots for the responses of the drivetrain $\bar{\phi}_1$, the first edgewise blade motion $\mathbf{q}[1]_1$ and the hub ϕ_1 to uniform wind speed $u_{n,1}$ oscillations. The responses from the drivetrain and the hub are multiplied by the radius of the blade R to make them comparable with the edgewise blade response.

For low excitation frequencies the edgewise blade motion is in phase with the excitation and in counter phase with the drivetrain and the hub. The drivetrain and the hub are in phase. The drivetrain shows a very small response, leading to an almost rigid connection between hub and generator. The edgewise blade

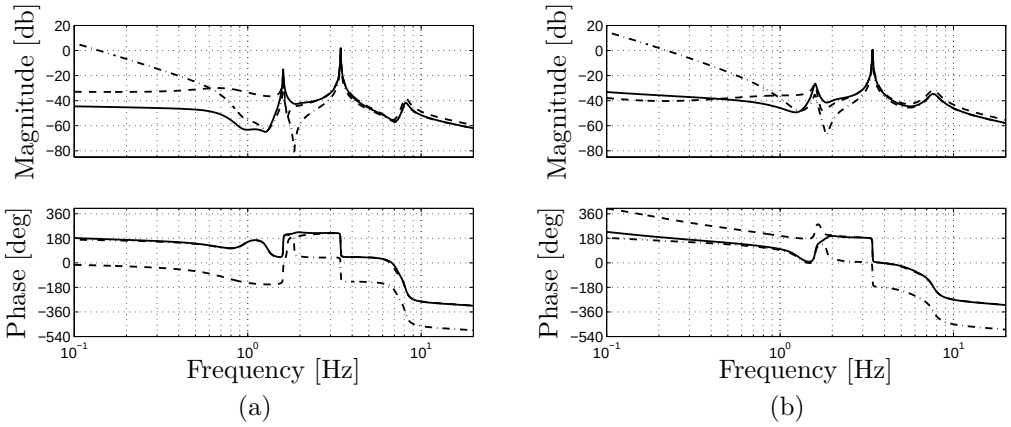

Figure 3.18: Bode plots for responses of the drivetrain $\bar{\phi}_1$ '–', the hub ϕ_1 '–·–' and the edgewise blade $\mathbf{q}[1]_1$ motion '- -' to wind speed $u_{n,1}$ oscillations, for the three bladed configuration (3.6). a) $u_{n,0} = 5$ m/s and b) $u_{n,0} = 15$ m/s. The magnitude is given in [m/(m/s)].

response is small, and since the blade motion is described in a frame following the hub, this show that the blades follow the hub almost as rigid bodies. All in all the response at low frequencies is an almost rigid body motion of drivetrain, hub and blades.

When the excitation frequency is increased the response of the hub reduces while the response of the edgewise blade motion and the drivetrain stay almost constant. Before the first edgewise natural frequency (≈ 1.5 Hz) all the responses decrease. The reason for this decrease is the interaction with the first flapwise mode as discussed under the section about edgewise blade motion of the one blade configuration (Section 3.2.1). The interaction between the flexible drivetrain and the generator makes the first edgewise natural frequency higher than the first edgewise natural frequency for the one blade configuration.

At the first resonance peak (≈ 1.5 Hz) the hub and the drivetrain are in phase, resulting in large generator speed oscillations. The edgewise blade and the hub responses are in counter phase, and the hub response is a bit smaller than the edgewise response, meaning that the absolute edgewise oscillations of the blade tip are small and in phase with the generator. All in all, the first resonance peak is mainly caused by drivetrain vibrations and results in considerable generator speed oscillations. Note that the phase increase at the first edgewise resonance peak, which indicates that the pole is in the RHP, hence unstable. This instability is caused by the negative damping from the ideal power regulation of the generator (2.76).

Between the two resonance peaks the drivetrain response is larger than the hub response, showing that there are considerably generator speed oscillations. The phase between the responses shift such that the drivetrain and the edgewise

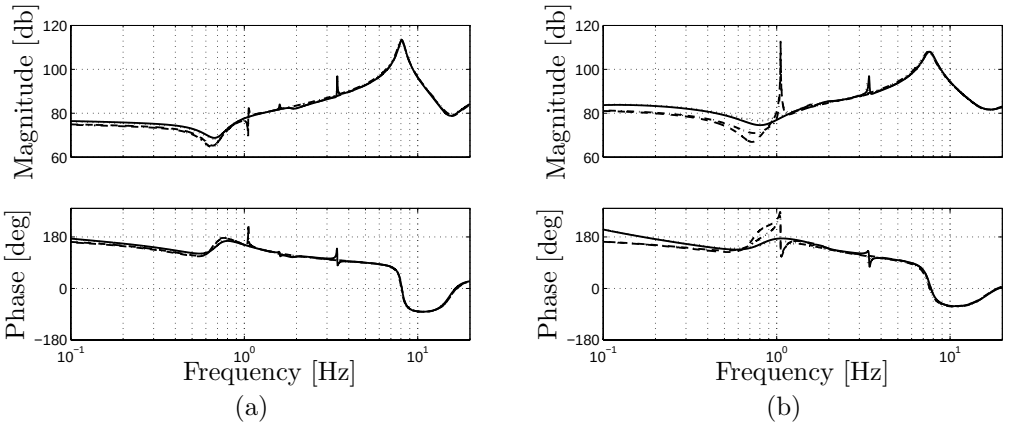

Figure 3.19: Bode plots for pitch moment $M_{pitch,1}$ response to wind speed $u_{n,1}$ oscillations. Three bladed configuration '–' and one blade configuration '- -' with AMM2, three bladed configuration '$\cdots$' and one blade configuration '$- \cdot -$' with AMM1. a) $u_{n,0} = 5$ m/s and b) $u_{n,0} = 15$ m/s. The magnitude is given in [Nm/(m/s)].

blade motion are in phase and the hub is in counter phase.

Approaching the second natural frequency (≈ 3.5 Hz) the responses become similar in size, and since the hub and the drivetrain are in counter phase, this means that the generator speed is almost constant. That is, the response is a combination of blade motion and drivetrain.

The hub acts as a simple support of edgewise bending of the blade, and therefore the first edgewise natural frequency is higher than for the one blade configuration, where the hub acts as a clamped support (constance rotor speed). The assumed edgewise mode shape used in the assumed mode approximated blade model are based on a clamped support, hence the mode shapes are not the true mode shapes in this case.

Pitch Moment Response

Figure 3.19 shows the pitch moment response for two three bladed configurations based on the AMM1 and AMM2, respectively, and from two one blade configuration based on the AMM1 and AMM2, respectively. The responses from all four models are seen to agree well for almost all frequencies, except for low frequency excitation at 15 m/s and at the edgewise resonance peaks.

For low excitation frequencies the pitch moment for the three bladed configurations is higher than for the one blade configurations, especially at 15 m/s. This difference is caused by the difference in edgewise response for the one blade and the three bladed configurations (Figure 3.16).

As discussed above the edgewise resonance peaks are different for the one

blade and the three bladed configurations. These differences is caused by the inclusion of the drivetrain in the three bladed configuration, which change the edgewise response and thereby the pitch moment.

Four Versus Three Assumed Structural Modes

Figure 3.16, 3.17 and 3.19 also compares the one blade and three bladed configurations based on the assumed mode model with three structural modes (AMM1) and four structural modes (AMM2). It is seen that responses of the models based on three structural modes agree very well with the models based on four structural modes. This indicates that models based on three structural modes (AMM1) are sufficient for analyze of fundamental blade and pitch moment responses, and interaction between pitch action and blade motion.

3.3.2 Blade Response to Pitch Angle Oscillations

Three AMM2s are combined with the drivetrain model (2.80) and (3.1) to impose pitch angle oscillations, the rotor and wind speed are constant. The governing equations becomes

$$
\begin{bmatrix}
\mathbf{M} & \mathbf{0} & \mathbf{0} & \mathbf{0} & -\mathbf{F}[:,7] & \mathbf{0} & \mathbf{0} & \mathbf{0} & -\mathbf{F}[:,3] \\
\mathbf{0} & \mathbf{M} & \mathbf{0} & \mathbf{0} & -\mathbf{F}[:,7] & \mathbf{0} & \mathbf{0} & \mathbf{0} & -\mathbf{F}[:,3] \\
\mathbf{0} & \mathbf{0} & \mathbf{M} & \mathbf{0} & -\mathbf{F}[:,7] & \mathbf{0} & \mathbf{0} & \mathbf{0} & -\mathbf{F}[:,3] \\
\mathbf{0} & \mathbf{0} & \mathbf{0} & 1 & 0 & 0 & 0 & 0 & 0 \\
\mathbf{M}_\phi & \mathbf{M}_\phi & \mathbf{M}_\phi & \mathbf{0} & 3M_\phi & 0 & 0 & 0 & -3\mathbf{f}_\phi[3] \\
\mathbf{0} & \mathbf{0} & \mathbf{0} & \mathbf{0} & 0 & 1 & 0 & 0 & 0 \\
\mathbf{0} & \mathbf{0} & \mathbf{0} & \mathbf{0} & M_{\bar{\phi}} & 0 & M_{\bar{\phi}} & 0 & 0 \\
\mathbf{0} & \mathbf{0} & \mathbf{0} & \mathbf{0} & 0 & 0 & 0 & 1 & 0 \\
\mathbf{0} & \mathbf{0} & \mathbf{0} & \mathbf{0} & 0 & 0 & 0 & 0 & 1
\end{bmatrix}
\begin{bmatrix}
\ddot{\mathbf{q}}_1 \\ \ddot{\mathbf{q}}_2 \\ \ddot{\mathbf{q}}_3 \\ \ddot{\phi}_1 \\ \ddot{\phi}_1 \\ \ddot{\bar{\phi}}_1 \\ \ddot{\bar{\phi}}_1 \\ \ddot{\beta}_1 \\ \ddot{\beta}_1
\end{bmatrix} +
$$

$$
\begin{bmatrix}
\mathbf{K} & \mathbf{0} & \mathbf{0} & \mathbf{0} & -\mathbf{F}[:,6] & \mathbf{0} & \mathbf{0} & -\mathbf{F}[:,1] & -\mathbf{F}[:,2] \\
\mathbf{0} & \mathbf{K} & \mathbf{0} & \mathbf{0} & -\mathbf{F}[:,6] & \mathbf{0} & \mathbf{0} & -\mathbf{F}[:,1] & -\mathbf{F}[:,2] \\
\mathbf{0} & \mathbf{0} & \mathbf{K} & \mathbf{0} & -\mathbf{F}[:,6] & \mathbf{0} & \mathbf{0} & -\mathbf{F}[:,1] & -\mathbf{F}[:,2] \\
\mathbf{0} & \mathbf{0} & \mathbf{0} & 0 & -1 & 0 & 0 & 1 & 0 \\
\mathbf{K}_\phi & \mathbf{K}_\phi & \mathbf{K}_\phi & \mathbf{0} & 3D_\phi & -K_{\bar{\phi}} & -D_{\bar{\phi}} & -3\mathbf{f}_\phi[1] & -3\mathbf{f}_\phi[2] \\
\mathbf{0} & \mathbf{0} & \mathbf{0} & \mathbf{0} & 0 & K_{\bar{\phi}} & -1 & 0 & 0 \\
\mathbf{0} & \mathbf{0} & \mathbf{0} & \mathbf{0} & -E_{gen} & 0 & D_{\bar{\phi}} - E_{gen} & 0 & 0 \\
\mathbf{0} & \mathbf{0} & \mathbf{0} & \mathbf{0} & 0 & 0 & 0 & 1 & 0 \\
\mathbf{0} & \mathbf{0} & \mathbf{0} & \mathbf{0} & 0 & 0 & 0 & G & D
\end{bmatrix}
\begin{bmatrix}
\mathbf{q}_1 \\ \mathbf{q}_2 \\ \mathbf{q}_3 \\ \phi_1 \\ \dot{\phi}_1 \\ \dot{\bar{\phi}}_1 \\ \bar{\phi}_1 \\ \beta_1 \\ \dot{\beta}_1
\end{bmatrix} =
\begin{bmatrix}
\mathbf{0} \\ \mathbf{0} \\ \mathbf{0} \\ 0 \\ 0 \\ 0 \\ 0 \\ 0 \\ G
\end{bmatrix} \beta_{ref}
\tag{3.7}
$$

where β_{ref} is the input in the Bode plot analysis and $\mathbf{q}_i$ for $i = 1, 2, 3$ are the outputs corresponding to the ith and $\mathbf{q}[j]_i$ $j = 1, 2, 3, 4$ are the first edgewise, first and second flapwise and first torsional mode of motion of the ith blade.

Figure 3.20 shows the response to pitch angle oscillations of one blade in the three bladed configuration (3.7). As for the one blade configuration (Figure 3.8) and the wind to blade analysis (Figure 3.15), the response for low excitation frequencies is dominated by the first flapwise mode. Again, the edgewise blade

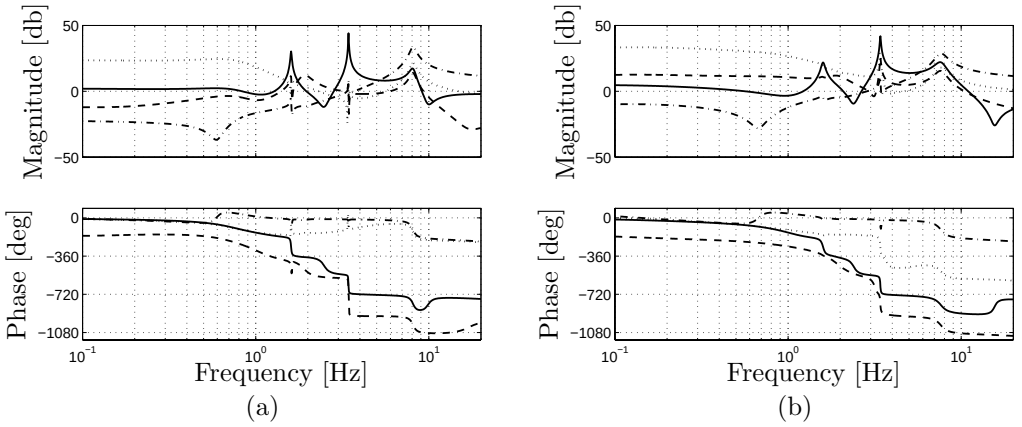

Figure 3.20: Bode plot for the response of one blade in the three bladed configuration (3.7) to pitch angle β_1 oscillations. '–' edgewise response $\mathbf{q}[1]_1$, '$\cdots$' first flapwise response $\mathbf{q}[2]_1$, '- -' second flapwise response $\mathbf{q}[3]_1$ and '$-\cdot-$'' torsional response $\mathbf{q}[4]_1$. a) $u_{n,0} = 5$ m/s and b) $u_{n,0} = 15$ m/s. The magnitude is given in [m/rad].

motion has an extra resonance peak compared to the one blade configuration, caused by the interaction between the edgewise motion and the flexible drivetrain.

Three Bladed Configuration Versus One Blade Configuration

Figure 3.21 and 3.22 compare the response from the three bladed configuration (3.7) and the one blade configuration (3.4). As for the previously case with wind excitation the edgewise response is the one which shows the most difference between the one blade configuration and the three bladed configuration. The reason is, as before, that the edgewise blade motion is more directly affected by the drivetrain motion than the flapwise and torsional blade motion. The edgewise response is discussed further below.

The first and second flapwise and the first torsional modes agree very well with the results from the one blade configuration for low excitation frequencies. The influence from the edgewise resonance peaks changes corresponding to the change in edgewise response.

At higher excitation frequencies there is a considerable difference between the responses of first and second flapwise modes for the one blade configuration and the three bladed configuration. This is caused by the large edgewise response at high frequencies, which makes the difference between the one and the three bladed configurations more pronounced.

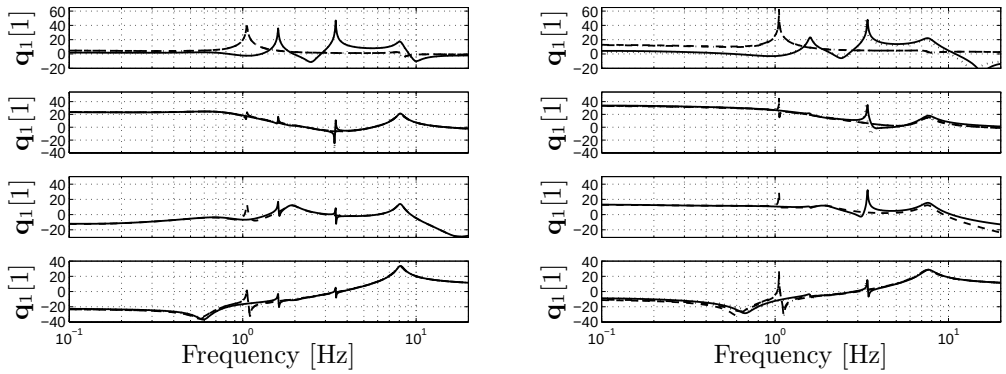

Figure 3.21: Magnitude of blade response to pitch angle β_1 oscillations. Three bladed '–' and one blade '- -' configurations of AMM2, three bladed'$\cdots$' and one blade '$-\cdot-$' configurations of AMM1. a) $u_{n,0} = 5$ m/s and b) $u_{n,0} = 15$ m/s. The magnitude is given in [m/rad] on a db scale.

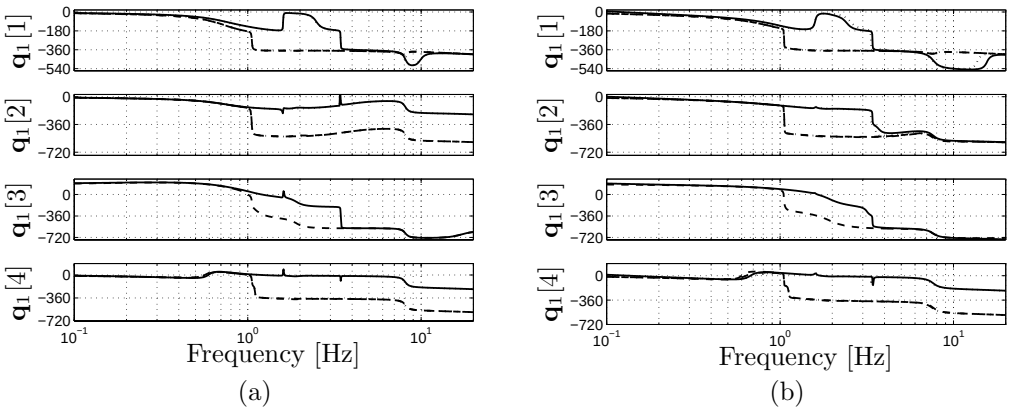

Figure 3.22: Phase between blade response and pitch angle β_1 oscillations. Three bladed '–' and one blade '- -' configurations of AMM2, three bladed'$\cdots$' and one blade '$-\cdot-$' configurations of AMM1. a) $u_{n,0} = 5$ m/s and b) $u_{n,0} = 15$ m/s. The phase is given in [deg].

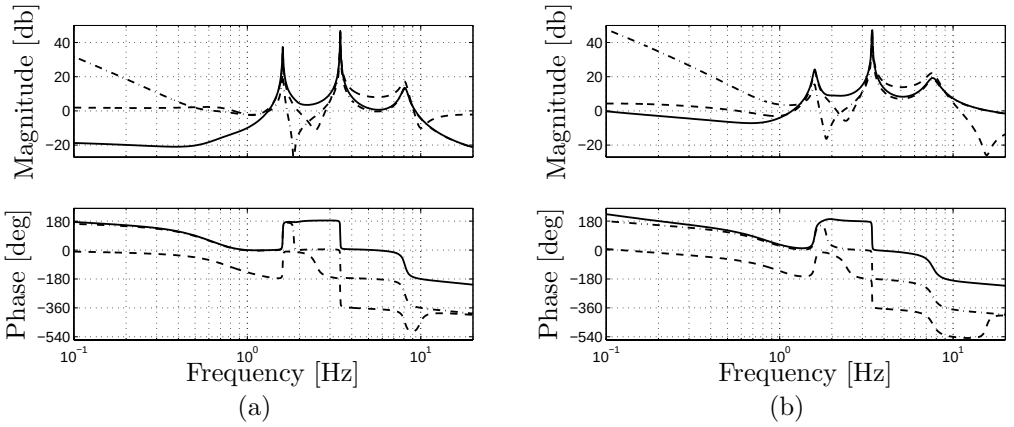

Figure 3.23: Bode plots for the responses the drivetrain $\bar{\phi}_1$ '-', the hub ϕ_1 '$-\cdot-$' and the edgewise blade motion $\mathbf{q}[1]_1$ '–' to pitch angle oscillations β_1, for the three bladed configuration (3.7). a) $u_{n,0} = 5$ m/s and b) $u_{n,0} = 15$ m/s. The magnitude is given in [m/rad].

Drivetrain Response

Figure 3.23 shows the Bode plot for responses of the drivetrain $\bar{\phi}_1$, the edgewise blade motion $\mathbf{q}[1]_1$ and the hub ϕ_1 to pitch angle oscillations. The responses from the drivetrain and the hub are multiplied by the radius of the blade R to make them comparable with the edgewise blade response. The edgewise, drivetrain and hub responses behave like in the previous case with wind excitation (Figure 3.18), except that the edgewise response is higher at high excitation frequencies. This is caused by the strong coupling between the pitch action and the edgewise motion, as discussed previously in Section 3.2.2.

Pitch Moment Response

Figure 3.24 shows the pitch moment response for two three bladed configurations based on the AMM1 and AMM2, respectively, and from two one blade configurations based on the AMM1 and AMM2, respectively. The pitch moment response for the model based on the three bladed configurations agrees very well to the pitch moment response for the one blade configurations for almost all frequencies. Again the influence from the edgewise motion differs for the two configurations, corresponding to the differences in edgewise response for the two configurations.

Four Versus Three Assumed Structural Modes

Figure 3.21, 3.22 and 3.24 compare responses of the one blade and three bladed configurations based on the assumed mode models with three structural modes (AMM1) and four structural modes (AMM2). For all cases the responses of the

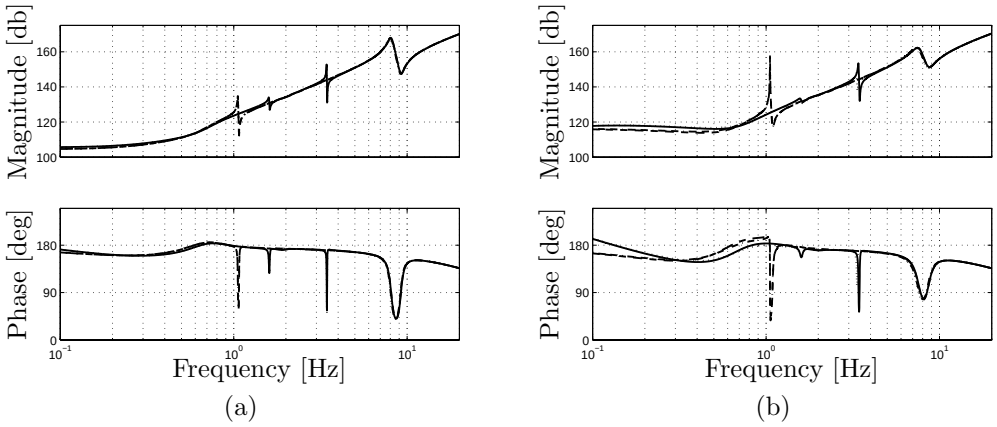

Figure 3.24: Bode plot for pitch moment $M_{pitch,1}$ response to pitch angle β_1 oscillations. Three bladed '–' and one blade '- -' configurations of AMM2, three bladed'$\cdots$' and one blade '$-\cdot-$' configurations of AMM1. a) $u_{n,0} = 5$ m/s and b) $u_{n,0} = 15$ m/s. The magnitude is given in [Nm/rad].

models based on three structural modes agree very well with the corresponding models based on four structural modes. Again this indicates that models based on three structural modes (AMM1) are sufficient for analyze of fundamental blade motion and interaction between pitch action and blade motion.

3.4 Potentials for Fatigue Load Reducing Control

Figure 3.8(b) shows that low frequency variations in pitch angle affects the flapwise blade motion stronger than the edgewise blade motion. Therefore the potentials for using pitch control to control blade motion is larger for flapwise blade motion than for edgewise blade motion. A pitch angle change affects the flapwise blade motion more than the edgewise blade motion because the flapwise blade motion are much more affected by aerodynamic forces, which depends on the pitch angle. Figure 3.2(b) shows that low frequency variations in wind speed affect the flapwise blade motion the most. Since the flapwise blade motion is most affected by both wind speed variations and pitch action there is a high potential for using pitch control for reducing the effect of wind speed changes on flapwise blade motion.

Wind shear and gravity effects are caused by the rotation of the rotor and therefore they excite the blade at a frequency corresponding to the rotation frequency of the rotor. Figure 3.2, 3.15, 3.8 and 3.20 shows that for the test blade, wind speed and pitch oscillations below approximately 0.2 Hz affect the blade in a quasi steady manner. Since the rotation frequency of the rotor of the test turbine is at most 0.2 Hz, a load reducing controller, which concerns loads dependent on the rotation of the rotor, can be designed without including blade dynamic.

Table 3.1: Quasi steady relations between control input and blade deflection, and between the disturbances and blade deflection at $u_{n,0} = 15$ m/s.

	u	v	θ
β_1	-0.012 m/deg	-0.32 m/deg	-0.11 deg/deg
$u_{n,1}$	-0.013 m/(m/s)	-0.29 m/(m/s)	-0.093 deg/(m/s)
$u_{n,2}$	-0.009 m/(m/s)	-0.23 m/(m/s)	-0.066 deg/(m/s)
$\sin(\phi_1 + \dot{\phi}_0 t)$	0.46 m	0.20 m	-0.09 deg
$\cos(\phi_1 + \dot{\phi}_0 t)$	-0.0053 m	0.0012 m	-0.015 deg

Table 3.1 quantifies the effect of a pitch change and the effect of the estimated and known disturbances on the blade deflection. As discussed above, a pitch angle change has a stronger effect on flapwise blade deflection than on edgewise blade deflection. It is also seen that a pitch angle change has a small effect on the torsional deflection. A change in the uniform wind speed and the wind shear have a considerably effect on the flapwise blade deflection, while it has almost no effect on edgewise and torsional blade deflections. All in all there is a high potential for using pitch control to reduce the flapwise blade motion caused by wind speed variations and wind shear.

The effect of gravity ($\sin(\phi_1 + \dot{\phi}_0 t)$ and $\sin(\phi_1 + \dot{\phi}_0 t)$) is strongest on the edgewise blade deflection, but the effect of a pitch angle change is small on the edgewise blade deflection. Therefore the potential for using pitch control to reduce the considerable effect of gravity on the edgewise blade motion is low.

3.5 Summary

The blade and pitch moment responses to wind speed and pitch angle oscillations are analyzed using an one blade configuration and a three bladed configuration including drivetrain flexibility and generator model. The blade and pitch moment responses of the one blade configuration are analyzed in details, showing how structural coupling between modes and the aerodynamic forces affect the individual modes of blade motion and the pitch moment.

Responses of one blade in the three bladed configuration are compared to the responses of the one blade configuration. The flapwise and torsional blade motion agree well for the one blade and the three bladed configurations, while the edgewise blade response is considerably different for the two configurations. The edgewise blade motion of the three bladed configuration interacts with the drive train flexibility and the generator speed, leading to a different response than for the one blade configuration. The responses up to about 1 Hz are however seen to agree fairly well, hence the one blade configuration can be sufficient for analyze of effects with frequencies below 1 Hz.

Results computed with the assumed mode model based on four structural

modes (AMM2) are compared with corresponding results computed with the assumed mode model based on three structural modes (AMM1). The first edgewise, first flapwise and first torsional responses agree very well for both versions. Also the drivetrain response and the pitch moment response agree very well for the two versions of the assumed mode model. This indicates that the assumed mode model based on three structural modes (AMM1) is sufficient for fundamental blade and pitch response analysis.

The analysis shows that there is a high potential for using pitch control to reduced fatigue loads on the blade caused by wind shear and uniform wind speed variations. It is also shown that there is a very low potential for using pitch control to reduce the edgewise blade motion caused by gravity. The analysis shows that for load reducing controllers concerning loads that varies slower than 0.2 Hz (for the particular test wind turbine) it is not necessary to include blade dynamics in the control design.

Chapter 4
State Estimate and Control Design

This chapter gives an application example of the developed assumed mode model. In Chapter 3 it was suggested that there is a high potential for using pitch control to reduce fatigue loads on wind turbine blades caused by wind shear and uniform wind speed variations. It was also suggested that the potential for using pitch control to reduce the edgewise blade motion caused by gravity is low. This chapter concerns the development of a state estimator, a rotor speed controller and a superimposed load reducing controller for a three bladed wind turbine. The controllers are designed for region 3, where the main objective for the pitch controller is to limit the energy extracted from the wind, such that it corresponds to the capacity of the generator and thereby keep the rotational speed constant. The state estimator estimates both the states of the model, the incoming wind speed $u_{n,1}$ and the wind shear $u_{n,2}$. The estimator estimates the incoming wind speed well and the wind shear very well. The estimated wind components are used in a fatigue load reducing controller. The controller reduces the flapwise blade motion caused by wind shear considerably while it is not capable of reducing the effects of gravity.

4.1 Turbine Configuration

The three bladed aeroelastic wind turbine model (2.82) is extended to include the rotor position ϕ_1, individual pitch, gravity and wind shear. The rotor position is included since it is used to determine the effect of gravity and wind shear. The power control of the generator is assumed to be ideal, hence the generator model (2.76) is applicable.

The extended turbine model is

$$\dot{\mathbf{x}} = \mathbf{A}\mathbf{x} + \mathbf{B}\mathbf{u}_{wt} \tag{4.1}$$

where $\mathbf{x} = [\mathbf{q}_1, \mathbf{q}_2, \mathbf{q}_3, \phi_1, \dot{\phi}_1, \bar{\phi}_1, \dot{\bar{\phi}}_1]^{\mathrm{T}}$ is the state vector,

$$\mathbf{A} = \begin{bmatrix} \mathbf{M} & \mathbf{0} & \mathbf{0} & \mathbf{0} & -\mathbf{F}[:,7] & \mathbf{0} & \mathbf{0} \\ \mathbf{0} & \mathbf{M} & \mathbf{0} & \mathbf{0} & -\mathbf{F}[:,7] & \mathbf{0} & \mathbf{0} \\ \mathbf{0} & \mathbf{0} & \mathbf{M} & \mathbf{0} & -\mathbf{F}[:,7] & \mathbf{0} & \mathbf{0} \\ \mathbf{0} & \mathbf{0} & \mathbf{0} & -1 & 0 & 0 & 0 \\ \mathbf{M}_\phi & \mathbf{M}_\phi & \mathbf{M}_\phi & 0 & 3M_\phi & 0 & 0 \\ \mathbf{0} & \mathbf{0} & \mathbf{0} & 0 & 0 & -1 & 0 \\ \mathbf{0} & \mathbf{0} & \mathbf{0} & 0 & M_{\bar{\phi}} & 0 & M_{\bar{\phi}} \end{bmatrix}^{-1} \begin{bmatrix} -\mathbf{K} & \mathbf{0} & \mathbf{0} & \mathbf{0} & \mathbf{F}[:,6] & \mathbf{0} & \mathbf{0} \\ \mathbf{0} & -\mathbf{K} & \mathbf{0} & \mathbf{0} & \mathbf{F}[:,6] & \mathbf{0} & \mathbf{0} \\ \mathbf{0} & \mathbf{0} & -\mathbf{K} & \mathbf{0} & \mathbf{F}[:,6] & \mathbf{0} & \mathbf{0} \\ \mathbf{0} & \mathbf{0} & \mathbf{0} & 0 & -1 & 0 & 0 \\ -\mathbf{K}_\phi & -\mathbf{K}_\phi & -\mathbf{K}_\phi & 0 & -3D_\phi & K_{\bar{\phi}} & D_{\bar{\phi}} \\ \mathbf{0} & \mathbf{0} & \mathbf{0} & 0 & 0 & 0 & -1 \\ \mathbf{0} & \mathbf{0} & \mathbf{0} & 0 & E_{gen} & -K_{\bar{\phi}} & E_{gen} + D_{\bar{\phi}} \end{bmatrix} \tag{4.2}$$

$$\mathbf{B} = \begin{bmatrix} \mathbf{M} & \mathbf{0} & \mathbf{0} & \mathbf{0} & -\mathbf{F}[:,7] & \mathbf{0} & \mathbf{0} \\ \mathbf{0} & \mathbf{M} & \mathbf{0} & \mathbf{0} & -\mathbf{F}[:,7] & \mathbf{0} & \mathbf{0} \\ \mathbf{0} & \mathbf{0} & \mathbf{M} & \mathbf{0} & -\mathbf{F}[:,7] & \mathbf{0} & \mathbf{0} \\ \mathbf{0} & \mathbf{0} & \mathbf{0} & -1 & 0 & 0 & 0 \\ \mathbf{M}_\phi & \mathbf{M}_\phi & \mathbf{M}_\phi & 0 & 3M_\phi & 0 & 0 \\ \mathbf{0} & \mathbf{0} & \mathbf{0} & 0 & 0 & -1 & 0 \\ \mathbf{0} & \mathbf{0} & \mathbf{0} & 0 & M_{\bar{\phi}} & 0 & M_{\bar{\phi}} \end{bmatrix}^{-1}$$

$$\begin{bmatrix} \mathbf{F}[:,1:3] & \mathbf{0} & \mathbf{0} & \mathbf{F}[:,4:5] & \mathbf{0} & \mathbf{0} & \mathbf{F}[:,8] & \mathbf{F}[:,9] & \mathbf{0} & \mathbf{0} & \mathbf{F}[:,10:11] & \mathbf{F}[:,12] & \mathbf{0} & \mathbf{0} & \mathbf{F}[:,13] \\ \mathbf{0} & \mathbf{F}[:,1:3] & \mathbf{0} & \mathbf{0} & \mathbf{F}[:,4:5] & \mathbf{0} & \mathbf{F}[:,8] & \mathbf{0} & \mathbf{F}[:,9] & \mathbf{0} & \mathbf{F}[:,10:11] & \mathbf{0} & \mathbf{F}[:,12] & \mathbf{0} & \mathbf{F}[:,13] \\ \mathbf{0} & \mathbf{0} & \mathbf{F}[:,1:3] & \mathbf{0} & \mathbf{0} & \mathbf{F}[:,4:5] & \mathbf{F}[:,8] & \mathbf{0} & \mathbf{0} & \mathbf{F}[:,9] & \mathbf{F}[:,10:11] & \mathbf{0} & \mathbf{0} & \mathbf{F}[:,12] & \mathbf{F}[:,13] \\ \mathbf{0} & \mathbf{0} & \mathbf{0} & \mathbf{0} & \mathbf{0} & \mathbf{0} & 0 & 0 & 0 & 0 & \mathbf{0} & 0 & 0 & 0 & 0 \\ \mathbf{f}_\phi[1:3] & \mathbf{f}_\phi[1:3] & \mathbf{f}_\phi[1:3] & \mathbf{K}_\phi^f & \mathbf{K}_\phi^f & \mathbf{K}_\phi^f & 3\mathbf{f}_\phi[4] & \mathbf{f}_\phi[5] & \mathbf{f}_\phi[5] & \mathbf{f}_\phi[5] & \mathbf{f}_\phi[6:7] & \mathbf{f}_\phi[8] & \mathbf{f}_\phi[8] & \mathbf{f}_\phi[8] & \mathbf{f}_\phi[9] \\ \mathbf{0} & \mathbf{0} & \mathbf{0} & \mathbf{0} & \mathbf{0} & \mathbf{0} & 0 & 0 & 0 & 0 & \mathbf{0} & 0 & 0 & 0 & 0 \\ \mathbf{0} & \mathbf{0} & \mathbf{0} & \mathbf{0} & \mathbf{0} & \mathbf{0} & 0 & 0 & 0 & 0 & \mathbf{0} & 0 & 0 & 0 & 0 \end{bmatrix} \tag{4.3}$$

and

$$\begin{aligned} \mathbf{u}_{wt} = [&\beta_1, \dot{\beta}_1, \ddot{\beta}_1, \beta_2, \dot{\beta}_2, \ddot{\beta}_2, \beta_3, \dot{\beta}_3, \ddot{\beta}_3, \sin(\phi_1 + t\dot{\phi}_0), \cos(\phi_1 + t\dot{\phi}_0), \sin(\phi_1 + t\dot{\phi}_0 + \tfrac{2\pi}{3}), \cos(\phi_1 + t\dot{\phi}_0 + \tfrac{2\pi}{3}), \\ &\sin(\phi_1 + t\dot{\phi}_0 + 2\tfrac{2\pi}{3}), \cos(\phi_1 + t\dot{\phi}_0 + 2\tfrac{2\pi}{3}), u_{n,1}, u_{n,2}^1, u_{n,2}^2, u_{n,2}^3, u_{t,1}, \dot{u}_{n,1}, \dot{u}_{n,2}^1, \dot{u}_{n,2}^2, \dot{u}_{n,2}^3, \dot{u}_{t,1}]^{\mathrm{T}} \end{aligned} \tag{4.4}$$

where the subscript on the pitch angles and the superscript on the wind speeds denotes the particular blade. The submatrices are defined in (2.65) and (2.74).

The three individual pitch actuators are modelled by the second order model (3.1), where the gains are chosen as $G = 20^2$ and $D = 2\sqrt{G}$. This choice of pitch actuator gains gives a pitch system which follows the pitch reference close in the frequency range used in this application, but leads to a much less numerical stiff system than the gains used in Chapter 3. This actuator model is only used to obtain the pitch rate and acceleration from a pitch reference input, and it neglects any actuator dynamic.

4.2 State Estimator

In this section a model of the wind speed variations are developed and a state estimator, estimating both the wind variations and the states of the model, is derived.

First, models of the variations of the uniform wind speed and of the wind shear experienced by the individual blades are derived. Next, the wind models are combined with a wind turbine model and this combined model is used in a state estimator. In the state estimator design, the generator speed and the flapwise deflections of each blade are assumed to be measurable. Based on these measurements the constructed state estimator estimates the states of the model and the variations of the wind speeds.

4.2.1 Wind Model

The uniform wind speed $u_{n,1}$ can be modelled by a step function (cf. [45]), which in a state space formulation is given by:

$$\dot{u}_{n,1} = 0 \tag{4.5}$$

The variations of wind speed experienced by the individual blades because of wind shear $u_{n,2}$ is a function of the rotor position. If the wind shear is assumed to be linear, the wind speed variation for the individual blade is a harmonic oscillating function, oscillating at the rotors rotation frequency. The wind shear components experienced by the individual blades is approximated by

$$\begin{aligned}
u^1_{n,2} =& \bar{u}_{n,2} \cos\left(\dot{\phi}_0 t + \phi_1\right) , & \dot{u}^1_{n,2} \approx& -\dot{\phi}_0 \bar{u}_{n,2} \sin\left(\dot{\phi}_0 t + \phi_1\right) \\
u^2_{n,2} =& \bar{u}_{n,2} \cos\left(\dot{\phi}_0 t + \phi_1 + \frac{2\pi}{3}\right) , & \dot{u}^2_{n,2} \approx& -\dot{\phi}_0 \bar{u}_{n,2} \sin\left(\dot{\phi}_0 t + \phi_1 + \frac{2\pi}{3}\right) \\
u^3_{n,2} =& \bar{u}_{n,2} \cos\left(\dot{\phi}_0 t + \phi_1 + 2\frac{2\pi}{3}\right) , & \dot{u}^3_{n,2} \approx& -\dot{\phi}_0 \bar{u}_{n,2} \sin\left(\dot{\phi}_0 t + \phi_1 + 2\frac{2\pi}{3}\right)
\end{aligned} \tag{4.6}$$

where $\bar{u}_{n,2}$ is the magnitude of the wind shear and the superscript on $u_{n,2}$ refer

to the particular blade. The relations (4.6) can be rewritten as

$$\begin{bmatrix} u^1_{n,2} \\ u^2_{n,2} \\ u^3_{n,2} \end{bmatrix} \approx \mathbf{H}_1 \begin{bmatrix} \bar{u}_{n,2}\cos(\dot{\phi}_0+\phi) \\ -\dot{\phi}_0\bar{u}_{n,2}\sin(\dot{\phi}_0+\phi) \end{bmatrix}, \quad \begin{bmatrix} \dot{u}^1_{n,2} \\ \dot{u}^2_{n,2} \\ \dot{u}^3_{n,2} \end{bmatrix} \approx \mathbf{H}_2 \begin{bmatrix} \bar{u}_{n,2}\cos(\dot{\phi}_0+\phi) \\ -\dot{\phi}_0\bar{u}_{n,2}\sin(\dot{\phi}_0+\phi) \end{bmatrix} \tag{4.7}$$

where:

$$\mathbf{H}_1 = \begin{bmatrix} 1 & 0 \\ -\frac{1}{2} & \frac{\sqrt{3}}{2\dot{\phi}_0} \\ -\frac{1}{2} & -\frac{\sqrt{3}}{2\dot{\phi}_0} \end{bmatrix}, \quad \mathbf{H}_2 = \begin{bmatrix} 0 & 1 \\ -\frac{\sqrt{3}}{2}\dot{\phi}_0 & -\frac{1}{2} \\ \frac{\sqrt{3}}{2}\dot{\phi}_0 & -\frac{1}{2} \end{bmatrix} \tag{4.8}$$

Using this notation (4.7) the contribution from wind shear on all three blades can be modelled by a single harmonic oscillator. In state space formulation this becomes

$$\begin{bmatrix} \dot{\tilde{u}}_{n,2} \\ \ddot{\tilde{u}}_{n,2} \end{bmatrix} = \begin{bmatrix} 0 & 1 \\ -\dot{\phi}_0^2 & 0 \end{bmatrix} \begin{bmatrix} \tilde{u}_{n,2} \\ \dot{\tilde{u}}_{n,2} \end{bmatrix} \tag{4.9}$$

whereby $\bar{u}_{n,2}\cos(\dot{\phi}_0+\phi) \approx \tilde{u}_{n,2}$ and $-\dot{\phi}_0\bar{u}_{n,2}\sin(\dot{\phi}_0+\phi) \approx \dot{\tilde{u}}_{n,2}$.

4.2.2 Design

In the estimator model the pitch action for each blade and the rotor position are given as known external effects. The wind models from above are included in the model

$$\dot{\mathbf{x}}_{est} = \mathbf{A}_{est}\mathbf{x}_{est} + \mathbf{B}_{est}\mathbf{u}_{wt}[1:15] \tag{4.10}$$

where $\mathbf{x}_{est} = [\mathbf{q}_1, \mathbf{q}_2, \mathbf{q}_3, \ddot{\bar{\phi}}, \dot{\bar{\phi}}, \bar{\phi}, u_{n,1}, \tilde{u}_{n,2}, \dot{\tilde{u}}_{n,2}]^{\mathrm{T}}$,

$$\mathbf{A}_{est} = \begin{bmatrix} \mathbf{M} & \mathbf{0} & \mathbf{0} & -\mathbf{F}[:,7] & \mathbf{0} & \mathbf{0} & -\mathbf{F}[:,11] & \mathbf{0} & \mathbf{0} \\ \mathbf{0} & \mathbf{M} & \mathbf{0} & -\mathbf{F}[:,7] & \mathbf{0} & \mathbf{0} & -\mathbf{F}[:,11] & \mathbf{0} & \mathbf{0} \\ \mathbf{0} & \mathbf{0} & \mathbf{M} & -\mathbf{F}[:,7] & \mathbf{0} & \mathbf{0} & -\mathbf{F}[:,11] & \mathbf{0} & \mathbf{0} \\ \mathbf{M}_\phi & \mathbf{M}_\phi & \mathbf{M}_\phi & -3M_\phi & \mathbf{0} & \mathbf{0} & -\mathbf{f}_\phi[:,7] & \mathbf{0} & \mathbf{0} \\ \mathbf{0} & \mathbf{0} & \mathbf{0} & 0 & 0 & -1 & 0 & 0 & 0 \\ \mathbf{0} & \mathbf{0} & \mathbf{0} & 0 & M_{\bar{\phi}} & 0 & M_{\bar{\phi}} & 0 & 0 \\ \mathbf{0} & \mathbf{0} & \mathbf{0} & 0 & 0 & 0 & 1 & 0 & 0 \\ \mathbf{0} & \mathbf{0} & \mathbf{0} & 0 & 0 & 0 & 0 & -1 & 0 \\ \mathbf{0} & \mathbf{0} & \mathbf{0} & 0 & 0 & 0 & 0 & 0 & 1 \end{bmatrix}^{-1} \begin{bmatrix} -\mathbf{K} & \mathbf{0} & \mathbf{0} & \mathbf{F}[:,6] & \mathbf{0} & \mathbf{0} & \mathbf{F}[:,8] & & \\ \mathbf{0} & -\mathbf{K} & \mathbf{0} & \mathbf{F}[:,6] & \mathbf{0} & \mathbf{0} & \mathbf{F}[:,8] & & \\ \mathbf{0} & \mathbf{0} & -\mathbf{K} & \mathbf{F}[:,6] & \mathbf{0} & \mathbf{0} & \mathbf{F}[:,8] & \mathbf{H} & \\ -\mathbf{K}_\phi & -\mathbf{K}_\phi & -\mathbf{K}_\phi & -3D_\phi & K_{\bar{\phi}} & D_{\bar{\mathbf{i}}} & 3\mathbf{f}_\phi[4] & & \\ \mathbf{0} & \mathbf{0} & \mathbf{0} & 0 & 0 & 1 & 0 & 0 & 0 \\ \mathbf{0} & \mathbf{0} & \mathbf{0} & 0 & -M_{\bar{\phi}} & 0 & -M_{\bar{\phi}} & 0 & 0 \\ \mathbf{0} & \mathbf{0} & \mathbf{0} & 0 & 0 & 0 & 0 & 0 & 0 \\ \mathbf{0} & \mathbf{0} & \mathbf{0} & 0 & 0 & 0 & 0 & 0 & -1 \\ \mathbf{0} & \mathbf{0} & \mathbf{0} & 0 & 0 & 0 & 0 & -\dot{\phi}_0^2 & 0 \end{bmatrix} \tag{4.11}$$

where

$$\mathbf{H} = \begin{bmatrix} \mathbf{F}[:,9] & \mathbf{0} & \mathbf{0} & \mathbf{F}[:,12] & \mathbf{0} & \mathbf{0} \\ \mathbf{0} & \mathbf{F}[:,9] & \mathbf{0} & \mathbf{0} & \mathbf{F}[:,12] & \mathbf{0} \\ \mathbf{0} & \mathbf{0} & \mathbf{F}[:,9] & \mathbf{0} & \mathbf{0} & \mathbf{F}[:,12] \\ \mathbf{f}_\phi[5] & \mathbf{f}_\phi[5] & \mathbf{f}_\phi[5] & \mathbf{f}_\phi[8] & \mathbf{f}_\phi[8] & \mathbf{f}_\phi[8] \end{bmatrix} \begin{bmatrix} \mathbf{H}_1 \\ \mathbf{H}_2 \end{bmatrix} \tag{4.12}$$

and

$$\mathbf{B}_{est} = \begin{bmatrix} \mathbf{M} & \mathbf{0} & \mathbf{0} & -\mathbf{F}[:,7] & \mathbf{0} & \mathbf{0} & -\mathbf{F}[:,11] & \mathbf{0} & \mathbf{0} \\ \mathbf{0} & \mathbf{M} & \mathbf{0} & -\mathbf{F}[:,7] & \mathbf{0} & \mathbf{0} & -\mathbf{F}[:,11] & \mathbf{0} & \mathbf{0} \\ \mathbf{0} & \mathbf{0} & \mathbf{M} & -\mathbf{F}[:,7] & \mathbf{0} & \mathbf{0} & -\mathbf{F}[:,11] & \mathbf{0} & \mathbf{0} \\ \mathbf{M}_\phi & \mathbf{M}_\phi & \mathbf{M}_\phi & -3M_\phi & \mathbf{0} & \mathbf{0} & -\mathbf{f}_\phi[:,7] & \mathbf{0} & \mathbf{0} \\ \mathbf{0} & \mathbf{0} & \mathbf{0} & 0 & 0 & -1 & 0 & 0 & 0 \\ \mathbf{0} & \mathbf{0} & \mathbf{0} & 0 & M_{\bar{\phi}} & 0 & M_{\bar{\phi}} & 0 & 0 \\ \mathbf{0} & \mathbf{0} & \mathbf{0} & 0 & 0 & 0 & 1 & 0 & 0 \\ \mathbf{0} & \mathbf{0} & \mathbf{0} & 0 & 0 & 0 & 0 & -1 & 0 \\ \mathbf{0} & \mathbf{0} & \mathbf{0} & 0 & 0 & 0 & 0 & 0 & 1 \end{bmatrix}^{-1} \begin{bmatrix} \mathbf{F}[:,1:3] & \mathbf{0} & \mathbf{0} & \mathbf{F}[:,4:5] & \mathbf{0} & \mathbf{0} \\ \mathbf{0} & \mathbf{F}[:,1:3] & \mathbf{0} & \mathbf{0} & \mathbf{F}[:,4:5] & \mathbf{0} \\ \mathbf{0} & \mathbf{0} & \mathbf{F}[:,1:3] & \mathbf{0} & \mathbf{0} & \mathbf{F}[:,4:5] \\ \mathbf{f}_\phi[1:3] & \mathbf{f}_\phi[1:3] & \mathbf{f}_\phi[1:3] & \mathbf{K}_\phi^f & \mathbf{K}_\phi^f & \mathbf{K}_\phi^f \\ \mathbf{0} & \mathbf{0} & \mathbf{0} & \mathbf{0} & \mathbf{0} & \mathbf{0} \\ \mathbf{0} & \mathbf{0} & \mathbf{0} & \mathbf{0} & \mathbf{0} & \mathbf{0} \\ \mathbf{0} & \mathbf{0} & \mathbf{0} & \mathbf{0} & \mathbf{0} & \mathbf{0} \\ \mathbf{0} & \mathbf{0} & \mathbf{0} & \mathbf{0} & \mathbf{0} & \mathbf{0} \\ \mathbf{0} & \mathbf{0} & \mathbf{0} & \mathbf{0} & \mathbf{0} & \mathbf{0} \end{bmatrix} \tag{4.13}$$

The states of the estimator model (4.10) is estimated by a Kalman filter [25]

$$\dot{\hat{\mathbf{x}}}_{est} = \mathbf{A}_{est}\hat{\mathbf{x}}_{est} + \mathbf{B}_{est}\mathbf{u}_{wt}[1:15] + \mathbf{L}\left(\mathbf{y} - \mathbf{C}\hat{\mathbf{x}}_{est}\right) \tag{4.14}$$

where $\hat{\mathbf{x}}_{est}$ is the estimate of the states, $\mathbf{L}$ is a gain matrix, $\mathbf{y}$ holds the measurements and $\mathbf{C}$ is the observation matrix which picks the states corresponding to the measurements $\mathbf{y}$. The measurements are assumed to be $\mathbf{y} = [\dot{\phi} + \dot{\tilde{\phi}}, v_1, v_2, v_3]^{\mathrm{T}}$, the generator speed and the individual flapwise deflection of the three blades. The generator speed is known from the generator controller and the flapwise deflection can be related to a measure of the strain at the blade root by e.g. strain gauges.

The gain matrix $\mathbf{L}$ is computed by a method based on the error of the estimate $\mathbf{e} = \hat{\mathbf{x}}_{est} - \mathbf{x}_{est}$. The error of the estimate is described by:

$$\dot{\mathbf{e}} = \mathbf{A}_{est}\mathbf{e} - \mathbf{LCe} \tag{4.15}$$

Compare (4.15) to the typical equation for a full state feedback control system:

$$\dot{\tilde{\mathbf{x}}} = \tilde{\mathbf{A}}\tilde{\mathbf{x}} + \tilde{\mathbf{B}}\tilde{\mathbf{u}} \quad \text{with} \quad \tilde{\mathbf{u}} = \tilde{\mathbf{G}}\tilde{\mathbf{x}} \tag{4.16}$$

It is seen that $-\mathbf{LC}$ corresponds to $\tilde{\mathbf{B}}\tilde{\mathbf{G}}$ in a typical control system (4.16). Therefore the gain matrix $\mathbf{L}$ can be found by the Linear-Quadratic-Regulator (LQR) method for computing control gains for full state feedback control systems. The LQR method computes the $\tilde{\mathbf{G}}$ which minimize the cost function

$$J = \int_0^\infty \left(\tilde{\mathbf{x}}^{\mathrm{T}}\tilde{\mathbf{Q}}\tilde{\mathbf{x}} + \tilde{\mathbf{u}}^{\mathrm{T}}\tilde{\mathbf{R}}\tilde{\mathbf{u}}\right) \mathrm{d}t \tag{4.17}$$

where $\tilde{\mathbf{Q}}$ and $\tilde{\mathbf{R}}$ are weight matrices, here a diagonal matrices with entries chosen to optimize the estimator performance. Setting $\tilde{\mathbf{x}} = \mathbf{e}$, $\tilde{\mathbf{A}} = \mathbf{A}_{est}$ and $\tilde{\mathbf{B}}$ to the identity matrix, the cost function (4.17) corresponds to minimize the error $\mathbf{e}$, and solving $-\mathbf{LC} = \tilde{\mathbf{B}}\tilde{\mathbf{G}}$ for $\mathbf{L}$ gives the estimator gain. The standard MATLAB® function *lqr* is used to compute the gain matrix.

4.3 Control Design

This section concerns the development of a cyclic pitch controller for region 3. First, a collective pitch controller is designed to control the rotor speed by regulating the energy extracted from the wind. Next, a cyclic pitch controller based on the rotor position and the estimated variations of the wind speeds is developed. The objective for the cyclic pitch controller is to reduce the effect of the oscillating loads on the blade caused by wind speeds variations, wind shear and gravity. The controller gives a specified pitch demand to each blade, which is added to the collective pitch demand from the rotor speed controller.

4.3.1 Rotor Speed Controller

The rotor speed controller is a classic PID controller. It is based on a measure of the rotation speed of the generator and pitch all blades collective to keep the rotor speed constant. The gains of the PID controller are computed by an optimization algorithm which maximize the damping of the least damped structural modes.

4.3.2 Fatigue Load Reducing Control

The collective pitch demand from the rotor speed controller is modulated by a specified pitch demand for each blade to minimize the effect from gravity and the estimated wind speed oscillations.

Design

Although, Chapter 3 only predicts a high potential for using pitch control to reduce the effect of wind speed variations and not to reduce the effect of gravity, the controller designed in this section will aim at reducing both kind of disturbances. When the controller is tested it is divided into three cases; one where both kind of disturbances are concerned, one where only wind speed variations are concerned and finally one where only gravity effects are concerned.

In Chapter 3 it was found that controllers concerning disturbances depending on rotor position, such as gravity and wind shear, could be designed without including blade dynamic. Therefore this controller can be designed without including the pitch rate and acceleration.

The controller regulates the pitch of the individual blade according to the external effects on the individual blade, therefore the controller can be designed by a one blade model. The model for the first blade is

$$\mathbf{M}\dot{\mathbf{q}}_1 = -\mathbf{K}\mathbf{q}_1 + \mathbf{B}\beta_{ref,1} + \mathbf{B}_e \begin{bmatrix} \sin(\phi_1 + \dot{\phi}_0 t) \\ \cos(\phi_1 + \dot{\phi}_0 t) \\ u_{n,1} \\ u^1_{n,2} \\ \dot{u}^1_{n,2} \end{bmatrix} \tag{4.18}$$

where $\mathbf{B} = \mathbf{F}[:, 1]$ is the system's gain on the control input and $\mathbf{B}_e = \begin{bmatrix}\mathbf{F}[:, 4:5] & \mathbf{F}[:, 8:9] & \mathbf{F}[:, 12]\end{bmatrix}$ is the system's gain on the disturbances.

The objective for this controller is to minimize the fatigue loads on the blades caused by gravity and the estimated wind speed variations and wind shear. This is achieve by a controller on the form (cf. [45])

$$\beta_{ref,1} = f_{con}(\mathbf{x}) + \mathbf{G}_e \begin{bmatrix} \sin(\phi_1 + \dot{\phi}_0 t) \\ \cos(\phi_1 + \dot{\phi}_0 t) \\ u_{n,1} \\ u^1_{n,2} \\ \dot{u}^1_{n,2} \end{bmatrix} \tag{4.19}$$

where $f_{con}(\mathbf{x})$ is the original pitch controller of the wind turbine, in this case the PID rotor speed controller, $\sin(\phi_1 + \dot{\phi}_0 t)$ and $\cos(\phi_1 + \dot{\phi}_0 t)$ are the known disturbance from gravity, and $u_{n,1}$, $u^1_{n,2}$ and $\dot{u}^1_{n,2}$ are the estimated wind speed components. Inserting (4.19) into (4.18) gives:

$$\mathbf{M}\dot{\mathbf{q}}_1 = -\mathbf{K}\mathbf{q}_1 + \mathbf{B}f_{con}(\mathbf{x}) + (\mathbf{B}\mathbf{G}_e + \mathbf{B}_e)\begin{bmatrix}\sin(\phi_1 + \dot{\phi}_0 t)\\ \cos(\phi_1 + \dot{\phi}_0 t)\\ u_{n,1}\\ u^1_{n,2}\\ \dot{u}^1_{n,2}\end{bmatrix} \tag{4.20}$$

The gain matrix $\mathbf{G}_e$ is chosen such that $(\mathbf{B}\mathbf{G}_e + \mathbf{B}_e)$ is minimized, whereby the effect of the disturbances is minimized.

Implementation

To convert the wind shear estimate from the estimator designed in Section 4.2 and the blade position to the values for the individual blades as used in (4.19) they are multiplied by a transformations matrixes. The contribution to the pitch demand for the individual blades becomes:

$$\begin{aligned}
\beta_{ref,1} &= \mathbf{G}_e \begin{bmatrix}1&0&0&0&0\\0&1&0&0&0\\0&0&1&0&0\\0&0&0&1&0\\0&0&0&0&1\end{bmatrix}\begin{bmatrix}\sin(\phi_1 + \dot{\phi}_0 t)\\ \cos(\phi_1 + \dot{\phi}_0 t)\\ u_{n,1}\\ \tilde{u}_{n,2}\\ \dot{\tilde{u}}_{n,2}\end{bmatrix}\\
\beta_{ref,2} &= \mathbf{G}_e \begin{bmatrix}\frac{\sqrt{3}}{2}&-\frac{1}{2}&0&0&0\\-\frac{1}{2}&-\frac{\sqrt{3}}{2}&0&0&0\\0&0&1&0&0\\0&0&0&-\frac{1}{2}&\frac{\sqrt{3}}{2\dot{\phi}_0}\\0&0&0&-\frac{\sqrt{3}}{2\dot{\phi}_0}&-\frac{1}{2}\end{bmatrix}\begin{bmatrix}\sin(\phi_1 + \dot{\phi}_0 t)\\ \cos(\phi_1 + \dot{\phi}_0 t)\\ u_{n,1}\\ \tilde{u}_{n,2}\\ \dot{\tilde{u}}_{n,2}\end{bmatrix}\\
\beta_{ref,3} &= \mathbf{G}_e \begin{bmatrix}-\frac{\sqrt{3}}{2}&-\frac{1}{2}&0&0&0\\-\frac{1}{2}&\frac{\sqrt{3}}{2}&0&0&0\\0&0&1&0&0\\0&0&0&-\frac{1}{2}&-\frac{\sqrt{3}}{2\dot{\phi}_0}\\0&0&0&\frac{\sqrt{3}}{2\dot{\phi}_0}&-\frac{1}{2}\end{bmatrix}\begin{bmatrix}\sin(\phi_1 + \dot{\phi}_0 t)\\ \cos(\phi_1 + \dot{\phi}_0 t)\\ u_{n,1}\\ \tilde{u}_{n,2}\\ \dot{\tilde{u}}_{n,2}\end{bmatrix}
\end{aligned} \tag{4.21}$$

This controller can be reduced to only concern effects of wind speed variations by setting the upper left 2 times 2 submatrix of the three transformations matrices in (4.21) to zero. Likewise the controller can be reduced to only concern effects of gravity by setting the lower right 3 times 3 submatrix of the three transformations matrices in (4.21) to zero.

4.4 Results

In this section the state estimator and the controllers, designed in the previous sections, are applied to the test turbine (Appendix C) at a mean wind speed of 15 m/s. First, the state estimator is tested at three wind scenarios, next, five different control set-ups are tested at the same wind scenarios. The state estimator works well at all scenarios. The load reducing controller reduce the flapwise loads caused by wind shear while the loads caused by gravity is unaffected by the controller.

4.4.1 Estimator

The estimates of wind speed and wind shear are tested for three cases: First, a step in the uniform wind and no wind shear. Second, a step in wind shear from 0 to 20 %[1] and a constant uniform wind component. Third, a turbulent wind field with a turbulence intensity[2] on 8 % and a 20 % wind shear. The turbulent wind field refers to time variations in the uniform incoming wind, not to any spatial differences in the wind field, since the model is not capable of handling this.

Figure 4.1 shows the first two cases; step in uniform wind and step in wind shear. The estimate of the step in the uniform wind component (Figure 4.1(a)) is seen to follow the true value well, reaching 80 % of the true value after 2 second. The step in uniform wind does not affect the estimate of the wind shear. The estimate of the step in wind shear (Figure 4.1(b)) shows a very good agreement with the true value, and the estimate of the uniform wind component is not affected by the wind shear.

Figure 4.2 shows the estimate of the wind components of a turbulent wind field with a wind shear of 20 %. The variations of the uniform wind component $u_{n,1}$ is seen to lag about 1 second after the true wind and therefore also miss the fast oscillations. Anyway the magnitude of the uniform wind component are well estimate. The wind shear is very well estimated both in time and magnitude.

4.4.2 Controller

Five different control set-ups are tested on the test turbine (Appendix C) at four different load cases. Tables 4.1 to 4.4 show the performance of the five control set-ups on a step in uniform wind, a step in wind shear, a high turbulent incoming wind and a low turbulent incoming wind, respectively.

Control Set-Ups

The five different control set-ups are:

[1] The wind speed at the top of the rotor is 20 % higher than at the bottom of the rotor.

[2] Turbulence intensity $\equiv \frac{\mathrm{RMS}(u_{n,1}-\mathrm{mean}(u_{n,1}))}{\mathrm{mean}(u_{n,1})}$

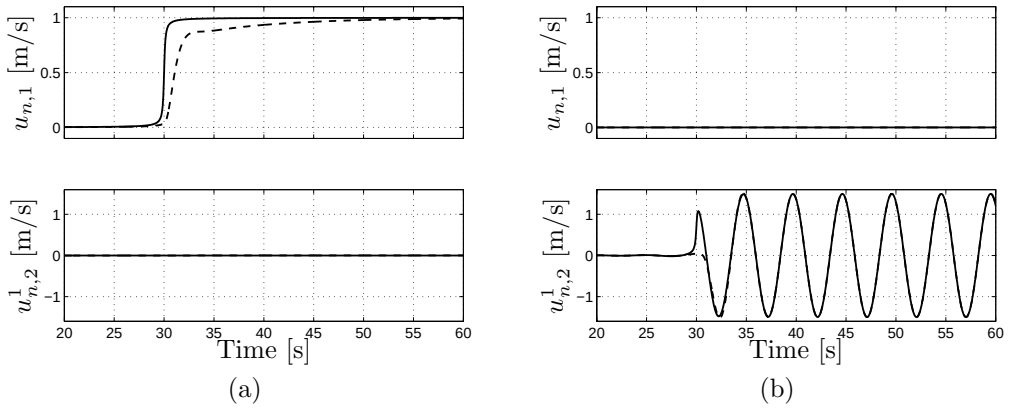

Figure 4.1: Estimate of wind components at one blade for $u_{n,0} = 15$ m/s. '–' true wind, '- -' estimate of the wind. Top graphs: uniform wind variation component. Bottom graphs: wind shear component. a) Step in uniform wind, no wind shear. b) Step in wind shear, constant uniform wind.

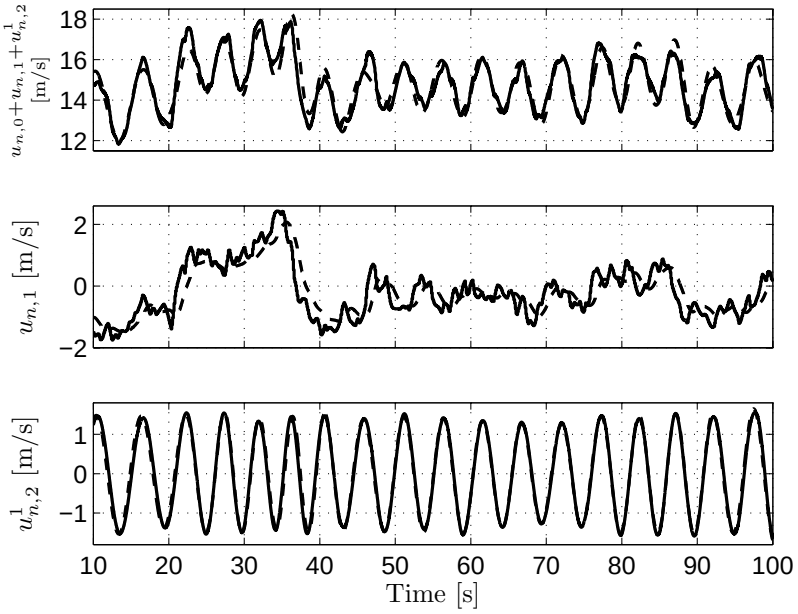

Figure 4.2: Estimate of turbulent wind components at one blade for $u_{n,0} = 15$ m/s and turbulence intensity on 8 %. '–' true wind, '- -' estimate of the wind. Top graph: The sum of the uniform wind and the effect of wind shear. Middle graph: The uniform wind variation component. Bottom graph: The wind shear component.

1. Uncontrolled turbine
2. Only the rotor speed PID-controller (denoted PID)
3. The rotor speed PID-controller and the full load reducing controller (denoted LRC_1)
4. The rotor speed PID-controller and that part of the load reducing controller which concerns the wind speed variations (denoted LRC_2)
5. The rotor speed PID-controller and that part of the load reducing controller which concerns the effects of gravity (denoted LRC_3)

Control Performance Measures

Six measures are used to quantify the performance of the controllers: The Root-Mean-Square (RMS) of the rotor speed error $\text{RMS}(\dot{\phi}_1+\dot{\bar{\phi}}_1)$, of the rate of edgewise blade motion $\text{RMS}(\dot{u})$, of the rate of flapwise blade motion $\text{RMS}(\dot{v})$, of the rate of torsional blade motion $\text{RMS}(\dot{\theta})$ and the cost of using control is measured by the actuator duty (AD) defined by:

$$\text{AD} = \frac{1}{t}\int_0^t |\dot{\beta}|\mathrm{d}t \tag{4.22}$$

The Root-Mean-Square (RMS) is defined by:

$$\text{RMS}(\xi) = \sqrt{\frac{1}{t}\int_0^t \xi^2 \mathrm{d}t} \tag{4.23}$$

In the following the control performance measures from the different control set-ups at the different test cases are shown and discussed.

Step in Uniform Wind Speed

Table 4.1 shows the control performance measures for the five different control set-ups at the case with a step in the uniform wind speed and no wind shear (Figure 4.1(a)). In this case, with no wind shear, the gravity is the main contributor to blade motion.

In the uncontrolled case the $\text{RMS}(\dot{u})$ is relative high compared to $\text{RMS}(\dot{v})$ since gravity affects the edgewise blade motions the most. The RMS value for the torsional blade motion is also relative high, mainly driven by the structural coupling to the edgewise blade motion. The negative damping imposed by the generator model (2.77) makes the generator speed continually increase after the step in wind speed, therefore the RMS of the generator speed error ($\text{RMS}(\dot{\phi}_1+\dot{\bar{\phi}}_1)$) is very high. As there is no controller, the is no pitch action.

Table 4.1: Control performance measures for the uncontrolled system and the four controllers: PID rotor speed controller (PID), PID rotor speed controller and the full load reducing controller (LCR_1), PID rotor speed controller and the load reducing controller concerning wind speed variations (LCR_2), PID rotor speed controller and the load reducing controller concerning effects of gravity (LCR_3). For a step in the uniform wind speed and no wind shear (Figure 4.1(a)) and operation conditions corresponding to $u_{n,0} = 15$ m/s

Mode	Uncontrolled	PID	LRC_1	LRC_2	LRC_3
RMS($\dot{u}$)	0.48	0.44	0.43	0.44	0.42
RMS($\dot{v}$)	0.08	0.10	0.19	0.13	0.19
RMS($\dot{\theta}$)	0.52	0.48	0.53	0.48	0.53
RMS($\dot{\phi}_1 + \dot{\bar{\phi}}_1$)	1.29	0.028	0.023	0.023	0.028
AD	0	0.029	0.25	0.036	0.26

The objective for the PID rotor speed controller is to keep constant generator speed, and when the controller is applied the generator speed error is highly reduced. The PID controller has a small decreasing effect on the edgewise and torsional blade motion, while the flapwise blade motion increase slightly. However, none of these variations are of an important size. The pitch activity is relative low compare to the following cases, because there is only one incident where the pitch controller is in use, at the wind step.

The control performance measures for the LQR_2 are almost the same as for the PID control set-up. This is because there in only one incident with variations of the wind speed, the step in uniform wind speed.

Likewise the control performance measures for the LRC_3 are almost the same as for the LRC_1. Showing that the only part of the load reducing controller there is in play is the part which concerns gravity effects.

When the full load reducing controller is applied (LRC_1) the controller changes the pitch during the rotation of the rotor to minimize the effect of gravity, therefore the pitch activity is highly increased. The edgewise blade motion decrease a negligible amount while the flapwise and torsional blade motion increase. The RMS values for the rotor speed errors is the same as for the PID controller.

In summary this case shows that the PID rotor speed controller works well and that the load reducing controller is not capable of reducing the blade motion caused by gravity, as predicted in Chapter 3.

Step in Wind Shear

Table 4.2 shows the control performance measures for the five controllers for the case with constant uniform wind and a step in wind shear from 0 to 20 % (Figure 4.1(b)).

Table 4.2: Control performance measures for the uncontrolled system and the four controllers: PID rotor speed controller (PID), PID rotor speed controller and the full load reducing controller (LCR_1), PID rotor speed controller and the load reducing controller concerning wind speed variations (LCR_2), PID rotor speed controller and the load reducing controller concerning effects of gravity (LCR_3). For a constant uniform wind speed and a step in wind shear (Figure 4.1(b)) and operation conditions corresponding to $u_{n,0} = 15$ m/s

Mode	Uncontrolled	PID	LRC_1	LRC_2	LRC_3
RMS($\dot{u}$)	0.42	0.42	0.43	0.44	0.41
RMS($\dot{v}$)	0.53	0.53	0.13	0.13	0.51
RMS($\dot{\theta}$)	0.58	0.58	0.50	0.46	0.62
RMS($\dot{\phi}_1 + \dot{\bar{\phi}}_1$)	0	0	0	0	0
AD	0	0	0.69	0.58	0.24

The uncontrolled case shows that the wind shear has no effect on the energy extracted from the wind since the wind shear is assumed to be linear and it is a linear turbine model, therefore the rotor speed stays constant. The PID controller is out of action since there are no rotor speed variations. The LRC_3 is again seen to increase the pitch activity without reducing the blade motion. The wind shear makes the LRC_2 active. It reduces the flapwise blade motion with 75 % and the torsional blade motion with 14 %, while the edgewise blade motion increase 5 %. The cost is a considerable pitch activity.

Figure 4.3 shows the wind speed at one blade together with the blade motion, pitch activity and pitch moment for the PID controller and the LRC_2 controller. The figure shows how the torsional and especial the flapwise blade motion are reduced by the controller. The pitch moment oscillates before the wind shear is imposed. These oscillations are caused by the steady state deformed blade's rotation in the gravity field. The wind shear reduce the magnitude of the pitch moment oscillations by 15 %, because the effect of gravity and wind shear on the pitch moment is in counter phase. The pitch activity impose by the LCR_2 controller increases the magnitude of the pitch moment oscillations by 23 %, but the effect from gravity is still the major contributor to the pitch moment.

The full load reducing controller (LRC_1) has the same reduction as the LRC_2 of the flapwise blade motion, a very small reduction of the edgewise blade motion compare to the LRC_2 and an increase in the torsional blade motion. However, the pitch activity increase 9 % compare to the LRC_2.

In summary this case shows that the load reducing controller can reduce flapwise blade motion caused by wind shear considerably. Whereas the reduction of gravity loads has a minor effect at a high costs.

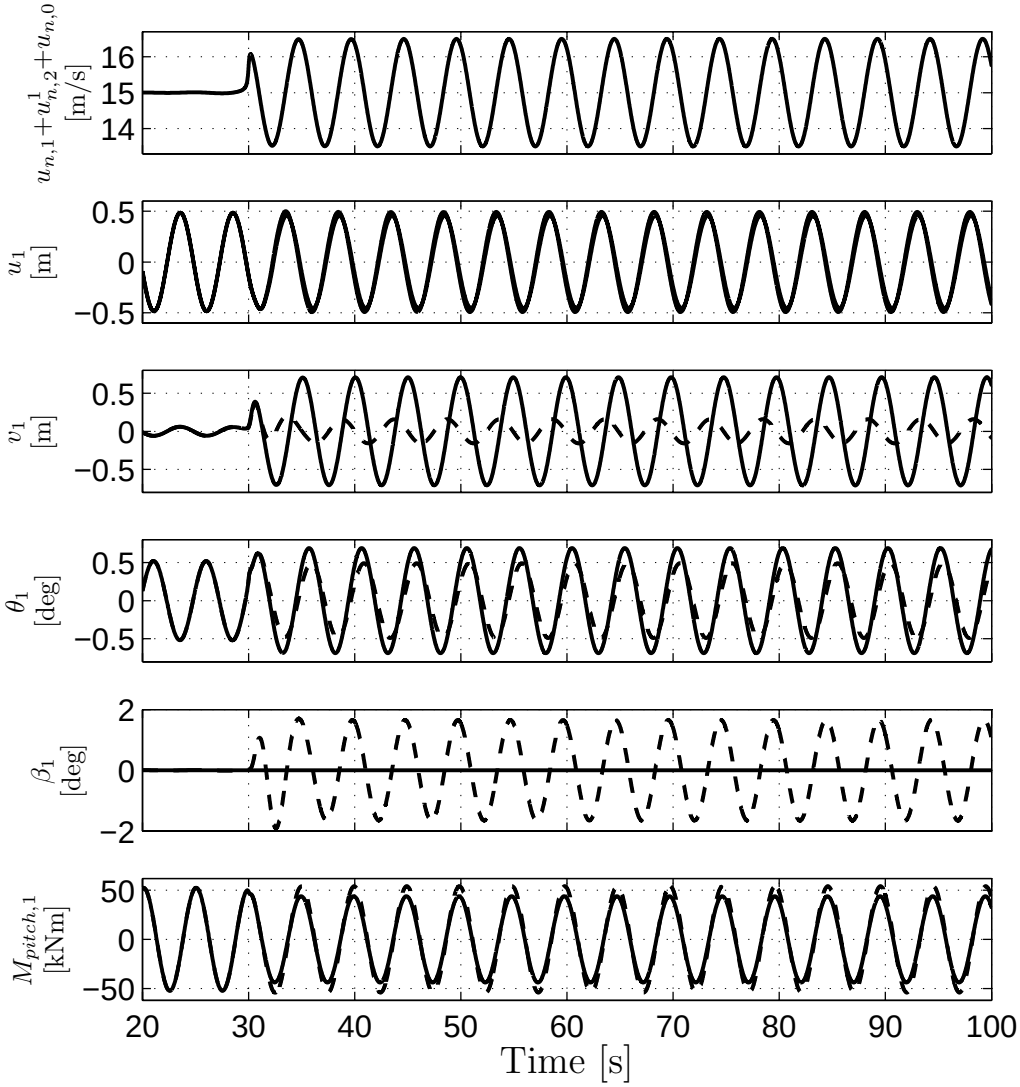

Figure 4.3: The wind speed, blade motion, pitch action and moment for one blade. '–' PID controlled, '- -' LRC_2 controlled. For the case with a constant uniform wind speed and a step in wind shear (Figure 4.1(b)) and operation conditions corresponding to $u_{n,0} = 15$ m/s.

Table 4.3: Control performance measures for the uncontrolled system and the four controllers: PID rotor speed controller (PID), PID rotor speed controller and the full load reducing controller (LCR_1), PID rotor speed controller and the load reducing controller concerning wind speed variations (LCR_2), PID rotor speed controller and the load reducing controller concerning effects of gravity (LCR_3). For a turbulent wind series with turbulence intensity on 8 % and a wind shear on 20 % (Figure 4.2) and operation conditions corresponding to $u_{n,0} = 15$ m/s

Mode	Uncontrolled	PID	LRC_1	LRC_2	LRC_3
RMS($\dot{u}$)	0.40	0.41	0.43	0.44	0.40
RMS($\dot{v}$)	0.68	0.92	0.81	0.81	0.90
RMS($\dot{\theta}$)	0.80	0.87	0.81	0.77	0.90
RMS($\dot{\phi}_1 + \dot{\bar{\phi}}_1$)	1.08	0.17	0.15	0.15	0.17
AD	0	0.71	1.19	1.17	0.72

Turbulent Wind

Table 4.3 shows the control performance measures for the five controllers for the case with a turbulent inflow and a 20 % wind shear (Figure 4.2).

The generator speed of the uncontrolled case is unstable, as in the case with a step in uniform wind, caused by the negative damping imposed by the generator model (2.77).

The generator speed is stabilized by the PID controller, but it increase the flapwise blade motion by 35 % and the torsional blade motion by 9 %, and cost a considerable amount of pitch activity.

When the LRC_2 is applied the edgewise blade motion is increased by 7 % while the flapwise blade motion is reduced by 12 % and the torsional blade motion is reduced by 11 %, compared to the PID controlled case. The rotor speed error is reduced by 11 %, while the pitch activity is increased by 65 %. The flapwise blade motion however is still 19 % above the level for the uncontrolled case.

Again the LRC_3 does not improve performance compared to the the PID controller, but it increases the pitch activity considerably.

Table 4.4 shows the control results for the same wind series (Figure 4.2) with the turbulence scaled to half. In this case with less turbulence the load reducing controller perform better. The LRC_2 reduce the flapwise blade motion by 39 % and the torsional blade motion by 11 %, compare to the PID controller. This is an increase in reduction of flapwise blade motion on 27 percentage points compare to the high turbulent case (Table 4.3).

Figure 4.4 shows the time series for wind, blade motion, pitch action and moment for the PID controller and the LRC_2 to the low turbulence case (Table 4.4). The magnitude of the pitch moment oscillations is approximately 25 % higher for the PID controller than for the LRC_2 controller.

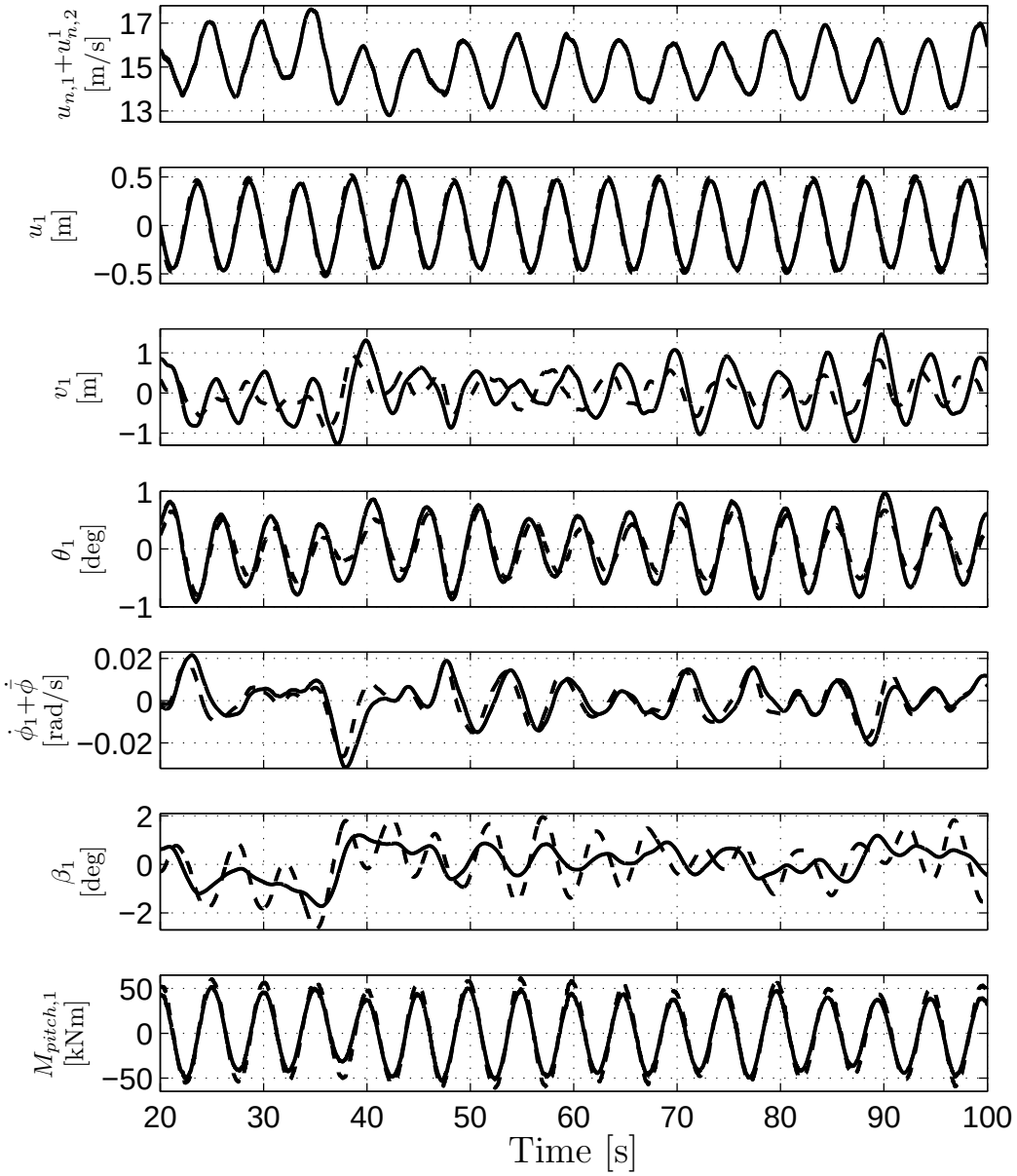

Figure 4.4: The wind speed, the motion, pitch activity and moment for one blade. '–' PID controller, '- -' LRC_2 controller. Applied to the turbulent wind series (Figure 4.1(b)) with the turbulence intensity scaled to 4 %. Operation conditions corresponding to $u_{n,0} = 15$ m/s.

Table 4.4: Control performance measures for the uncontrolled system and the four controllers: PID rotor speed controller (PID), PID rotor speed controller and the full load reducing controller (LCR_1), PID rotor speed controller and the load reducing controller concerning wind speed variations (LCR_2), PID rotor speed controller and the load reducing controller concerning effects of gravity (LCR_3). For the turbulent wind series and a wind shear on 20 % (Figure 4.2) with the turbulence intensity on 4 %. Operation conditions corresponding to $u_{n,0} = 15$ m/s

Mode	Uncontrolled	PID	LRC_1	LRC_2	LRC_3
RMS($\dot{u}$)	0.40	0.41	0.43	0.44	0.40
RMS($\dot{v}$)	0.64	0.70	0.41	0.43	0.67
RMS($\dot{\theta}$)	0.70	0.73	0.64	0.60	0.76
RMS($\dot{\phi}_1 + \dot{\bar{\phi}}_1$)	0.54	0.086	0.077	0.077	0.087
AD	0	0.35	0.94	0.88	0.41

In summary these two cases show that the relative performance of the load reducing controller reduce with increased turbulence. Furthermore the controller is again found not to be capable of reducing loads caused by gravity.

Effect of Turbulence Intensity

The examples above shows that the performance of the load reducing controller decreases with increasing turbulence. The effect of turbulence on the performance of the load reducing controller (LRC_2) is illustrated in Figure 4.5. This figure shows the ration between the control performance measures for the PID controller and the LRC_2 controller versus turbulence intensity. Since the edgewise blade motion is primarily driven by the gravity it is almost unaffected by the increased turbulence and the control action. The flapwise blade motion is highly affected by both turbulence and pitch action, and the load reducing control performance is seen to decrease with increasing turbulence. There is a small decrease in the relative load reduction with increased turbulence for the torsional motion while the effect of the LRC_2 on the generator error is unchanged by the increased turbulence. The pitch activity for the LRC_2 approach the pitch activity for the PID controller as the turbulence increase.

The effect of the load reducing controller decrease at increasing turbulence intensity, since the wind speed differences experienced by the individual blades caused by turbulence approached the wind speed variations caused by wind shear. When the wind speed variations from turbulence and wind shear approach each other, the control action for reducing the effect of turbulence will blur the control action to reduce the effect of wind shear.

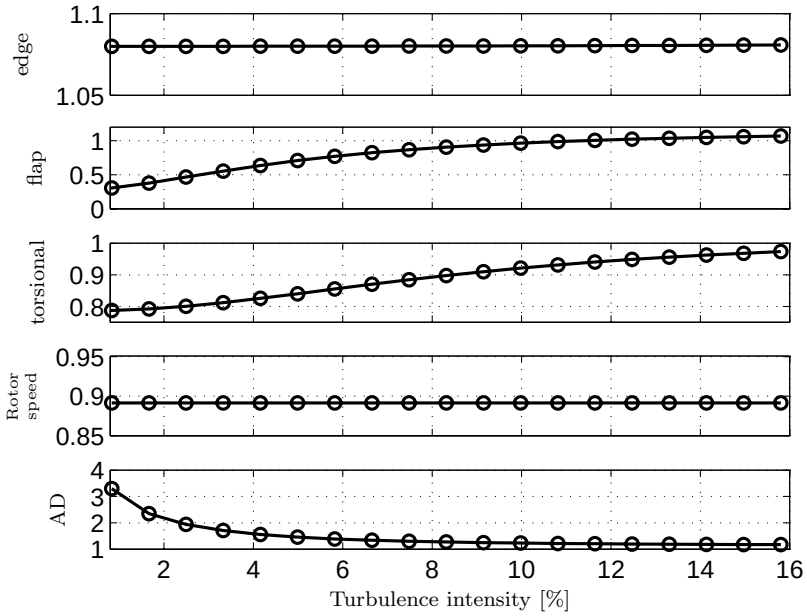

Figure 4.5: The effect of turbulence intensity on the control performance at $u_{n,0} = 15$ m/s. The ratio between the RMS value from the PID and the LRC_2 controlled cases for edgewise, flapwise and torsional blade motion and rotor speed error, respectively, and ratio between the pitch activity (AD) for the LRC_2 and the PID controlled cases.

4.5 Summary

This chapter gives an application example of the developed aeroelastic wind turbine blade model: The development of a state estimator and a fatigue load reducing cyclic pitch controller. The state estimator, apart from estimating the states of the model, estimates the uniform wind speed and the wind shear. The estimates of the wind speed and wind shear agree well with the true wind components.

The control development concerns region 3, where the wind speed is above rated wind speed and the primary objective of the controller is to reduce the energy extracted from the wind, such that it fits the capacity of the generator. The primary objective is fulfilled by a collective pitch controller of the PID type, which stabilize the instability imposed by the negative damping from the generator model. The PID controller however increase the fatigue loads on the blades.

An additional fatigue load reducing controller is developed, which superimpose a specify pitch demand for the individual blades onto the collective pitch demand from the PID rotor speed controller. The load reducing controller uses the rotor position and the estimated wind speed and wind shear to minimize the effect from gravity, uniform wind speed changes and wind shear.

The load reducing controller is not capable of reducing the fatigue loads caused by gravity. The reason for this is that the edgewise blade motion, which is most affect by gravity, is almost unaffected by pitch changes, and therefore the pitch controller can not be used for reducing edgewise blade fatigue loads. This conclusion is in agreement with [30].

The load reducing controller is capable of reducing the effect of wind shear by up to 75 % under ideal conditions, but the performance of the load reducing controller decrease when the turbulence in the incoming wind increase. At high turbulence the load reducing controller loses its effect, and the fatigue loads can exceed the fatigue loads without the controller. This is because the stochastic loads from the turbulence becomes larger than the deterministic loads from wind shear. This conclusion is in agreement with [46].

Chapter 5
Conclusion

This thesis concerns the development of a low order linear aeroelastic state space model of a wind turbine blade, which includes the effect of pitch action, rotor speed variations, gravity, uniform wind speed variations and wind shear. As wind turbines have become larger the interaction between blade motion, pitch action, wind shear, gravity and the controller has become even more important than perviously. The aeroelastic model developed in this thesis includes these effects, yet it is transparent and linear, and therefore highly suitable for control design and analysis.

5.1 The Aeroelastic Model

The development of the primary aeroelastic model is divided into four sub-models, where each sub-model provides information about the coupling phenomena between the blade, pitch action, rotor speed variations, etc.

First, nonlinear partial differential equations of structural motion of a wind turbine blade are derived. Furthermore equations of motion for the pitch action and rotor speed are derived. The equations are discussed in details and terms coupling the equations are emphasized. This sub-model is based on Bernoulli-Euler beam theory and derived by Hamilton's principle. The derivation follows [12] extending their work to include gravity, pitch action and rotor speed variations.

Secondly, a finite difference discretization of the steady state partial differential equations of motion is combined with blade element momentum theory to model the flow conditions and aerodynamic forces at different mean wind speeds, rotor speeds and pitch angles. This aeroelastic sub-model is used to compute the steady state deformation of the wind turbine blade at different operation conditions. The results agree very well with results from HAWCStab [10].

Third, the partial differential equations of motion are linearized about the steady state deformed blade and combined with an unsteady aerodynamic model. This aeroelastic sub-model is used to compute aeroelastic modes of motions for the blade. The aeroelastic modes for the undeformed blade agree very well with results from HAWCStab. The difference between aeroelastic modes of motion for the undeformed and the steady state deformed blade are discussed. The steady state deformation leads to a stronger coupling between edgewise and torsional blade motion, caused by the relative large flapwise blade deformation.

Finally, the linear partial differential equations of aeroelastic motion are approximated by a modal expansion based on the method of assumed modes. The

aeroelastic assumed mode model has many similarities with a 2D blade section model. It can be used instead of a 2D blade section model in many applications, giving a more transparent connection to a real turbine blade and including more effects, such as blade deformation and centrifugal stiffness.

The aeroelastic equations for pitch action and rotor speed are also approximated by assumed mode models. Furthermore models of drivetrain flexibility and generator torque are derived. Three blade models are combined with the drivetrain and generator models leading to an aeroelastic model of a three bladed wind turbine.

5.2 Applications

In this thesis the aeroelastic model is used to analyze the blade response to wind speed and pitch angle oscillations, and to suggest a load reducing controller.

Blade Response Analysis

The blade response analysis shows how the blade interacts with wind speed and pitch angle oscillations. The response of the individual modes of one blade is discussed in details, showing how interaction with other blade modes shift in magnitude and phase, and thereby increase or reduces the response of the particular mode.

The response of a three bladed configuration is compared with the response of a one blade configuration showing that the first flapwise and first torsional responses agree well for the two configurations. The edgewise response however differs considerably, because it interact with the drivetrain flexibility.

The responses of models based on three structural modes are compare to models based on four structural modes showing that the inclusion of one extra flapwise mode does not changes the responses of the other modes. This indicates that the version based on three structural model is enough for analyze of basic blade motion, and interaction between pitch action and blade motion.

The analysis shows that there is a high potential for using pitch control to reduced fatigue loads on the blade caused by wind shear and uniform wind speed variations. It is also shown that there is a very low potential for using pitch control to reduce the edgewise blade motion caused by gravity. The analysis shows that for load reducing controllers concerning loads that varies slower than 0.2 Hz (for the particular test turbine) it is not necessary to include blade dynamic in the control design.

State Estimation and Control Design

A state estimator is developed that estimates both the states of a three bladed wind turbine model, the uniform wind speed and the wind shear with good agree-

ment.

The estimated wind speed and wind shear are used in a load reducing controller focusing on minimizing the blade motion caused by wind speed variations, wind shear and gravity. Under ideal conditions the controller reduces the flapwise blade motion caused by wind shear with 75 % and torsional blade motion with 14 % while the edgewise blade motion are almost unaffected by the controller. The performance of the load reducing controller decreases with increased turbulence in the wind and can exceed the loads of the uncontrolled case. The controller is not capable of reducing blade motion caused by gravity.

5.3 Ongoing Applications

The aeroelastic assumed mode model is used in an ongoing project on analyze of pitch actuators. The project concerns the pitch actuator dynamic, the interaction between blade and pitch actuator and the effect of steady state deformation of the blade on the pitch actuator properties.

References

[1] The Danish Wind Industry Association (DWIA). http://www.windpower.org.

[2] R. E. Sheldahl, P. C. Klimas, and L. V. Feltz. Aerodynamic performance of a 5-m-diameter darrieus turbine. *Journal of Energy*, 4(5):227–232, 1980.

[3] NWTC Design Codes (ADAMS2AD by D. J. Laino and J. Jonkman). http://wind.nrel.gov/designcodes/simulators/adams2ad/. Last modified 12-August-2005; accessed 12-August-2005.

[4] NWTC Design Codes (AeroDyn by D. J. Laino). http://wind.nrel.gov/designcodes/simulators/aerodyn/. Last modified 05-July-2005; accessed 05-July-2005.

[5] T. J. Larsen, A. Hansen, and T. Buhl. Aeroelastic effects of large blade deflections for wind turbines. *Proceedings of the special topic conference "The Science of making Torque from Wind"*, pages 238–246, 2004.

[6] T. J. Larsen, H. A. Madsen, A. M. Hansen, and K. Thomsen. Investigations of stability effects of an offshore wind turbine using the new aeroelastic code hawc2. *Proceedings of the conference "Copenhagen Offshore Wind 2005"*, 2005.

[7] NWTC Design Codes (FAST by J. Jonkman). http://wind.nrel.gov/designcodes/simulators/fast/. Last modified 12-August-2005; accessed 12-August-2005.

[8] NWTC Design Codes (SymDyn by K. Stol and G. Bir). http://wind.nrel.gov/designcodes/simulators/symdyn/. Last modified 26-May-2005; accessed 26-May-2005.

[9] V.A. Riziotis, S.G. Voutsinas, E.S. Politis, and P.K. Chaviaropoulos. Aeroelastic stability of wind turbines: The problem, the methods and the issues. *Wind Energy*, 7(4):373–392, 2004.

[10] M. H. Hansen. Aeroelastic stability analysis of wind turbines using an eigenvalue approach. *Wind Energy*, 7(2):133–143, 2004.

[11] J. G. Leishman and T. S. Beddoes. A semi-empirical model for dynamic stall. *Journal of the American Helicopter Society*, Vol. 34(3):3–17, July 1989.

[12] D. H. Hodges and E. H. Dowell. Nonlinear equations of motion for the elastic bending and torsion of twisted nonuniform rotor blades. Technical Report TN D-7818, NASA, December 1974.

[13] J. Wendell. Aeroelastic stability of wind turbine rotor blades. Technical Report E(11.1)-4131, U.S. Department of Energy, September 1978.

[14] P. P. Friedmann. Aeroelastic scaling for rotary-wing aircraft with applications. *Journal of Fluids and Structures*, 19(5):635–650, 2004.

[15] F. M. Jensen, B. G. Falzon, J. Ankersen, and H. Stang. Structural testing and numerical simulation of a 34m composite wind turbine blade. *Composite Structures*, 76(1-2):52–61, 2006.

[16] C. E. S. Cesnik, D. H. Hodges, and V. G. Sutyrin. Cross-sectional analysis of composite beams including large initial twist and curvature effects. *AIAA Journal*, 34(9):1913–1920, 1996.

[17] Y. Wenbin, D. H. Hodges, V. Volovoi, and C. E. S. Cesnik. On timoshenko-like modeling of initially curved and twisted composite beams. *International Journal of Solids and Structures*, 39(19):5101–5121, 2002.

[18] Y. Wenbin, V. Volovoi, D. H. Hodges, and X. Hong. Validation of the variational asymptotic beam sectional analysis. *AIAA Journal*, 40(10):2105–2112, 2002.

[19] Y. C. Fung. *An Introduction to the Theory of Aeroelasticity*. Dover Pubns; Reprint edition (January 1994), 1955.

[20] T. Thoedorsen. General theory of aerodynamic instability and the mechanism of flutter. *NACA report 496*, 1935.

[21] P. K. Chaviaropoulos, N. N. Soerensen, M. O. L. Hansen, I. G. Nikolaou, K. A. Aggelis, J. Johansen, M. Gaunaa, T. Hambraus, H. F. Geyr, C. Hirsch, K. Shun, S. G. Voutsinas, G. Tzabiras, Y. Perivolaris, and S. Z. Dyrmose. Viscous and aeroelastic effects on wind turbine blades. the viscel project. part II: Aeroelastic stability investigations. *Wind Energy*, 6(4):387–404, 2003.

[22] J. J. Block and T. W. Strganac. Applied active control for a nonlinear aeroelastic structure. *Journal of Guidance, Control, and Dynamics*, 21(6):838–845, 1998.

[23] G. F. Franklin, J. D. Powell, and A. Emami-Naeini. *Feedback Control of Dynamic Systems*. Prentice Hall, 4 edition, 2002.

[24] E. A. Bossanyi. The design of closed loop controllers for wind turbines. *Wind Energy*, 3:149–163, 2000.

[25] H. Kwakernaak and R. Sivan. *Linear optimal control systems*. Wiley: New York, 1972.

[26] S. Skogestad and I. Postlethwaite. *Multivariable feedback control: Analysis and design*. Wiley: Chichester, 1996.

[27] T. Knudsen, P. Andersen, and S. Tøffner-Clausen. Comparing pi and robust pitch controllers on a 400kw wind turbine by full scale tests. In *Proceedings of European Wind Conference, Dublin*, October 1997.

[28] L. Ljung. *System Identification: Theory for the User (2nd Edition)*. Prentice Hall, 2 edition, 1998.

[29] E. A. Bossanyi. Wind turbine control for load reduction. *Wind Energy*, 6:229–244, 2003.

[30] D. Trudnowski and D. LeMieux. Independent pitch control using rotor position feedback for wind-shear and gravity fatigue reduction in a wind turbine. In *American Control Conference, 2002. Proceedings of the 2002*, volume 6, pages 4335–4340, 2002.

[31] C. D. Johnson. Theory of disturbance- accommodating controllers. *Advances in Control and Dynamic Systems*, 12:387–489, 1976.

[32] K. A. Stol and M. J. Balas. Periodic disturbance accommodating control for blade load mitigation in wind turbines. *Journal of Solar Energy Engineering, Transactions of the ASME*, 125(4):379–385, 2003.

[33] K. A. Stol. Disturbance tracking control and blade load mitigation for variable-speed wind turbines. *Journal of Solar Energy Engineering, Transactions of the ASME*, 125(4):396–401, 2003.

[34] B. M. Street, M. Balas, and K. Stol. Periodic and non-periodic disturbance accommodating control of the controls advanced research turbine (cart). *Collection of ASME Wind Energy Symposium Technical Papers AIAA Aerospace Sciences Meeting and Exhibit*, pages 124–132, 2004.

[35] A. D. Wright and M. J. Balas. Design of controls to attenuate loads in the controls advanced research turbine. *Collection of ASME Wind Energy Symposium Technical Papers AIAA Aerospace Sciences Meeting and Exhibit*, pages 76–86, 2004.

[36] L. Kendall, M. J. Balas, Y. J. Lee, and L. J. Fingersh. Application of proportional-integral and disturbance accommodating control to variable speed variable pitch horizontal axis wind turbines. *Wind Engineering*, 21(1):21–38, 1997.

[37] K. A. Stol. Disturbance tracking control and blade load mitigation for variable-speed wind turbines. *Journal of Solar Energy Engineering, Transactions of the ASME*, 125(4):396–401, 2003.

[38] T. T. Ekelund. Yaw control for reduction of structural dynamic loads in wind turbines. *Journal of Wind Engineering and Industrial Aerodynamics*, 85(3):241–262, 2000.

[39] W. Flügger. *Handbook of Engineering Mechanics*. Mcgraw-Hill, 1962.

[40] L. Meirovitch. *Analytical Methods in Vibrations*. MacMillan Company, New York, 1967.

[41] J. J. Thomsen. *Vibrations and Stability: Advanced Theory, Analysis, and Tools*. Springer-Verlag: Berlin - Heidelberg - New York, 2003.

[42] M. O. L. Hansen. *Aerodynamics of Wind Turbines*. James & James, 2001.

[43] M. H. Hansen, M. Gaunaa, and H. A. Madsen. A Beddoes-Leishman type dynamic stall model in state-space and indicial formulation. Technical Report Risø -R-1354(EN), Risø National Laboratory, (available from www.risoe.dk), August 2004.

[44] R. T. Jones. The unsteady lift of a wing of finite aspect ratio. *NACA report 681*, 1940.

[45] K. A. Stol. *Dynamics Modeling and Periodic Control of Horizontal-Axis Wind Turbines*. PhD thesis, University of Colorado, Department of Aerospace Engineering Sciences, December 2001.

[46] T. Buhl, K. Thomsen, H. Markou, T. S. Mogensen, A. J. Larsen, N. K. Poulsen, E. S. Politis, V. Riziotis, and T. G. van Engelen. Design guidelines for integrated aeroelastic control of wind turbines. Technical Report Risø -R-1577(EN), Risø National Laboratory, (available from www.risoe.dk), December 2006.

[47] J. Jonkman. NREL 5 MW baseline wind turbine. Technical report, NREL/NWTC, 1617 Cole Boulevard; Golden, CO 80401-3393, USA, 2005.

Appendix A
Coordinate Transformations

The derivation of the transformation matrices follows the method used in [12]. The major difference between [12] and these matrices is the inclusion of the pitch angle β.

The transformation between the initial (X, Y, Z)-frame and the $(\hat{x}, \hat{y}, \hat{z})$-frame is based on direct geometric considerations and given by

$$\begin{bmatrix} \hat{\mathbf{i}} \\ \hat{\mathbf{j}} \\ \hat{\mathbf{k}} \end{bmatrix} = \mathbf{T}_\phi \begin{bmatrix} \mathbf{I} \\ \mathbf{J} \\ \mathbf{K} \end{bmatrix} = \begin{bmatrix} \cos(\phi(t)) & 0 & -\sin(\phi(t)) \\ 0 & 1 & 0 \\ \sin(\phi(t)) & 0 & \cos(\phi(t)) \end{bmatrix} \begin{bmatrix} \mathbf{I} \\ \mathbf{J} \\ \mathbf{K} \end{bmatrix} \tag{A.1}$$

and the transformation between the $(\hat{x}, \hat{y}, \hat{z})$-frame and the (x, y, z)-frame is given by:

$$\begin{bmatrix} \mathbf{i} \\ \mathbf{j} \\ \mathbf{k} \end{bmatrix} = \mathbf{T}_\beta \begin{bmatrix} \hat{\mathbf{i}} \\ \hat{\mathbf{j}} \\ \hat{\mathbf{k}} \end{bmatrix} = \begin{bmatrix} \cos(\beta(t)) & \sin(\beta(t)) & 0 \\ -\sin(\beta(t)) & \cos(\beta(t)) & 0 \\ 0 & 0 & 1 \end{bmatrix} \begin{bmatrix} \hat{\mathbf{i}} \\ \hat{\mathbf{j}} \\ \hat{\mathbf{k}} \end{bmatrix} \tag{A.2}$$

The principle axis of each cross section of the blade is described by the (η, ξ, ζ)-frame with origin at ea, where η and ξ are the principle axis of the cross section and the ζ-axis points outwards along the elastic axis of the deformed blade. This frame has the unit vectors $(\tilde{\mathbf{i}}, \tilde{\mathbf{j}}, \tilde{\mathbf{k}})$ given by the following transformation

$$\begin{aligned} \begin{bmatrix} \tilde{\mathbf{i}} \\ \tilde{\mathbf{j}} \\ \tilde{\mathbf{k}} \end{bmatrix} =& \mathbf{T}_e \begin{bmatrix} \mathbf{i} \\ \mathbf{j} \\ \mathbf{k} \end{bmatrix} = \begin{bmatrix} \cos(\hat{\theta}(s,t)) & \sin(\hat{\theta}(s,t)) & 0 \\ -\sin(\hat{\theta}(s,t)) & \cos(\hat{\theta}(s,t)) & 0 \\ 0 & 0 & 1 \end{bmatrix} \\ & \begin{bmatrix} 1 & 0 & 0 \\ 0 & \sqrt{1-v'(s,t)^2} & -v'(s,t) \\ 0 & v'(s,t) & \sqrt{1-v'(s,t)^2} \end{bmatrix} \\ & \begin{bmatrix} \sqrt{\frac{1-(l'_{pi}(s)+u'(s,t))^2-v'(s,t)}{1-v'(s,t)^2}} & 0 & -\frac{l'_{pi}(s)+u'(s,t)}{\sqrt{1-v'(s,t)^2}} \\ 0 & 1 & 0 \\ \frac{l'_{pi}(s)+u'(s,t)}{\sqrt{1-v'(s,t)^2}} & 0 & \sqrt{\frac{1-(l'_{pi}(s)+u'(s,t))^2-v'(s,t)}{1-v'(s,t)^2}} \end{bmatrix} \begin{bmatrix} \mathbf{i} \\ \mathbf{j} \\ \mathbf{k} \end{bmatrix} \end{aligned} \tag{A.3}$$

where $\hat{\theta}$ is the rotation of the blade around the elastic axis. This transformation (A.3) is based on Euler angles (cf. [12]), the first matrix is rotation about the $\hat{z}$-axis, the next matrix is rotation about the x-axis and the last matrix is rotation about the z-axis.

The rotation of the principle axis of the blade sections as a function of the s coordinate is given by the differential equation

$$\mathbf{T}_e' = \begin{bmatrix} 0 & \tilde{\omega}_k & -\tilde{\omega}_j \\ -\tilde{\omega}_k & 0 & \tilde{\omega}_i \\ \tilde{\omega}_j & -\tilde{\omega}_i & 0 \end{bmatrix} \mathbf{T}_e \;\Rightarrow\; \begin{bmatrix} 0 & \tilde{\omega}_k & -\tilde{\omega}_j \\ -\tilde{\omega}_k & 0 & \tilde{\omega}_i \\ \tilde{\omega}_j & -\tilde{\omega}_i & 0 \end{bmatrix} = \mathbf{T}_e' \mathbf{T}_e^{-1} \tag{A.4}$$

where $(\tilde{\omega}_i, \tilde{\omega}_j, \tilde{\omega}_k)$ is the rotation about the $(\tilde{\mathbf{i}}, \tilde{\mathbf{j}}, \tilde{\mathbf{k}})$-directions, respectively, and it is utilized that $\mathbf{T}_\phi' = \mathbf{T}_\beta' = \mathbf{0}$. The rotation about the $\tilde{\mathbf{k}}$-direction is also measured by changes in the twist coordinates of the blade, (the pretwist $\tilde{\theta} = \tilde{\theta}(s)$ and the elastic twist $\theta_{ela} = \theta_{ela}(s,t)$). Hence

$$(\tilde{\theta} + \theta_{ela})' = \tilde{\omega}_k = \hat{\theta}' + v'(u'' + l_{pi}'') + \mathcal{O}(\epsilon^3) \tag{A.5}$$

using the order scheme (page 14).

Rearranging and intergrading (A.5) leads to an expression for the rotation of each blade section around the elastic axis

$$\hat{\theta} = \tilde{\theta} + \theta_{ela} - \int_0^s v'(u'' + l_{pi}'')\mathrm{d}\rho = \tilde{\theta} + \theta \;, \quad \theta = \theta(s,t) = \theta_{ela} - \int_0^s v'(u'' + l_{pi}'')\mathrm{d}\rho \tag{A.6}$$

where θ is the time dependent twist of the blade relative to the (x, y, z)-frame. Inserting (A.6) into the expression for $\mathbf{T}_e$ leads to the transformation matrix of the elastic properties. Replacing $\tilde{\theta}$ with $\bar{\theta}$ in $\mathbf{T}_e$ gives the transformation matrix $\mathbf{T}_c$ of the chord:

$$\begin{bmatrix} \bar{\mathbf{i}} & \bar{\mathbf{j}} & \bar{\mathbf{k}} \end{bmatrix}^{\mathrm{T}} = \mathbf{T}_c \begin{bmatrix} \mathbf{i} & \mathbf{j} & \mathbf{k} \end{bmatrix}^{\mathrm{T}} \tag{A.7}$$

Note that $\mathbf{T}^{\mathrm{T}}\mathbf{T} = \mathbf{I}$ holds for all the transformations matrices.

Appendix B
Matrices in the Linear Equations of Motion

This appendix presents the matrices for the linear equations of motion (2.55), (2.67) and (2.71).

Abbreviations

In the following description of terms in the linear equations of motions some abbreviations are used to shorten the notation and to help the physical interpretation.

The steady state apparent wind speed, the components of the steady state apparent wind speed in the $x-$, y-directions, along the chord and normal to the chord are given by

$$\begin{aligned}
U_0 =& \sqrt{V_{n,0}^2 + (\dot{\phi}_0 w_0)^2} \\
U_x =& \dot{\phi}_0 w_0 \cos(\beta_0) + V_{n,0} \sin(\beta_0) \\
U_y =& -\dot{\phi}_0 w_0 \sin(\beta_0) + V_{n,0} \cos(\beta_0) \\
\bar{U}_x =& \dot{\phi}_0 w_0 \cos(\beta_0 + \theta_0 + \bar{\theta}) + V_{n,0} \sin(\beta_0 + \theta_0 + \bar{\theta}) \\
\bar{U}_y =& -\dot{\phi}_0 w_0 \sin(\beta_0 + \theta_0 + \bar{\theta}) + V_{n,0} \cos(\beta_0 + \theta_0 + \bar{\theta})
\end{aligned}$$

respectively. The position of the elastic axis, the three quarter point and the aerodynamic center in the (x, y, z)-frame are given by

$$\begin{aligned}
u_{ea} =& (l_{pi} + u_0) \cos(\beta_0) - v_0 \sin(\beta_0) \\
v_{ea} =& (l_{pi} + u_0) \sin(\beta_0) + v_0 \cos(\beta_0) \\
u_{3/4} =& (l_{pi} + u_0) \cos(\beta_0) - v_0 \sin(\beta_0) - l_{3/4} \cos(\theta_0 + \bar{\theta} + \beta_0) \\
v_{3/4} =& (l_{pi} + u_0) \sin(\beta_0) + v_0 \cos(\beta_0) - l_{3/4} \sin(\theta_0 + \bar{\theta} + \beta_0) \\
u_{ac} =& l_{pi} + u_0 + l_{ac} \cos(\theta_0 + \bar{\theta}) \\
v_{ac} =& v_0 + l_{ac} \sin(\theta_0 + \bar{\theta})
\end{aligned}$$

respectively. The position of the aerodynamic center in the $(\hat{x}, \hat{y}, \hat{z})$-frame is given by

$$\begin{aligned}
\hat{u}_{ac} =& (l_{pi} + u_0) \cos(\beta_0) - v_0 \sin(\beta_0) + l_{ac} \cos(\theta_0 + \bar{\theta} + \beta_0) \\
\hat{v}_{ac} =& (l_{pi} + u_0) \sin(\beta_0) + v_0 \cos(\beta_0) + l_{ac} \sin(\theta_0 + \bar{\theta} + \beta_0)
\end{aligned}$$

for the $\hat{x}$- and $\hat{y}$-coordinates, respectively.

The static lift coefficient in the x- and y-directions, in the chord direction and normal to the chord and in the $\hat{x}$- and $\hat{y}$-directions are given by

$$
\begin{aligned}
C_x &= C_L^{st}\frac{U_y}{U_0} + C_D^{st}\frac{U_x}{U_0} & \qquad C_y &= C_L^{st}\frac{U_x}{U_0} - C_D^{st}\frac{U_y}{U_0} \\
\bar{C}_x &= C_L^{st}\frac{\bar{U}_y}{U_0} + C_D^{st}\frac{\bar{U}_x}{U_0} & \qquad \bar{C}_y &= C_L^{st}\frac{\bar{U}_x}{U_0} - C_D^{st}\frac{\bar{U}_y}{U_0} \\
\hat{C}_x &= C_L^{st}\frac{V_{n,0}}{U_0} + C_D^{st}\frac{\dot{\phi}_0 w_0}{U_0} & \qquad \hat{C}_y &= C_L^{st}\frac{\dot{\phi}_0 w_0}{U_0} - C_D^{st}\frac{V_{n,0}}{U_0}
\end{aligned}
$$

respectively. It should be noted that $\frac{U_x}{U_0}$ and $\frac{U_x}{U_0}$ are projection of a vector in the apparent wind direction onto the x- and y-directions, $\frac{\bar{U}_x}{U_0}$ and $\frac{\bar{U}_y}{U_0}$ are projections onto the cord direction and normal to the chord, $\frac{V_{n,0}}{U_0}$ and $\frac{\dot{\phi}_0 w_0}{U_0}$ are projections onto the $\hat{x}$- and $\hat{y}$-directions.

The change in aerodynamic coefficients caused by a change in angle of attack projected onto the x- and y-directions, the direction of the chord, normal to the chord and onto the $\hat{x}$- and $\hat{y}$-directions are given by

$$
\begin{aligned}
c_y &= (1-\Phi)C_L^{st}\frac{U_x}{U_0} + \Phi c_{l,\alpha}\frac{U_y}{U_0} + \Phi c_{d,\alpha}\frac{U_x}{U_0} \\
c_x &= (1-\Phi)C_L^{st}\frac{U_y}{U_0} - \Phi c_{l,\alpha}\frac{U_x}{U_0} + \Phi c_{d,\alpha}\frac{U_y}{U_0} \\
\bar{c}_y &= (1-\Phi)C_L^{st}\frac{\bar{U}_x}{U_0} + \Phi c_{l,\alpha}\frac{\bar{U}_y}{U_0} + \Phi c_{d,\alpha}\frac{\bar{U}_x}{U_0} \\
\bar{c}_x &= (1-\Phi)C_L^{st}\frac{\bar{U}_y}{U_0} - \Phi c_{l,\alpha}\frac{\bar{U}_x}{U_0} + \Phi c_{d,\alpha}\frac{\bar{U}_y}{U_0} \\
\hat{c}_y &= (1-\Phi)C_L^{st}\frac{\dot{\phi}_0 w_0}{U_0} + \Phi c_{l,\alpha}\frac{V_{n,0}}{U_0} + \Phi c_{d,\alpha}\frac{\dot{\phi}_0 w_0}{U_0} \\
\hat{c}_x &= (1-\Phi)C_L^{st}\frac{V_{n,0}}{U_0} - \Phi c_{l,\alpha}\frac{\dot{\phi}_0 w_0}{U_0} + \Phi c_{d,\alpha}\frac{V_{n,0}}{U_0}
\end{aligned}
$$

respectively. The change in aerodynamic coefficients caused by a change in the angle of attack at the three quarter point projected onto the x- and y-directions,

the $\hat{x}$- and $\hat{y}$-directions and the direction of the chord are given by

$$
\begin{aligned}
c_{x,3/4} &= ((C_L^{st} - c_{d,\alpha})\frac{U_y}{U_0} + c_{l,\alpha}\frac{U_x}{U_0}) \\
c_{y,3/4} &= ((C_L^{st} - c_{d,\alpha})\frac{U_x}{U_0} - c_{l,\alpha}\frac{U_y}{U_0}) \\
\hat{c}_{x,3/4} &= (C_L^{st} - c_{d,\alpha})\frac{\dot{\phi}_0 w_0}{U_0} - c_{l,\alpha}\frac{V_{n,0}}{U_0} \\
\hat{c}_{y,3/4} &= (C_L^{st} - c_{d,\alpha})\frac{V_{n,0}}{U_0} + c_{l,\alpha}\frac{\dot{\phi}_0 w_0}{U_0} \\
\bar{c}_{x,3/4} &= ((C_L^{st} - c_{d,\alpha})\frac{\bar{U}_y}{U_0} + c_{l,\alpha}\frac{\bar{U}_x}{U_0})
\end{aligned}
$$

respectively. The steady state aerodynamic amplification factor is given by $K_0 = \frac{1}{2}\rho c U_0^2$ and $T_0 = \frac{c}{2U_0}$ is the time constant in the aerodynamic model.

Matrices for Blade Model

The matrixes of the linear partial differential equation of blade motion (2.55) are

$$\tilde{\mathbf{M}} = \begin{bmatrix} \tilde{\mathbf{M}}_{st} & \mathbf{0}_{6\times4} \\ \mathbf{0}_{4\times6} & \mathbf{0}_{4\times4} \end{bmatrix} + \tilde{\mathbf{M}}_{aero} \tag{B.1}$$

where

$$\tilde{\mathbf{M}}_{st} = \begin{bmatrix} 1 & 0 & 0 & 0 & 0 & 0 \\ 0 & 1 & 0 & 0 & 0 & 0 \\ 0 & 0 & 1 & 0 & 0 & 0 \\ 0 & 0 & 0 & m & 0 & -ml_{cg}\sin(\bar{\theta}+\theta_0) \\ 0 & 0 & 0 & 0 & m & ml_{cg}\cos(\bar{\theta}+\theta_0) \\ 0 & 0 & 0 & -ml_{cg}\sin(\bar{\theta}+\theta_0) & ml_{cg}\cos(\bar{\theta}+\theta_0) & I_{ea} \end{bmatrix}$$

$$\tilde{\mathbf{M}}_{aero} = \begin{bmatrix} 0 & 0 & 0 & 0 & 0 & 0 & 0 & 0 & 0 & 0 \\ 0 & 0 & 0 & 0 & 0 & 0 & 0 & 0 & 0 & 0 \\ 0 & 0 & 0 & 0 & 0 & 0 & 0 & 0 & 0 & 0 \\ 0 & 0 & 0 & K_0T_0\pi\frac{U_y}{U_0^2}\frac{U_y}{U_0} & -K_0T_0\pi\frac{U_x}{U_0^2}\frac{U_y}{U_0} & 0 & 0 & 0 & 0 & 0 \\ 0 & 0 & 0 & -K_0T_0\pi\frac{U_y}{U_0^2}\frac{U_x}{U_0} & K_0T_0\pi\frac{U_x}{U_0^2}\frac{U_x}{U_0} & 0 & 0 & 0 & 0 & 0 \\ 0 & 0 & 0 & -K_0T_0\pi\frac{U_y}{U_0^2}\frac{\bar{U}_x}{U_0}l_{ac} - cK_0T_0\frac{\pi}{2}\frac{U_y}{U_0^2} & K_0T_0\pi\frac{U_x}{U_0^2}\frac{\bar{U}_x}{U_0}l_{ac} + cK_0T_0\frac{\pi}{2}\frac{U_x}{U_0^2} & 0 & 0 & 0 & 0 & 0 \\ 0 & 0 & 0 & -\frac{A_1\alpha_0}{U_0}\frac{U_x}{U_0} & -\frac{A_1\alpha_0}{U_0}\frac{U_y}{U_0} & 0 & 1 & 0 & 0 & 0 \\ 0 & 0 & 0 & -\frac{A_2\alpha_0}{U_0}\frac{U_x}{U_0} & -\frac{A_2\alpha_0}{U_0}\frac{U_y}{U_0} & 0 & 0 & 1 & 0 & 0 \\ 0 & 0 & 0 & \frac{\pi T_0}{T_p}\frac{U_y}{U_0^2} & -\frac{\pi T_0}{T_p}\frac{U_x}{U_0^2} & 0 & 0 & 0 & 1 & 0 \\ 0 & 0 & 0 & 0 & 0 & 0 & 0 & 0 & 0 & 1 \end{bmatrix}$$

$$\tilde{\mathbf{K}} = \begin{bmatrix} \tilde{\mathbf{K}}_{st} & \mathbf{0}_{6\times4} \\ \mathbf{0}_{4\times6} & \mathbf{0}_{4\times4} \end{bmatrix} + \begin{bmatrix} \tilde{\mathbf{K}}_{aero,1,1} & \tilde{\mathbf{K}}_{aero,1,2} \\ \tilde{\mathbf{K}}_{aero,2} \end{bmatrix} \tag{B.2}$$

where

$$\tilde{\mathbf{K}}_{st} = \begin{bmatrix} 0 & 0 & 0 & -1 & 0 & 0 \\ 0 & 0 & 0 & 0 & -1 & 0 \\ 0 & 0 & 0 & 0 & 0 & -1 \\ -\dot{\phi}_0^2 m\cos^2(\beta 0) & \dot{\phi}_0^2 m\sin(\beta_0)\cos(\beta_0) & \dot{\phi}_0^2 ml_{cg}\sin(\bar{\theta}+\theta_0+\beta_0)\cos(\beta_0) & 0 & 0 & 0 \\ \dot{\phi}_0^2 m\sin(\beta_0)\cos(\beta_0) & -\dot{\phi}_0^2 m\sin^2(\beta 0) & -\dot{\phi}_0^2 ml_{cg}\sin(\bar{\theta}+\theta_0+\beta_0)\sin(\beta_0) & 0 & 0 & 0 \\ \dot{\phi}_0^2 ml_{cg}\sin(\bar{\theta}+\theta_0+\beta_0)\cos(\beta_0) & -\dot{\phi}_0^2 ml_{cg}\sin(\bar{\theta}+\theta_0+\beta_0)\sin(\beta_0) & 0 & 0 & 0 & 0 \end{bmatrix}$$

$$\tilde{\mathbf{K}}_{aero,1,1} = \begin{bmatrix} 0 & 0 & 0 & 0 & 0 & 0 \\ 0 & 0 & 0 & 0 & 0 & 0 \\ 0 & 0 & 0 & 0 & 0 & 0 \\ 0 & 0 & -K_0 c_y & K_0(c_y - C_y)\frac{U_y}{U_0^2} + \rho c U_0 C_x \frac{U_x}{U0} & -K_0(c_y - C_y)\frac{U_x}{U_0^2} + \rho c U_0 C_x \frac{U_y}{U0} & -cK_0\frac{\pi}{2}\frac{U_y}{U_0^2} - K_0 l_{3/4}\frac{\bar{U}_x}{U_0^2}\Phi c_{y,3/4} \\ 0 & 0 & -K_0 c_x & K_0(c_x - C_x)\frac{U_y}{U_0^2} - \rho c U_0 C_y \frac{U_x}{U0} & -K_0(c_x - C_x)\frac{U_x}{U_0^2} - \rho c U_0 C_y \frac{U_y}{U0} & cK_0\frac{\pi}{2}\frac{U_x}{U_0^2} - K_0 l_{3/4}\frac{\bar{U}_x}{U_0^2}\Phi c_{x,3/4} \\ 0 & 0 & \begin{pmatrix} -K_0 l_{ac}\left(c_x - \bar{C}_x\right) \\ -cK_0\Phi c_{m,\alpha} \end{pmatrix} & \begin{pmatrix} \rho c U_0\left(cC_M^{st} - l_{ac}\bar{C}_y\right)\frac{U_x}{U_0} \\ +K_0\left(c\Phi c_{m,\alpha} + l_{ac}\left(\bar{c}_x - \bar{C}_x\right)\right)\frac{U_y}{U_0^2} \end{pmatrix} & \begin{pmatrix} \rho c U_0\left(cC_M^{st} + l_{ac}\bar{C}_y\right)\frac{U_y}{U_0} \\ -K_0\left(c\Phi c_{m,\alpha} + l_{ac}\left(\bar{c}_x - \bar{C}_x\right)\right)\frac{U_x}{U_0^2} \end{pmatrix} & \begin{pmatrix} cK_0 T_0\frac{\pi}{2} + K_0 T_0 \pi l_{ac}\frac{\bar{U}_x}{U_0} \\ +K_0\left(c\Phi c_{m,\alpha} - l_{ac}\bar{c}_{x,3/4}\right)l_{3/4}\frac{\bar{U}_x}{U_0^2} \end{pmatrix} \end{bmatrix}$$

$$\tilde{\mathbf{K}}_{aero,1,2} = \begin{bmatrix} 0 & 0 & 0 & 0 \\ 0 & 0 & 0 & 0 \\ 0 & 0 & 0 & 0 \\ K_0 c_{y,3/4} & K_0 c_{y,3/4} & 0 & -K_0\left(c_{l,f}\frac{U_y}{U_0} + c_{d,f}\frac{U_x}{U_0}\right) \\ K_0 c_{x,3/4} & K_0 c_{x,3/4} & 0 & K_0\left(c_{l,f}\frac{U_x}{U_0} - c_{d,f}\frac{U_y}{U_0}\right) \\ cK_0 c_{m,\alpha} + K_0 l_{ac}\bar{c}_{x,3/4} & cK_0 c_{m,\alpha} + K_0 l_{ac}\bar{c}_{x,3/4} & 0 & -cK_0 c_{m,f} + K_0 l_{ac}\left(c_{l,f}\frac{\bar{U}_x}{U_0} - c_{d,f}\frac{\bar{U}_y}{U_0}\right) \end{bmatrix}$$

$$\tilde{\mathbf{K}}_{earo,2} = \begin{bmatrix} 0 & 0 & -\frac{A_1 b_1}{T_0} & \frac{A_1 b_1}{T_0}\frac{U_y}{U_0^2} & -\frac{A_1 b_1}{T_0}\frac{U_x}{U_0^2} & \frac{A_1 b_1}{T_0} l_{3/4}\frac{\bar{U}_x}{U_0^2} & \frac{b_1}{T_0} & 0 & 0 & 0 \\ 0 & 0 & -\frac{A_2 b_2}{T_0} & \frac{A_2 b_2}{T_0}\frac{U_y}{U_0^2} & -\frac{A_2 b_2}{T_0}\frac{U_x}{U_0^2} & \frac{A_2 b_2}{T_0} l_{3/4}\frac{\bar{U}_x}{U_0^2} & 0 & \frac{b_2}{T_0} & 0 & 0 \\ 0 & 0 & -\frac{C_{L,\alpha}}{T_0 T_p}\Phi & \frac{C_{L,\alpha}}{T_0 T_p}\Phi\frac{U_y}{U_0^2} & -\frac{C_{L,\alpha}}{T_0 T_p}\Phi\frac{U_x}{U_0^2} & \frac{C_{L,\alpha}}{T_0 T_p}\Phi l_{3/4}\frac{\bar{U}_x}{U_0^2} - \frac{\pi}{T_p} & -\frac{C_{L,\alpha}}{T_0 T_p} & -\frac{C_{L,\alpha}}{T_0 T_p} & \frac{1}{T_0 T_p} & 0 \\ 0 & 0 & 0 & 0 & 0 & 0 & 0 & 0 & -\frac{f_{st}}{C_{L,\alpha} T_0 T_f} & \frac{1}{T_0 T_f} \end{bmatrix}$$

$$\tilde{\mathbf{K}}_s = \begin{bmatrix} 0 & 0 & 0 & 0 & 0 & 0 & \\ 0 & 0 & 0 & 0 & 0 & 0 & \\ 0 & 0 & 0 & 0 & 0 & 0 & \mathbf{0}_{6\times 4} \\ \dot{\phi}_0^2 m w_0 & 0 & \dot{\phi}_0^2 m w_0 l_{cg}\sin(\bar{\theta}+\theta_0) & 0 & 0 & 0 & \\ 0 & \dot{\phi}_0^2 m w_0 & -\dot{\phi}_0^2 m w_0 l_{cg}\cos(\bar{\theta}+\theta_0) & 0 & 0 & 0 & \\ -\dot{\phi}_0^2 m w_0 l_{cg}\sin(\bar{\theta}+\theta_0) & \dot{\phi}_0^2 m w_0 l_{cg}\cos(\bar{\theta}+\theta_0) & GJ & 0 & 0 & 0 & \\ \multicolumn{6}{c}{\mathbf{0}_{4\times 6}} & \mathbf{0}_{4\times 4} \end{bmatrix} \tag{B.3}$$

$$\tilde{\mathbf{K}}_{ss} = \begin{bmatrix} 0 & 0 & 0 & \\ 0 & 0 & 0 & \\ 0 & 0 & 0 & \mathbf{0}_{6\times 7} \\ -\dot{\phi}_0^2 \int_s^R m w_0 \mathrm{d}\gamma + EI_\eta \cos^2(\bar{\theta}) + EI_\xi \sin^2(\bar{\theta}) & (EI_\eta - EI_\xi)\cos(\bar{\theta})\sin(\bar{\theta}) & -\Big((EI_\eta - EI_\xi)\big((u_0'' + 1/2 l_{pi}'')\sin(2\bar{\theta}) - v_0'' \cos(2\bar{\theta})\big)\Big) & \\ (EI_\eta - EI_\xi)\cos(\bar{\theta})\sin(\bar{\theta}) & -\dot{\phi}_0^2 \int_s^R m w_0 \mathrm{d}\gamma + EI_\eta \sin^2(\bar{\theta}) + EI_\xi \cos^2(\bar{\theta}) & \Big((EI_\eta - EI_\xi)\big(v_0'' \sin(2\bar{\theta}) + (u_0'' + l_{pi}'')\cos(2\bar{\theta})\big)\Big) & \\ -(EI_\eta - EI_\xi)\left((u_0'' + 1/2 l_{pi}'')\sin(2\bar{\theta}) - v_0'' \cos(2\bar{\theta})\right) & (EI_\eta - EI_\xi)\left(v_0'' \sin(2\bar{\theta}) + (u_0'' + l_{pi}'')\cos(2\bar{\theta})\right) & 0 & \\ & \mathbf{0}_{4\times 6} & & \mathbf{0}_{4\times 7} \end{bmatrix} \tag{B.4}$$

$$\tilde{\mathbf{F}} = \begin{bmatrix} \mathbf{0}_{3\times 7} \\ \tilde{\mathbf{F}}_{st} \quad \mathbf{0}_{10\times 6} \\ \mathbf{0}_{4\times 7} \end{bmatrix} + \begin{bmatrix} \mathbf{0}_{3\times 13} \\ \tilde{\mathbf{F}}_{aero,1} \\ \tilde{\mathbf{F}}_{aero,2} \end{bmatrix} \tag{B.5}$$

where

$$\tilde{\mathbf{F}}_{st} = \begin{bmatrix} \dot{\phi}_0^2 m(\hat{u}_0 \sin(\beta_0) - \hat{v}_0 \cos(\beta_0)) & \dot{\phi}_0^2 m(\hat{u}_0 \cos(\beta_0) + \hat{v}_0 \sin(\beta_0)) & \dot{\phi}_0^2 m l_{cg}(\hat{u}_0 \cos(\bar{\theta} + \beta_0) + \hat{v}_0 \sin(\bar{\theta} + \beta_0)) \\ 2\dot{\phi}_0 \left(m l_{cg} \hat{v}_0 \cos(\bar{\theta})\right)' & 2\dot{\phi}_0 \left(m l_{cg} \hat{v}_0 \sin(\bar{\theta})\right)' & 0 \\ -m(v_0 + l_{cg}\sin(\bar{\theta} + \theta_0)) & m(u_0 + l_{cg}\cos(\bar{\theta} + \theta_0)) & I_{ea} - m l_{cg}(u_0 \cos(\bar{\theta}) + v_0 \sin(\bar{\theta})) \\ mg\cos(\beta_0) & -mg\sin(\beta_0) & -mgl_{cg}\sin(\beta_0 + \bar{\theta} + \theta_0) \\ \Big((u_0'' + l_{pi}'')\int_s^R m w_0 \mathrm{d}\gamma - (u_0' + l_{pi}')m w_0 & \Big(v_0'' \int_s^R m w_0 \mathrm{d}\gamma - v_0' m w_0 & mgl_{cg}(v_0' \cos(\bar{\theta}) - (u_0' + l_{pi}')\sin(\bar{\theta})) \\ -\big(m l_{cg}\cos(\bar{\theta} + \theta_0)'g\Big) & -\big(m l_{cg}\sin(\bar{\theta} + \theta_0)'g\Big) & \\ 2\dot{\phi}_0 \Big(m\hat{u}_0 \cos(\beta_0) - \big(m l_{cg} w_0 \cos(\bar{\theta} + \theta_0)\big)' & 2\dot{\phi}_0 \Big(v_0'' \int_s^R m w_0 \mathrm{d}\gamma - \big(m l_{cg} w_0 \sin(\bar{\theta} + \theta_0)\big)' & 2\dot{\phi}_0 m l_{cg} \Big(\hat{u}_0 \sin(\bar{\theta} + \theta_0 + \beta 0) \\ + (u_0'' + l_{pi}'')\int_s^R m w_0 \mathrm{d}\gamma - (u_0' + l_{pi}')m w_0\Big) & - m\hat{u}_0 \sin(\beta_0) - v_0' m w_0\Big) & + w_0(v_0' \cos(\bar{\theta}) - (u_0' + l_{pi}')\sin(\bar{\theta}))\Big) \\ m w_0 \cos(\beta_0) & -m w_0 \sin(\beta_0) & -m w_0 l_{cg}\sin(\bar{\theta} + \beta_0) \end{bmatrix}^{\mathrm{T}}$$

$$\tilde{F}_{aero,1} = \begin{bmatrix} K_0(C_y - c_y) & K_0(C_x - c_x) & cK_0\Phi c_{m,\alpha} + K_0 l_{ac}(\bar{C}_x - \bar{c}_x) \\ \tilde{F}_{\dot{\beta},1} & \tilde{F}_{\dot{\beta},2} & \tilde{F}_{\dot{\beta},3} \\ -K_0T_0\pi\frac{\dot{\phi}_0 w_0 u_{ea}+V_{n,0}v_{ea}}{U_0}\frac{U_y}{U_0} & K_0T_0\pi\frac{\dot{\phi}_0 w_0 u_{ea}+V_{n,0}v_{ea}}{U_0}\frac{U_x}{U_0} & \left(K_0T_0\pi l_{ac}\frac{\bar{U}_x}{U_0} + cK_0T_0\frac{\pi}{2}\right)\frac{\dot{\phi}_0 w_0 u_{ea}+V_{n,0}v_{ea}}{U_0} \\ 0 & 0 & 0 \\ 0 & 0 & 0 \\ -K_0\left(c_y - C_y\right)\frac{w_0 V_{n,0}}{U_0^2} - \rho cU_0 C_x\frac{\dot{\phi}_0 w_0}{U_0} & -K_0\left(c_x - C_x\right)\frac{w_0 V_{n,0}}{U_0^2} + \rho cU_0 C_y\frac{\dot{\phi}_0 w_0}{U_0} & \left(K_0\left(l_{ac}(\bar{C}_x - \bar{c}_x) - \Phi c c_{m,\alpha}\right)\frac{w_0 V_{n,0}}{U_0}\right. \\ & & \left. + \rho cU_0\left(l_{ac}\bar{C}_y - cC_M^{st}\right)\frac{\dot{\phi}_0 w0^2}{U_0}\right) \\ -K_0T_0\pi\frac{w_0 V_{n,0}}{U_0^2}\frac{U_y}{U_0} & K_0T_0\pi\frac{w_0 V_{n,0}}{U_0^2}\frac{U_x}{U_0} & K_0T_0\left(c\frac{\pi}{2} + \pi l_{ac}\frac{\bar{U}_x}{U_0}\right)\frac{w_0 V_{n,0}}{U_0^2} \\ K_0\left(c_y - C_y\right)\frac{\dot{\phi}_0 w_0}{U_0^2} - \rho cU_0 C_x\frac{V_{n,0}}{U_0} & K_0\left(c_x - C_x\right)\frac{\dot{\phi}_0 w_0}{U_0^2} + \rho cU_0 C_y\frac{V_{n,0}}{U_0} & \left(K_0\left(l_{ac}(\bar{c}_x - \bar{C}_x) + c\Phi c_{m,\alpha}\right)\frac{\dot{\phi}_0 w_0}{U_0^2}\right. \\ & & \left. + \rho cU_0\frac{V_{n,0}}{U_0}\left(l_{ac}\bar{C}_y - cC_M^{st}\right)\right) \\ K_0\left(c_y - C_y\right)\frac{\dot{\phi}_0 w_0}{U_0^2} - \rho cU_0 C_x\frac{V_{n,0}}{U_0} & K_0\left(c_x - C_x\right)\frac{\dot{\phi}_0 w_0}{U_0^2} + \rho cU_0 C_y\frac{V_{n,0}}{U_0} & \left(K_0\left(l_{ac}(\bar{c}_x - \bar{C}_x) + c\Phi c_{m,\alpha}\right)\frac{\dot{\phi}_0 w_0}{U_0^2}\right. \\ & & \left. + \rho cU_0\frac{V_{n,0}}{U_0}\left(l_{ac}\bar{C}_y - cC_M^{st}\right)\right) \\ -K_0\left(c_y - C_y\right)\frac{V_{n,0}}{U_0^2} + \rho cU_0 C_x\frac{\dot{\phi}_0 w_0}{U_0} & -K_0\left(c_x - C_x\right)\frac{V_{n,0}}{U_0^2} - \rho cU_0 C_y\frac{\dot{\phi}_0 w_0}{U_0} & \left(K_0\left(l_{ac}(\bar{c}_x - \bar{C}_x) + c\Phi c_{m,\alpha}\right)\frac{V_{n,0}}{U_0^2}\right. \\ & & \left. - \rho cU_0\frac{\dot{\phi}_0 w_0}{U_0}\left(l_{ac}\bar{C}_y - cC_M^{st}\right)\right) \\ K_0T_0\pi\frac{U_y}{U_0}\frac{\dot{\phi}_0 w_0}{U_0^2} & -K_0T_0\pi\frac{U_x}{U_0}\frac{\dot{\phi}_0 w_0}{U_0^2} & -K_0T_0\left(c\frac{\pi}{2} + \pi l_{ac}\frac{\bar{U}_x}{U_0}\right)\frac{\dot{\phi}_0 w_0}{U_0^2} \\ K_0T_0\pi\frac{U_y}{U_0}\frac{\dot{\phi}_0 w_0}{U_0^2} & -K_0T_0\pi\frac{U_x}{U_0}\frac{\dot{\phi}_0 w_0}{U_0^2} & -K_0T_0\left(c\frac{\pi}{2} + \pi l_{ac}\frac{\bar{U}_x}{U_0}\right)\frac{\dot{\phi}_0 w_0}{U_0^2} \\ K_0T_0\pi\frac{U_y}{U_0}\frac{V_{n,0}}{U_0^2} & -K_0T_0\pi\frac{U_x}{U_0}\frac{V_{n,0}}{U_0^2} & -K_0T_0\left(c\frac{\pi}{2} + \pi l_{ac}\frac{\bar{U}_x}{U_0}\right)\frac{V_{n,0}}{U_0^2} \end{bmatrix}^{\mathrm{T}}$$

$$\begin{aligned}
\tilde{F}_{\dot{\beta},1} =& -K_0T_0\pi\frac{U_y}{U_0} + K_0\left(C_y - C_L^{st}\frac{U_x}{U0}\right)\frac{\dot{\phi}_0 w_0 u_{ea} + V_{n,0}v_{ea}}{U_0^2} - K_0\Phi c_{y,3/4}\frac{\dot{\phi}_0 w_0 v_{ea} - V_{n,0}u_{ea}}{U_0} - \rho cU_0 C_x\frac{\dot{\phi}_0 w_0 u_{ea} + V_{n,0}v_{ea}}{U_0} \\
\tilde{F}_{\dot{\beta},2} =& K_0T_0\pi\frac{U_x}{U_0} + K_0\left(C_x - C_L^{st}\frac{U_y}{U0}\right)\frac{\dot{\phi}_0 w_0 u_{ea} + V_{n,0}v_{ea}}{U_0^2} + K_0\Phi c_{x,3/4}\frac{\dot{\phi}_0 w_0 v_{ea} - V_{n,0}u_{ea}}{U_0} + \rho cU_0 C_y\frac{\dot{\phi}_0 w_0 u_{ea} + V_{n,0}v_{ea}}{U_0} \\
\tilde{F}_{\dot{\beta},3} =& cK_0T_0\frac{\pi}{2} + K_0T_0\pi l_{ac}\frac{\bar{u}_x}{U_0} + K_0\Phi\left(l_{ac}\bar{c}_{x,3/4} - cc_{m,\alpha}\right)\frac{\dot{\phi}_0 w_0 u_{3/4} + V_{n,0}v_{3/4}}{U_0^2} \\
& + K_0\Phi l_{ac}\left(\bar{C}_x - C_L^{st}\frac{\bar{U}_y}{U_0}\right)\frac{\dot{\phi}_0 w_0 u_{ea} + V_{n,0}v_{ea}}{U_0^2} + \rho cU_0\left(l_{ac}\bar{C}_y - cC_M^{st}\right)\frac{\dot{\phi}_0 w_0 v_{ea} - V_{n,0}u_{ea}}{U_0}
\end{aligned}$$

$$
\tilde{F}_{aero,2} = \begin{bmatrix}
-\frac{A_1 b_1}{T_0} & 0 & 0 & 0 & 0 & 0 & -\frac{A_1 b_1}{T_0}\frac{V_{n,0} w_0}{U_0^2} & \frac{A_1 \alpha_0}{U_0}\frac{\dot{\phi}_0 w_0^2}{U_0} & \frac{A_1 b_1}{T_0}\frac{\dot{\phi}_0 w_0}{U_0^2} & \frac{A_1 b_1}{T_0}\frac{\dot{\phi}_0 w_0}{U_0^2} & \frac{A_1 b_1}{T_0}\frac{V_{n,0}}{U_0^2} & \frac{A_1 \alpha_0}{U_0}\frac{V_{n,0}}{U_0} & \frac{A_1 \alpha_0}{U_0}\frac{V_{n,0}}{U_0} & -\frac{A_1 \alpha_0}{U_0}\frac{\dot{\phi}_0 w_0}{U_0} \\
-\frac{A_2 b_2}{T_0} & 0 & 0 & 0 & 0 & 0 & -\frac{A_2 b_2}{T_0}\frac{V_{n,0} w_0}{U_0^2} & \frac{A_2 \alpha_0}{U_0}\frac{\dot{\phi}_0 w_0^2}{U_0} & \frac{A_2 b_2}{T_0}\frac{\dot{\phi}_0 w_0}{U_0^2} & \frac{A_2 b_2}{T_0}\frac{\dot{\phi}_0 w_0}{U_0^2} & \frac{A_2 b_2}{T_0}\frac{V_{n,0}}{U_0^2} & \frac{A_2 \alpha_0}{U_0}\frac{V_{n,0}}{U_0} & \frac{A_2 \alpha_0}{U_0}\frac{V_{n,0}}{U_0} & -\frac{A_2 \alpha_0}{U_0}\frac{\dot{\phi}_0 w_0}{U_0} \\
\frac{\Phi C_{L,\alpha}}{T_0 T_p} & 0 & 0 & 0 & 0 & 0 & -\frac{\Phi C_{L,\alpha}}{T_0 T_p}\frac{V_{n,0} w_0}{U_0^2} & \pi T_0 \frac{V_{n,0} w_0}{U_0^2} & \frac{\Phi C_{L,\alpha}}{T_0 T_p}\frac{\dot{\phi}_0 w_0}{U_0^2} & \frac{\Phi C_{L,\alpha}}{T_0 T_p}\frac{\dot{\phi}_0 w_0}{U_0^2} & \frac{\Phi C_{L,\alpha}}{T_0 T_p}\frac{V_{n,0}}{U_0^2} & \frac{\pi}{T_0 T_p}\frac{V_{n,0}}{U_0} & \frac{\pi}{T_0 T_p}\frac{V_{n,0}}{U_0} & \frac{\pi}{T_0 T_p}\frac{\dot{\phi}_0 w_0}{U_0} \\
0 & 0 & 0 & 0 & 0 & 0 & 0 & 0 & 0 & 0 & 0 & 0 & 0 & 0
\end{bmatrix}
$$

Matrices for Pitch Action Model

The matrices in the linear pitch action model (2.67) are

$$\tilde{M}_\beta = \tilde{M}_\beta^{st} + \tilde{M}_\beta^{aero} \tag{B.6}$$

where

$$\begin{aligned}
\tilde{M}_\beta^{st} &= I_{cg} + m\left((u_0 + l_{pi} + l_{cg}\cos(\bar{\theta}+\theta_0))^2 + (v_0 + l_{cg}\sin(\bar{\theta}+\theta_0))^2\right) \\
\tilde{M}_\beta^{aero} &= -K_0 T_0 \left(c\frac{\pi}{2} + \pi\frac{U_y}{U_0}v_{ac} - \pi\frac{U_x}{U_0}u_{ac}\right)\frac{\dot{\phi}_0 w_0 \hat{u}_{ea} - V_{n,0}\hat{v}_{ea}}{U_0^2}
\end{aligned}$$

$$\tilde{D}_\beta = \tilde{D}_\beta^{st} + \tilde{D}_\beta^{aero} \tag{B.7}$$

where

$$\begin{aligned}
\tilde{D}_\beta^{st} =& 0 \\
\tilde{D}_\beta^{aero} =& cK_0T_0\frac{\pi}{2} - K_0T_0\pi\left(\frac{U_x}{U_0}u_{ac} - \frac{U_y}{U_0}v_{ac}\right) \\
&+ c\rho U_0\left(cC_M^{st} + C_x v_{ac} + C_y u_{ac}\right)\frac{U_x v_{ea} + U_y u_{ea}}{U_0} \\
&+ K_0\Phi\left(cc_{m,\alpha} + c_{x,3/4}u_{ac} + c_{y,3/4}v_{ac}\right)\frac{U_x u_{3/4} - U_y u_{3/4}}{U_0^2} \\
&+ K_0\left(C_x u_{ac} - C_y v_{ac} + C_L^{st}\left(\frac{U_y}{U_0}u_{ac} + \frac{U_x}{U_0}v_{ac}\right)\right)\frac{U_x u_{ea} - U_y u_{ea}}{U_0^2}
\end{aligned}$$

$$\tilde{K}_\beta = \tilde{K}_\beta^{st} + \tilde{K}_\beta^{aero} \tag{B.8}$$

where

$$\begin{aligned}
\tilde{K}_\beta^{st} =& \dot{\phi}_0 m\left(\hat{u}_{cg}^2 + \hat{v}_{cg}^2\right) \\
\tilde{K}_\beta^{aero} =& -cK_0\Phi c_{m,\alpha} - K_0\left(c_x u_{ac} + c_y v_{ac}\right) - K_0\left(C_x u_{ac} + C_y v_{ac}\right)
\end{aligned}$$

$$\tilde{\mathbf{M}}_\beta = \tilde{\mathbf{M}}_\beta^{st} + \tilde{\mathbf{M}}_\beta^{aero} \tag{B.9}$$

where

$$\tilde{\mathbf{M}}_\beta^{st} =$$

$$\begin{bmatrix} 0 & 0 & 0 & -m(v_0 + l_{cg}\sin(\bar{\theta}+\theta_0)) & m(u_0 + l_{pi} + l_{cg}\cos(\bar{\theta}+\theta_0) & I_{cg} + ml_{cg}^2 & \mathbf{0}_{1\times 4} \end{bmatrix}$$

$$\tilde{\mathbf{M}}_\beta^{aero} = \begin{bmatrix} 0 \\ 0 \\ 0 \\ K_0T_0\left(\pi\frac{\dot{\phi}_0 w_0}{U_0}\hat{u}_{ac} - \pi\frac{V_{n,0}}{U_0}\hat{v}_{ac} + c\frac{\pi}{2}\right)\frac{U_y}{U_0^2} \\ K_0T_0\left(\pi\frac{\dot{\phi}_0 w_0}{U_0}\hat{u}_{ac} - \pi\frac{V_{n,0}}{U_0}\hat{v}_{ac} + c\frac{\pi}{2}\right)\frac{U_x}{U_0^2} \\ 0 \\ \mathbf{0}_{4\times 1} \end{bmatrix}^{\mathrm{T}}$$

$$\tilde{\mathbf{K}}_\beta =$$

$$\begin{bmatrix} \dot{\phi}_0 w_0 m \left(\hat{u}_{cg}\sin(\beta_0) + \hat{v}_{cg}\cos(\beta_0)\right) - K_0 C_y \\ \dot{\phi}_0 w_0 m \left(\hat{u}_{cg}\cos(\beta_0) - \hat{v}_{cg}\sin(\beta_0)\right) - K_0 C_x \\ -cK_0\Phi c_{m,\alpha} - K_0\left(c_y v_{ac} + c_x u_{ac}\right) + K_0 l_{ac}\left(C_x\cos(\theta_0+\bar{\theta}) - C_y\sin(\theta_0+\bar{\theta})\right) \\ \mathbf{K}_0\left(c\Phi c_{m,\alpha} + (c_x + C_x)u_{ac} + (c_y - C_y)v_{ac}\right)\frac{U_y}{U_0^2} - \rho c U_0\left(cC_M^{st} + C_x v_{ac} + C_y u_{ac}\right)\frac{U_x}{U_0} \\ \mathbf{K}_0\left(c\Phi c_{m,\alpha} + (c_x + C_x)u_{ac} + (c_y - C_y)v_{ac}\right)\frac{U_x}{U_0^2} + \rho c U_0\left(cC_M^{st} + C_x v_{ac} + C_y u_{ac}\right)\frac{U_y}{U_0} \\ K_0 T_0\left(c\frac{\pi}{2} - \pi\frac{U_x}{U_0}u_{ac} + \pi\frac{U_y}{U_0}v_{ac}\right) - K_0\Phi\left(cc_{m,\alpha} - c_y v_{ac} - c_x u_{ac}\right)\frac{l_{3/4}\bar{U}_x}{U_0^2} \\ K_0\left(c_{y,3/4}v_{ac} + c_{x,3/4}u_{ac} - cc_{m,\alpha}\right) \\ K_0\left(c_{y,3/4}v_{ac} + c_{x,3/4}u_{ac} - cc_{m,\alpha}\right) \\ 0 \\ K_0\left(\left(\frac{U_y}{U_0}c_{l,f} - \frac{U_x}{U_0}c_{d,f}\right)v_{ac} - \left(\frac{U_x}{U_0}c_{l,f} + \frac{U_y}{U_0}c_{d,f}\right)u_{ac} - cc_{m,f}\right) \end{bmatrix}^{\mathrm{T}}$$

$$\tilde{\mathbf{f}}_\beta = \tilde{\mathbf{f}}_\beta^{st} + \tilde{\mathbf{f}}_\beta^{aero} \tag{B.8}$$

where

$$\tilde{\mathbf{f}}_\beta^{st} = \begin{bmatrix} 0 & gm\hat{v}_{cg} & 2\dot{\phi}_0 m\hat{u}_{cg}\hat{v}_{cg} & -mw_0\hat{v}_{cg} & 0 & 0 & 0 & 0 \end{bmatrix}$$

$$\tilde{\mathbf{f}}_\beta^{aero} =$$

$$\begin{bmatrix} 0 \\ 0 \\ K_0\left(c\Phi c_{m,\alpha} + (c_x + C_x)u_{ac} + (c_y - C_y)v_{ac}\right)\frac{V_{n,0}w_0}{U_0^2} + \rho c U_0\left(cC_M^{st} - C_x v_{ac} - C_y u_{ac}\right)\frac{\dot{\phi}_0 w_0^2}{U_0} \\ K_0 T_0\left(\pi\frac{U_x}{U_0}u_{ac} - \pi\frac{U_y}{U_0}v_{ac} - c\frac{\pi}{2}\right)\frac{V_{n,0}w_0}{U_0^2} \\ -K_0\left(c\Phi c_{m,\alpha}(c_y - C_y)v_{ac} + (c_x + C_x)u_{ac}\right)\frac{\dot{\phi}_0 w_0}{U_0^2} - \rho c U_0\left(cC_M^{st} + C_x v_{ac} + C_y u_{ac}\right)\frac{V_{n,0}}{U_0} \\ K_0\left(c\Phi c_{m,\alpha}(c_y - C_y)v_{ac} + (c_x + C_x)u_{ac}\right)\frac{V_{n,0}}{U_0^2} - \rho c U_0\left(cC_M^{st} + C_x v_{ac} + C_y u_{ac}\right)\frac{\dot{\phi}_0 w_0}{U_0} \\ K_0 T_0\left(c\frac{\pi}{2} - \pi\frac{U_x}{U_0}u_{ac} + \pi\frac{U_y}{U_0}v_{ac}\right)\frac{\dot{\phi}_0 w_0}{U_0^2} \\ -K_0 T_0\left(c\frac{\pi}{2} - \pi\frac{U_x}{U_0}u_{ac} + \pi\frac{U_y}{U_0}v_{ac}\right)\frac{V_{n,0}}{U_0^2} \end{bmatrix}$$

Matrices for Rotor Speed Model

The matrices of the linear rotor speed equation (2.71) are

$$\tilde{M}_\phi = \tilde{M}_\phi^{st} + \tilde{M}_\phi^{aero} \tag{B.8}$$

where

$$\begin{aligned} \tilde{M}_\phi^{st} &= mw_0^2 \\ \tilde{M}_\phi^{aero} &= K_0 w_0 T_0 \pi \frac{V_{n,0}}{U_0}\frac{V_{n,0}w_0}{U_0^2} \end{aligned}$$

$$\tilde{D}_\phi = K_0 w_0 \left(\hat{C}_y - \hat{c}_y\right) \frac{w_0 V_{n,0}}{U_0^2} + \rho c U_0 w_0 \frac{\dot{\phi}_0 w_0^2}{U_0} \tag{B.9}$$

$$\tilde{K}_{\phi,\sin} = g m w_0 \ , \quad \tilde{K}_{\phi,\cos} = g m \hat{u}_{cg} \tag{B.10}$$

$$\tilde{\mathbf{M}}_\phi = \tilde{\mathbf{M}}_\phi^{st} + \tilde{\mathbf{M}}_\phi^{aero} \tag{B.11}$$

where

$$\tilde{\mathbf{M}}_\phi^{st} = \begin{bmatrix} 0 & 0 & 0 & m w_0 \cos(\beta_0) & -m w_0 \sin(\beta_0) & 0 & 0 & 0 & 0 & 0 \end{bmatrix}$$

$$\tilde{\mathbf{M}}_\phi^{aero} = \begin{bmatrix} 0 & 0 & 0 & K_0 T_0 \pi \frac{U_y}{U_0} \frac{w_0 V_{n,0}}{U_0^2} & K_0 T_0 \pi \frac{U_x}{U_0} \frac{w_0 V_{n,0}}{U_0^2} & 0 & 0 & 0 & 0 & 0 \end{bmatrix}$$

$$\tilde{\mathbf{K}}_\phi = \tilde{\mathbf{K}}_\phi^{st} + \tilde{\mathbf{K}}_\phi^{aero} \tag{B.12}$$

where

$$\tilde{\mathbf{K}}_\phi^{st} = \mathbf{0}_{1\times 10}$$

$$\tilde{\mathbf{K}}_\phi^{aero} = \begin{bmatrix} 0 \\ 0 \\ K_0 w_0 \hat{c}_y \\ -k_0 \left(\hat{c}_y - \hat{C}_y\right) \frac{U_y}{U_0^2} + \rho c U_0 w_0 \hat{C}_x \frac{U_x}{U_0} \\ -k_0 \left(\hat{c}_y - \hat{C}_y\right) \frac{U_x}{U_0^2} - \rho c U_0 w_0 \hat{C}_x \frac{U_y}{U_0} \\ -K_0 w_0 T_0 \pi \frac{V_{n,0}}{U_0} - K_0 w_0 \Phi \hat{c}_{y,3(4} \frac{l_{3/4} \bar{U}_x}{U_0^2} \\ -K_0 w_0 \hat{c}_{y,3/4} \\ -K_0 w_0 \hat{c}_{y,3/4} \\ 0 \\ K_0 w_0 \left(\frac{\dot{\phi}_0 w_0}{U_0} c_{d,f} - \frac{V_{n,0}}{U_0} c_{l,f}\right) \end{bmatrix}^{\mathrm{T}}$$

$$\tilde{\mathbf{f}}_\phi = \tilde{\mathbf{f}}_\phi^{st} + \tilde{\mathbf{f}}_\phi^{aero} \tag{B.13}$$

where

$$\tilde{\mathbf{f}}_\phi^{st} = \begin{bmatrix} 0 & 0 & m w_0 \hat{v}_{cg} & 0 & 0 & 0 & 0 \end{bmatrix}$$

$$\tilde{\mathbf{f}}_{\phi}^{aero} = \begin{bmatrix} K_0 w_0 \hat{c}_y \\ \left(-K_0 w_0 T_0 \pi \frac{V_{n,0}}{U_0} - K_0 w_0 \Phi \hat{c}_{y,3/4} \frac{V_{n,0} \hat{v}_{3/4} - \dot{\phi}_0 w_0 \hat{u}_{3/4}}{U_0^2} \right. \\ \left. -k_0 w_0 \left(\hat{C}_y - C_L^{st} \frac{\dot{\phi}_0 w_0}{U_0} \right) \frac{V_{n,0} \hat{v}_{ea} - \dot{\phi}_0 w_0 \hat{u}_{ea}}{U_0^2} - \rho c U_0 w_0 \hat{C}_x \frac{V_{n,0} \hat{u}_{ea} + \dot{\phi}_0 w_0 v_{ea}}{U_0^2} \right) \\ -K_0 w_0 T_0 \pi \frac{V_{n,0}}{U_0} \frac{V_{n,0} v_{ea} - \dot{\phi}_0 w_0 \hat{u}_{ea}}{U_0^2} \\ -K_0 w_0 \left(\Phi \hat{c}_{y,3/4} - C_L^{st} \frac{\dot{\phi}_0 w_0}{U_0} + \hat{C}_y \right) \frac{\dot{\phi}_0 w_0}{U_0^2} + \rho c U_0 w_0 \hat{C}_x \frac{V_{n,0}}{U_0} \\ K_0 w_0 \left(\Phi \hat{c}_{y,3/4} - C_L^{st} \frac{\dot{\phi}_0 w_0}{U_0} + \hat{C}_y \right) \frac{V_{n,0}}{U_0^2} + \rho c U_0 w_0 \hat{C}_x \frac{\dot{\phi}_0 w_0}{U_0} \\ -K_0 w_0 T_0 \pi \frac{V_{n,0}}{U_0} \frac{\dot{\phi}_0 w_0}{U_0^2} K_0 w_0 T_0 \pi \frac{V_{n,0}}{U_0} \frac{V_{n,0}}{U_0^2} \end{bmatrix}^{\mathrm{T}}$$

Appendix C
Test Turbine

The properties of the wind turbine blade, drivetrain and generator used as example throughout this thesis is based on NREL's 5 MW baseline wind turbine [47] with some modifications to fit the limitations of the developed aeroelastic model. That is, the shaft tilt and precone of the blades are set to zero.

The wind turbine model is developed for studies of multi mega watt wind turbines. The turbine parameters are fictitious and do not represent an actual wind turbine, but do represent a good approximation of what an actual wind turbine of that size would look like. It is a 5 MW wind turbine with a hub hight on 90 m and rotor diameter on 126 m. The blades are 61.5 m long and weigher 17740 kg each. All aerodynamic and structural properties are found in ref. [47].

It is a pitch regulated variable speed wind turbine with a cut in wind speed of 5 m/s, rated wind speed of 11 m/s and a cut out wind speed of 25 m/s. The pitch setting and rotor speed corresponding to different wind speeds are given in table C.1.

Table C.1: Pitch angle and rotor speed for different wind speeds.

Wind Speed [m/s]	Pitch Angle [deg]	Rotor Speed [RPM]
5	0.0	7.5
6	0.0	7.5
7	0.0	8.3
8	0.0	9.5
9	0.0	10.7
10	0.0	11.9
11	0.0	12.1
12	3.9	12.1
13	6.6	12.1
14	8.6	12.1
15	10.4	12.1
16	12.0	12.1
17	13.5	12.1
18	14.9	12.1
19	16.2	12.1
20	17.5	12.1
21	18.7	12.1
22	19.9	12.1
23	21.0	12.1
24	22.1	12.1
25	23.2	12.1

P1

(Journal Article)

A low-order model for analyzing effects of blade fatigue load control

Wind Energy **9(5)**:421-436, 2006

WIND ENERGY
Wind Energ. 2006; **9**:421–436
Published online 22 March 2006 in Wiley Interscience
(www.interscience.wiley.com) **DOI**: 10.1002/we.195

A Low-order Model for Analysing Effects of Blade Fatigue Load Control

B. S. Kallesøe*, Department of Mechanical Engineering, Technical University of Denmark, Nils Koppels Allé, Building 404, DK-2800 Lyngby, Denmark

Key words:
horizontal axis turbines;
control;
stability;
fatigue loads;
wing section

A new low-order mathematical model is introduced to analyse blade dynamics and blade load-reducing control strategies for wind turbines. The model consists of a typical wing section model combined with a rotor speed model, leading to four structural degrees of freedom (flapwise, edgewise and torsional blade oscillations and rotor speed). The aerodynamics is described by an unsteady aerodynamic model. The equations of motion are derived in non-linear and linear form. The linear equations of motion are used for stability analysis and control design. The non-linear equations of motion are used for time simulations to evaluate control performance. The stability analysis shows that the model is capable of predicting classical flutter and stall-induced vibrations. The results from the stability analysis are compared with known results, showing good agreement. The model is used to compare the performance of one proportional–integral–derivative controller and two full-state feedback controllers. Copyright © 2006 John Wiley & Sons, Ltd.

Received 25 August 2005; Revised 23 December 2005; Accepted 2 January 2006

Introduction

This article introduces a new mathematical model for analysing active fatigue load-reducing control systems on wind turbine blades. The model is used to design and compare one classical single-state feedback controller and two modern full-state feedback controllers.

The development of increasingly cost-efficient wind turbines is leading to large wind turbine constructions with minimized material usage, resulting in relatively flexible structures. This development leads to an increase in the response from the wind turbine to turbulent inflow, wind shear, tower shadow, etc. and thereby to an increase in the fatigue loads on it. Wind turbines are normally designed for a lifetime of 20 years, hence fatigue is an important design constraint. Pitch control can, aside from power regulation, be used to reduce the fatigue loads. Most wind turbine controllers today are based on classical proportional–integral–derivative (PID) controllers, but there is increasing interest in modern full-state feedback controllers such as the linear–quadratic regulator (LQR)[1] and the disturbance-accommodating controller (DAC),[2] primarily because they can handle multiple control inputs and multiple control objectives (e.g. power regulation and fatigue load reduction) in a straightforward manner. Classical PID controllers can be arranged in cascades to handle both multiple control objectives and multiple control inputs, but this can lead to unwanted interaction between the individual PID controllers.

*Correspondence to: B. S. Kallesøe, Department of Mechanical Engineering, Technical University of Denmark, Nils Koppels Allé, Building 404, DK-2800 Lyngby, Denmark.
E-mail: bsk@mek.dtu.dk
Contract/grant sponsor: Technical University of Denmark.
Contract/grant sponsor: Risø National Laboratory.

A number of articles show that active control can reduce the fatigue loads on wind turbines.[3–6] Bossanyi[3] compares a PID controller and a linear–quadratic–Gaussian (LQG)[1] full-state feedback controller. The LQG controller uses a Kalman filter[1] as state estimator. Different sensor set-ups are used for both controllers and it is found that a significant fatigue load reduction can be obtained when using the LQG controller compared with the PID controller. This work includes both numerical simulations of a wind turbine model and full-scale wind turbine tests. Kendall *et al*.[4] use another variant of full-state feedback control, disturbance-accommodating control (DAC). Using this strategy, both the model states and the incoming wind are estimated by Kalman filters and used in the controller. The measured control input is the rotor speed error. They show a reduction in fatigue loads both in numerical simulations and full-scale experiments. As in the two examples above, most of the work on fatigue load-reducing control of wind turbines uses comprehensive wind turbine models.

Typical wing section models are widely used for stability analysis and control design. The article by Theodorsen[7] gives a method for computing the aerodynamic forces on a two-dimensional lifting surface with attached flow. The method is used by Theodorsen and Garrick[8] to compute theoretical flutter and divergence boundaries for a typical wing section with two degrees of freedom (flapwise and torsional). The results are compared with experiments. A variety of control designs are applied to wing section models. For instance, Block and Strganac[9] examine flutter suppression with a full-state feedback controller and a Kalman state estimator, using a trailing edge flap as control actuator. Almost all articles dealing with control of wing sections use flaps as control actuator and wing sections with only flapwise and torsional degrees of freedom. The combined flapwise–edgewise motion of a wing section is studied by Chaviaropoulos *et al*.,[10] who analyse stall-induced vibrations. They also examine combined flapwise–torsional motions, studying classical flutter. This is done using two different models, each with two structural degrees of freedom.

The scope of the present work is to set up a typical wing section model describing the motion of one flapwise, one edgewise and one torsional mode of vibration of a wind turbine blade and the variation in the rotation speed of the rotor. The purpose of this model is to get insight into the interaction between blade dynamics and control; it is not a suitable tool for designing operational wind turbine controllers, because important physical aspects such as tower motion are not taken into account. The aerodynamic forces are described by an unsteady aerodynamic model suggested by Hansen *et al*.[11] The aeroelastic model is used to examine stability and to design and evaluate three different pitch controllers. The stability analysis shows that the model is capable of predicting divergence, classical flutter and stall-induced vibrations. The stability boundaries for classical flutter and divergence are compared with Theodorsen and Garrick's results,[8] showing good agreement. The control section compares the blade fatigue load and pitch actuator duty for the implemented controllers. It is stressed that this is not a comparison between applicable turbine controllers, but an analysis of the effect on blade fatigue load using control.

The following section describes the model and the governing equations. In section three the aeroelastic stability analysis is presented and discussed. Section four deals with the design and evaluation of controllers.

Model and Equations

In this section the structural model is described and the structural equations of motion are derived. The aerodynamic model is presented and the equations connecting the aerodynamic and structural models are derived. This aeroelastic model is extended with a controller and a pitch actuator model, giving an aeroservoelastic model.

Structural Model

Figure 1 shows the wing section model, which describes the motion of a turbine blade section located at a distance R from the hub and rotating with an angular frequency $\dot{\phi} = \dot{\phi}(t)$ (where $\dot{(\ )}$ denotes differentiation with respect to time). The model describes one flapwise, one edgewise and one torsional mode of vibration of the turbine blade. The rotational motion of the turbine blade in the rotor plane is simplified by unfolding it to a

DOI: 10.1002/we

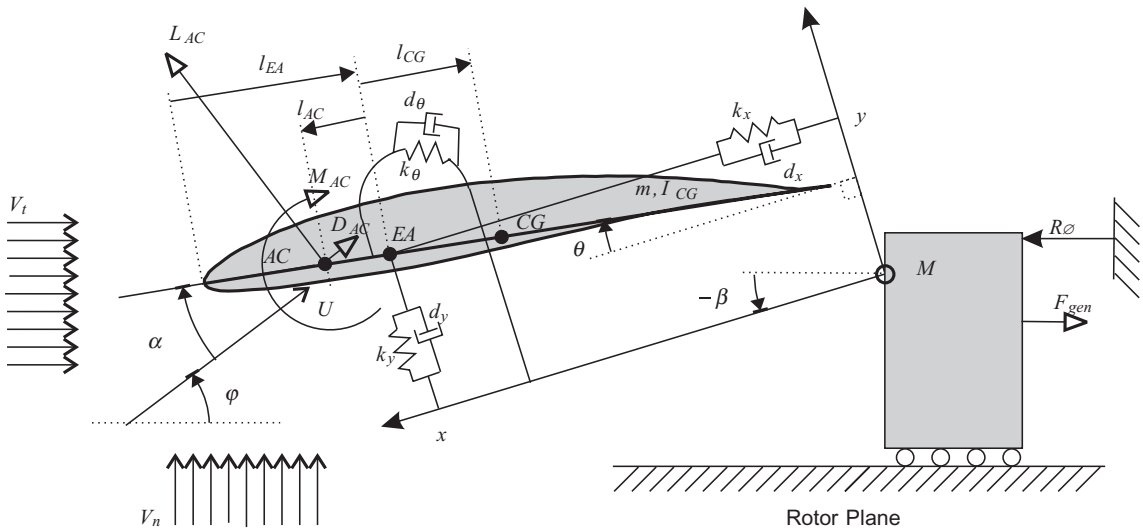

Figure 1. Wing section model

translatory motion of the blade section. Modelling a rotational motion as a translatory motion ignores the centripetal force, but the main effect from this force can be modelled by additional stiffness of the suspension.

The inertia of the rotor, gearbox and generator is described by the mass M, which slides frictionless on the unfolded rotor plane. The position of the section in the unfolded rotor plane is given by $R\phi = R\phi(t)$. The generator torque is modelled as a linear force F_{gen} acting on the mass M. The force is given by a constant effect generator model $F_{\text{gen}} = P_0/(R\dot{\phi})$, where P_0 is the part of the generator effect that corresponds to the blade section.

The deflection of the section is described by $x = x(t)$, $y = y(t)$ and $\theta = \theta(t)$ for the edgewise and flapwise directions and rotation respectively. The x and y axes are mutually perpendicular and attached to the mass M at a pitch angle $\beta = \beta(t)$. The rotation θ of the section is measured clockwise from the x axis. The section is suspended by linear springs k_x, k_y and k_θ and viscous dampers d_x, d_y and d_θ in the x and y directions and rotation respectively. The suspension forces act at the elastic axis EA, which is assumed to be located on the chord at a distance l_{EA} behind the leading edge. The inertia of the section is modelled by the mass m and the rotational inertia I_{CG} per unit spanwise length and related to the centre of gravity CG, which is assumed to be on the chord at a distance l_{CG} behind the elastic axis EA.

The stiffness of the suspension and the inertia of the section are given by the modal stiffness and inertia of the first flapwise, first edgewise and first torsional modes of vibration of a typical 40 m turbine blade (Table I). The masses M and m are determined by comparing the modal inertia of the blade and the sum of inertia of the rotor, gearbox and generator.

The airflow around the section is characterized by an apparent wind whose speed and direction are given by U and ψ respectively. The airflow leads to the aerodynamic forces $L_{\text{AC}} = L_{\text{AC}}(t)$ and $D_{\text{AC}} = D_{\text{AC}}(t)$, perpendicular and parallel to the apparent wind respectively, and the aerodynamic moment $M_{\text{AC}} = M_{\text{AC}}(t)$. The aerodynamic forces act at the aerodynamic centre AC, which is on the chord at a distance l_{AC} ahead of the elastic axis EA.

In summary, the state of the model is given by $\{x, y, \theta, \beta, \phi\}$, where β is constant or given by external forces controlled by a controller. The model is exposed to the external loads $\{L_{\text{AC}}, D_{\text{AC}}, M_{\text{AC}}, F_{\text{gen}}\}$, where $F_{\text{gen}} = F_{\text{gen}}(\dot{\phi}, P_0)$ with the chosen generator model.

Structural Equations of Motion

The structural equations of motions are derived using Lagrange's equations.[12] The equations are expressed in $\{x, y, \theta, \beta, \phi\}$ co-ordinates. The pitch angle β is given by external forces, e.g. a controller, hence no equation of motion is derived for this co-ordinate. The kinetic energy for the system is

DOI: 10.1002/we

Table I. Parameters based on mode shape expansion of first flapwise, first edgewise and first torsional modes of vibration for a turbine blade

Description	Parameter	Value
Mass per length of wing section	m	$50\,\mathrm{kg\,m^{-1}}$
Rotational inertia of wing section	I_{CG}	10 m kg
Density of air	ρ	$1{\cdot}2\,\mathrm{kg\,m^{-3}}$
Edgewise frequency	ω_x	$1{\cdot}7 \times 2\pi\,\mathrm{rad\,s^{-1}}$
Flapwise frequency	ω_y	$1{\cdot}1 \times 2\pi\,\mathrm{rad\,s^{-1}}$
Torsional frequency	ω_θ	$8 \times 2\pi\,\mathrm{rad\,s^{-1}}$
Edgewise damping	ζ_{x}	1%
Flapwise damping	ζ_y	1%
Torsional damping	ζ_θ	1%
Length of chord	c	1 m
Elastic axis from wing tip	l_{EA}	0·3 m
Centre of gravity behind elastic axis	l_{CG}	0·1 m
Aerodynamic centre ahead of elastic axis	l_{EA}	0·05 m
Aerofoil profile		NACA 63–415

$$
\begin{aligned}
T = {} & \tfrac{1}{2}L_{\mathrm{CG}}\left(\dot\theta+\dot\beta\right)^2 + \tfrac{1}{2}\,MR^2\dot\phi^2 \\
& + \tfrac{1}{2}m\left\{\dot x\cos(\beta) - \dot y\sin(\beta) + l_{\mathrm{CG}}\left(\dot\theta+\dot\beta\right)\sin(\theta+\beta) - \dot\beta[x\sin(\beta)+y\cos(\beta)] + R\dot\phi\right\}^2 \\
& + \tfrac{1}{2}m\left\{\dot y\cos(\beta) + \dot x\sin(\beta) - l_{\mathrm{CG}}\left(\dot\theta+\dot\beta\right)\cos(\theta+\beta) + \dot\beta[x\cos(\beta)-y\sin(\beta)]\right\}^2
\end{aligned}
$$

The potential energy of the system is

$$
V = \tfrac{1}{2}(\omega_x^2 m x^2 + \omega_y^2 m y^2 + \omega_\theta^2 I_{\mathrm{EA}}\theta^2)
$$

where $I_{\mathrm{EA}} = I_{\mathrm{CG}} + l_{\mathrm{CG}}^2 m$ is the moment of rotational inertia with respect to the elastic axis and $\omega_\theta = \sqrt{k_x/m}$, $\omega_y = \sqrt{k_y/m}$ and $\omega_\theta = \sqrt{k_\theta/I_{\mathrm{EA}}}$ are the natural angular frequencies for motion in the x and y directions and rotation respectively. Using Lagrange's equations, the equations of motion become

$$
\begin{aligned}
& \ddot x + 2\zeta_x\omega_x\dot x + \omega_x^2 x + R\ddot\phi\cos(\beta) + l_{\mathrm{CG}}\left(\ddot\theta+\ddot\beta\right)\sin(\theta) + l_{\mathrm{CG}}\left(\dot\theta+\dot\beta\right)^2\cos(\theta) \\
& \quad - \left(\ddot\beta y + 2\dot\beta\dot y + \dot\beta^2 x\right) = m^{-1}[L_{\mathrm{AC}}\sin(\psi+\beta) - D_{\mathrm{AC}}\cos(\psi+\beta)]
\end{aligned} \tag{1a}
$$

$$
\begin{aligned}
& \ddot y + 2\zeta_y\omega_y\dot y + \omega_y^2 y - R\ddot\phi\sin(\beta) - l_{\mathrm{CG}}\left(\ddot\theta+\ddot\beta\right)\cos(\theta) + l_{\mathrm{CG}}\left(\dot\theta+\dot\beta\right)^2\sin(\theta) \\
& \quad + \left(\ddot\beta x + 2\dot\beta\dot x + \dot\beta^2 y\right) = m^{-1}[L_{\mathrm{AC}}\cos(\psi+\beta) + D_{\mathrm{AC}}\sin(\psi+\beta)]
\end{aligned} \tag{1b}
$$

$$
\begin{aligned}
& \ddot\theta + 2\zeta_\theta\omega_\theta\dot\theta + \omega_\theta^2\theta + \ddot\beta + R\ddot\phi r_{\mathrm{EA}}^{-2}\sin(\theta+\beta) + r_{\mathrm{EA}}^{-2}\{\ddot x\sin(\theta) - \ddot y\cos(\theta) \\
& \quad + \dot\beta^2[y\cos(\theta) - x\sin(\theta)] - 2\dot\beta[\dot y\sin(\theta) + \dot x\cos(\theta)] - \ddot\beta[y\sin(\theta)+x\cos(\theta)]\} \\
& = I_{\mathrm{EA}}^{-1}[L_{\mathrm{AC}}l_{\mathrm{AC}}\cos(\alpha) + D_{\mathrm{AC}}l_{\mathrm{AC}}\sin(\alpha) + M_{\mathrm{AC}}]
\end{aligned} \tag{1c}
$$

$$
RM\ddot\phi - m(2\zeta_x\omega_x\dot x + \omega_x^2 x)\cos(\beta) + m(2\zeta_y\omega_y\dot y + \omega_y^2 y)\sin(\beta) = -F_{gen} = -\frac{P_0}{R\dot\phi} \tag{1d}
$$

The second terms in (1a)–(1c) are linear viscous damping terms added to describe the structural damping effects in the turbine blade. The damping ratios are $\zeta_x = d_x/(2\sqrt{k_x m})$, $\zeta_y = d_y/(2\sqrt{k_y m})$ and $\zeta_\theta = d_\theta/(2\sqrt{k_\theta I_{\mathrm{EA}}})$, and $r_{\mathrm{EA}} = \sqrt{I_{\mathrm{EA}}/(I_{\mathrm{CG}}m)}$ is the radius of gyration.

DOI: 10.1002/we

For use in stability analysis and control design the equations of motion (1) are linearized. This is done by assuming small oscillations around the equilibrium position of the section:

$$x(t) = x_0 + \varepsilon x_1(t), \quad y(t) = y_0 + \varepsilon y_1(t), \quad \theta(t) = \theta_0 + \varepsilon\theta_1(t)$$
$$\beta(t) = \beta_0 + \varepsilon\beta_1(t), \quad \phi(t) = \Omega_0 t + \varepsilon\phi_1(t) \tag{2}$$

where $(\,)_0$ denotes the equilibrium position, $(\,)_1$ denotes the small oscillations and $\varepsilon << 1$ is a bookkeeping parameter. The average rotor speed is denoted Ω_0, indicating that ϕ is in a steady state, not a static equilibrium. In control application, Ω_0 corresponds to the target rotor speed. The aerodynamic forces are also split into an average and an oscillating part:

$$L_{AC} = L_{AC,0} + \varepsilon L_{AC,1}, \quad D_{AC} = D_{AC,0} + \varepsilon D_{AC,1}, \quad M_{AC} = M_{AC,0} + \varepsilon M_{AC,1} \tag{3}$$

Inserting (2) and (3) in (1), using Taylor expansions assuming $\varepsilon << 1$ and balancing terms of order ε^0 leads to the structural equilibrium equations

$$m\omega_x^2 x_0 = L_{AC,0}\sin(\psi_0 + \beta_0) - D_{AC,0}\cos(\psi_0 + \beta_0) \tag{4a}$$
$$m\omega_y^2 y_0 = L_{AC,0}\cos(\psi_0 + \beta_0) + D_{AC,0}\sin(\psi_0 + \beta_0) \tag{4b}$$
$$I_{EA}\omega_\theta^2\theta_0 = L_{AC,0}l_{AC}\cos(\alpha_0) + D_{AC,0}l_{AC}\sin(\alpha_0) + cM_{AC,0} \tag{4c}$$
$$\frac{P_0}{R\Omega_0} = m\omega_x^2 x_0\cos(\beta_0) - m\omega_y^2 y_0\sin(\beta_0) \tag{4d}$$

Equations (4a)–(4c) give the equilibrium position $\{x_0, y_0, \theta_0\}$ of the section. Equation (4d) gives the constant effect P_0 corresponding to a given average rotation speed Ω_0. Balancing terms of order ε^1 leads to the linear approximations to the equations of motion

$$\begin{aligned}\ddot{x}_1 + 2\zeta_x\omega_x\dot{x}_1 + \omega_x^2 x_1 + R\ddot{\phi}_1\cos(\beta_0) + l_{CG}\left(\ddot{\theta}_1 + \ddot{\beta}_1\right)\sin(\theta_0) - \ddot{\beta}_1 y_0 \\ = m^{-1}[L_{AC,1}\sin(\psi_0 + \beta_0) - D_{AC,1}\cos(\psi_0 + \beta_0)] \\ + m^{-1}[L_{AC,0}(\psi_1 + \beta_1)\cos(\psi_0 + \beta_0) + D_{AC,0}(\psi_1 + \beta_1)\sin(\psi_0 + \beta_0)]\end{aligned} \tag{5a}$$

$$\begin{aligned}\ddot{y}_1 + 2\zeta_y\omega_y\dot{y}_1 + \omega_y^2 y_1 - R\ddot{\phi}_1\sin(\beta_0) - l_{CG}\left(\ddot{\theta}_1 + \ddot{\beta}_1\right)\cos(\theta_0) + \ddot{\beta}_1 x_0 \\ = m^{-1}[L_{AC,1}\cos(\psi_0 + \beta_0) + D_{AC,1}\sin(\psi_0 + \beta_0)] \\ + m^{-1}[-L_{AC,0}(\psi_1 + \beta_1)\sin(\psi_0 + \beta_0) + D_{AC,0}(\psi_1 + \beta_1)\cos(\psi_0 + \beta_0)]\end{aligned} \tag{5b}$$

$$\begin{aligned}\ddot{\theta}_1 + 2\zeta_\theta\omega_\theta\dot{\theta}_1 + \omega_\theta^2\theta_1 + \ddot{\beta}_1 + r_{EA}^{-2}R\ddot{\phi}_1 l_{CG}\sin(\theta_0 + \beta_0) \\ + r_{EA}^{-2}l_{CG}[\ddot{x}_1\sin(\theta_0) - \ddot{y}_1\cos(\theta_0)] - r_{EA}^{-2}\ddot{\beta}_1 l_{CG}[y_0\sin(\theta_0) + x_0\cos(\theta_0)] \\ = I_{EA}^{-1}[L_{AC,1}l_{AC}\cos(\alpha_0) + D_{AC,1}l_{AC}\sin(\alpha_0) + M_{AC,1}] \\ + I_{EA}^{-1}[-L_{AC,0}l_{AC}\alpha_1\sin(\alpha_0) + D_{AC,0}l_{AC}\alpha_1\cos(\alpha_0)]\end{aligned} \tag{5c}$$

$$\begin{aligned}RM\ddot{\phi}_1 - \frac{P_0}{R\Omega_0^2}\dot{\phi}_1 = 2m[\zeta_x\omega_x\dot{x}_1\cos(\beta_0) - \zeta_y\omega_y\dot{y}_1\sin(\beta_0)] \\ + m\omega_x^2[x_1\cos(\beta_0) - x_0\beta_1\sin(\beta_0)] - m\omega_y^2[y_1\sin(\beta_0) + y_0\beta_1\cos(\beta_0)]\end{aligned} \tag{5d}$$

It is seen that the choice of generator model $F_{gen} = P_0/(R\dot{\phi})$ leads to a negative linear damping term in the linear equation for the rotor speed ϕ_1.

DOI: 10.1002/we

Aerodynamic Model

The aerodynamic forces on the section are described by an unsteady aerodynamic state space model, suggested by Hansen *et al*.[11] The model is based on the Beddoes–Leishman dynamic stall model[13] and uses aerofoil data and time constants to compute the unsteady aerodynamic coefficients. Only a brief description of the model will be given here. The aerodynamic state equations are[11]

$$\dot{z}_1 + T_u^{-1}(b_1 + c\tfrac{\dot{U}}{2U^2})z_1 = b_1 A_1 T_u^{-1}\alpha_{3/4} \tag{6a}$$

$$\dot{z}_2 + T_u^{-1}(b_2 + c\tfrac{\dot{U}}{2U^2})z_2 = b_2 A_2 T_u^{-1}\alpha_{3/4} \tag{6b}$$

$$\dot{z}_3 + T_p^{-1} z_3 = T_p^{-1} C_{L,\alpha}(\alpha_E - \alpha^0) + \tfrac{T_u}{T_P}\tfrac{\pi}{U}\left[U\dot{\alpha} + \dot{U}\alpha - (l_{EA} - \tfrac{c}{2})\ddot{\alpha} - \ddot{y}\right] \tag{6c}$$

$$\dot{z}_4 + T_f^{-1} z_4 = T_f^{-1} f^{st}(z_3 / C_{L,\alpha} + \alpha^0) \tag{6d}$$

where the first two equations (z_1, z_2) are approximations to Theodorsen's function[7] describing the shed vorticity, the last two equations (z_3, z_4) describe the dynamics of the trailing edge separation point, having $z_4 = 1$ for fully attached flow and $z_4 = 0$ for fully separated flow, $T_u = (c/2U)$ is a normalized time constant, $T_p = 1{\cdot}7T_u$ and $T_f = 6T_u$ are time lags for the pressure and the boundary layer respectively and $b_1 = 0{\cdot}0455$, $b_2 = 0{\cdot}3$, $A_1 = 0{\cdot}165$ and $A_2 = 0{\cdot}335$ are time lags and magnitudes suggested by Jones.[14] The apparent wind speed is $U = U(t)$. The effective angle of attack is $\alpha_E = \alpha_{3/4}(1 - A_1 - A_2) + z_1 + z_2$, α^0 is the angle of attack where the static lift coefficient is zero, and $C_{L,\alpha}$ is the slope of the linear part of the static lift curve. The $f^{st}(\alpha)$ function describes the static trailing edge separation point.[11] The unsteady aerodynamic coefficients are[11]

$$C_L^{dyn} = C_{L,\alpha}(\alpha_E - \alpha^0)z_4 + C_L^{fs}(\alpha_E)(1 - z_4) + T_u\tfrac{\pi}{U}\left[U\dot{\alpha} + \dot{U}\alpha - (l_{EA} - \tfrac{c}{2})\ddot{\alpha} - \ddot{y}\right] \tag{7a}$$

$$C_D^{dyn} = C_D^{st}(\alpha_E) + (\alpha - \alpha_E)C_L^{dyn} + \tfrac{1}{2}\left[C_D^{st}(\alpha_E) - C_D^0\right]\left[\sqrt{f^{st}(\alpha_E)} - \sqrt{z_4} - f^{st}(\alpha_E) + z_4\right] \tag{7b}$$

$$C_M^{dyn} = C_M^{st}(\alpha_E) - \tfrac{\pi}{2U^2}\left\{(\tfrac{3c}{4} - l_{EA})(U\dot{\alpha} + \dot{U}\alpha) + (l_{EA} - \tfrac{c}{2})\ddot{y} + \left[\tfrac{1}{32} + (l_{EA} - \tfrac{c}{2})^2\right]\ddot{\alpha}\right\} \tag{7c}$$

where $C_D^0 = C_D^{st}(\alpha^0)$ is the static drag coefficient at the angle of attack with zero lift. The $C_L^{fs}(\alpha)$ function is the lift curve for fully separated flow.[11] The last terms in (7a) and (7c) are apparent mass terms. This formulation of the apparent mass includes more effects than Reference 11 but corresponds to References 7 and 8.

The aerodynamic model is linearized by splitting the aerodynamic states into a static and an oscillating part, i.e. $z_i(t) = z_{i,0} + \varepsilon z_{i,1}(t)$ for $i = \{1, 2, 3, 4\}$, Taylor expanding all non-linear terms, assuming $\varepsilon << 1$, and balancing terms of order ε^0 to get the equilibrium states[11]

$$z_{1,0} = A_1\alpha^0, \quad z_{2,0} = A_2\alpha^0, \quad z_{3,0} = C_{L,\alpha}(\alpha_0 - \alpha^0), \quad z_{4,0} = f^{st}(\alpha^0) \tag{8}$$

where α_0 is the static angle of attack, which is derived later. Balancing terms of order ε^1 gives the linear approximations

$$\begin{aligned}
\dot{z}_{1,1} + T_1^{-1} z_{1,1} &= A_1 T_1^{-1}\alpha_{3/4}^1 - \tfrac{A_1\alpha_0}{U_0}\dot{U}_1 \\
\dot{z}_{2,1} + T_2^{-1} z_{2,1} &= A_2 T_2^{-1}\alpha_{3/4}^1 - \tfrac{A_2\alpha_0}{U_0}\dot{U}_1 \\
\dot{z}_{3,1} + T_p^{-1} z_{3,1} &= T_p^{-1}\left(C_{L,\alpha}\alpha_E^1 + \tfrac{\pi}{2U_0^2}\left[U_0\dot{\alpha}_1 - \tfrac{1}{2}(2l_{CG} - c)\ddot{\alpha}_1 - \ddot{y}_1\right]\right) \\
\dot{z}_{4,1} + T_f^{-1} z_{4,1} &= T_f^{-1}\tfrac{df^{st}}{d\alpha}\Big|_{\alpha=\alpha_0}\tfrac{z_{3,1}}{C_{L,\alpha}}
\end{aligned} \tag{9}$$

where $T_1 = c/(2U_0 b_1)$ and $T_2 = c/(2U_0 b_2)$. The unsteady aerodynamic coefficients (7) are linearized by inserting $C_i^{dyn}(t) = C_i^{st}(\alpha_0) + \varepsilon C_{i,1}(t)$ for $i = \{L, D, M\}$, where C_i^{st} are the static aerodynamic coefficients, and the above expansions into (7), Taylor expanding, assuming $\varepsilon << 1$, and balancing terms of order ε^1. The linear approximations then become

DOI: 10.1002/we

$$
\begin{aligned}
C_{\mathrm{L},1} &= c_{\mathrm{l},\alpha}\alpha_{\mathrm{E},1} + c_{\mathrm{l,f}}z_{4,1} + \tfrac{\pi}{2U_0^2}[U_0\dot{\alpha}_1 - \tfrac{1}{2}(2l_{\mathrm{CG}} - c)\ddot{\alpha}_1 - \ddot{y}_1] \\
C_{\mathrm{D},1} &= c_{\mathrm{d},\alpha}\alpha_{\mathrm{E},1} + c_{\mathrm{d,f}}z_{4,1} + C_{\mathrm{L}}^0(\alpha_1 - \alpha_{\mathrm{E},1}) \\
C_{\mathrm{M},1} &= c_{\mathrm{m},\alpha}\alpha_{\mathrm{E},1} + c_{\mathrm{m,f}}z_{4,1} + \tfrac{-\pi}{2U_0^2}\left[\left(\tfrac{3c}{4} - l_{\mathrm{EA}}\right)(U_0\dot{\alpha}_1 + \dot{U}_1\alpha_0) + \left(l_{\mathrm{EA}} - \tfrac{c}{2}\right)\ddot{y}_1 + \tfrac{1}{4}\left[\tfrac{1}{8} + (2l_{\mathrm{EA}} - c)^2\right]\ddot{a}_1\right]
\end{aligned} \tag{10}
$$

where $c_{\mathrm{l},\alpha}$, $c_{\mathrm{d},\alpha}$, $c_{\mathrm{m},\alpha}$, $c_{\mathrm{l,f}}$, $c_{\mathrm{l,f}}$, and $c_{\mathrm{l,f}}$ hold terms from the Taylor expansions.

Relations between Structural Model and Aerodynamic Model

The aerodynamic model is coupled to the structural model through the angle of attack α and the apparent wind speed U partially induced by the motion of the section. The apparent wind speed U, the angle of attack α and the angle of attack at the three-quarter-chord point, $\alpha_{3/4}$, are given by

$$
\begin{aligned}
U &= \sqrt{[V_n - \dot{y}\cos(\beta) - \dot{x}\sin(\beta)]^2 + [V_t + R\dot{\phi} + \dot{x}\cos(\beta) - \dot{y}\sin(\beta)]^2} \\
\alpha &= \theta + \beta + \tan^{-1}\left(\frac{V_{\mathrm{n}} - \dot{y}\cos(\beta) - \dot{x}\sin(\beta)}{V_{\mathrm{t}} + R\dot{\phi} + \dot{x}\cos(\beta) - \dot{y}\sin(\beta)}\right) \\
\alpha_{3/4} &= \theta + \beta + \tan^{-1}\left(\frac{V_{\mathrm{n}} - \dot{y}\cos(\beta) - \dot{x}\sin(\beta) + (3/4\,c - l_{\mathrm{EA}})(\dot{\theta} + \dot{\beta})\cos(\theta - \beta)}{V_{\mathrm{t}} + R\dot{\phi} + \dot{x}\cos(\beta) - \dot{y}\sin(\beta) + (3/4\,c - l_{\mathrm{EA}})(\dot{\theta} + \dot{\beta})\sin(\theta - \beta)}\right)
\end{aligned} \tag{11}
$$

where $V_{\mathrm{n}} = V_{\mathrm{n}}(t)$ and $V_{\mathrm{t}} = V_{\mathrm{t}}(t)$ are the free wind normal to the rotor plane and the wind changes in the rotor plane caused by turbulence respectively.

Equations (11) are linearized by inserting (2), $V_{\mathrm{n}}(t) = V_{\mathrm{n},0} + \varepsilon V_{\mathrm{n},1}(t)$ and $V_{\mathrm{t}}(t) = \varepsilon V_{\mathrm{t},1}(t)$ and Taylor expanding non-linear terms. Balancing terms of order ε^0 leads to the static expressions

$$
U_0 = \sqrt{V_{\mathrm{n},0}^2 + R\Omega_0^2}, \quad \alpha_0 = \alpha_{3/4,0} = \theta_0 + \beta_0 + \tan^{-1}\left(\tfrac{V_{\mathrm{n},0}}{R\Omega_0}\right) \tag{12}
$$

Balancing terms of order ε^1 leads to the linear approximations

$$
\begin{aligned}
U_1 &= \frac{R\Omega_0[V_{\mathrm{t},1} + R\dot{\phi}_1 + \dot{x}_1\cos(\beta_0) - \dot{y}_1\sin(\beta_0)] + V_{\mathrm{n},0}[V_{\mathrm{n},1} - \dot{y}_1\cos(\beta_0) - \dot{x}_1\sin(\beta_0)]}{U_0} \\
\alpha_1 &= \theta_1 + \beta_1 + \frac{R\Omega_0[V_{\mathrm{n},1} - \dot{y}_1\cos(\beta_0) - \dot{x}_1\sin(\beta_0)] - V_{\mathrm{n},0}[V_{\mathrm{t},1} + R\dot{\phi}_1 + \dot{x}_1\cos(\beta_0) - \dot{y}_1\sin(\beta_0)]}{U_0^2} \\
\alpha_{3/4,1} &= \alpha_1 + (\dot{\theta}_1 + \dot{\beta}_1)\left(\tfrac{3c}{4} - l_{\mathrm{EA}}\right)\frac{R\Omega_0\cos(\theta_0 + \beta_0) - V_{\mathrm{n},0}\sin(\theta_0 + \beta_0)}{U_0^2}
\end{aligned} \tag{13}
$$

The structural model is coupled to the aerodynamic model through the aerodynamic forces

$$
L_{\mathrm{AC}} = \tfrac{1}{2}\rho c U^2 C_{\mathrm{L}}^{\mathrm{dyn}}, \quad D_{\mathrm{AC}} = \tfrac{1}{2}\rho c U^2 C_{\mathrm{D}}^{\mathrm{dyn}}, \quad M_{\mathrm{AC}} = \tfrac{1}{2}\rho c^2 U^2 C_{\mathrm{M}}^{\mathrm{dyn}} \tag{14}
$$

ρ is the density of air.

The static parts of the aerodynamic forces are given by

$$
L_{\mathrm{AC},0} = \tfrac{\rho c U_0^2}{2} C_{\mathrm{L}}^{\mathrm{st}}(\alpha_0), \quad D_{\mathrm{AC},0} = \tfrac{\rho c U_0^2}{2} C_{\mathrm{D}}^{\mathrm{st}}(\alpha_0), \quad M_{\mathrm{AC},0} = \tfrac{\rho c^2 U_0^2}{2} C_{\mathrm{M}}^{\mathrm{st}}(\alpha_0) \tag{15}
$$

The linear approximations to the oscillating aerodynamic forces are given by

$$
\begin{aligned}
L_{\mathrm{AC},1} &= \tfrac{\rho c}{2}[U_0^2 C_{\mathrm{L},1} + 2U_0 U_1 C_{\mathrm{L}}^{\mathrm{st}}(\alpha_0)] \\
D_{\mathrm{AC},1} &= \tfrac{\rho c}{2}[U_0^2 C_{\mathrm{D},1} + 2U_0 U_1 C_{\mathrm{D}}^{\mathrm{st}}(\alpha_0)] \\
M_{\mathrm{AC},1} &= \tfrac{\rho c^2}{2}[U_0^2 C_{\mathrm{M},1} + 2U_0 U_1 C_{\mathrm{M}}^{\mathrm{st}}(\alpha_0)]
\end{aligned} \tag{16}
$$

Aeroelastic Model

The aeroelastic model does not include the variation in the rotor speed or a controller, hence $\dot{\phi} \equiv \Omega_0$, $\beta \equiv \beta_0$ and $\dot{\beta} \equiv 0$.

DOI: 10.1002/we

The non-linear aeroelastic model is a combination of the structural equations (1a)–(1c) and the aerodynamic equations (6) and (7) connected by (11) and (14).

The linearized aeroelastic model is a combination of the linear structural equations (5a)–(5c) and the linear aerodynamic equations (9) and (10) connected by (11)–(16). The linear aeroelastic model can be stated as

$$\dot{\boldsymbol{\varphi}} = A\boldsymbol{\varphi} \tag{17}$$

where $\boldsymbol{\varphi} = \{x_1, y_1, \theta_1, z_{1,1}, z_{2,1}, z_{3,1}, z_{4,1}, \dot{x}_1, \dot{y}_1, \dot{\theta}_1\}^{\mathrm{T}}$ is the linear state vector and A holds the coefficients from (5a)–(5c), (9), (10) and (11)–(16), setting $\beta = \beta_0$, $\ddot{\beta} = \dot{\beta} = 0$, $\ddot{\phi} = 0$ and $\dot{\phi} = \Omega_0$.

Pitch Actuator

Most wind turbines today have controllable blade pitch angle; a controller requests a pitch angle and an electric or hydraulic pitch actuator adjusts the actual blade pitch angle. In this work the pitch actuator is described by the second-order model

$$I_\beta \ddot{\beta} + d_\beta \ddot{\beta} = k_\beta(\beta_{\mathrm{ref}} - \beta) \tag{18}$$

where $I_\beta = 0{\cdot}044$, $d_\beta = 1{\cdot}33$ and $k_\beta = 20$ are the moment of inertia, damping and stiffness fitted to give a response similar to a wind turbine pitch actuator and β_{ref} is the pitch angle requested by the controller. The non-linear implementation of the pitch actuator model includes dead-band, maximum pitch angle, maximum pitch rate and maximum pitch acceleration. The dead-band is introduced to prevent the pitch actuator from working continually, adjusting to negligible changes in pitch angle request. The maxima of pitch angle, pitch rate and pitch acceleration are introduced to describe the finite power and flexibility of the pitch actuator.

Aeroservoelastic Model

The aeroservoelastic model includes the rotor speed variable ϕ, allowing for the design of a rotor speed controller. The non-linear aeroservoelastic model is a combination of the structural equations (1) and the aerodynamic equations (6) and (7) connected by (11) and (14) and the pitch actuator equation (18).

The linear version of the aeroservoelastic model is a combination of the linear structural equations (5) and the linear aerodynamic equations (9) and (10) connected by (11)–(16) and the pitch actuator equation (18). The linear aeroservoelastic model can be stated as

$$\dot{\tilde{\boldsymbol{\varphi}}} = \tilde{A}\tilde{\boldsymbol{\varphi}} + \mathrm{b}\beta_{\mathrm{ref}} \tag{19}$$

where $\tilde{\boldsymbol{\varphi}} = \{x_1, y_1, \theta_1, \phi_1, \beta_1, z_{1,1}, z_{2,1}, z_{3,1}, z_{4,1}, \dot{x}_1, \dot{y}_1, \dot{\theta}_1, \dot{\phi}_1, \dot{\beta}_1\}^{\mathrm{T}}$ is the linear state vector, β_{ref} is the pitch angle requested by the controller and $\tilde{\mathbf{A}}$ and b hold the coefficients from (5), (9), (10), (11)–(16) and (18).

Time Simulations of Aeroservoelastic Model

The non-linear equations (1), (6), (7) and (18) are implemented in a SIMULINK® environment together with the controllers designed in the aeroservoelastic analysis. This simulation platform is used to evaluate the performance of the designed controllers. The performance of the controllers is evaluated by simulating the response of the sections to a turbulent inflow.

Aeroelastic Stability Analysis

This section deals with the stability of the equilibrium states (4a)–(4c) and (8) based on eigenvalue analysis of (17). The results show that the aeroelastic system is capable of predicting both classical flutter and stall-induced vibrations. First a test of the model is done by comparing its stability boundaries with the work of Theodorsen and Garrick (referred to simply as 'Theodorsen' hereafter).[8] Next the influence of the aerodynamic model on the structural stability properties is analysed. Finally, stability and aeroelastic modes of the aeroelastic system versus wind speed are discussed for two different angles of attack.

DOI: 10.1002/we

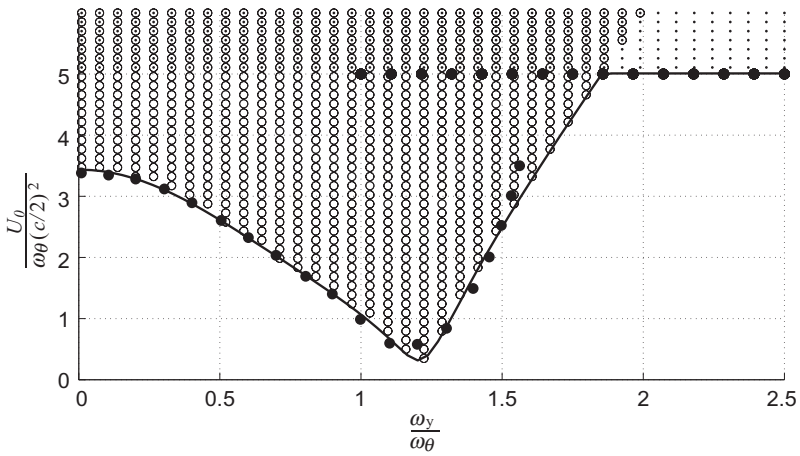

Figure 2. Stability properties for the equilibrium position of the blade section as a function of apparent wind speed and ratio between flapwise and torsional natural frequencies. The white areas are stable regions and the areas with '○', '•' or both are unstable regions. The '○' denote flutter instability and the '•' denote divergence instability. The full line marks the stability boundaries found with the present model and the '●' denote Theodorsen's results

Comparing with Theodorsen

Figure 2 shows the normalized velocity $U_0/(\omega_\theta(c/2)^2)$ where the wing section loses stability versus the ratio between flapwise and torsional natural frequencies, ω_y/ω_θ. The stability boundaries from both Theodorsen and the present work are shown. The parameters used in this experiment are similar to Theodorsen's parameters for this particular example; the static lift coefficient is set to the theoretical value 2π and the static drag and moment coefficients are set to zero.

The equilibrium is assumed unstable at a given apparent wind speed if one eigenvalue has a positive real part. If the eigenvalue is real and positive, the solution is exponentially growing (divergence). If the eigenvalue is complex with a positive real part, the linear solution is oscillating with exponentially growing amplitude (classical flutter).

The agreement between the two results is seen to be good, especially for $\omega_y/\omega_\theta < 1$ and for the divergence boundaries. The divergence limit is supposed to agree perfectly with Theodorsen's results, because it is determined by the linear relation between the aerodynamic forces and the stiffness of the section support.

Structural, Aerodynamic and Aeroelastic Behaviour

This subsection deals with the aerodynamic force influence on the stability of the section. This is done by looking at the eigenvalues of the aeroelastic system.

Figure 3(a) shows the eigenvalues of the structural model and of the aeroelastic system. The structural model has three pairs of complex conjugate eigenvalues describing the edgewise, flapwise and torsional motion of the section. The real part of these eigenvalues is slightly negative, corresponding to the structural damping ζ_x, ζ_y and ζ_θ. The imaginary part of the structural eigenvalues corresponds to the resonance frequency for the edgewise (~1·7 Hz), flapwise (~1·1 Hz) and torsional (~8 Hz) modes of vibration. The aeroelastic system has four eigenvalues more than the structural model, corresponding to the four aerodynamic states, all heavily damped compared with the structural eigenvalues. The two pairs of complex conjugate eigenvalues describing the edgewise (~1·7 Hz) and torsional (~8 Hz) modes are seen to be only little affected by the inclusion of the aerodynamic forces. The real part of the pair of complex conjugate eigenvalues describing the flapwise (~1·1 Hz) mode is seen to be drawn into the negative complex plane by the inclusion of the aerodynamic forces, corresponding to increased flapwise damping.

DOI: 10.1002/we

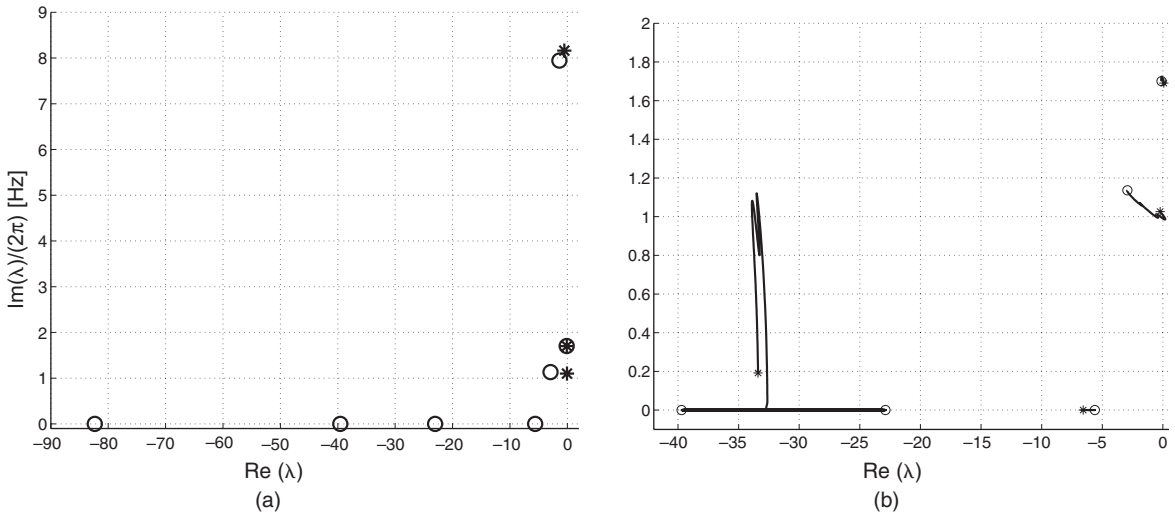

Figure 3. (a) Eigenvalues λ for the structural (*) and aeroelastic (○) models plotted in the complex plane. Exploiting the symmetry, only the upper half-plane is shown. The parameters are as given in Table I with $U_0 = 70\,m\,s^{-1}$ and $\alpha = 2°$. (b) Root locus showing the most sensitive aeroelastic eigenvalues as the angle of attack changes from $\alpha = 2°$ (○) to $\alpha = 19°$ (*)

The effect of the angle of attack on the aeroelastic behaviour of the section is examined by monitoring the eigenvalues for different angles of attack. Figure 3(b) shows the aeroelastic eigenvalues as a function of angle of attack. It is seen that, as the angle of attack increases, two of the aerodynamic eigenvalues approach each other on the real axis, collide and move into the complex plane. The interpretation of this is that the trailing edge separation point begins to oscillate when the section goes into stall.

Influence of Apparent Wind Speed

This subsection deals with the behaviour of the section in response to different apparent wind speeds U_0.

Figure 4 shows the aeroelastic eigenvalues and the contents of flapwise, edgewise and torsional motion in the corresponding eigenvectors as a function of apparent wind speed U_0 at two different angles of attack, 2° and 19°. The figures are zoomed in on the the less damped structural eigenvalues, because the aeroelastic eigenvalues are heavily damped.

In the case $\alpha = 2°$ (Figure 4(a)) the airflow around the section is fully attached. The eigenvalue marked by I is dominated by edgewise (x) motion; it has a small aerodynamic damping because the coupling between this structural mode and the aerodynamic forces is small. The eigenvalue marked by II is primarily a flapwise (y) mode which is aerodynamically damped. The eigenvalue marked by III is primarily a torsional (θ) mode for low air speeds but a combined torsional and flapwise mode for higher air speeds. The section is unstable for air speeds above $U_0 = 175\,m\,s^{-1}$. This instability (combined torsional and flapwise motion) is known as classical flutter, where the flutter mode changes from well damped to highly unstable within a relatively small increase in air speed.

In the case $\alpha = 19°$ (Figure 4(b)) the section is in the stall region. The mode corresponding to the eigenvalue marked by I is dominated by edgewise motion at low air speeds, but flapwise motion increases with increasing air speed. The mode is seen to be unstable for air speeds above $U_0 = 40\,m\,s^{-1}$. This instability (combining edgewise and flapwise motion) is known as stall-induced vibration (or stall flutter). The onset of this instability is strongly affected by the structural damping, and the instability can be removed by adding a realizable amount of damping.[15] The eigenvalues marked by II and III are dominated by flapwise (y) and torsional motion respectively. The edgewise (x) and flapwise (y) components of mode III increase with increasing air

DOI: 10.1002/we

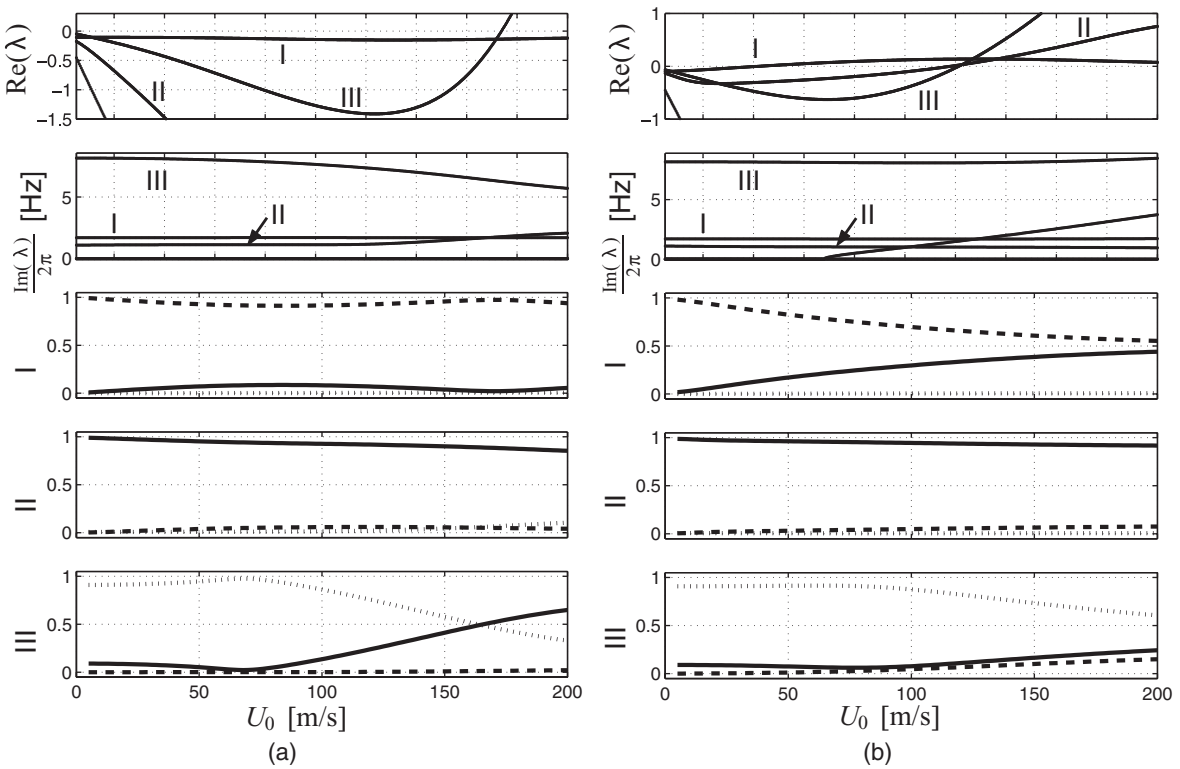

Figure 4. Behaviour of the eigenvalues λ and the corresponding normalized eigenvectors of the aeroelastic system (17) versus apparent air speed U_0 for angles of attack (a) $\alpha = 2°$ and (b) $\alpha = 19°$. The broken, full and dotted lines represent the x, y and θ components of the eigenvectors respectively

speed and become unstable for air speeds above $U_0 = 122\,\mathrm{m\,s^{-1}}$. Because this instability occurs at much higher air speeds than the stall flutter instability discussed above, it does not affect the operational limit for the section.

Figure 4(b) shows that above $U_0 = 68\,\mathrm{m\,s^{-1}}$ there are four eigenvalues with an imaginary part. Three of them are identified as structural modes of vibration. The last one represents oscillations at the trailing edge separation point, also discussed in relation to Figure 3(b).

Aeroservoelastic Analysis

In this section the aeroservoelastic model is used to design and analyse three different feedback controllers: one PID controller and two full-state feedback controllers. The scope of this section is to analyse how control affects the turbine blade; it is not an analysis of an operational wind turbine controller.

Control Objectives

This study will be limited to operations where the generator produces constant effect P_0 and the purpose of the pitch controller is to limit the energy extracted from the wind and to keep the rotor speed constant at $\dot{\phi} \approx \Omega_0$. Aside from the purpose of power regulation the pitch controller can also be used to reduce the fatigue loads of the wind turbine, i.e. to minimize the amplitude of the vibrations of a section of the turbine structure, such as blade or tower vibration. The present model only describes the turbine blade; hence only fatigue loads on the blades are discussed. An operational wind turbine controller has to take tower vibrations into account as

DOI: 10.1002/we

well, but this model is for qualitative analysis of control strategies, not for design of controllers to be implemented on wind turbines in operation.

Measures of Control Performance

To design and evaluate wind turbine controllers at rated power, the control objectives and the cost of using control are quantified by measures for the rotor speed error, the fatigue loads on the blade and the pitch activity. The rotor speed control performance can be measured by the RMS value of the rotor speed error:

$$\mathrm{RMS}(\Delta\phi) = \frac{1}{t}\sqrt{\int_0^t \Delta\phi^2 \mathrm{d}t}, \quad \Delta\phi = \dot{\phi}(t) - \Omega_0 \tag{20}$$

The fatigue load on the blade can be quantified by the RMS value of flapwise, edgewise and torsional velocities:

$$\mathrm{RMS}(\dot{x}, \dot{y}, \dot{\theta}) = \frac{1}{t}\sqrt{\int_0^t \Delta(\dot{x}, \dot{y}, \dot{\theta})^2 \mathrm{d}t} \tag{21}$$

giving a measure on the oscillations of the blade in the different directions. The cost of using control is measured by the actuator duty

$$\mathrm{AD} = \frac{1}{t}\int_0^t |\dot{\beta}| \mathrm{d}t \tag{22}$$

counting the total number of degrees pitched per time unit. These measures are just some of many ways to quantify control performance.

Controller Strategies

Most wind turbines today are controlled by a series of PID controllers. PID controllers are single-input, single-output (SISO) systems. The particular PID controller implemented here uses the rotor speed error $\Delta\phi$ to construct the control signal

$$\beta_{\mathrm{ref}} = K_{\mathrm{P}}\Delta\phi + K_{\mathrm{I}}\int_0^t \Delta\phi \mathrm{d}t + K_{\mathrm{D}}\frac{\mathrm{d}\Delta\phi}{\mathrm{d}t} \tag{23}$$

where K_{P} is a proportional gain, K_{I} is an integral gain and K_{D} is a derivative gain, all to be tuned to optimize control performance. One of the main advantages of a PID controller is its simplicity and robustness; only little knowledge about the controlled system is needed to design a robust PID controller. One of the disadvantages of the PID controller is that it is a SISO controller. Full-state feedback controllers are generic multiple-input, multiple-output (MIMO) systems, using all states in a linear model of the controlled system to construct an arbitrary number of control outputs. The full-state feedback controller implemented here belongs to the set of linear–quadratic (LQ) controllers. LQ controllers are based on a linear model of the controlled system, and the feedback gains are determined by a linear–quadratic optimization algorithm. The particular controller implemented here only has one control output, β_{ref}, leading to

$$\beta_{\mathrm{ref}} = \mathbf{K}_{\mathrm{LQR}} T\tilde{\boldsymbol{\varphi}} \tag{24}$$

where $K_{\mathrm{LQR}} = \{k_1, k_2, \ldots, k_{14}\}^{\mathrm{T}}$ is the gain matrix containing the linear weights on the state variable $\tilde{\boldsymbol{\varphi}}$.

Equation (24) suggests that all states are measurable; the controller is then called a linear–quadratic regulator (LQR). In most real systems, not all states in the linear model will be measurable. If this is the case, the non-measurable states are constructed using a state estimator, e.g. a Kalman filter.[1] A system where all states are measurable always leads to superior control performance compared with a system using a state estimator for some of the states; hence LQR controllers can be seen as an upper bound for the performance of any LQ type of controller. When designing LQ controllers, the gain matrix $\mathbf{K}_{\mathrm{LQR}}$ is chosen such that a quadratic cost function, evaluated on the linearized system (19), is minimized.[16] The linear–quadratic cost function is

$$J = \int_0^\infty (\tilde{\boldsymbol{\varphi}}^T Q\tilde{\boldsymbol{\varphi}} + \omega\beta_{\mathrm{ref}}^2)\mathrm{d}t \tag{25}$$

DOI: 10.1002/we

where the scalar control output β_{ref} is given by (24), $\mathbf{Q}$ is a weight matrix determining the importance of reducing errors in the particular states and ω is a weight on the pitch activity. The objectives for the controller are quantified in the weights $\mathbf{Q}$ and ω. The optimization problem (25) leads to the algebraic Riccati equation[16]

$$\tilde{\mathbf{A}}^{\mathrm{T}}\mathbf{S} + \mathbf{S}\tilde{\mathbf{A}} - \mathbf{S}\mathbf{b}\omega^{-1}\mathbf{b}^{\mathrm{T}}\mathbf{S} + \mathbf{Q} = 0 \tag{26}$$

which is solved for $\mathbf{S}$. The gain matrix is then given by

$$\mathbf{K}_{\mathrm{LQR}} = \omega^{-1}\mathbf{b}^{\mathrm{T}}\mathbf{S} \tag{27}$$

Both (26) and (27) are solved using standard MATLAB® tools.

Control Design

All controllers are designed to have the same RMS($\Delta\phi$) value, making it possible to compare the actuator activity AD and the effect on fatigue loads, RMS($\dot{x}$, $\dot{y}$, $\dot{\theta}$).

PID Controller

The PID controller is designed using an optimization algorithm which minimizes the actuator activity AD at a given rotor speed error RMS($\Delta\phi$). The optimization algorithm uses the linearized aeroservoelastic model to evaluate the response to a turbulent inflow. The optimization leads to the following PID gains: {1·1, 0·94, 0·15}.

LQR Controller

Two different LQR controllers are designed, one minimizing only the rotor speed error RMS($\Delta\phi$) and one minimizing the rotor speed error RMS($\Delta\phi$) and flapwise RMS($\dot{y}$) and edgewise RMS($\dot{x}$) motions. The weight matrix for the first LQR controller (LQR_1) is $\mathbf{Q}$ = diag({0, 0, 0, 1, 0, 0, 0, 0, 0, 0, 0, 0, 1, 0}) with penalties only on the ϕ and $\dot{\phi}$ states. The weight $w = 16{\cdot}67$ on the control activity is chosen to fit the RMS($\Delta\phi$) value. The weight matrix for the second LQR controller (LQR_2) is $\mathbf{Q}$ = diag({0·5, 0·5, 0, 1, 0, 0, 0, 0, 0, 0, 0, 0, 1, 0}) with penalties on both the ϕ and $\dot{\phi}$ states and the flapwise y and edgewise x states. The control activity weight is $\omega = 2{\cdot}5$. The steady states are subtracted from the feedback signals used in the LQR controllers. For the rotor speed the steady state value is the target rotor speed Ω_0 and for the velocity states $\dot{x}$, $\dot{y}$ and $\dot{\theta}$ it is zero. The steady state values for the aerodynamic states $z_{1,2,3,4}$ are computed using (8) at the average wind speed. The steady state positions of x, y and θ are tracked by filtering the measured time-varying signal through a second-order lowpass filter, with centre frequencies at half the natural frequency for the three directions.

Control Performance

The controller performances are evaluated by 100 s long time simulations of the non-linear equations (1), (6), (7) and (18). The wing section is exposed to a turbulent wind generated by TurbSim[17] using a Von Karman wind turbulence model with a turbulence intensity of 19% and a mean wind speed of 10 m s^{-1}. Figure 5(a) shows a zoom on the series of normal V_n and tangential V_t wind components used in the simulations.

Figure 5(b) shows a zoom on the rotor speed. Even when the rotor speed does not look to be similar for the PID controller and the two LQR controllers, RMS($\Delta\phi$) is the same for all simulations, as seen in Table II. Figure 5(c) shows a zoom on the pitch activity. It is seen that the LQR controllers have less amplitude on the 10 s time scale oscillations compared with the PID controller, resulting in less pitch activity. Table II shows that the AD measure for the LQR_1 controller is 44% smaller than the AD for the PID controller. The LQR_2 controller also has less amplitude than the PID controller on the 10 s time scale, but it has a lot of activity on the 1 s time scale, increasing the pitch activity. The pitch activity on the 1 s time scale is a result of the feedback of the flapwise and edgewise motions of the wing section. Table II shows that the AD measure for the LQR_2 controller is 2·3 times higher than the AD for the PID controller. Figure 5(d) shows a zoom on the flapwise motion. It is seen that both LQR controllers have less flapwise activity than the PID controller; in particular,

DOI: 10.1002/we

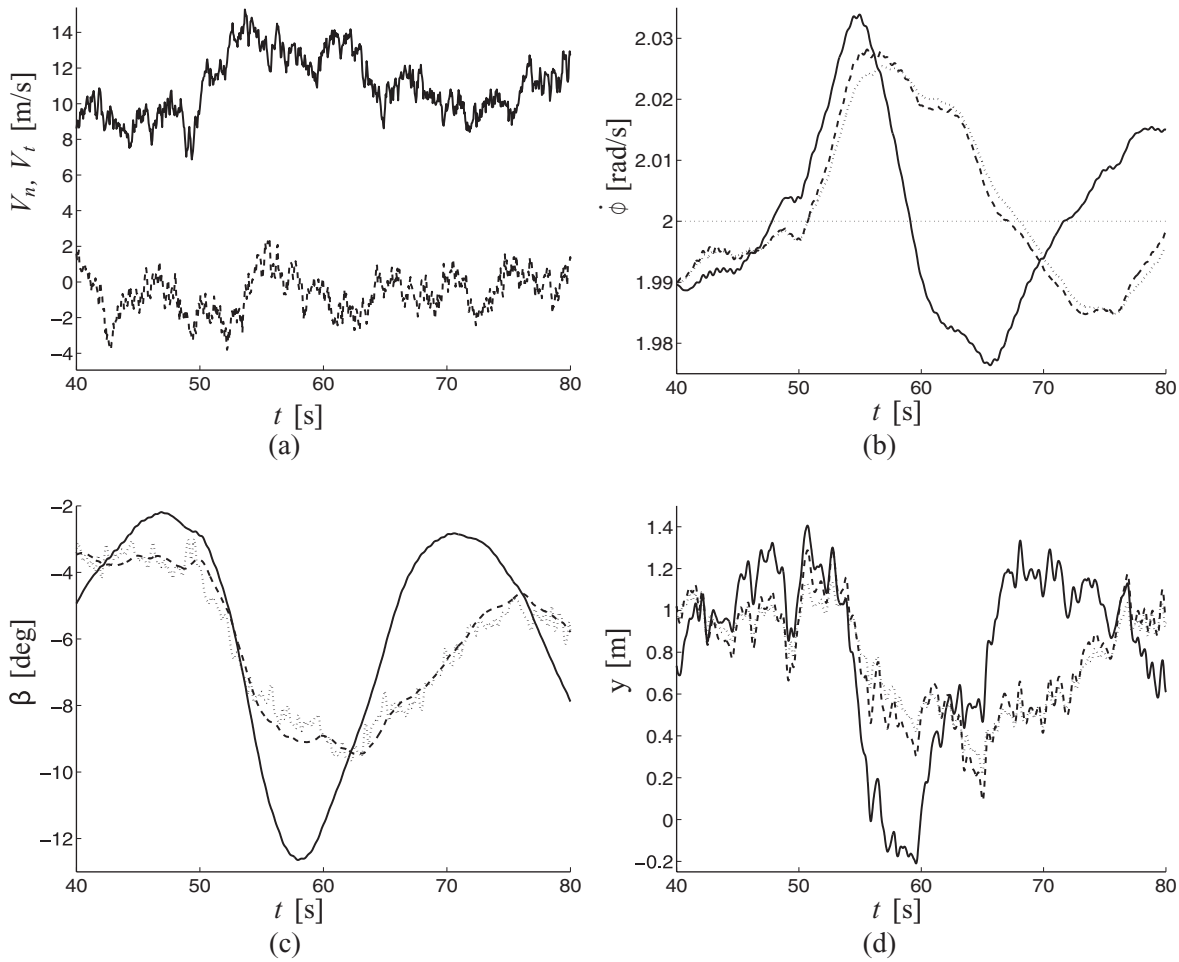

Figure 5. A zoom on the results from time simulations of the non-linear model exposed to turbulent inflow. (a) Turbulent inflow. The full line is the wind normal to the rotor plane and the broken line is the wind tangential to the rotor plane. (b) Rotor speed. (c) Pitch angle. (d) Flapwise displacement. The full lines are the results from the PID controller, the broken lines are the results from the LQR_1 controller and the dotted lines are the results from the LQR_2 controller

Table II. Control results

Controller	RMS($\Delta\phi$)	AD	RMS($\dot{x}$)	RMS($\dot{y}$)	RMS($\dot{\theta}$)
PID	0·012	0·56	0·11	0·37	0·023
LQR_1	0·012	0·31	0·13	0·36	0·023
LQR_2	0·012	1·31	0·042	0·27	0·030
With dead-band					
PID	0·014	0·59	0·12	0·38	0·023
LQR_1	0·013	0·27	0·13	0·36	0·023
LQR_2	0·012	1·11	0·026	0·30	0·031
With dead-band and limits on actuator acceleration and speed					
PID	0·014	0·59	0·12	0·38	0·023
LQR_1	0·013	0·27	0·13	0·36	0·018
LQR_2	0·012	1·28	0·16	0·47	0·018

DOI: 10.1002/we

the LQR_2 controller results in a smoother flapwise behaviour than the other two controllers. This is as expected, because the LQR_2 controller has reduction of flapwise motion as an explicit control objective. Table II shows that the measure of flapwise motion is approximatively the same for the LQR_1 and PID controllers but 25% less for the LQR_2 controller.

Table II shows the effect of including a dead-band and limits on the speed and acceleration of the pitch actuator. The dead-band is $\pm 0{\cdot}2°$, the maximum actuator speed is $\pm 10\,\mathrm{deg\,s^{-1}}$ and the maximum acceleration is $\pm 8\,\mathrm{deg\,s^{-2}}$. Table II shows that the pitch activity increases for the PID controller when the dead-band is introduced. This is because the controller loses the effect of the small-amplitude control action and instead uses larger control action, resulting in an increase in control action. Both LQR controllers have a reduction in pitch activity of approximately 15% when the dead-band is introduced. The flapwise and torsional motions are almost unaffected by the dead-band, while the measure of edgewise motion is reduced for the LQR_2 controller. The introduction of limits on the speed and acceleration of the pitch actuator does not affect the performance of the PID and the LQR_1 controllers, because these controllers do not break the introduced limits. The LQR_2 controller is strongly affected by the introduction of the limits, because this controller relies on unrealistically high accelerations of the pitch angle.

Conclusion

This work provides a low-order mathematical model of a blade section suitable for qualitative analysis of blade fatigue loads and control strategies for reduction of them. The model is not intended as a design tool for designing wind turbine controllers, but as a tool to gain knowledge about the interaction between blade and imposed control action.

The model is used for stability analysis, where it is shown that the model is capable of predicting both classical flutter and stall-induced vibrations. It is found that the section can go into classical flutter (combined torsional and flapwise vibrations) even when the section is in the stall region, with negative slope on the static lift curve.

Two LQR full-state feedback controllers are designed and compared with a PID controller. The PID controller and one of the LQR controllers are designed to minimize control activity at a given rotor speed error. The other LQR controller is designed to minimize both flapwise and edgewise motions and control activity at a given rotor speed error. For this set-up the LQR controllers perform slightly better than the PID controller, resulting in less control activity and lower fatigue loads. The inclusion of a dead-band leads to a small reduction in control activity for the LQR controllers but a small increase in control activity for the PID controller. The inclusions of limits on pitch acceleration and rate has no influence on the PID controller and the LQR controller designed for minimizing control activity. The LQR controller designed for reducing flapwise and edgewise motions and control activity is strongly affected by the limits on pitch acceleration and rate, because it relies on unrealistic pitch response.

Acknowledgements

The author thanks Morten Hartvig Hansen, Risø National Laboratory for his inspiring ideas and helpful discussions related to this work. This work is partly funded by the Technical University of Denmark and Risø National Laboratory.

References

1. Skogestad S, Postlethwaite I. *Multivariable Feedback Control: Analysis and Design.* Wiley: Chichester, 1996.
2. Johnson CD. Theory of disturbance-accommodating controllers. *Advances in Control and Dynamic Systems* 1976; **12**: 387–489.

DOI: 10.1002/we

3. Bossanyi EA. Wind turbine control for load reduction. *Wind Energy* 2003; **6**: 229–244.
4. Kendall L, Balas MJ, Lee YJ, Fingersh LJ. Application of proportional-integral and disturbance accommodating control to variable speed variable pitch horizontal axis wind turbines. *Wind Engineering* 1997; **21**: 21–38.
5. Stol KA. Disturbance tracking control and blade load mitigation for variable-speed wind turbines. *Journal of Solar Energy Engineering, Transactions of the ASME* 2003; **125**: 396–401.
6. Ekelund TT. Yaw control for reduction of structural dynamic loads in wind turbines. *Journal of Wind Engineering and Industrial Aerodynamics* 2000; **85**: 241–262.
7. Thoedorsen T. General theory of aerodynamic instability and the mechanism of flutter. *NACA Report* 496, 1935.
8. Theodorsen T, Garrick IE. Mechanism of flutter, a theoretical and experimental investigation of the flutter problem. *NACA Report* 685, 1940.
9. Block JJ, Strganac TW. Applied active control for a nonlinear aeroelastic structure. *Journal of Guidance, Control, and Dynamics* 1998; **21**: 838–845.
10. Chaviaropoulos PK, Soerensen NN, Hansen MOL, Nikolaou IG, Aggelis KA, Johansen J, Gaunaa M, Hambraus T, von Geyr HF, Hirsch C, Shun K, Voutsinas SG, Tzabiras G, Perivolaris Y, Dyrmose SZ. Viscous and aeroelastic effects on wind turbine blades. The Viscel project. Part II: Aeroelastic stability investigations. *Wind Energy* 2003; **6**: 387–404.
11. Hansen MH, Gaunaa M, Madsen HA. A Beddoes–Leishman type dynamic stall model in state-space and indicial formulation. *Technical Report Risø-R-1354(EN)*, Risø National Laboratory, Roskilde, 2004.
12. Thomsen JJ. *Vibrations and Stability: Advanced Theory, Analysis, and Tools.* Springer: New York, NY, 2003.
13. Leishman JG, Beddoes TS. A semi-empirical model for dynamic stall. *Journal of the American Helicopter Society* 1989; **34**: 3–17.
14. Jones RT. The unsteady lift of a wing of finite aspect ratio. *NACA Report 681*, 1940.
15. Chaviaropoulos P, Politis ES, Sørensen NN, Hansen M, Bulder BH, Winkelaar D, Saravanos DA, Philippidis T, Galiotis C, Hansen MOL, Kossivas T. Recent advances on damped wind turbine rotor blades, the Dampblade project. *European Wind Energy Conference*, Madrid, 2003.
16. Kwakernaak H, Sivan R. *Linear Optimal Control Systems.* Wiley: New York, NY, 1972.
17. Kelley N, Jonkman B. *TurbSim; NWTC Design Codes* [Online]. The National Wind Technology Center, USA. Available: http://wind.nrel.gov/designcodes/preprocessors/turbsim/. (Accessed 23 January 2006)

DOI: 10.1002/we

P2

(Conference Article)

Equations of Motion for a Rotor Blade, Including Gravity and Pitch Action

European Wind Energy Conference, Athens, Greece, 27 February - 2 March, 2006

Equations of Motion for a Rotor Blade, Including Gravity and Pitch Action

B. S. Kallesøe, Department of Mechanical Engineering, Technical University of Denmark, Nils Koppels Allé, Building 404, DK-2800 Lyngby, Denmark. E-mail: bsk@mek.dtu.dk

A new set of partial differential equations of motion for a wind turbine blade are derived. The equations includes the effects from gravity, pitch action, and varying rotor speed. The physical interpretation of the individual terms in the equations are discussed. The partial differential equations are transformed into approximating ordinary differential equations by the method of mode shape expansion. The structure of the ordinary differential equations are similar to the structure of the equations of motion for a blade section model. The ordinary differential equations are used to simulate a sudden pitch change of a rotating blade.

Introduction

This paper introduces a new set of partial differential equations of motion for a wind turbine blade, including the effects from gravity, pitch action, and varying rotor speed.

As wind turbines become larger, the coupling between blade modes of vibration and the influence from pitch action, rotor speed variations, and gravity on the blades become more pronounced. To reduce the fatigue loads on the blades it is important to analysis and understands these coupling phenomena and to take them into account, when designing blades and control algorithm.

The frequently cited paper by Hodges and Dowell [1] develops the nonlinear partial differential equations of motion for a twisted helicopter rotor blade. Wendell [2] develops partial differential equations of motion for a rotating wind turbine blade. Both of these works describe the flapwise, edgewise, and torsional degrees of freedom for a blade rotating with constant rotor speed and without any pitch action or gravity effects.

The contribution of this work is to setup the coupled nonlinear partial differential equations of motion of a horizontal axis wind turbine blade, including the effects of gravity, pitch action, and varying rotor speed. The coupling between blade and tower motion is not included in this model. An analysis of this model can give insight in how different terms couple the modes of motion. The model can also be transformed into a set of ordinary differential equations of motion by the method of mode shape expansion [3] leading to a system useable for fast simulations or analytical analysis.

The following section presents the model. In Section 3, the equations of motion are derived using Hamilton's principle [3]. In Section 4, the partial equations of motion are discussed, Section 5 gives an application example, where the model is transformed into ordinary differential equations and used for numerical simulations.

Description of Model

The model consists of a rotating inextensible blade with flapwise, edgewise and torsional degrees of freedom and exposed to gravity and non-conservative forces (e.g. aerodynamic forces). The blade can pitch and the rotor speed can vary.

Figure 1(a) shows the blade rotating in the rotor plane. The Y-axis of the inertial (X, Y, Z)-frame is pointing down wind and the (X, Z)-plane span the rotor plane. The $(\hat{x}, \hat{y}, \hat{z})$-frame is rotating with the blade, such that the $\hat{z}$-axis is aligned with the pitch axis of the blade and the $\hat{y}$-axis is aligned with the Y-axis. The angle between the two frames is denoted ϕ. Figure 1(b) shows a cross section of the blade looking outwards along the $\hat{z}$-axis. The position of the blade is described in the (x, y, z)-frame which is rotated β (the pitch angle) around the $\hat{z}$-axis. The shear center[1] and the tension center[2] of the blade are assumed to coincide and are described by the elastic axis (ea).

[1] The point on the blade cross section where a force in the cross section plane only causes bending, no twist.

[2] The point on the blade cross section where a tension force does not cause any bending.

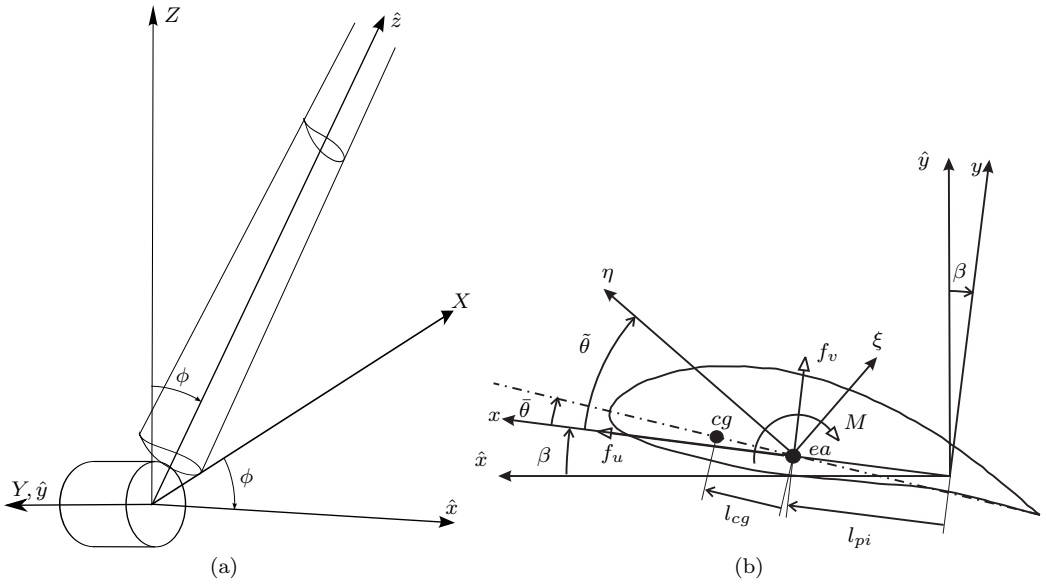

Figure 1: a) The inertial (X, Y, Z)-frame and the rotating $(\hat{x}, \hat{y}, \hat{z})$-frame with the $\hat{z}$-axis aligned with the pitch axis of the blade. b) Cross section of the blade looking outwards along the $\hat{z}$-axis

The position of ea in the (x, y, z)-frame is given by $(u(s,t) + l_{pi}(s), v(s,t), w)$, where t is the time and s is the distance from the root of the blade measured along ea, u and v are the deflection from the undeformed position in the x and y-directions respectively, l_{pi} is the undeformed position of ea on the x-axis. The position in the z-direction is given by $w = w_0(l_{pi}(s)) + w_1(l_{pi}(s), u(s,t), v(s,t))$, handeling the inextensible of the blade. The total length of ea is denoted R.

The principle (η, ξ)-axis, for the elastic properties of each blade section, is rotated the angle $\tilde{\theta}(s,t) + \theta(s,t)$ relative to the (x, z)-plane, where $\tilde{\theta}$ is the pretwist of the elastic properties and θ is the elastic twist of the blade section. The inertia of the blade is described by a concentrated mass $m(s)$ and a moment of rotational inertia $I_{cg}(s)$ (for rotation in the cross section plane) for each blade section, both related to the center of gravity cg. The center of gravity is assumed to be located on the chord the distance l_{cg} from ea. The chord is rotated the angle $\bar{\theta}(s,t) + \theta(s,t)$ relative to the (x, z)-plane, where $\bar{\theta}$ is the pretwist of the chord.

The forces on the blade are described by four force components; three translatory ($f_u(s,t)$, $f_v(s,t)$, $f_w(s,t)$) acting in the (x, y, z)-directions respectively and a rotation moment $M(s,t)$. The forces act at the elastic axis of the blade.

Derivation of the Equations of Motion

The derivation of the equations of motion follows the method used in [1]. First the elastic, potential and kinetic energies for the system are setup, and the equations of motion and boundary condition equations are derived from these energy expressions using Hamilton's principle [3].

Order Scheme

To avoid unnecessary complications of the equations of motion high order terms are neglected. This is done in a consisting manner by introducing an ordering scheme, assuming $(\frac{u}{R}, \frac{v}{R}, \frac{l_{pi}}{R}, \frac{l_{cg}}{R}, \theta, c\tilde{\theta}', c\bar{\theta}', \ddot{\beta}, \ddot{\phi}, \frac{m' l_{cg}}{m l'_{cg}})$ to be of order ϵ, where c is the length of the chord, $\epsilon \ll 1$ is a bookkeeping parameter denoting the smallness of terms, $\dot{(\,)} \equiv \frac{\mathrm{d}}{\mathrm{d}t}$ and $(\,)' \equiv \frac{\mathrm{d}}{\mathrm{d}s}$. The angular acceleration of the rotor and pitch are assumed to be $\ddot{\phi}R \sim \ddot{u}$ and $\ddot{\beta}c \sim \ddot{u}$ respectively. The ordering scheme is applied such that terms of order ϵ^{n+2} or higher are neglected, where n is the lowest order of a term in the expression.

Transformations

Before deriving the equations of motion a transformation between the rotating (x, y, z)-frame in which the blade deflection is described and the inertial (X, Y, Z)-frame is found

$$\left[\mathbf{i}, \mathbf{j}, \mathbf{k}\right]^{\mathrm{T}} = \mathbf{T}_\beta \mathbf{T}_\phi \left[\mathbf{I}, \mathbf{J}, \mathbf{K}\right]^T \tag{1}$$

where $[\mathbf{i}, \mathbf{j}, \mathbf{k}]^T$ and $[\mathbf{I}, \mathbf{J}, \mathbf{K}]^T$ are the unit vectors in the (x, y, z) and (X, Y, Z)-frames respectively. The matrixes $\mathbf{T}_\beta$ and $\mathbf{T}_\phi$ are the transformations from the $(\hat{x}, \hat{y}, \hat{z})$-frame to the (x, y, z)-frame and from the (X, Y, Z)-frame to the $(\hat{x}, \hat{y}, \hat{z})$-frame respectively. Both matrixes are given in the appendix.

The transformation between the principle axis and the (x, y, z)-frame is given by $\mathbf{T}_e$ and between the chord and the (x, y, z)-frame is given by $\mathbf{T}_c$. Both matrixes are given in the appendix.

Elastic Energy

The strain in the blade is measured by Green's strain tensor (cf. [1])

$$2[\mathrm{d}s, \mathrm{d}\eta, \mathrm{d}\xi][\epsilon_{ij}][\mathrm{d}s, \mathrm{d}\eta, \mathrm{d}\xi]^{\mathrm{T}} = \mathrm{d}\mathbf{r}_1 \cdot \mathrm{d}\mathbf{r}_1 - \mathrm{d}\mathbf{r}_0 \cdot \mathrm{d}\mathbf{r}_0 \tag{2}$$

where d denotes the differential, ϵ_{ij} is the strain tensor and

$$\mathbf{r}_0 = \left[\mathbf{I}, \mathbf{J}, \mathbf{K}\right] \mathbf{T}_\phi^{-1} \mathbf{T}_\beta^{-1} \left[\left[l_{pi}, 0, w_0\right]^{\mathrm{T}} + (\mathbf{T}_e\big|_{u=v=\theta=0})^{-1} \left[\eta_0, \xi_0, 0\right]^{\mathrm{T}}\right] \tag{3}$$

is a position vector describing a point in the undeformed blade, where (η_0, ξ_0) is the position of the point in the undeformed blade section. The same point in the deformed blade is given by

$$\mathbf{r}_1 = \left[\mathbf{I}, \mathbf{J}, \mathbf{K}\right] \mathbf{T}_\phi^{-1} \mathbf{T}_\beta^{-1} \left[\left[l_{pi} + u, v, w_0 + w_1\right]^{\mathrm{T}} + \mathbf{T}_e^{-1} \left[\eta_1, \xi_1, 0\right]^{\mathrm{T}}\right] \tag{4}$$

where (η_1, ξ_1) is the position of the point in the deformed blade section.

Assuming uniaxial stress in the blade the variation of the elastic energy becomes

$$\delta V_{ela} = \int_0^R \iint_A \left(\sigma_{ss}\delta\epsilon_{ss} + \sigma_{s\eta}\delta\epsilon_{s\eta} + \sigma_{s\xi}\delta\epsilon_{s\xi}\right) \mathrm{d}\eta\mathrm{d}\xi\mathrm{d}s \tag{5}$$

where $\sigma_{ss} = E\epsilon_{ss}$, $\sigma_{s\eta} = G\epsilon_{s\eta}$, $\sigma_{s\xi} = G\epsilon_{s\xi}$, $\epsilon_{ss} = \epsilon_{11}$, $\epsilon_{s\eta} = 2\epsilon_{12}$ and $\epsilon_{s\xi} = 2\epsilon_{13}$, where E is the tensile modulus of elasticity (Young's modulus) and G is the torsional modulus of elasticity.

Potential Energy

The potential energy from the gravity field is described by

$$V_{gra} = \int_0^R \mathbf{r}_{cg}^{\mathrm{T}} \cdot \mathbf{g}\mathrm{d}s \tag{6}$$

where $\mathbf{g} = [0, 0, -g]^{\mathrm{T}}$ is the gravity field and

$$\mathbf{r}_{cg} = \left[\mathbf{I}, \mathbf{J}, \mathbf{K}\right] \mathbf{T}_\phi^{-1} \mathbf{T}_\beta^{-1} \left[\left[l_{pi} + u, v, w_0 + w_1\right]^{\mathrm{T}} + \mathbf{T}_c^{-1} \left[l_{cg}, 0, 0\right]^{\mathrm{T}}\right] \tag{7}$$

is a position vector describing the center of gravity.

Kinetic Energy

The kinetic energy of the blade is given by

$$T = \int_0^R \left(\frac{1}{2} m \dot{\mathbf{r}}_{cg}^{\mathrm{T}} \cdot \dot{\mathbf{r}}_{cg} + \frac{1}{2} I_{cg} (\dot{\beta} + \dot{\theta})^2\right) \mathrm{d}s \tag{8}$$

where $\dot{\beta} + \dot{\theta}$ is the angular velocity of the blade section around the elastic axis.

Non-conservative forces

The non-conservative forces are taken into account by describing the work done by them for any admissible variation

$$\delta Q = \int_0^R (\mathbf{f} \cdot \delta \mathbf{r}_{ea} + M\delta(\theta + \beta)) \, \mathrm{d}s \tag{9}$$

where $\mathbf{f} = [f_u, f_v, f_w]$ are forces acting at the elastic axis in the (x, y, z)-directions respectively and M is a twisting moment on the blade.

$$\mathbf{r}_{ea} = \left[\mathbf{I}, \mathbf{J}, \mathbf{K}\right] \mathbf{T}_\phi^{-1} \mathbf{T}_\beta^{-1} \left[l_{pi} + u, v, w_0 + w_1\right]^{\mathrm{T}} \tag{10}$$

is a position vector describing the elastic axis.

Equations of motion

By demanding that any admissible variation of the action integral $H \equiv \int_{t_1}^{t_2} (T - V_{ela} - V_{gra} - Q)\mathrm{d}t$ is zero, a set of boundary condition equations and a set of partial differential equations of motion are derived (Hamilton's principle [3]). First the equations of motion are presented followed by a discussion of the boundary conditions.

Bending Motion

The equation of motion of the x and y-directions becomes

$$\begin{aligned} &m(\ddot{u} - \ddot{\theta} l_{cg} \sin(\bar{\theta})) + F_{u,1}(\ddot{\beta}, \dot{\beta}, \dot{\phi}, \dot{v}, \dot{\theta}, u', u, v, \theta, \beta) + F_{u,2}(\dot{\phi}, \dot{u}, \dot{v}, u', v, \theta, \beta) \\ &\quad + F_{u,3}(\phi, \beta, \theta, u', v') + F_{u,4}(u'', v'', \theta) + F_{u,5}(\ddot{\phi}, \beta) = f_u + \left((u' + l'_{pi}) \int_r^s f_w \mathrm{d}\rho \right)' \end{aligned} \tag{11a}$$

$$\begin{aligned} &m(\ddot{v} + \ddot{\theta} l_{cg} \cos(\bar{\theta})) + F_{v,1}(\ddot{\beta}, \dot{\beta}, \dot{\phi}, \dot{v}, \dot{u}', u, v, \theta, \beta) + F_{v,2}(\dot{\phi}, \dot{u}, \dot{v}, u', v, \theta, \beta) \\ &\quad + F_{v,3}(\phi, \beta, \theta, u', v') + F_{v,4}(u'', v'', \theta) + F_{v,5}(\ddot{\phi}, \beta) = f_v + \left(v' \int_r^s f_w \mathrm{d}\rho \right)' \end{aligned} \tag{11b}$$

The direction of the the x and y-axis can be swapped by changing the β angle, hence the only difference between the terms in (11b) and (11a) are the directions of projection of the forces. In the following the individual terms in (11) will be shown and the physical interpretation of them will be discussed. Because of the similarity between the terms from (11a) and (11b) only the terms from (11a) will be discussed.

The influence of pitch action is described by

$$\begin{aligned} F_{u,1} = &- \ddot{\beta} m(v + l_{cg} \sin(\bar{\theta})) - \dot{\beta}^2 m(u + l_{pi} + l_{cg} \cos(\bar{\theta}) - l_{cg} \theta \sin(\bar{\theta})) \\ &- 2\dot{\beta} m(\dot{v} + \dot{\theta} l_{cg} \cos(\bar{\theta})) + 2\dot{\beta}\dot{\phi} \big(m l_{cg} ((u + l_{pi}) \sin(\beta) + v \cos(\beta) + l_{cg} \sin(\bar{\theta} + \beta)) \cos(\bar{\theta}) \big)' \\ &+ \left((u' + l'_{pi}) \int_s^R 2m\dot{\beta}\dot{\phi}((u + l_{pi}) \sin(\beta) + v \cos(\beta) + l_{cg} \sin(\bar{\theta} + \beta)) \mathrm{d}\rho \right)' \end{aligned} \tag{12a}$$

$$\begin{aligned} F_{v,1} = &\ddot{\beta} m(u + l_{pi} + l_{cg} \cos(\bar{\theta})) - \dot{\beta}^2 m(v + l_{cg} \sin(\bar{\theta}) + l_{cg} \theta \cos(\bar{\theta})) \\ &+ 2\dot{\beta} m(\dot{u} - \dot{\theta} l_{cg} \sin(\bar{\theta})) + 2\dot{\beta}\dot{\phi} \big(m l_{cg} ((u + l_{pi}) \sin(\beta) + v \cos(\beta) + l_{cg} \sin(\bar{\theta} + \beta)) \sin(\bar{\theta}) \big)' \\ &+ \left(v' \int_s^R 2m\dot{\beta}\dot{\phi}((u + l_{pi}) \sin(\beta) + v \cos(\beta) + l_{cg} \sin(\bar{\theta} + \beta)) \mathrm{d}\rho \right)' \end{aligned} \tag{12b}$$

where the first term in (12a) is the fictive acceleration of cg in the x-direction associated with the angular acceleration of the (x, y, z)-frame about the z-axis, the second term is the fictive centrifugal force associated with the angular velocity of the (x, y, z)-frame about the z-axis and the offset of cg in the x-direction, the third term is the fictive coriolis force associated with the angular velocity of the (x, y, z)-frame about the z-axis and the velocity of cg in the y-direction. The fourth term in (12a) is the spatial derivative of the moment caused by the offset of cg and the fictive coriolis force

in the z-direction. The coriolis force is associated with the angular velocity of the (x, y, z)-frame about the z-axis and about the $\hat{y}$-axis. The last term is the bending moment caused by the the fictive coriolis force in the z-direction on the remaining part of the blade, from this point to the tip. The influence from the constant rotor speed is described by

$$\begin{aligned} F_{u,2} =& -\dot{\phi}^2 m((u + l_{pi})\cos(\beta) - v\sin(\beta) + l_{cg}\cos(\bar{\theta} + \beta) - l_{cg}\theta\sin(\bar{\theta} + \beta))\cos(\beta) \\ & - \dot{\phi}^2\big(ml_{cg}w_0(\cos(\bar{\theta}) - \theta\sin(\bar{\theta}))\big)' - 2\dot{\phi}ml'_{cg}(\dot{u}\cos(\beta) - \dot{v}\sin(\beta))\cos(\bar{\theta}) \\ & - \left((u' + l'_{pi})\int_s^R m\big(\dot{\phi}^2 w_0 + 2\dot{\phi}(\dot{u}\cos(\beta) - \dot{v}\sin(\beta))\big)\mathrm{d}\rho\right)' \end{aligned} \tag{13a}$$

$$\begin{aligned} F_{v,2} =& \dot{\phi}^2 m((u + l_{pi})\cos(\beta) - v\sin(\beta) + l_{cg}\cos(\bar{\theta} + \beta) - l_{cg}\theta\sin(\bar{\theta} + \beta))\sin(\beta) \\ & - \dot{\phi}^2\big(ml_{cg}w_0(\sin(\bar{\theta}) + \theta\cos(\bar{\theta}))\big)' - 2\dot{\phi}ml'_{cg}(\dot{u}\cos(\beta) - \dot{v}\sin(\beta))\sin(\bar{\theta}) \\ & - \left(v'\int_s^R m\big(\dot{\phi}^2 w_0 + 2\dot{\phi}(\dot{u}\cos(\beta) - \dot{v}\sin(\beta))\big)\mathrm{d}\rho\right)' \end{aligned} \tag{13b}$$

where the first term in (13a) is the fictive centrifugal force associated with the rotation in the rotor plane and the offset of cg in the x-direction projected onto the x-direction. The second and third terms in (13a) are the spatial derivative of the moment caused by the distance from cg to ea in the x-direction and the fictive centrifugal and coriolis force in the z-direction respectively. The centrifugal force is associated with the rotation in the rotor plane and the offset of cg from the center of rotation, and the coriolis force is associated with the rotation in the rotor plane and the velocity of cg in the $\hat{x}$-direction. The last term in (13a) is the bending moment from the fictive centrifugal and coriolis forces in the z-directions on the reminding part of the blade from this point to the tip. The influence from gravity is described by

$$\begin{aligned} F_{u,3} =& mg\sin(\phi)\cos(\beta) + \big((l_{cg}(u' + l'_{pi}))'\cos(\bar{\theta})\cos(\beta) + (l_{cg}v')'\sin(\bar{\theta})\cos(\beta)\big)mg\sin(\phi) \\ & - \big(ml_{cg}(\cos(\bar{\theta}) - \theta\sin(\bar{\theta}))\big)'g\cos(\phi) + \left((u' + l'_{pi})\int_s^R mg\cos(\phi)\mathrm{d}\rho\right)' \end{aligned} \tag{14a}$$

$$\begin{aligned} F_{v,3} =& -mg\sin(\phi)\sin(\beta) + \big((l_{cg}(u' + l'_{pi}))'\sin(\bar{\theta})\cos(\beta) - (l_{cg}v')'\sin(\bar{\theta})\sin(\beta)\big)mg\sin(\phi) \\ & - \big(ml_{cg}(\sin(\bar{\theta}) + \theta\cos(\bar{\theta}))\big)'g\cos(\phi) + \left(v'\int_s^R mg\cos(\phi)\mathrm{d}\rho\right)' \end{aligned} \tag{14b}$$

where the first term in (14a) is the x-component of the gravity force, the second term is the spatial derivative of the moment caused by $\hat{x}$-component of the gravity force and the offset of cg in the z-direction, the third term is the spatial derivative of the moment caused by the distance between cg and ea in the x-direction and the z-component of the gravity force. The last term in (14a) is the bending moment from the z-component of the gravity force on the remaining part of the blade, from this point to the tip. The restoring force caused by the bending stiffness of the blade is described by

$$\begin{aligned} F_{u,4} =& \big(E(I_\eta\cos^2(\tilde{\theta}) + I_\xi\sin^2(\tilde{\theta}))u''\big)'' + \big(E(I_\eta - I_\xi)\cos(\tilde{\theta})\sin(\tilde{\theta})v''\big)'' \\ & - \big(E(I_\eta - I_\xi)\theta(u''\sin(2\tilde{\theta}) - v''\cos(2\tilde{\theta}) + l''_{pi}\sin(\tilde{\theta})\cos(\tilde{\theta}))\big)'' \end{aligned} \tag{15a}$$

$$\begin{aligned} F_{v,4} =& \big(E(I_\eta\sin^2(\tilde{\theta}) + I_\xi\cos^2(\tilde{\theta}))v''\big)'' + \big(E(I_\eta - I_\xi)\cos(\tilde{\theta})\sin(\tilde{\theta})u''\big)'' \\ & + \big(E(I_\eta - I_\xi)\theta(u''\cos(2\tilde{\theta}) + v''\sin(2\tilde{\theta}))\big)'' - \big(l''_{pi}\theta E(I_\eta\sin^2(\theta) + I_\xi\cos^2(\theta))\big)'' \end{aligned} \tag{15b}$$

where the first term is the bending stiffness in the x-direction, the second term is the coupling to the v-direction, and the last term is the coupling to the twist. The principle moments of inertia is given by $I_\eta = \iint_A \eta^2\mathrm{d}\eta\mathrm{d}\xi$ and $I_\eta = \iint_A \xi^2\mathrm{d}\eta\mathrm{d}\xi$. The effect of an angular acceleration of the rotor is described by

$$F_{u,5} = m\ddot{\phi}w_0\cos(\beta)\ , \quad F_{v,5} = -m\ddot{\phi}w_0\sin(\beta) \tag{16}$$

which is the fictive angular acceleration of cg associated with the angular acceleration of the (x, y, z)-frame about the Y-axis. The right hand side of (11a) and (11b) describes the external

forces, f_u and f_v are the forces in the x and y-direction respectively and the last term is the bending moment from the external force in the z-direction on the remaining part of the blade, from this point to the tip.

Torsional Motion

The equation of torsional motion is

$$\begin{aligned}(I_{cg} + ml_{cg}^2)\ddot{\theta} - ml_{cg}(\ddot{u}\sin(\bar{\theta}) - \ddot{v}\cos(\bar{\theta})) + F_{\theta,1}(\dot{\phi}, u', v', u, v, \beta) + F_{\theta,2}(\ddot{\beta}, \dot{\beta}, \dot{u}, \dot{v}, u, v) \\ + F_{\theta,3}(\ddot{\phi}, \beta) + F_{\theta,4}(\phi, u', v', \theta, \beta) + F_{\theta,5}(u'', v'', \theta') + F_{\theta,6}(\theta') = M \end{aligned} \quad (17)$$

where the constant rotor speed leads to the fictive centrifugal forces

$$\begin{aligned}F_{\theta,1} = ml_{cg}\dot{\phi}^2((u + l_{pi})\cos(\beta) - v\sin(\beta) + l_{cg}\cos(\bar{\theta} + \beta))\sin(\bar{\theta} + \beta) \\ + ml_{cg}w_0\dot{\phi}^2(v'\cos(\bar{\theta}) - (u' + l'_{pi})\sin(\bar{\theta}))\end{aligned} \quad (18)$$

where the first term is associated with the offset of cg in the $\hat{x}$-direction and the second is associated with the distance from center of rotation to cg. The influence from the pitch action is described by

$$F_{\theta,2} = (I_{cg} + ml_{cg}^2)\ddot{\beta} + ml_{cg}\dot{\beta}^2((u + l_{pi})\sin(\bar{\theta}) - v\cos(\bar{\theta})) + 2ml_{cg}\dot{\beta}(\dot{u}\cos(\bar{\theta}) + \dot{v}\sin(\bar{\theta})) \quad (19)$$

where the first term is the fictive angular acceleration associated with the angular acceleration of the (x, y, z)-frame about the z-axis, the second term is the fictive centrifugal force associated with the rotation of the (x, y, z)-frame about the z-axis, and the last term is the fictive coriolis force associated with the rotation of the (x, y, z)-frame about the z-axis and the velocity of cg in the chord direction. The acceleration of the rotor leads to the following term

$$F_{\theta,3} = -m\ddot{\phi}w_0 l_{cg}\sin(\bar{\theta} + \beta) \quad (20)$$

which is the fictive angular acceleration of cg associated with the angular acceleration of the (x, y, z) frame about the Y-axis. The effect of gravity is described by

$$F_{\theta,4} = -l_{cg}(\sin(\beta + \bar{\theta}) + \theta\cos(\beta + \bar{\theta}))mg\sin(\phi) + l_{cg}(v'\cos(\bar{\theta}) - (u' + l'_{pi})\sin(\bar{\theta}))mg\cos(\phi) \quad (21)$$

where the first term is the twisting moment caused by the $\hat{x}$-component of the gravity force and the distance between cg and ea, in the $\hat{y}$-direction. The last term is the twisting moment caused by the distance between cg and ea and the z-component of the gravity force projected onto the cross section of the deformed blade. The elastic coupling between the bending and twisting of the blade is described by

$$\begin{aligned}F_{\theta,5} = -\big(EI_{\eta\eta\xi}(\tilde{\theta} + \theta)'(u''\sin(\tilde{\theta}) - v''\cos(\tilde{\theta}))\big)' + \big(EI_{\eta\xi\xi}(\tilde{\theta} + \theta)'(u''\cos(\tilde{\theta}) + v''\sin(\tilde{\theta}))\big)' \\ - (EI_\eta - EI_\xi)\big((u''^2 - v''^2)\cos(\tilde{\theta})\sin(\tilde{\theta}) - u''v''\cos(2\tilde{\theta})\big) \\ - EI_\eta l''_{pi}(u''\cos(\tilde{\theta}) + v''\sin(\tilde{\theta}))\sin(\tilde{\theta}) + EI_\xi l''_{pi}(u''\sin(\tilde{\theta}) - v''\cos(\tilde{\theta}))\cos(\tilde{\theta})\end{aligned} \quad (22)$$

where $I_{\eta\eta\xi} = \iint_A \eta(\eta^2 + \xi^2)\mathrm{d}\eta\mathrm{d}\xi$ and $I_{\eta\xi\xi} = \iint_A \xi(\eta^2 + \xi^2)\mathrm{d}\eta\mathrm{d}\xi$. The restoring force caused by torsional stiffness is given by

$$F_{\theta,6} = -(GJ\theta')' \quad (23)$$

where the polar moment of inertia is $J = \iint_A \left(\eta^2 + \xi^2\right)\mathrm{d}\eta\mathrm{d}\xi$. The right hand side describes the external moment on the blade M.

Boundary Conditions

The boundary conditions for the root of the blade is given by the geometric constrains

$$u(0, t) = u'(0, t) = v(0, t) = v'(0, t) = \theta(0, t) = 0 \quad (24)$$

because the coordinate frame used to describe the blade follows the root of the blade.

The boundary conditions for the tip of the blade are determined by the boundary condition equations derived by Hamilton's principle [3], which leads to

$$\begin{aligned} &u''(R,t) = v''(R,t) = \theta'(R,t) = 0 \\ &EI_\eta I_\xi u'''(R,t) = ml_{cg}(\dot{\phi}^2 w_0 - g\cos(\phi))\left(I_\xi \sin(\tilde{\theta}-\bar{\theta})\sin(\tilde{\theta}) + I_\eta \cos(\tilde{\theta}-\bar{\theta})\cos(\tilde{\theta})\right) \\ &EI_\eta I_\xi v'''(R,t) = ml_{cg}(\dot{\phi}^2 w_0 - g\cos(\phi))\left(I_\xi \cos(\tilde{\theta}-\bar{\theta})\sin(\tilde{\theta}) - I_\eta \sin(\tilde{\theta}-\bar{\theta})\cos(\tilde{\theta})\right) \end{aligned} \tag{25}$$

If $l_{cg}(R) \neq 0$ the boundary conditions for the tip are functions of rotor speed $\dot{\phi}$ and rotor position ϕ and therefore time-varying. But most modern wind turbine blades are tapered at the tip, leading to $l_{cg}(R)/R \ll \epsilon$, making the time-varying boundary conditions negligible.

Discussion

Comparing the equations of motion (11) and (17) with [1] it is noticed that the gravity terms (14), (21), the pitch action terms (12a), (19) and the terms involving varying rotor speed (16), (23) are new. On the other hand the terms involving warp effects in [1] are not included here because this effect is neglected.

In the following discussion the x and y-direction will be denoted edgewise and flapwise, corresponding to a non-twisted blade. The inertia terms in (11) is seen to couple the edgewise and flapwise motions to the torsional motion of the blade. The degree of coupling is seen to depend on the pretwist of the chord. The first term in (12) shows that an acceleration of the pitch angle excites the edgewise and flapwise motion depending on the flapwise and edgewise deflection respectively. That is, an acceleration of the pitch angle of a flapwise deflected blade excites the edgewise motion of the blade. The first term in the integral in (13) is a restoring force dependent on the rotation speed of the rotor, known as centrifugal stiffness. The effect of gravity (14) and (21) is seen to vary with the ϕ-angle, as expected. The restoring force (15) couples the bending motion to the torsional motion. The degree of coupling is dependent on the edgewise and flapwise deflection of the blade. An acceleration of the rotor excite the edgewise and flapwise motion (16), the excitation is dependent on the pitch angle. The inertia term for (17) couples the torsional motion to the edgewise and flapwise motion. The degree of coupling to the edgewise and the flapwise motion is dependent on the pretwist of the chord. First term in (19) shows a strong coupling between pitch acceleration and torsional motion. The effect of rotor acceleration (20) on the torsional motion is dependent on the pitch setting and the pretwist of the blade. The bending motion is coupled to the torsional motion through the bending stiffness (22).

As suggested in the introduction the partial differential equations of motion can be transformed into approximating ordinary differential equations by the method of mode shape expansion. Using one edgewise $u(s,t) = u_s(s)u_t(t)$, one flapwise $v(s,t) = v_s(s)v_t(t)$, and one torsional $\theta(s,t) = \theta_s(s)\theta_t(t)$ mode, where (u_s, v_s, θ_s) are know mode shape functions describing the shape of the deformed blade and (u_t, v_t, θ_t) are unknown time functions, leads to

$$\mathbf{M}\ddot{\mathbf{q}} + \big(\mathbf{K} + \mathbf{K}_c(\dot{\phi}^2, \beta)\big)\mathbf{q} = \mathbf{f}(\dot{\mathbf{q}}, \mathbf{q}, \ddot{\beta}, \dot{\beta}, \beta, \ddot{\phi}, \dot{\phi}, \phi) \tag{26}$$

where $\mathbf{q} = [u_t, v_t, \theta_t]^{\mathrm{T}}$, $\mathbf{M}$ is the inertia matrix, $\mathbf{K}$ is the stiffness, $\mathbf{K}_c$ is the centrifugal stiffness, and $\mathbf{f}$ holds nonlinear stiffness terms, linear and nonlinear forcing terms from pitch action, rotor acceleration and rotation, and gravity. The structure of (26) is seen to be similar to the equations of motion of a blade section model, therefore (26) can be used to get a formal connection between a Blade section model and a full turbine blade model. Blade section models are widely used in aeroelastic analysis, control design, etc. [4, 5].

An improved description of the blade motion can be achieved if more mode shapes or coupled mode shapes are used. The drawback of this is a more complicated system, making analytical analysis and qualitative interpretation harder.

Application Example

In this example a simplified blade is described by a mode shape expansion of the present model, including one flapwise, one edgewise and one torsional mode (26). The mode shapes of a cantilever beam are used [6]. These mode shapes are not taking the rotation into account, using special designed mode shapes will lead to better results. The 40 m blade has uniform properties with coinciding pitch and elastic axis, and no pretwist of the chord or principle axis. The center of gravity has an offset on $l_{cg} = 0.1$ m, the offset decreases to zero at the tip, as to avoid time-varying boundary conditions. Initially the pitch angle is zero.

Figure 2 shows the blade tip deflection from the present model and from HAWC2 [7, 8], a combined finite element and multi body dynamic code from Risø National Laboratory. The blade is rotating with a constant angular velocity on 1 rad/s and at 20 seconds a 2 degrees pitch change is imposed. The damping in the present model is incorporated by adding a viscous damping term in each of the resulting ordinary differential equations from the mode shape expansion.

The edgewise motion is dominated by gravity, which is seen as the big oscillations on the 6 seconds scale (corresponding to the rotor speed on 1 rad/s). The faster oscillations on the 1 second scale is caused by the vibrations of the blade excited by the oscillations caused by gravity.

Initially the flapwise motion is not affected by gravity because the flap direction is normal to the gravity field. After the pitch action at 20 seconds the flap direction is no longer normal to the gravity field and the gravity excited the flapwise motion. The gravity effect on the flapwise motion is seen as the oscillations on the 6 seconds scale. The pitch action excites some of the high order flap modes, this is seen as the fast oscillations just after the pitch action. These high order flap motions are not captured by the present model because it is only based on one flapwise mode.

The twist of the blade is seen to be excited by the pitch action, and there is a good agreement between the results from the two models.

This experiment shows how a mode shape expansion of the present model, resulting in three approximating ordinary differential equations, can describe the influence of gravity and pitch action almost as well as a complicated finite element code.

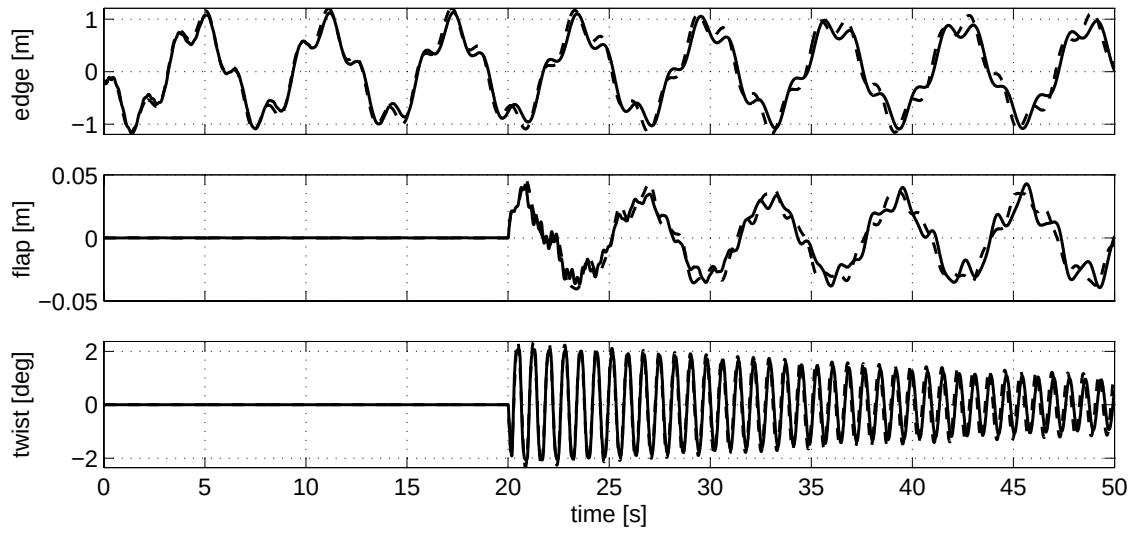

Figure 2: Tip deflection of a blade rotating with a constant speed of 2π and with a 2 deg pitch change at 20 seconds. '$\cdots$' the present model, '–' HAWC2 [7, 8], a combined finite element and multi body dynamic code from Risø National Laboratory.

Conclusion

This work provides a new set of partial differential equations of motion for a wind turbine blade rotating in a gravity field with variable rotor speed and pitch action. The model can be used for analyse of the interaction between different modes of blade motion and pitch action, gravity and varying rotor speed.

An example is included where the partial differential equations of motion are transformed into three ordinary differential equations of motion by the method of mode shape expansion. This simplified model is used to simulate the blade motion of a rotating blade exposed to a pitch change. The example shows that the model is capable of describing the influence of pitch action and gravity.

The simplified mode shape version of the model is intended to be further developed, leading to a tool for qualitative analyse of interaction between control and blade motion.

Appendix

Coordinate Transformations

The derivation of the transformations matrices follows the method used in [1]. The major difference between [1] and these matrices is the inclusion of the pitch angle β.

The transformation between the initial (X, Y, Z)-frame and the $(\hat{x}, \hat{y}, \hat{z})$-frame is given by

$$\begin{bmatrix} \hat{\mathbf{i}} \\ \hat{\mathbf{j}} \\ \hat{\mathbf{k}} \end{bmatrix} = \mathbf{T}_\phi \begin{bmatrix} \mathbf{I} \\ \mathbf{J} \\ \mathbf{K} \end{bmatrix} = \begin{bmatrix} \cos(\phi(t)) & 0 & -\sin(\phi(t)) \\ 0 & 1 & 0 \\ \sin(\phi(t)) & 0 & \cos(\phi(t)) \end{bmatrix} \begin{bmatrix} \mathbf{I} \\ \mathbf{J} \\ \mathbf{K} \end{bmatrix} \tag{27}$$

and between the $(\hat{x}, \hat{y}, \hat{z})$-frame and the (x, y, z)-frame is given by

$$\begin{bmatrix} \mathbf{i} \\ \mathbf{j} \\ \mathbf{k} \end{bmatrix} = \mathbf{T}_\beta \begin{bmatrix} \hat{\mathbf{i}} \\ \hat{\mathbf{j}} \\ \hat{\mathbf{k}} \end{bmatrix} = \begin{bmatrix} \cos(\beta(t)) & \sin(\beta(t)) & 0 \\ -\sin(\beta(t)) & \cos(\beta(t)) & 0 \\ 0 & 0 & 1 \end{bmatrix} \begin{bmatrix} \hat{\mathbf{i}} \\ \hat{\mathbf{j}} \\ \hat{\mathbf{k}} \end{bmatrix} \tag{28}$$

The principle axis of each cross section of the blade is described by the (η, ξ, ζ)-frame with origin at ea, where η and ξ are the principle axis of the cross section and the ζ-axis points outwards along the elastic axis of the deformed blade. This frame has the unit vectors $(\tilde{\mathbf{i}}, \tilde{\mathbf{j}}, \tilde{\mathbf{k}})$ given by the following transformation

$$\begin{aligned} \begin{bmatrix} \tilde{\mathbf{i}} \\ \tilde{\mathbf{j}} \\ \tilde{\mathbf{k}} \end{bmatrix} = \mathbf{T}_e \begin{bmatrix} \mathbf{i} \\ \mathbf{j} \\ \mathbf{k} \end{bmatrix} = & \begin{bmatrix} \cos(\hat{\theta}(s,t)) & \sin(\hat{\theta}(s,t)) & 0 \\ -\sin(\hat{\theta}(s,t)) & \cos(\hat{\theta}(s,t)) & 0 \\ 0 & 0 & 1 \end{bmatrix} \\ & \begin{bmatrix} 1 & 0 & 0 \\ 0 & \sqrt{1-v'(s,t)^2} & -v'(s,t) \\ 0 & v'(s,t) & \sqrt{1-v'(s,t)^2} \end{bmatrix} \\ & \begin{bmatrix} \sqrt{\frac{1-(l'_{pi}(s)+u'(s,t))^2-v'(s,t)}{1-v'(s,t)^2}} & 0 & -\frac{l'_{pi}(s)+u'(s,t)}{\sqrt{1-v'(s,t)^2}} \\ 0 & 1 & 0 \\ \frac{l'_{pi}(s)+u'(s,t)}{\sqrt{1-v'(s,t)^2}} & 0 & \sqrt{\frac{1-(l'_{pi}(s)+u'(s,t))^2-v'(s,t)}{1-v'(s,t)^2}} \end{bmatrix} \begin{bmatrix} \mathbf{i} \\ \mathbf{j} \\ \mathbf{k} \end{bmatrix} \end{aligned} \tag{29}$$

where $\hat{\theta}$ is the rotation of the blade around the elastic axis. The first matrix in (29) is the rotation about the $\hat{z}$-axis, the next matrix is the rotation about the x-axis and the last matrix is the rotation about the z-axis.

The chord is described by the $(\bar{\mathbf{i}}, \bar{\mathbf{j}}, \bar{\mathbf{k}})$ unit vectors parallel to the chord, normal upwards from the chord and parallel to the elastic axis respectively. This set of unit vectors is given by

$$\begin{bmatrix} \bar{\mathbf{i}} & \bar{\mathbf{j}} & \bar{\mathbf{k}} \end{bmatrix}^{\mathrm{T}} = \mathbf{T}_c \begin{bmatrix} \mathbf{i} & \mathbf{j} & \mathbf{k} \end{bmatrix}^{\mathrm{T}} \tag{30}$$

where $\mathbf{T}_c$ is equal to $\mathbf{T}_e$ except that the twist $\hat{\theta}$ includes another pretwist.

The rotation of the principle axis of the blade sections as a function of the s coordinate is given by the differential equation

$$\mathbf{T}'_e = \begin{bmatrix} 0 & \tilde{\omega}_k & -\tilde{\omega}_j \\ -\tilde{\omega}_k & 0 & \tilde{\omega}_i \\ \tilde{\omega}_j & -\tilde{\omega}_i & 0 \end{bmatrix} \mathbf{T}_e \;\Rightarrow\; \begin{bmatrix} 0 & \tilde{\omega}_k & -\tilde{\omega}_j \\ -\tilde{\omega}_k & 0 & \tilde{\omega}_i \\ \tilde{\omega}_j & -\tilde{\omega}_i & 0 \end{bmatrix} = \mathbf{T}'_e \mathbf{T}_e^{-1} \tag{31}$$

where $(\tilde{\omega}_i, \tilde{\omega}_j, \tilde{\omega}_k)$ is the rotation about the $(\tilde{\mathbf{i}}, \tilde{\mathbf{j}}, \tilde{\mathbf{k}})$-directions respectively, and it is utilized that $\mathbf{T}'_\phi = \mathbf{T}'_\beta = \mathbf{0}$. The rotation about the $\tilde{\mathbf{k}}$-direction is also measured by changes in the twist coordinates of the blade, (the pretwist $\tilde{\theta} = \tilde{\theta}(s)$ and the elastic twist $\theta = \theta(s,t)$). Hence

$$(\tilde{\theta} + \theta)' = \tilde{\omega}_k = \hat{\theta}' + v'u'' + \mathcal{O}(\epsilon^3) \tag{32}$$

using the order scheme (page 2).

Rearranging and intergrading (32) leads to an expression for the rotation of each blade section around the elastic axis

$$\hat{\theta} = \tilde{\theta} + \theta - \int_0^s v'u'' \mathrm{d}\rho \tag{33}$$

Inserting (33) into the expression for $\mathbf{T}_e$ leads to the transformation matrix of the elastic properties. Replacing $\tilde{\theta}$ with $\bar{\theta}$ in $\mathbf{T}_e$ gives the transformation matrix $\mathbf{T}_c$ of the chord.

References

[1] Hodges DH and Dowell EH. Nonlinear equations of motion for the elastic bending and torsion of twisted nonuniform rotor blades. Technical Report TN D-7818, NASA, December 1974.

[2] Wendell J. Aeroelastic stability of wind turbine rotor blades. Technical Report E(11.1)-4131, U.S. Department of Energy, September 1978.

[3] Thomsen JJ. *Vibrations and stability: advanced theory, analysis, and tools*. Springer-Verlag: Berlin - Heidelberg - New York, 2003.

[4] Block JJ and Strganac TW. Applied active control for a nonlinear aeroelastic structure. *Journal of Guidance, Control, and Dynamics*, 21(6):838–845, 1998.

[5] Chaviaropoulos PK, Soerensen NN, Hansen MOL, Nikolaou IG, Aggelis KA, Johansen J, Gaunaa M, Hambraus T, von Geyr HF, Hirsch C, Shun K, Voutsinas SG, Tzabiras G, Perivolaris Y, and Dyrmose SZ. Viscous and aeroelastic effects on wind turbine blades. the viscel project. part II: Aeroelastic stability investigations. *Wind Energy*, 6(4):387–404, 2003.

[6] Flügger W. *Handbook of Engineering Mechanics*. Mcgraw-Hill, 1962.

[7] Larsen TJ, Hansen A, and Buhl T. Aeroelastic effects of large blade deflections for wind turbines. *Proceedings of the special topic conference "The Science of making Torque from Wind"*, pages 238–246, 2004.

[8] Larsen TJ, Madsen HA, Hansen AM, and Thomsen K. Investigations of stability effects of an offshore wind turbine using the new aeroelastic code hawc2. *Proceedings of the conference "Copenhagen Offshore Wind 2005"*, 2005.

P3

(Journal Article)

Equations of Motion for a Rotor Blade, Including Gravity, Pitch Action and Rotor Speed Variations

Wind Energy, In press

WIND ENERGY
Wind Energ. (in press)
Published online in Wiley Interscience
(www.interscience.wiley.com) DOI: 10.1002/we.217

Research Article

Equations of Motion for a Rotor Blade, Including Gravity, Pitch Action and Rotor Speed Variations

B. S. Kallesøe*, Department of Mechanical Engineering, Technical University of Denmark, Nils Koppels Allé, Building 404, DK-2800 Lyngby, Denmark

Key Words:
horizontal axis turbines;
blade dynamic

This paper extends Hodges–Dowell's partial differential equations of blade motion, by including the effects from gravity, pitch action and varying rotor speed. New equations describing the pitch action and rotor speeds are also derived. The physical interpretation of the individual terms in the equations is discussed. The partial differential equations of motion are approximated by ordinary differential equations of motion using an assumed mode method. The ordinary differential equations are used to simulate a sudden pitch change of a rotating blade. This work is a part of a project on pitch blade interaction, and the model will be extended to include an aerodynamic model and be used for analysis of basic properties of pitch blade interaction. Copyright © 2007 John Wiley & Sons, Ltd.

Received 13 July 2006; Revised 21 November 2006; Accepted 5 December 2006

Introduction

As wind turbines become larger, the interaction between blade motion, pitch action, rotor speed variations and gravity becomes more pronounced. These interactions can result in increased fatigue loads on, for instance, blade components and pitch actuators. A fundamental analysis of the pitch blade interaction can help in the design of pitch actuators and/or solve pitch bearing problems. In further work, this structural model will be combined with an aerodynamic model.

Analysis of, for instance, blade pitch interaction can be split into two different approaches: analytical analysis, such as closed form solutions, direct interpretation of terms and perturbation theory, and numerical analysis, such as finite element analysis and computer simulations, with a variety of combinations in between. Numerical approaches give detailed and relatively precise information about a given blade response to a given operation situation. It can, however, be comprehensive to achieve general information about trends and the physics behind the observed effects, because such information relies on a series of simulations. An analytical approaches often give less accurate result than the numerical analysis, because it has to be very simplified, but it allows for studying general trends and physical interpretation.

In aeroelastic[1] and aeroservoelastic[2] analyses, 2-D blade section models[†] are often used. This is because the reduction in complexity especially in the aerodynamic models of a 2-D blade section model compared to a full 3-D model allows more thorough analytical analysis and much faster numerical simulations.

The frequently cited paper by Hodges and Dowell[3] develops the nonlinear partial differential equations of motion for a twisted helicopter rotor blade. Wendell[4] develops similar partial differential equations of motion

*Correspondence to: B. S. Kallesøe, Department of Mechanical Engineering, Technical University of Denmark, Nils Koppels Allé, Building 404, DK-2800 Lyngby, Denmark.
E-mail: bsk@mek.dtu.dk

[†]2-D blade section models refer to plane models of airfoils supported by springs in a 2-D plane flow field.

focusing on wind turbine applications. Both of these works can handle pre-twisted isotropic blades, but they do not take the interaction with gravity, pitch action and rotor speed variations into account. Their formulation as partial differential equations makes them suitable for analytical analysis. Real turbine blades are made of composite materials, making them anisotropic, leading to internal elastic coupling between different forms of blade motion, which cannot be described by the equations discussed above. The problem by modeling composite materials can be solved by detailed 3-D finite element modeling, which can be done using commercial software. This approach, however, leads to relatively large models with considerable computation time. A turbine blade can also be modeled as a beam, e.g. the reaches code HAWC2[5,6] or the commercial code CAMRAD II,[7] both combining a finite element beam model with multi-body formulation. By combining a beam model with a multi-body formulation, large deflections and rigid body motion such as pitch action can be taken into account. Cesnik, Hodges and Sutyrin[8] present the variational asymptotic beam section analysis (VABS). A method for relating the 3-D elastic energy of a composite blade with initial twist and curvature to the strain energy of a 1-D beam description. In Wenbin *et al*.,[9] the method is refined to produce a Timoshenko-like model for the 1-D strain energy based on the 3-D properties of a blade. Wenbin *et al*.[10] show that using this method to describe a composite blade with a beam model produces accurate results comparable to full 3-D finite element code, but with much less computation time.

This work is a part of a project on describing the interaction between pitch action and blade motion, focusing on control applications. The contribution of this work is to present a model which will be used to analyze the basic properties of interaction between pitch action, gravity effects, rotor speed variations and blade motion.

The blade model is similar to the partial differential equations of motion developed by Hodges[3] and Dowell extended to take pitch action, rotor speed variations and gravity into account. Further, new models for the pitch action and rotor speed are derived. Because the model is intended to be used for first-hand analysis of basic properties of the blade pitch interaction, it rejects features important for a detailed description such as tower motion, yaw error and motion. As a first approach and to keep the equations transparent and simple, the elastic energy is described by Bernoulli–Euler theory, not taking anisotropic and warping effects into account. The elastic energy could instead be described with the more correct and detailed but also more comprehensive description proposed by Cesnik *et al*.[8] and Wenbin *et al*.[9] The formulation of the partial differential equations of motion adopted here leads to a rather comprehensive formulation, compared to that of Wenbin et al,[10] but the detailed notation allows direct interpretation and analysis of individual terms in the equations. The equations are fully written out, and all terms are given a physical interpretation and discussed. A finite difference discretization of the model is used to compute frequencies and shapes for natural vibrations of a test blade. The partial differential equations of motion are transformed into approximating ordinary differential equations of motion by the method of assumed modes, which preserve the possibility of analytical analysis. The approximating ordinary differential equations of motion have a structure similar to the equations of motion for a 2-D blade section; hence, the model can be used to transform properties from a blade model to a 2-D blade section model. The pitch angle and rotor speed in the blade equations can be prescribed, given by external models or described by the pitch action and the rotor speed models derived in this work. The pitch action model can be combined with the blade model giving a pitch angle controlled by a pitch moment, or the pitch moment for a given pitch action and blade motion. The present rotor speed model can be expanded to include more blades, leading to a coupling between the individual blades motion.

The following section presents the model. In the third section, the equations of motion are derived using Hamilton's principle and discussed. In the fourth section, modes of natural vibrations of the blade are found and the blade is approximated by an assumed mode approximation, which is used in a test example.

Model Description

The system consists of a rotating inextensible blade with flapwise, edgewise and torsional degrees of freedom. The blade is exposed to pitch action, varying rotor speed and nonconservative forces (e.g. aerodynamic forces). The rotor speed is associated with a torque and a rotational moment of inertia, describing the generator and drive train without gearing and drive train flexibility. A pitch moment is associated with the pitch action, offer-

DOI: 10.1002/we

ing the possibility of controlling the pitch by a pitch moment or monitoring the pitch moment having a prescribed pitch.

The system does not include the influence from tower and yaw motion, drive train flexibility, precone blade, shaft tilt and warping. The shear center* and the tension center† of the blade are assumed to coincide. These simplifications are justified because the focus is on analyzing pitch blade interaction, not to give a complete description of a wind turbine.

Figure 1 (a) shows the blade rotating in the rotor plane. The *Y*-axis of the (*X, Y, Z*)-frame points downwind and the (*X*, *Z*)-axis spans the rotor plane, with the *Z*-axis pointing upward. Since the tower-top and yaw position are assumed fixed, the (*X, Y, Z*)-frame becomes an inertial frame. The ($\hat{x}$, $\hat{y}$, $\hat{z}$)-frame rotates with the hub, such that the $\hat{z}$-axis is aligned with the pitch axis *pi* of the blade and the $\hat{y}$-axis is aligned with the *Y*-axis. The angle between the two frames is denoted ϕ (the azimuth angle of the rotor).

Figure 1 (b) shows a cross section of the blade looking outward along the $\hat{z}$-axis. The position of the blade is described in the (*x, y, z*)-frame, which is rotated β (the pitch angle) around the $\hat{z}$-axis. The elastic principle (η, ξ)-axis of each blade section, is rotated the angle $\tilde{\theta} + \theta$ relative to the (*x*, *z*)-plane, where $\tilde{\theta} = \tilde{\theta}(s)$ is the pre-twist of the elastic properties and $\theta = \theta(s, t)$ is the time-dependent twist of the blade section.

The position of the elastic axis *ea* in the (*x, y, z*)-frame is given by ($u + l_{pi}$, v, w), where $u = u(s, t)$ and $v = v(s, t)$ are the deflection from the undeformed position in the *x*- and *y*-direction, respectively, and $l_{pi} = l_{pi}(s)$ is the undeformed position of *ea* on the *x*-axis. The position in the *z*-direction is given by $w = \int_r^s \sqrt{\left(1-\left(l'_{pi}+u'\right)^2 - v'^2\right)}\mathrm{d}s$, based on the inextensibility of the blade. The *w* coordinate is split into a static part $w_0 = \int_r^s \sqrt{1-l'^2_{pi}}\,\mathrm{d}s$ and an approximation to the time-dependent part $w_1 = -\frac{1}{2}\int_r^s \sqrt{u'^2+v'^2+2l'_{pi}u'}\,\mathrm{d}s$. The independent variables *t* and *s* are the time and the distance from the root of the blade measured along *ea*, respectively. The radius of the hub is *r* and the radius of the rotor is *R*, measured along the elastic axis.

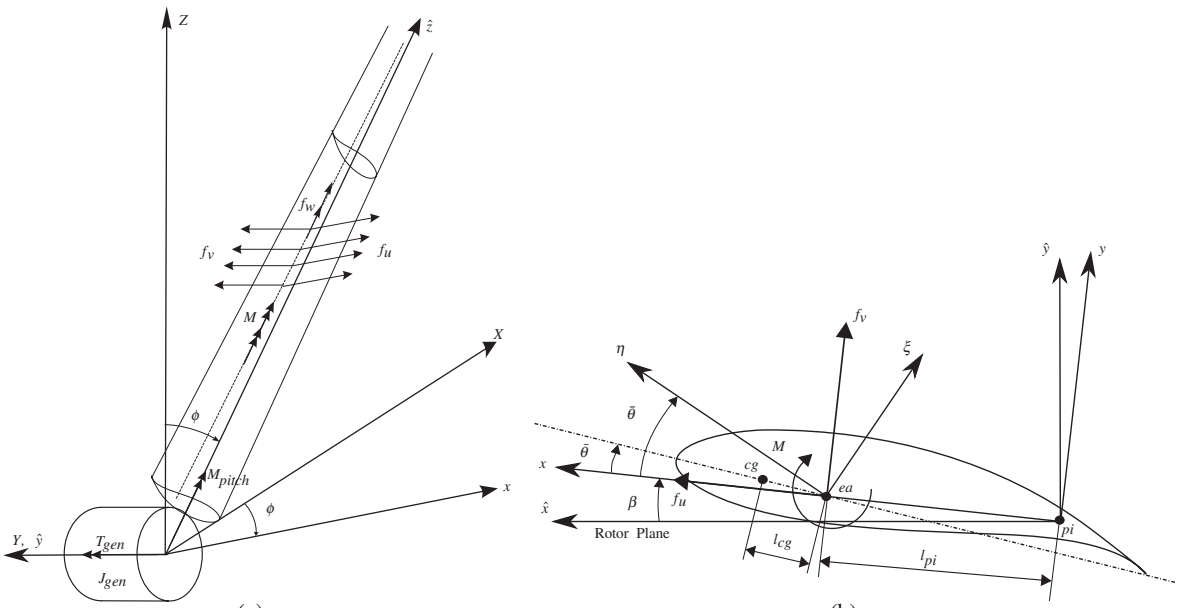

Figure 1. (a) The inertial (X, Y, Z)-frame and the rotating ($\hat{x}$, $\hat{y}$, $\hat{z}$)-frame with the $\hat{z}$-axis aligned with the pitch axis of the blade. The external forces (f_u, f_v, f_w) act at the elastic axis in the ($\hat{x}$, $\hat{y}$, $\hat{z}$)-directions, respectively. (b) Cross section of the blade looking outward along the $\hat{z}$-axis

*The point on the blade cross section where a force in the cross section plane only causes bending, no twist.
†The point on the blade cross section where a tension force does not cause any bending.

DOI: 10.1002/we

The sum of rotational inertia of the hub, gearbox and generator is described by J_{gen}. The inertia of the blade is described by a concentrated mass $m = m(s)$ and a moment of rotational inertia $I_{cg} = I_{cg}(s)$ (for rotation in the cross section plane) for each blade section, both related to the center of gravity cg. The center of gravity is assumed to be located on the chord, the distance $l_{cg} = l_{cg}(s)$ from ea. The chord is rotated, the angle $\bar{\theta} + \theta$ relative to the (x, z)-plane, where $\bar{\theta} = \bar{\theta}(s)$ is the pre-twist of the chord.

The external forces, such as aerodynamic forces, on the blade are described by four components; three forces $(f_u, f_v, f_w) = (f_u(s, t), f_v(s, t), f_w(s, t))$ in the (x, y, z)-directions, respectively and a twisting moment $M = M(s, t)$. The forces act at the elastic axis of the blade.

The pitch moment M_{pitch} is associated with this pitch angle rotation and the generator torque is given by T_{gen}.

In summary, the state of the system is given by $(u, v, \theta, \beta, \phi)$ where (ϕ, β) can be prescribed, given by external models or described by the derived equations. The system is exposed to the external loads $(f_u, f_v, f_w, M, T_{gen}, M_{pitch})$, where (T_{gen}, M_{pitch}) only affects the (ϕ, β) equations, respectively.

Derivation of the Equations of Motion

The derivation of the equations of motion follows the method used in Hodges and Dowell.[3] First, the potential and kinetic energies for the system are set-up, then the equations of motion and boundary condition equations are derived from these energy expressions using the extended Hamilton's principle.[11]

Order Scheme

To avoid unnecessary complications of the equations of motion, relatively small terms are neglected. This is done in a consistent manner by introducing an ordering scheme, assuming $\left(\frac{u}{R}, \frac{v}{R}, \frac{l_{pi}}{R}, \frac{l_{cg}}{R}, \theta, c\tilde{\theta}', c\bar{\theta}', \frac{m'l_{cg}}{ml'_{cg}}\right)$ to be of order ε, where $c = c(s)$ is the local chord, $\varepsilon << 1$ is a bookkeeping parameter denoting the smallness of terms, $\dot{(\,)} \equiv \frac{\mathrm{d}}{\mathrm{d}t}$ and $(\,)' \equiv \frac{\mathrm{d}}{\mathrm{d}s}$. The angular acceleration of the rotor is assumed to be $\ddot{\phi}R \sim \ddot{u}$. The ordering scheme is applied such that terms of order ε^{n+2} or higher are neglected, where n is the lowest order of a term in the expression.

Transformations

Before deriving the equations of motion, a transformation between the rotating (x, y, z)-frame in which the blade deflection is described and the inertial (X, Y, Z)-frame is found:

$$[\mathbf{i}, \mathbf{j}, \mathbf{k}]^{\mathrm{T}} = \mathbf{T}_{\beta}\mathbf{T}_{\phi}[\mathbf{I}, \mathbf{J}, \mathbf{K}]^{T} \tag{1}$$

where $[\mathbf{i}, \mathbf{j}, \mathbf{k}]^{\mathrm{T}}$ and $[\mathbf{I}, \mathbf{J}, \mathbf{K}]^{\mathrm{T}}$ are the unit vectors in the (x, y, z) and (X, Y, Z)-frames, respectively. The matrices $\mathbf{T}_{\beta}$ and $\mathbf{T}_{\phi}$ are the transformations from the $(\hat{x}, \hat{y}, \hat{z})$-frame to the (x, y, z)-frame and from the (X, Y, Z)-frame to the $(\hat{x}, \hat{y}, \hat{z})$-frame, respectively. Both matrices are given in Appendix A.

The transformation between the principle axis and the (x, y, z)-frame is given by $\mathbf{T}_e$ and between the chord and the (x, y, z)-frame is given by $\mathbf{T}_c$. Both matrices are given in Appendix A.

Potential Energy

The strain in the blade is measured by Green's strain tensor (cf. Hodges and Dowell[3]):

$$2[\mathrm{d}s, \mathrm{d}\eta, \mathrm{d}\xi][\varepsilon_{ij}][\mathrm{d}s, \mathrm{d}\eta, \mathrm{d}\xi]^{\mathrm{T}} = \mathrm{d}\mathbf{r}_1 \cdot \mathrm{d}\mathbf{r}_1 - \mathrm{d}\mathbf{r}_0 \cdot \mathrm{d}\mathbf{r}_0 \tag{2}$$

where d denotes the differential, ε_{ij} is the strain tensor and

$$\mathbf{r}_0 = [\mathbf{I}, \mathbf{J}, \mathbf{K}]\mathbf{T}_{\phi}^{\mathrm{T}}\mathbf{T}_{\beta}^{\mathrm{T}}\left[[l_{pi}, 0, w_0]^{\mathrm{T}} + (\mathbf{T}_e|_{u=v=\theta=0})^{\mathrm{T}}[\eta_0, \xi_0, 0]^{\mathrm{T}}\right] \tag{3}$$

DOI: 10.1002/we

is a position vector describing a point in the undeformed blade, where (η_0, ξ_0) is the position of the point in the undeformed blade section. The same point in the deformed blade is given by

$$\mathbf{r}_1 = [\mathbf{I}, \mathbf{J}, \mathbf{K}]\mathbf{T}_\phi^{\mathrm{T}}\mathbf{T}_\beta^{\mathrm{T}}[[l_{pi} + u, v, w_0 + w_1]^{\mathrm{T}} + \mathbf{T}_c^{\mathrm{T}}[\eta_1, \xi_1, 0]^{\mathrm{T}}] \tag{4}$$

where (η_1, ξ_1) is the position of the point in the deformed blade section.

Assuming uniaxial stress $\sigma_{22} = \sigma_{33} = \sigma_{23} = 0$, where σ_{ij} is the stress tensor. Applying Hook's law gives $\varepsilon_{22} = \varepsilon_{33} = -v\varepsilon_{11}$, where v is Poisson's ratio. By expanding these relations to second order of the bookkeeping parameter ε, it can be shown that $\eta_1 = \eta_0$ and $\xi_1 = \xi_0$ to second order. Expanding the remanding strain tensor components to second order of ε gives

$$\begin{aligned} \varepsilon_{11} &= -u''\left(\eta\cos(\bar{\theta}) - \xi\sin\left(\hat{\theta}\right)\right) - v''\left(\eta\sin\left(\hat{\theta}\right) + \xi\cos(\bar{\theta})\right) \\ \varepsilon_{12} &= -\frac{1}{2}\xi\theta', \quad \varepsilon_{13} = \frac{1}{2}\eta\theta' \end{aligned} \tag{5}$$

Using engineering strain $\varepsilon_{ss} = \varepsilon_{11}$, $\varepsilon_{s\eta} = 2\varepsilon_{12}$, $\varepsilon_{s\xi} = 2\varepsilon_{13}$ and stresses $\sigma_{ss} = E\varepsilon_{ss}$, $\sigma_{s\eta} = G\varepsilon_{s\eta}$, $\sigma_{s\xi} = G\varepsilon_{s\xi}$ where E is the tensile modulus of elasticity (Young's modulus) and G is the shear modulus of elasticity, the elastic energy becomes

$$\delta V_{ela} = \int_r^R \iint_A (\sigma_{ss}\delta\varepsilon_{ss} + \sigma_{s\eta}\delta\varepsilon_{s\eta} + \sigma_{s\xi}\delta\varepsilon_{s\xi})\mathrm{d}\eta\mathrm{d}\xi\mathrm{d}s \tag{6}$$

The potential energy associated with the gravity field measured from the inertial frame (X, Y, Z) is described by

$$V_{gra} = \int_r^R \mathbf{r}_{cg}^T \cdot \mathbf{g}\mathrm{d}s \tag{7}$$

where $\mathbf{g} = [0, 0, -g]^{\mathrm{T}}$ is the gravity field and

$$\mathbf{r}_{cg} = [\mathbf{I}, \mathbf{J}, \mathbf{K}]\mathbf{T}_\phi^{\mathrm{T}}\mathbf{T}_\beta^{\mathrm{T}}[[l_{pi} + u, v, w_0 + w_1]^{\mathrm{T}} + \mathbf{T}_c^{\mathrm{T}}[l_{cg}, 0, 0]^{\mathrm{T}}] \tag{8}$$

is a position vector describing the center of gravity.

Kinetic Energy

The inertia of the system is described by a mass pr. length m, a moment of rotational inertia pr. length I_{cg} of the blade and a moment of rotational inertia J_{gen} that describes the hub, gear box and generator. The use of concentrated mass description of the blade inertia, instead of a more general description integration over the cross section, leads much to less complexity in the derivation. A general description will lead to extra terms, such as rotational inertiae about x- and y-axis, but these terms turn out to be relatively small anyway. The kinetic energy of the system is given by

$$T = \frac{1}{2}J_{gcn}\dot{\phi}^2 + \int_r^R \left(\frac{1}{2}m\mathbf{r}_{cg}^{\mathrm{T}} \cdot \dot{\mathbf{r}}_{cg} + \frac{1}{2}I_{cg}\left(\dot{\beta} + \dot{\theta}\right)^2\right)\mathrm{d}s \tag{9}$$

where $\dot{\beta} + \dot{\theta}$ is the angular velocity of the blade section around the elastic axis.

Nonconservative Forces

The nonconservative forces are taken into account by describing the variational work done by them for any admissible variation:

$$\delta Q = T_{gcn}\delta\phi + M_{pitch}\delta\beta + \int_r^R (\mathbf{f}^{\mathrm{T}} \cdot \delta\mathbf{r}_{ea} + M\delta(\theta + \beta))\mathrm{d}s \tag{10}$$

where $\mathbf{f} = \mathbf{T}_\phi^{\mathrm{T}}\mathbf{T}_\beta^{\mathrm{T}}[f_u, f_v, f_w]^{\mathrm{T}}$ and

$$\mathbf{r}_{ea} = [\mathbf{I}, \mathbf{J}, \mathbf{K}]\mathbf{T}_\phi^{\mathrm{T}}\mathbf{T}_\beta^{\mathrm{T}}[l_{pi} + u, v, w_0 + w_1]^{\mathrm{T}} \tag{11}$$

is a position vector describing the elastic axis.

DOI: 10.1002/we

Equations of Motion

By demanding that any admissible variation of the action integral $\delta H \equiv \int_{t_1}^{t_2}(\delta T - \delta V_{ela} - \delta V_{gra} + \delta Q)dt$ is zero, a set of partial differential equations of motion and a set of boundary condition equations are derived (extended Hamilton's principle[11]). The variation of the w_1 term leads to integral terms in the equations of motion, while the w_1 itself does not appear because it is relatively small. First, the partial differential equations of blade bending and torsional motion are presented, followed by the corresponding boundary conditions. Second, the equations of motion for the rotor azimuth angle and the pitch angle are presented.

Blade Bending Motion

The equation of motion of the *x*- and *y*-directions becomes

$$\begin{aligned} &m(\ddot{u} - \ddot{\theta} l_{cg}\sin(\bar{\theta})) + F_{u,1}(\ddot{\beta}, \dot{\beta}, \dot{\phi}, \dot{v}, \dot{\theta}, u', u, v, \theta, \beta) + F_{u,2}(\dot{\phi}, \dot{u}, \dot{v}, u', v, \theta, \beta) \\ &+ F_{u,3}(\phi, \beta, \theta, u', v') + F_{u,4}(u'', v'', \theta) + F_{u,5}(\ddot{\phi}, \beta) = f_u + \left((u' + l'_{pi})\int_s^R f_w \mathrm{d}\rho\right)' \end{aligned} \tag{12a}$$

$$\begin{aligned} &m(\ddot{v} + \ddot{\theta} l_{cg}\cos(\bar{\theta})) + F_{v,1}(\ddot{\beta}, \dot{\beta}, \dot{\phi}, \dot{\theta}, v', u, v, \theta, \beta) + F_{v,2}(\dot{\phi}, \dot{u}, \dot{v}, u', v, \theta, \beta) \\ &+ F_{v,3}(\phi, \beta, \theta, u', v') + F_{v,4}(u'', v'', \theta) + F_{v,5}(\ddot{\phi}, \beta) = f_v + \left(v'\int_s^R f_w \mathrm{d}\rho\right)' \end{aligned} \tag{12b}$$

The direction of the *x*- and *y*-axis can be swapped by changing the β angle, hence the only differences between the terms in equations (12a) and (12b) are the directions of projection of the forces. In the following, the individual terms in equation (12) are shown and the physical interpretation of them is discussed. Because of the similarity between the terms from equations (12a) and (12b), only the terms from equation (12a) will be discussed.

The influence of pitch action is described by

$$F_{u,1} = -\ddot{\beta} m v_{cg} - \dot{\beta}^2 m u_{cg} - 2\dot{\beta} m \dot{v}_{cg} + (T_1 l_{cg}\cos(\bar{\theta}))' + \left((u' + l'_{pi})\int_s^R T_1 \mathrm{d}\rho\right)' \tag{13a}$$

$$F_{u,1} = \ddot{\beta} m u_{cg} - \dot{\beta}^2 m v_{cg} + 2\dot{\beta} m \dot{u}_{cg} + (T_1 l_{cg}\sin(\bar{\theta}))' + \left(v'\int_s^R T_1 \mathrm{d}\rho\right)' \tag{13b}$$

Where $u_{cg} = u + l_{pi} + l_{cg}\cos(\bar{\theta}) - l_{cg}\theta\sin(\bar{\theta})$ and $v_{cg} = v + l_{cg}\sin(\bar{\theta}) + l_{cg}\theta\cos(\bar{\theta})$ are the *x* and *y* coordinates of the center of gravity in the (*x*, *y*, *z*)-frame, respectively, $T_1 = 2m\dot{\beta}\dot{\phi}((u + l_{pi})\sin(\beta) + v\cos(\beta) + l_{cg}\sin(\bar{\theta} + \beta))$ is the Coriolis force in the *z*-direction, associated with the angular velocity of the (*x*, *y*, *z*)-frame about the *z*-axis and about the $\hat{y}$-axis. The first term in equation (13a) is the fictitious force* in the *x*-direction associated with the angular acceleration of the (*x*, *y*, *z*)-frame about the *z*-axis. The second term is the fictitious centrifugal force associated with the angular velocity of the (*x*, *y*, *z*)-frame about the *z*-axis and the offset of *cg* in the *x*-direction. The third term is the Coriolis force associated with the angular velocity of the (*x*, *y*, *z*)-frame about the *z*-axis and the velocity of *cg* in the *y*-direction. The fourth term in equation (13a) is the spatial derivative of the moment caused by the offset of *cg* and the Coriolis force T_1. The last term is the bending moment caused by the Coriolis force T_1 on the remaining part of the blade, from this point to the tip. The influence from the rotor speed is described by

$$\begin{aligned} F_{u,2} = &-\dot{\phi}^2 m \hat{u}_{cg}\cos(\beta) - \dot{\phi}^2(m l_{cg} w_0(\cos(\bar{\theta}) - \theta\sin(\bar{\theta})))' - (l_{cg}T_2)'\cos(\bar{\theta}) \\ &- 2\dot{\phi} m l_{cg}(\dot{u}'\cos(\bar{\theta}) + \dot{v}'\sin(\bar{\theta}))\cos(\beta) - \left((u' + l'_{pi})\int_s^R(\dot{\phi}^2 m w_0 + T_2)\mathrm{d}\rho\right)' \end{aligned} \tag{14a}$$

$$\begin{aligned} F_{v,2} = &\dot{\phi}^2 m \hat{u}_{cg}\sin(\beta) - \dot{\phi}^2(m l_{cg} w_0(\sin(\bar{\theta}) + \theta\cos(\bar{\theta})))' - (l_{cg}T_2)'\sin(\bar{\theta}) \\ &+ 2\dot{\phi} m l_{cg}(\dot{u}'\cos(\bar{\theta}) + \dot{v}'\sin(\bar{\theta}))\sin(\beta) - \left(v'\int_s^R(\dot{\phi}^2 m w_0 + T_2)\mathrm{d}\rho\right)' \end{aligned} \tag{14b}$$

*Fictitious force refers to a force that occurs because the system is described in a moving frame.

DOI: 10.1002/we

where $\hat{u}_{cg} = (u + l_{pi})\cos(\beta) - v\sin(\beta) + l_{cg}\cos(\bar{\theta} + \beta) - l_{cg}\theta\sin(\bar{\theta} + \beta)$ is the $\hat{x}$ coordinate of the center of gravity given in the $(\hat{x}, \hat{y}, \hat{z})$-frame, $T_2 = 2m\dot{\phi}(\dot{u}\cos(\beta) - \dot{v}\sin(\beta))$ is the Coriolis force in the z-direction associated with the rotation in the rotor plane and the velocity of cg in the $\hat{x}$-direction The first term in equation (14a) is the fictitious centrifugal force associated with the rotation in the rotor plane and the offset of cg in the x-direction projected onto the x-direction. The second and third terms in equation (14a) are the spatial derivative of the moment caused by the distance from cg to ea in the x-direction and the fictitious centrifugal and the Coriolis force T_2, respectively. The centrifugal force is associated with the rotation in the rotor plane and the offset of cg from the center of rotation. The fourth term is the fictitious Coriolis force associated with the rotation of the blade in the rotor plane and the velocity of cg in the $\hat{z}$-direction The last term in equation (14a) is the bending moment from the fictitious centrifugal and the Coriolis force T_2 on the remaining part of the blade from this point to the tip. The influence from gravity is described by

$$\begin{aligned} F_{u,3} = {} & mg\sin(\phi)\cos(\beta) + \left((l_{cg}(u' + l'_{pi}))'\cos(\bar{\theta})\cos(\beta) + (l_{cg}v')'\sin(\bar{\theta})\cos(\beta)mg\sin(\phi)\right. \\ & \left. - (ml_{cg}(\cos(\bar{\theta}) - \theta\sin(\bar{\theta})))'g\cos(\phi) + \left((u' + l'_{pi})\int_s^R mg\cos(\phi)\mathrm{d}\rho\right)'\right. \end{aligned} \tag{15a}$$

$$\begin{aligned} F_{u,3} = {} & -mg\sin(\phi)\sin(\beta) + \left((l_{cg}(u' + l'_{pi}))'\sin(\bar{\theta})\cos(\beta) - (l_{cg}v')'\sin(\bar{\theta})\sin(\beta)\right)mg\sin(\phi) \\ & - (ml_{cg}(\sin(\bar{\theta}) - \theta\cos(\bar{\theta})))'g\cos(\phi) + \left(v'\int_s^R mg\cos(\phi)\mathrm{d}\rho\right)' \end{aligned} \tag{15b}$$

where the first term in equation (15a) is the x-component of the gravity force. The second term is the spatial derivative of the moment caused by the $\hat{x}$-component of the gravity force and the offset of cg in the z-direction. The third term is the spatial derivative of the moment caused by the distance between cg and ea in the x-direction and the z-component of the gravity force. The last term in equation (15a) is the bending moment from the z-component of the gravity force on the remaining part of the blade, from this point to the tip. The restoring force caused by the bending stiffness of the blade is described by

$$\begin{aligned} F_{u,4} = {} & \left(E\left(I_\xi\cos^2\left(\tilde{\theta}\right) + I_\eta\sin^2\left(\tilde{\theta}\right)\right)u''\right)'' + \left(E(I_\xi - I_\eta)\cos\left(\tilde{\theta}\right)\sin\left(\tilde{\theta}\right)v''\right)'' \\ & - \left(E(I_\xi - I_\eta)\theta\left(u''\sin\left(2\tilde{\theta}\right) - v''\cos\left(2\tilde{\theta}\right) + l''_{pi}\sin\left(\tilde{\theta}\right)\cos\left(\tilde{\theta}\right)\right)\right)'' \end{aligned} \tag{16a}$$

$$\begin{aligned} F_{v,4} = {} & \left(E\left(I_\xi\sin^2\left(\tilde{\theta}\right) + I_\eta\cos^2\left(\tilde{\theta}\right)\right)v''\right)'' + \left(E(I_\xi - I_\eta)\cos\left(\tilde{\theta}\right)\sin\left(\tilde{\theta}\right)u''\right)'' \\ & + \left(E(I_\xi - I_\eta)\theta\left(u''\cos\left(2\tilde{\theta}\right) + v''\sin\left(2\tilde{\theta}\right)\right)\right)'' - (l''_{pi}\theta E(I_\xi\sin^2(\theta) + I_\eta\cos^2(\theta)))'' \end{aligned} \tag{16b}$$

where the first term is the bending stiffness in the x-direction, the second term is the coupling to the v-direction, and the last term is the coupling to the twist. The principle moments of inertia are given by $I_\xi = \int\int_A \eta^2\mathrm{d}\eta\mathrm{d}\xi$ and $I_\eta = \int\int_A \xi^2\mathrm{d}\eta\mathrm{d}\xi$. The effect of an angular acceleration of the rotor is described by

$$F_{u,5} = m\ddot{\phi}w_0\cos(\beta), \quad F_{v,5} = -m\ddot{\phi}w_0\sin(\beta) \tag{17}$$

which is the fictitious angular acceleration of cg associated with the angular acceleration of the (x, y, z)-frame about the Y-axis. The right hand side of equations (12a) and (12b) describes the external forces, f_u and f_v are the forces in the x- and y-directions, respectively. The last term is the bending moment from the external force in the z-direction on the remaining part of the blade, from this point to the tip.

Blade Torsional Motion

The equation of torsional motion is

$$\begin{aligned} & \left(I_{cg} + ml_{cg}^2\right)\ddot{\theta} - ml_{cg}\left(\ddot{u}\sin(\bar{\theta}) - \ddot{v}\cos(\bar{\theta})\right) + F_{\theta,1}\left(\dot{\phi}, u', v', u, v, \beta\right) + F_{\theta,2}\left(\ddot{\beta}, \dot{\beta}, \dot{u}, \dot{v}, u, v\right) \\ & \quad + F_{\theta,3}\left(\ddot{\phi}, \beta\right) + F_{\theta,4}\left(\phi, u', v', \theta, \beta\right) + F_{\theta,5}\left(u'', v'', \theta'\right) + F_{\theta,6}\left(\theta'\right) = M \end{aligned} \tag{18}$$

DOI: 10.1002/we

where the rotor speed leads to the fictitious centrifugal forces:

$$F_{\theta,1} = ml_{cg}\dot{\phi}^2\hat{u}_{cg}\sin(\bar{\theta}+\beta) + ml_{cg}w_0\phi^2(v'\cos(\bar{\theta}) - (u'+l'_{pi})\sin(\bar{\theta})) \tag{19}$$

where the first term is associated with the offset of *cg* in the $\hat{x}$-direction and the second is associated with the distance from the center of rotation to *cg*. The influence from the pitch action is described by

$$\begin{aligned} F_{\theta,2} = {} & (I_{cg} + ml_{cg}^2)\ddot{\beta} - \ddot{\beta}ml_{cg}(u\cos(\bar{\theta}) + v\sin(\bar{\theta})) + ml_{cg}\dot{\beta}^2((u+l_{pi})\sin(\bar{\theta}) - v\cos(\bar{\theta})) \\ & + 2ml_{cg}\dot{\beta}(\dot{u}\cos(\bar{\theta}) + \dot{v}\sin(\bar{\theta})) \end{aligned} \tag{20}$$

where the first term is the fictitious angular acceleration associated with the angular acceleration of the (*x*, *y*, *z*)-frame about the *z*-axis. The second term is the fictitious centrifugal force associated with the rotation of the (*x*, *y*, *z*)-frame about the *z*-axis. The last term is the fictitious Coriolis force associated with the rotation of the (*x*, *y*, *z*)-frame about the *z*-axis and the velocity of *cg* in the chord direction. The acceleration of the rotor leads to the following term:

$$F_{\theta,3} = -m\ddot{\phi}w_0 l_{cg}\sin(\bar{\theta}+\beta) \tag{21}$$

which is the fictitious angular acceleration of *cg* associated with the angular acceleration of the (*x*, *y*, *z*)-frame about the *Y*-axis. The effect of gravity is described by

$$F_{\theta,4} = -l_{cg}(\sin(\beta+\bar{\theta}) + \theta\cos(\beta+\bar{\theta}))mg\sin(\phi) + l_{cg}(v'\cos(\bar{\theta}) - (u'+l'_{pi})\sin(\bar{\theta}))mg\cos(\phi) \tag{22}$$

where the first term is the twisting moment caused by the $\hat{x}$-component of the gravity force and the distance between *cg* and *ea* in the $\hat{y}$-direction. The last term is the twisting moment caused by the distance between *cg* and *ea* and the *z*-component of the gravity force projected onto the cross section of the deformed blade. The elastic coupling between the bending and twisting of the blade is described by

$$\begin{aligned} F_{\theta,5} = {} & -\left(EI_{\eta\eta\xi}(\tilde{\theta}+\theta)'(u''\sin(\bar{\theta}) - v''\cos(\theta))\right)' + \left(EI_{\eta\xi\xi}(\tilde{\theta}+\theta)'(u''\cos(\tilde{\theta}) + v''\sin(\tilde{\theta}))\right)' \\ & - (EI_{\xi} - EI_{\eta})((u''^2 - v''^2)\cos(\tilde{\theta})\sin(\tilde{\theta}) - u''v''\cos(2\tilde{\theta})) \\ & - EI_{\xi}l''_{pi}(u''\cos(\tilde{\theta}) + v''\sin(\tilde{\theta}))\sin(\tilde{\theta}) + EI_{\eta}l''_{pi}(u''\sin(\tilde{\theta}) - v''\cos(\tilde{\theta}))\cos(\tilde{\theta}) \end{aligned} \tag{23}$$

where $I_{\eta\eta\xi} = \int\int_A \eta(\eta^2 + \xi^2)\mathrm{d}\eta\mathrm{d}\xi$ and $I_{\eta\xi\xi} = \int\int_A \xi(\eta^2 + \xi^2)\mathrm{d}\eta\mathrm{d}\xi$. The restoring force caused by torsional stiffness is given by

$$F_{\theta,6} = -(GJ(\theta' + v'(u'' + l''_{pi})))' \tag{24}$$

where the polar moment of inertia is $J = \int\int_A (\eta^2 + \xi^2)d\eta d\xi$. The right hand side describes the external moment on the blade *M*.

Boundary Conditions

The boundary conditions for the root of the blade are given by the geometric constraints:

$$u(0,t) = u'(0,t) = v(0,t) = v'(0,t) = \theta(0,t) = 0 \tag{25}$$

because the coordinate frame used to describe the blade follows the root of the blade.

The boundary conditions for the tip of the blade are determined by the boundary condition equations derived by demanding any admissible variation of the action integral to be zero. The boundary conditions become

$$\begin{aligned} & u''(R,t) = v''(R,t) = \theta'(R,t) = 0 \\ & EI_{\xi}I_{\eta}u'''(R,t) = ml_{cg}(\dot{\phi}^2 w_0 - g\cos(\phi))(I_{\eta}\sin(\tilde{\theta}-\bar{\theta})\sin(\bar{\theta}) + I_{\xi}\cos(\tilde{\theta}-\bar{\theta})\cos(\tilde{\theta})) \\ & EI_{\xi}I_{\eta}v'''(R,t) = ml_{cg}(\dot{\phi}^2 w_0 - g\cos(\phi))(I_{\eta}\cos(\tilde{\theta}-\bar{\theta})\sin(\tilde{\theta}) - I_{\xi}\sin(\tilde{\theta}-\bar{\theta})\cos(\tilde{\theta})) \end{aligned} \tag{26}$$

DOI: 10.1002/we

If $l_{cg}(R) \neq 0$, the boundary conditions for the tip are functions of rotor speed $\dot{\phi}$ and rotor position ϕ and therefore time-varying. This is because an offset of the center of gravity from the elastic axis at the blade tip leads to a bending moment at the tip, caused by the gravity and centrifugal force. Most modern wind turbine blades, however, are tapered at the tip, leading to $l_{cg}(R)/R << \varepsilon$, making the time variation of the boundary conditions negligible.

Pitch Action

The equation of motion for the pitch angle is

$$\begin{aligned}&\int_r^R \left((I_{cg} + ml_{cg}^2)\left(\ddot{\theta} + \ddot{\beta}\right) + m\left(l_{pi}^2 + 2l_{cg}l_{pi}\cos(\bar{\theta})\right)\ddot{\beta} - m\ddot{u}l_{cg}\sin(\bar{\theta}) + m\ddot{v}(l_{pi} + l_{cg}\cos(\bar{\theta}))\right)\mathrm{d}s + F_{\beta,1}\left(\dot{\beta}, \dot{u}, u\right)\\ &\quad + F_{\beta,2}\left(\dot{\beta}, \dot{v}, v\right) + F_{\beta,3}\left(\dot{\phi}, u, v, \beta\right) + F_{\beta,4}\left(\ddot{\phi}, u, v, \beta\right) + F_{\beta,5}\left(u, v, \theta, \beta, \phi\right) + F_{\beta,6}\left(\ddot{\beta}, \ddot{u}, \ddot{v}, u, v\right)\\ &= M_{pitch} + \int_r^R (M + f_v(u + l_{pi}) - f_u v)\mathrm{d}s\end{aligned} \tag{27}$$

where

$$F_{\beta,1}\left(\dot{\beta}, \dot{v}, u\right) = 2\dot{\beta}\int_r^R m\dot{u}u_{cg}\mathrm{d}s, \quad F_{\beta,2}\left(\dot{\beta}, \dot{v}, u\right) = 2\dot{\beta}\int_r^R m\dot{v}v_{cg}\mathrm{d}s \tag{28}$$

are the moments caused by the fictitious Coriolis force associated with the relative velocity of the blade and rotation of the (x, y, z)-frame about the z-axis. The effect of the fictitious centrifugal force associated with the rotation of the (x, y, z)-frame about the $\hat{y}$-axis is described by

$$F_{\beta,3}\left(\dot{\phi}, u, v, \beta\right) = \dot{\phi}^2\int_r^R m\hat{u}_{cg}\hat{v}_{cg}\mathrm{d}s \tag{29}$$

where $\hat{v}_{cg} = (u + l_{pi})\sin(\beta) + v\cos(\beta) + l_{cg}\sin(\bar{\theta} + \beta)$ is the $\hat{y}$ coordinate of the center of gravity in the ($\hat{x}$,$\hat{y}$,$\hat{z}$)-frame. The effect of an angular acceleration of the (x, y, z)-frame about the $\hat{y}$-axis is described by

$$F_{\beta,4}\left(\ddot{\phi}, u, v, \beta\right) = -\ddot{\phi}\int_r^R mw_0\hat{v}_{cg}\mathrm{d}s \tag{30}$$

The gravity force is described by

$$F_{\beta,5}(u, v, \beta, \phi) = g\sin(\phi)\int_r^R m\hat{v}_{cg}\mathrm{d}s \tag{31}$$

and

$$F_{\beta,6}\left(\ddot{\beta}, \ddot{u}, \ddot{v}, u, v\right) = \ddot{\beta}\int_r^R m\left(u^2 + v^2 + 2l_{cg}\left(u\cos(\bar{\theta}) + v\sin(\bar{\theta})\right) + 2l_{pi}u\right)\mathrm{d}s + \int_r^R m(\ddot{v}u - \ddot{u}v)\mathrm{d}s \tag{32}$$

is nonlinear inertia.

If the pitch angle is prescribed or given by an external model, equation (27) can be used to compute the pitch moment, by solving for M_{pitch} and feed in the blade motion and pitch action.

Rotor Position

Assuming a rigid drive train and no gearing, the rotor position is described by

$$\begin{aligned}&J_{gcn}\ddot{\phi} + \int_r^R mw_0\left(w_0\ddot{\phi} + u\cos(\beta) - \ddot{v}\sin(\beta)\right)\mathrm{d}s\\ &\quad + F_{\phi,1}\left(\dot{\beta}, u, v, \beta\right) + F_{\phi,2}\left(\dot{\beta}, \dot{u}, \dot{v}, \dot{\theta}, \beta\right) + F_{\phi,3}\left(u, \phi\right) + F_{\phi,4}\left(\ddot{\beta}, u, v, \beta\right)\\ &= T_{gcn} + \int_r^R \left(\left(f_u\cos(\beta) - f_v\sin(\beta)\right)w_0 + f_w\left(v\sin(\beta) - (u + l_{pi})\cos(\beta)\right)\right)\mathrm{d}s\end{aligned} \tag{33}$$

The effect of the fictitious centrifugal force associated with rotation of the (x, y, z)-frame about the z-axis is described by

$$F_{\phi,1}\left(\dot{\beta}, u, v, \beta\right) = -\dot{\beta}^2\int_r^R mw_0\hat{u}_{cg}\mathrm{d}s \tag{34}$$

DOI: 10.1002/we

and

$$F_{\phi,2}(\dot{\beta}, \dot{u}, \dot{v}, \dot{\theta}, \beta) = -2\dot{\beta}\int_r^R mw_0(\dot{u}\sin(\beta) + \dot{v}\cos(\beta))\mathrm{d}s \tag{35}$$

describes the fictitious Coriolis force associated with the rotation of the (x, y, z)-frame about the z-axis and the relative velocity of the blade. The effect of gravity is described by

$$F_{\phi,3}(u, \phi) = g\sin(\phi)\int_r^R mw_0\mathrm{d}s + g\cos(\phi)\int_r^R m\hat{u}_{cg}\mathrm{d}s \tag{36}$$

and

$$F_{\phi,4}(\ddot{\beta}, u, v, \beta) = -\ddot{\beta}\int_r^R mw_0\hat{v}_{cg}\mathrm{d}s \tag{37}$$

describes the fictitious acceleration associated with an angular acceleration of the (x, y, z)-frame about the z-axis.

The effect from the forces on the blade and the motion of the blade on the rotor speed is described by the two integral terms in equation (33) and by equations (34) to (37).

The rotor speed equation (33) only includes the effects from one blade, but it can be extended to include the effects from more blades by adding an extra of the two integral terms in equation (33) and one of equations (34) to (37) for each extra blade.

Discussion

Comparing the partial differential equations of motion (equations (12) and (18)) with Hodges and Dowell's,[3] it is noticed that the gravity terms (equations (15) and (22)), the pitch action terms (equations (13a) and (20)) and the terms involving varying rotor speed (equations (17) and (24)) are new. On the other hand, the terms involving warp effects in Hodges and Dowell[3] are not included here because this effect can be neglected without essential loss of accuracy for most applications.[3]

In the following discussion, the x- and y-direction will be denoted edgewise and flapwise to help the physical interpretation. The inertia terms in equation (12) are seen to couple the edgewise and flapwise motions to the torsional motion of the blade. The degree of coupling is seen to depend on the pre-twist of the chord. The first term in equation (13) shows that an acceleration of the pitch angle excites the edgewise and flapwise motion depending on the flapwise and edgewise deflection, respectively. That is, an acceleration of the pitch angle of a flapwise deflected blade excites the edgewise motion of the blade. The first term in the integral in equation (14) is a restoring force dependent on the rotation speed of the rotor, known as centrifugal stiffness. The effect of gravity (equations (15) and (22)) is seen to vary with the ϕ-angle as expected. The restoring force (equation (16)) couples the bending motion to the torsional motion. The degree of coupling is dependent on the edgewise and flapwise deflection of the blade. An acceleration of the rotor excites the edgewise and flapwise motion (equation (17)), the excitation is dependent on the pitch angle. The inertia term from equation (18) couples the torsional motion to the edgewise and flapwise motion. The degree of coupling to the edgewise and the flapwise motion is dependent on the pre-twist of the chord. The first term in equation (20) shows a strong coupling between pitch acceleration and torsional motion. The effect of rotor acceleration (equation (21)) on the torsional motion is dependent on the pitch setting and the pre-twist of the blade. The bending motion is coupled to the torsional motion through the bending stiffness (equation (23)).

The first term in equation (27) shows the strong coupling between torsional motion and pitch motion. The first term in equation (32) shows the effect of blade deflection on the pitch inertia, and the second term in equation (32) shows how the motion of a deflected blade affects the pitch equation.

To avoid unnecessary complications, structural damping is not included in the derivation of the equations of motion, but a damping term e.g. viscus damping could easily be added to the equations describing the structural damping.

Extra degrees of freedom like tower, yaw motion or tilt can be included by introducing a new inertial frame, defining a transformation from the new inertial frame to the present inertial frame, and using this new trans-

DOI: 10.1002/we

formation in the description of the energies before applying Hamilton's method. This will lead to extra equations for the each extra degree of freedom and to periodic coefficients (like the gravity term).

Application Example

In this section, a finite difference discretization of the blade model is used to compute the modes of natural vibrations of a particular 63 m blade.[12] The frequencies and shapes of the natural modes of vibrations are compared to results from HAWCstab*,[13] showing good agreement. The modes are used as basic for an assumed mode discretization of the partial differential equations of motion, approximating them by three ordinary differential equations. The modes of natural vibrations of the assumed mode approximated model are compared with the previously derived modes, showing a reasonable agreement. To illustrate and test the pitch model, the assumed mode approximated model is used for time simulations of a rapid 2 deg pitch change. The response is compared to HAWC2†[5,6] showing good agreement.

Finite Difference Discretization

The spatial derivatives of an unforced and linearized version of the partial differential equations of motion (equations (12) and (18)) are approximated by a second-order finite difference approximation. The resulting approximating ordinary differential equations can be written as

$$\hat{\mathbf{M}}\ddot{\tilde{\mathbf{q}}} + \tilde{\mathbf{D}}\dot{\tilde{\mathbf{q}}} + \tilde{\mathbf{K}}\tilde{\mathbf{q}} = \mathbf{0} \tag{38}$$

where $\tilde{\mathbf{M}}$, $\tilde{\mathbf{D}}$ and $\tilde{\mathbf{K}}$ hold the constant coefficients from the discretization and $\tilde{\mathbf{q}} = [u_1, v_1, \theta_1, \ldots, u_n, v_n, \theta_n]$ holds the deformations at the n discretization points. Equation (38) is a differential eigenvalue problem where the eigenvalues give the frequency and damping of natural vibrations of the blade and the corresponding eigenvectors give the shape of the natural vibrations.

Table I compares the six lowest eigenfrequencies for the blade with results from HAWCstab.[13] A good agreement is seen for all frequencies. Figure 2 shows the shape of first, second and sixth modes. The shapes are compared to results from HAWCstab showing a good agreement.

Assumed Mode Approximation

The partial differential equations of motion are transformed into three approximating ordinary differential equations by the assumed mode method.[11,14] The time- and spatial-dependent state variables for the blade are approx-

Table I. Frequencies for the first six natural modes of the test blade

		Finite difference		Assumed mode	
Mode number	HAWC freq. [Hz]	freq. [Hz]	diff. %	freq. [Hz]	diff. %
1	0·69	0·70	1	0·63	7
2	1·08	1·14	6	1·04	4
3	1·96	1·97	1	—	—
4	3·97	4·05	2	—	—
5	4·51	4·55	1	—	—
6	7·83	7·79	1	7·97	2

The results from HAWCstab,[13] the finite difference approximation of the present model and for the assumed mode approximation. Both the frequencies and the relative difference to the HAWCstab results are given.

*A finite element code for stability analysis of wind turbines from Risø National Laboratory.
†A combined finite element and multi-body dynamic code from Risø National Laboratory.

DOI: 10.1002/we

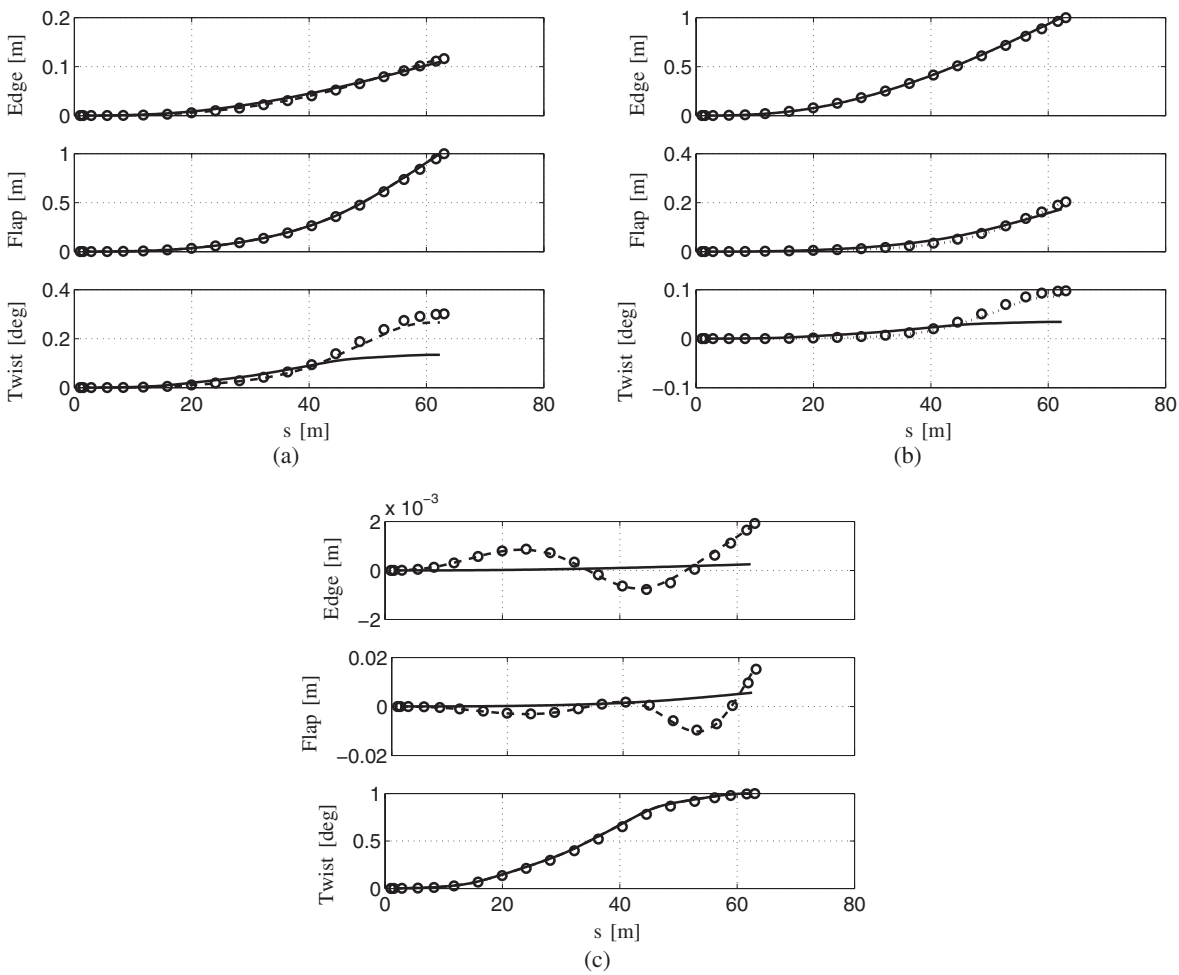

Figure 2. Modes of natural vibrations computed by the finite difference approximated model '- -' and the assumed mode approximated model '-' compared to the modes computed by HAWCstab[13] '○'. (a) First mode, (b) second mode, (c) sixth mode

imated by one edgewise $u(s, t) = u_s(s)u_t(t)$, one flapwise $v(s, t) = v_s(s)v_t(t)$ and one torsional $\theta(s, t) = \theta_s(s)\theta_t(t)$ mode. The mode shapes (u_s, v_s, θ_s) are the edgewise, flapwise and torsional contents of the second, first and sixth modes, respectively (the first modes dominated by edgewise, flapwise and torsional motion). The time-dependent wight functions (u_t, v_t, θ_t) are the new state variables of the system. The external forces on the blade are also split into a spatial part and a time-dependent part $f_u(s, t) = f_{u,s}(s)f_{u,t}(t)$, $f_v(s, t) = f_{v,s}(s)f_{v,t}(t)$, $f_w(s, t) = f_{w,s}(s)f_{w,t}(t)$ and $M(s,t) = M_s(s)M_t(t)$. The approximations are inserted into equations (12) and (18); the equations are wight by the corresponding spatial variable and integrated over the blade length, removing the spatial dependency.

The ordinary differential equation of blade motion becomes

$$\begin{aligned}&\mathbf{M}\ddot{\mathbf{q}} + 2\mathbf{D}(\dot{\phi}, \dot{\beta}, \beta)\dot{\mathbf{q}} + \mathbf{K}(\dot{\phi}, \dot{\beta}, \beta)\mathbf{q} + \mathbf{L}(\ddot{\beta}, \phi, \beta)\mathbf{q} + \mathbf{N}(\dot{\phi}, \dot{\beta}, \beta, \mathbf{q}) + \mathbf{F}_{ext,1}\mathbf{q}f_{w,t} \\ &\quad = \mathbf{F}(\ddot{\beta}, \ddot{\phi}, \dot{\beta}, \dot{\phi}, \beta, \phi) + \mathbf{F}_{ext,0}[f_{u,t}f_{v,t}f_{w,t}M_t]^{\mathrm{T}}\end{aligned} \tag{39}$$

DOI: 10.1002/we

where $\mathbf{q} = [u_t, v_t, \theta_t]^{\mathrm{T}}$ and the rest of the terms are given in equation (50) in Appendix B. Inserting the expansions into equation (27), the integrals can be computed and the equation of pitch action becomes

$$\begin{aligned}(I_{\beta,0} + I_{\beta,1}(\mathbf{q}))\ddot{\beta} + D_{\beta}(\dot{\mathbf{q}}, \mathbf{q})\dot{\beta} = M_{pitch} + (\mathbf{M}_{ext,0} + \mathbf{q}^{\mathrm{T}}\mathbf{M}_{ext,1})[f_{u,t} f_{v,t} M_t]^{\mathrm{T}} \\ + \mathbf{I}_{\beta,\mathbf{q}}\ddot{\mathbf{q}} + f_{\beta,\ddot{\mathbf{q}}}(\ddot{\mathbf{q}}, \mathbf{q}) + f_{\beta,\phi}(\ddot{\phi}, \dot{\phi}, \mathbf{q}) + f_{\beta,grav}(\mathbf{q})\sin(\phi)\end{aligned} \tag{40}$$

The individual terms are given in equation (51) in Appendix B. Inserting the expansions into equation (33) and computing the integrals, the equation of rotor position becomes

$$\begin{aligned}(J_{gcn} + I_{\phi})\ddot{\phi} + f_{\phi,g}(\phi, \beta, \mathbf{q}) = T_{gcn} + f_{\phi,\mathbf{q}}(\ddot{\mathbf{q}}, \beta) + I_{\phi,\beta}(\mathbf{q}, \beta)\ddot{\beta} + f_{\phi,\beta}(\dot{\beta}, \dot{\mathbf{q}}, \beta, \mathbf{q}) \\ + \mathbf{f}_{ext,0}(\beta)[f_{u,t} f_{v,t} f_{w,t}]^{\mathrm{T}} + f_{ext,1}(\mathbf{q}, \beta) f_{w,t}\end{aligned} \tag{41}$$

The individual terms are given in equation (52) in Appendix B. An unforced and linearized version of equation (39) gives a differential eigenvalue problem:

$$\mathbf{M}_{lin}\ddot{\mathbf{q}} + \mathbf{D}_{lin}\dot{\mathbf{q}} + \mathbf{K}_{lin}\mathbf{q} = \mathbf{0} \tag{42}$$

where the eigenvalue gives the frequency of natural vibrations of the assumed mode approximated model, and the eigenvectors give the coupling of the assumed modes in the natural vibrations. The found frequencies are compared with the previously found frequencies in Table I showing a good agreement. Figure 2 shows the natural mode shapes together with the previously found mode shapes. The edgewise and flapwise contents of the first and second modes are seen to agree very well with previous results. The torsional contents of the first mode are seen to disagree slightly from the previous results. The torsional contents of the second mode are seen to disagree with the previous result, but the value of the torsional contents is small compared to the edgewise and flapwise contents, hence the error is acceptable. The edgewise and flapwise contents of the sixth mode (first torsional mode) are seen to disagree quite a lot with the previous results. This is because the edgewise and flapwise contents are dominated by higher order edgewise and flapwise motion, which cannot be captured by this low order model. The value of the edgewise and flapwise contents is, however, small compared to the torsional contents, hence the error is acceptable.

Test Example

The pitch model is illustrated and tested by a numerical simulation where the rotor is rotating with a constant angular velocity $\dot{\phi}$ rad s^{-1}, and at 70 s, a 2 deg pitch change is imposed. The pitch change has a rise time of 0·2 s and 1·5% overshoot. No aerodynamic forces are included in this example. The pitch moment is computed by feeding (equation (40)) with the prescribed pitch action and the computed blade motion. The results from the simulations are compared with results from HAWC2*,[5,6] showing a good agreement.

Figure 3 shows the blade tip deflection and pitch moment from the present model and from HAWC2. The edgewise and flapwise motion are dominated by gravity, which is seen as the oscillations on the scale of 5 s (corresponding to the rotor speed on 0·79 rad s^{-1}). A small excitation of the flapwise motion is seen at the pitch action at 70 s. The torsional motion of the blade is strongly excited by the pitch action at 70 s. The pitch moment is high during the pitch action, and strongly effected by the torsional motion of the blade afterward. The flap motions agree very well for the two models. The amplitude of the flapwise motion on the scale of 5 s is a bit smaller for the present model than for HAWC2, and the excitation at 70 s is a bit more pronounced for the HAWC2 results, but still the two models agree well. The torsional motion agrees very well in amplitude, but there is a small disagreement in frequency. There is a good agreement between the pitch moment from the two models.

*A combined finite element and multi body dynamic code from Risø National Laboratory.

DOI: 10.1002/we

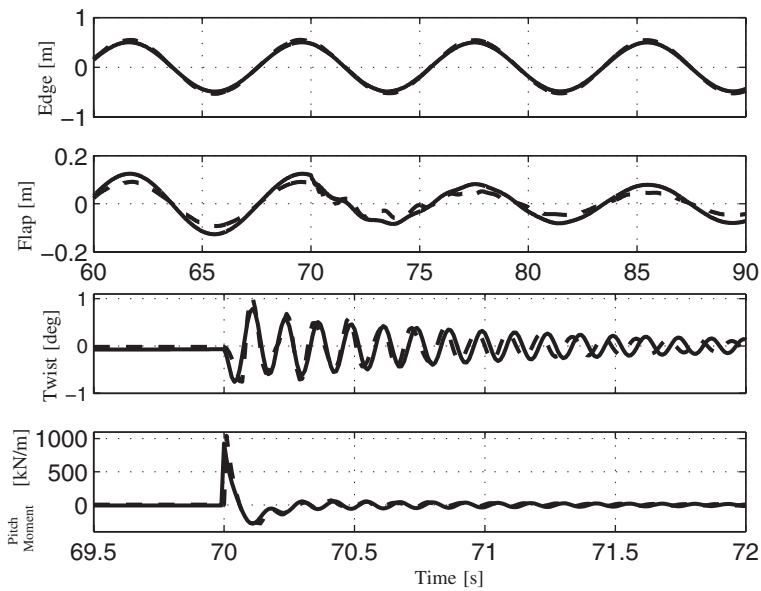

Figure 3. Tip deflection and pitch moment of a blade rotating with a constant speed of 2π and with a 2 deg pitch change at 70 s. '- - -' the present model, '-' HAWC2[5,6]

Discussion

The results from the finite difference discretized model show that the present model captures the fundamental properties of the blade as well as HAWCstab.[13] The results from the assumed mode model show that even with only three ordinary differential equations, important basic properties of the blade can be described, and that the pitch blade interaction can be modeled very well.

The relative simple structure of the equations of motion (equation (39)) makes them suitable for qualitative analysis of interaction between pitch action and blade motion and/or fast simulation. The structure of equation (39) is similar to the structure of the equations of motion of a 2-D blade section model (as those used in Chaviaropoulos *et al.*[1] and Block and Strganac[2]), therefore, the model has the same benefits as the 2-D blade section model, but with a clear connection to the real turbine blade. The rotor position model (equation (41)) can be used to analyze how the motion of one blade effects the rotor speed, but more important, it can easily be extended with more blades, giving a coupling between the motion of the individual blades. The rotor position model is extended with more blades by adding one of each term in equation (52) for each blade involved. An improved description of the blade motion can be achieved if more mode shapes or coupled mode shapes are used. The drawback of this is a more complicated system, making analytical analysis and interpretation harder.

Conclusion

This work extends the nonlinear partial differential equations of motion originally derived from Hodges and Dowell, taking pitch action, rotor speed variations and gravity into account. New equations are derived for the pitch action and rotor speed. Frequencies and shapes of natural vibrations of the blade are computed and compared to results from HAWCstab, showing a good agreement. The partial differential equations of motion are transformed into approximating ordinary differential equations of motion (equation (39)) by an assumed mode discretization. This model is suitable for basic analysis of interaction between pitch action and blade motion. The approximating ordinary differential equations of motion are used to simulate the response and pitch moment for a rotating turbine blade with a rapid 2 deg pitch change. The results from the simulation are compared to the results from HAWC2, showing a good agreement.

DOI: 10.1002/we

This work is a part of a project on pitch blade interaction, and the model will be extended to include an aerodynamic model and be used for analysis of basic properties of pitch blade interaction.

Acknowledgements

The author thanks Morten Hartvig Hansen, Risø National Laboratory for his inspiring ideas and helpful discussions related to this work. This work is founded partly by The Technical University of Denmark and Risø National Laboratory.

Appendix A

Coordinate Transformations

The derivation of the transformation matrices follows the method used in Hodges and Dowell.[3] The major difference between these matrices and those of Hodges and Dowell[3] is the inclusion of the pitch angle β.

The transformation between the initial (X, Y, Z)-frame and the ($\hat{x}$, $\hat{y}$, $\hat{z}$)-frame is given by

$$\begin{bmatrix}\hat{\mathbf{i}}\\ \hat{\mathbf{j}}\\ \hat{\mathbf{k}}\end{bmatrix} = \mathbf{T}_{\phi}\begin{bmatrix}\mathbf{I}\\ \mathbf{J}\\ \mathbf{K}\end{bmatrix} = \begin{bmatrix}\cos(\phi(t)) & 0 & -\sin(\phi(t))\\ 0 & 1 & 0\\ \sin(\phi(t)) & 0 & \cos(\phi(t))\end{bmatrix}\begin{bmatrix}\mathbf{I}\\ \mathbf{J}\\ \mathbf{K}\end{bmatrix} \tag{43}$$

and between the ($\hat{x}$,$\hat{y}$,$\hat{z}$)-frame and the (x, y, z)-frame is given by

$$\begin{bmatrix}\mathbf{i}\\ \mathbf{j}\\ \mathbf{k}\end{bmatrix} = \mathbf{T}_{\beta}\begin{bmatrix}\hat{\mathbf{i}}\\ \hat{\mathbf{j}}\\ \hat{\mathbf{k}}\end{bmatrix} = \begin{bmatrix}\cos(\beta(t)) & \sin(\beta(t)) & 0\\ -\sin(\beta(t)) & \cos(\beta(t)) & 0\\ 0 & 0 & 1\end{bmatrix}\begin{bmatrix}\hat{\mathbf{i}}\\ \hat{\mathbf{j}}\\ \hat{\mathbf{k}}\end{bmatrix} \tag{44}$$

The principle axis of each cross section of the blade is described by the ($\boldsymbol{\eta}$, $\boldsymbol{\xi}$, $\boldsymbol{\zeta}$)-frame with origin at ea, where η and ζ are the principle axes of the cross section and the ζ-axis points outward along the elastic axis of the deformed blade. This frame has the unit vectors ($\tilde{\mathrm{i}}$, $\tilde{\mathrm{j}}$, $\tilde{\mathrm{k}}$) given by the following transformation:

$$\begin{bmatrix}\tilde{\mathbf{i}}\\ \tilde{\mathbf{j}}\\ \tilde{\mathbf{k}}\end{bmatrix} = \mathbf{T}_{\mathrm{c}}\begin{bmatrix}\mathbf{i}\\ \mathbf{j}\\ \mathbf{k}\end{bmatrix} = \begin{bmatrix}\cos\left(\hat{\theta}(s,t)\right) & \sin\left(\hat{\theta}(s,t)\right) & 0\\ -\sin\left(\hat{\theta}(s,t)\right) & \cos\left(\hat{\theta}(s,t)\right) & 0\\ 0 & 0 & 1\end{bmatrix}$$
$$\begin{bmatrix}1 & 0 & 0\\ 0 & \sqrt{1-v'(s,t)^2} & -v'(s,t)\\ 0 & v'(s,t) & \sqrt{1-v'(s,t)^2}\end{bmatrix}$$
$$\begin{bmatrix}\sqrt{\dfrac{1-(l'_{pi}(s)+u'(s,t))^2-v'(s,t)^2}{1-v'(s,t)^2}} & 0 & -\dfrac{l'_{pi}(s)+u'(s,t)}{\sqrt{1-v'(s,t)^2}}\\ 0 & 1 & 0\\ \dfrac{l'_{pi}(s)+u'(s,t)}{\sqrt{1-v'(s,t)^2}} & 0 & \sqrt{\dfrac{1-(l'_{pi}(s)+u'(s,t))^2-v'(s,t)^2}{1-v'(s,t)^2}}\end{bmatrix}\begin{bmatrix}\mathbf{i}\\ \mathbf{j}\\ \mathbf{k}\end{bmatrix} \tag{45}$$

where $\tilde{\theta}$ is the rotation of the blade around the elastic axis. The first matrix in equation (45) is the rotation about the $\hat{z}$-axis, the next matrix is the rotation about the x-axis and the last matrix is the rotation about the y-axis.

DOI: 10.1002/we

The chord is described by the $(\bar{\mathbf{i}}, \bar{\mathbf{j}}, \bar{\mathbf{k}})$ unit vectors parallel to the chord, normal upward from the chord and parallel to the elastic axis, respectively. This set of unit vectors is given by

$$[\bar{\mathbf{i}} \quad \bar{\mathbf{j}} \quad \bar{\mathbf{k}}]^{\mathrm{T}} = \mathbf{T}_{\mathrm{c}}[\mathbf{i} \quad \mathbf{j} \quad \mathbf{k}]^{\mathrm{T}} \tag{46}$$

where $\mathbf{T}_c$ is equal to $\mathbf{T}_e$ except that the twist $\hat{\theta}$ includes the aerodynamic pre-twist instead of the elastic pre-twist.

The rotation of the principle axis of the blade sections as a function of the s coordinate is given by the differential equation:

$$\mathbf{T}_e' = \begin{bmatrix} 0 & \tilde{\omega}_k & -\tilde{\omega}_j \\ -\tilde{\omega}_k & 0 & \tilde{\omega}_i \\ \tilde{\omega}_j & -\tilde{\omega}_i & 0 \end{bmatrix} \mathbf{T}_c \Rightarrow \begin{bmatrix} 0 & \tilde{\omega}_k & -\tilde{\omega}_j \\ -\tilde{\omega}_k & 0 & \tilde{\omega}_i \\ \tilde{\omega}_j & -\tilde{\omega}_i & 0 \end{bmatrix} = \boldsymbol{T}_{\mathrm{c}}' \boldsymbol{T}_{\mathrm{c}}^{-1} \tag{47}$$

where $(\tilde{w}_i, \tilde{w}_j, \tilde{w}_k)$ is the rotation about the $(\tilde{\mathbf{i}}, \tilde{\mathbf{j}}, \tilde{\mathbf{k}})$-directions respectively, and it is utilized that $\mathbf{T}_\phi' = \mathbf{T}_\beta' = 0$. The rotation about the $\tilde{\mathbf{k}}$-direction is also measured by changes in the twist coordinates of the blade, (the pre-twist $\tilde{\theta} = \tilde{\theta}(s)$ and the elastic twist $\theta_{ela} = \theta_{ela}(s, t)$). Hence,

$$\left(\tilde{\theta} + \theta_{ela}\right)' = \tilde{\omega}_k = \hat{\theta} + v'(u'' + l_{pi}'') + O(\varepsilon^3) \tag{48}$$

using the order scheme (see previous discussion).

Rearranging and intergrading equation (48) lead to an expression for the rotation of each blade section around the elastic axis:

$$\hat{\theta} = \tilde{\theta} + \theta_{ela} - \int_0^s v'(u'' + l_{pi}')\mathrm{d}\rho = \tilde{\theta} + \theta, \quad 0 = \theta(s, t) = \theta_{ela} - \int_0^s v'(u'' + l_{pi}'')\mathrm{d}\rho \tag{49}$$

where θ is the time-dependent twist of the blade relative to the (x, y, z)-frame. Inserting equation (49) into the expression for $\mathbf{T}_e$ leads to the transformation matrix of the elastic properties. Replacing $\tilde{\theta}$ with $\bar{\theta}$ in $\mathbf{T}_e$ gives the transformation matrix $\mathbf{T}_c$ of the chord.

Note that $\mathbf{T}^{\mathrm{T}}\mathbf{T} = \mathbf{I}$ holds for all the transformation matrices.

Appendix B

Blade Model

The individual terms in the assumed mode approximated blade model (equation (39)) are

$$\begin{aligned}
\mathbf{D}(\dot{\phi}, \dot{\beta}, \beta) &= \dot{\phi}(\mathbf{D}_{\phi,s}\sin(\beta) + \mathbf{D}_{\phi,c}\cos(\beta)) + \dot{\phi}(\mathbf{D}_{\phi,a,s}\sin(\beta) + \mathbf{D}_{\phi,a,c}\cos(\beta)) + \dot{\beta}\mathbf{D}_\beta(\beta) \\
\mathbf{K}(\dot{\phi}, \dot{\beta}, \beta) &= \mathbf{K}_s + \mathbf{K} + \dot{\beta}^2\mathbf{K}_\beta + 2\dot{\beta}\dot{\phi}(\mathbf{K}_{\beta\phi,s}\sin(\beta) + \mathbf{K}_{\beta\phi,c}\cos(\beta)) \\
&\quad + \dot{\phi}^2(\mathbf{K}_{\phi,0} + \mathbf{K}_{\phi,ss}\sin^2(\beta) + \mathbf{K}_{\phi,cc}\cos^2(\beta) + \mathbf{K}_{\phi,sc}\sin(\beta)\cos(\beta)) \\
\mathbf{L}(\ddot{\beta}, \phi, \beta) &= \ddot{\beta}\mathbf{F}_{\beta,1} + g\sin(\phi)(\mathbf{F}_{g,1,s}\sin(\beta) + \mathbf{F}_{g,1,c}\cos(\beta)) + g\sin(\phi)\mathbf{F}_{g,2} \\
\mathbf{N}(\dot{\phi}, \dot{\beta}, \beta, \mathbf{q}) &= \theta_t\mathbf{F}_1\mathbf{q} + \mathbf{F}_2\left[u_t^2 v_t^2 \theta_t^2\right]^{\mathrm{T}} + 2\dot{\phi}\mathbf{Q}(\mathbf{F}_{3,s}\sin(\beta) + \mathbf{F}_{3,c}\cos(\beta))\dot{\mathbf{q}} \\
&\quad + 2\dot{\phi}\dot{\beta}\mathbf{Q}(\mathbf{F}_{4,s}\sin(\beta) + \mathbf{F}_{4,c}\cos(\beta))\mathbf{q} + \mathbf{f}_5 u_t v_t \\
\mathbf{F}(\ddot{\beta}, \ddot{\phi}, \dot{\beta}, \dot{\phi}, \beta, \phi) &= 2\dot{\phi}\dot{\beta}\mathbf{f}_{\phi\beta}(\beta) + \dot{\phi}^2\mathbf{f}_\phi + g(\mathbf{F}_{g,0} + \mathbf{F}_{g,s}\sin(\beta) + \mathbf{F}_{g,c}\cos(\beta))\begin{bmatrix}\sin(\phi) \\ \cos(\phi)\end{bmatrix} \\
&\quad + \mathbf{F}_{\beta,0}\begin{bmatrix}\beta \\ \dot{\beta}^2\end{bmatrix} + (\mathbf{F}_{\phi,0} + \mathbf{F}_{\phi,s}\sin(\beta) + \mathbf{F}_{\phi,s}\cos(\beta) + \mathbf{F}_{\phi,ss}\sin^2(\beta) \\
&\quad + \mathbf{F}_{\phi,cc}\cos^2(\beta) + \mathbf{F}_{\phi,sc}\sin(\beta)\cos(\beta))\begin{bmatrix}\ddot{\phi} \\ \dot{\phi}^2\end{bmatrix}
\end{aligned} \tag{50}$$

DOI: 10.1002/we

where the constants for the linear terms are

$$\mathbf{M} = \int_v^R \begin{bmatrix} mu_s^2 & 0 & -u_s\theta_s ml_{cg}\sin(\bar{\theta}) \\ 0 & mv_s^2 & v_s\theta_s ml_{cg}\cos(\bar{\theta}) \\ -u_s\theta_s ml_{cg}\sin(\bar{\theta}) & v_s\theta_s ml_{cg}\cos(\bar{\theta}) & (I_{cg}+ml_{cg}^2)\theta_s^2 \end{bmatrix} \mathrm{d}s$$

$$\mathbf{K}_s = \int_r^R \begin{bmatrix} E(I_\xi\cos^2(\tilde{\theta}) + I_\eta\sin^2(\tilde{\theta}))u_s''u_s'' & E(I_\xi - I_\eta)\cos(\tilde{\theta})\sin(\tilde{\theta})u_s''v_s'' & -E(I_\xi - I_\eta)\cos(\tilde{\theta})\sin(\tilde{\theta})l_{pi}''u_s''\theta_s \\ E(I_\xi - I_\eta)\cos(\tilde{\theta})\sin(\tilde{\theta})u_s''v_s'' & E(I_\xi\sin^2(\tilde{\theta}) + I_\eta\cos^2(\tilde{\theta}))v_s''v_s'' & -E(I_\xi\sin^2(\tilde{\theta}) + I_\eta\cos^2(\tilde{\theta}))l_{pi}''v_s''\theta_s \\ -E(I_\xi - I_\eta)\cos(\tilde{\theta})\sin(\tilde{\theta})l_{pi}''u_s''\theta_s & -E(I_\xi\sin^2(\tilde{\theta}) + I_\eta\cos^2(\tilde{\theta}))l_{pi}''u_s''\theta_s & GJ\theta_s'\theta_s' \end{bmatrix} \mathrm{d}s$$

$$\mathbf{K}_{\phi,0} = \int_r^R \begin{bmatrix} (u_s')^2\int_s^R mw_0\mathrm{d}\rho & 0 & -ml_{cg}w_0\sin(\bar{\theta})u_s'\theta_s \\ 0 & (v_s')^2\int_s^R mw_0\mathrm{d}\rho & ml_{cg}w_0\cos(\bar{\theta})v_s'\theta_s \\ -ml_{cg}w_0\sin(\bar{\theta})u_s'\theta_s & ml_{cg}w_0\cos(\bar{\theta})v_s'\theta_s & 0 \end{bmatrix} \mathrm{d}s$$

$$\mathbf{K}_{\phi,cc} = \int_r^R \begin{bmatrix} -mu_s^2 & 0 & ml_{cg}\sin(\bar{\theta})u_s\theta_s \\ 0 & 0 & 0 \\ ml_{cg}\sin(\bar{\theta})u_s\theta_s & 0 & 0 \end{bmatrix} \mathrm{d}s$$

$$\mathbf{K}_{\phi,ss} = \int_r^R \begin{bmatrix} 0 & 0 & 0 \\ 0 & -mv_s^2 & -l_{cg}m\cos(\bar{\theta})v_s\theta_s \\ 0 & -l_{cg}m\cos(\bar{\theta})v_s\theta_s & 0 \end{bmatrix} \mathrm{d}s$$

$$\mathbf{K}_{\dot{\phi},sc} = \int_r^R \begin{bmatrix} 0 & mu_sv_s & ml_{cg}\cos(\bar{\theta})u_s\theta_s \\ mu_sv_s & 0 & -l_{cg}m\sin(\bar{\theta})v_s\theta_s \\ ml_{cg}\cos(\bar{\theta})u_s\theta_s & -l_{cg}m\sin(\bar{\theta})v_s\theta_s & 0 \end{bmatrix} \mathrm{d}s$$

$$\mathbf{D}_{\phi,a,s} = \int_r^R \begin{bmatrix} 0 & -ml_{cg}\cos(\bar{\theta})v_su_s' & 0 \\ ml_{cg}\cos(\bar{\theta})u_s'v_s & -ml_{cg}\sin(\bar{\theta})v_sv_s' & 0 \\ 0 & +ml_{cg}\sin(\bar{\theta})v_sv_s' & 0 \end{bmatrix} \mathrm{d}s$$

$$\mathbf{D}_{\phi,a,c} = \int_r^R \begin{bmatrix} ml_{cg}\cos(\bar{\theta})u_su_s' & -ml_{cg}\sin(\bar{\theta})v_s'u_s & 0 \\ -ml_{cg}\cos(\bar{\theta})u_su_s' & 0 & 0 \\ ml_{cg}\sin(\bar{\theta})u_sv_s' & 0 & 0 \\ 0 & 0 & 0 \end{bmatrix} \mathrm{d}s$$

$$\mathbf{k}_\beta = \int_r^R \begin{bmatrix} -mu_s^2 & 0 & ml_{cg}\sin(\bar{\theta})u_s\theta_s \\ 0 & -mv_s^2 & -ml_{cg}\cos(\bar{\theta})v_s\theta_s \\ ml_{cg}\sin(\bar{\theta})u_s\theta_s & -ml_{cg}\cos(\bar{\theta})v_s\theta_s & 0 \end{bmatrix} \mathrm{d}s$$

$$\mathbf{D}_\beta = \int_r^R \begin{bmatrix} 0 & -mv_su_s & -ml_{cg}\cos(\bar{\theta})u_s\theta_s \\ mv_su_s & 0 & -ml_{cg}\sin(\bar{\theta})v_s\theta_s \\ ml_{cg}\cos(\bar{\theta})u_s\theta_s & ml_{cg}\sin(\bar{\theta})v_s\theta_s & 0 \end{bmatrix} \mathrm{d}s$$

DOI: 10.1002/we

$$\mathbf{F}_{\beta,1}=\int_r^R\begin{bmatrix}0 & -mv_su_s & -ml_{cg}\theta_su_s\cos(\bar{\theta})\\ mu_sv_s & 0 & -ml_{cg}\theta_sv_s\sin(\bar{\theta})\\ ml_{cg}u_s\theta_s\cos(\bar{\theta}) & ml_{cg}\theta_sv_s\sin(\bar{\theta}) & 0\end{bmatrix}\mathrm{d}s$$

$$\mathbf{K}_{\beta\phi,s}=\int_r^R\begin{bmatrix}-ml_{cg}u_su_s'\cos(\bar{\theta})-l_{pi}'u_s'\int_s^R mu_s\mathrm{d}\rho & 0 & 0\\ -u_s'^2\int_s^R m(l_{pi}+l_{cg}\cos(\bar{\theta}))mu_s\mathrm{d}\rho & & \\ -ml_{cg}u_sv_s'\sin(\bar{\theta}) & -u_s'^2\int_s^R m(l_{pi}+l_{cg}\cos(\bar{\theta}))\mathrm{d}\rho & 0\\ 0 & 0 & 0\end{bmatrix}\mathrm{d}s$$

$$\mathbf{K}_{\beta\phi,c}=\int_r^R\begin{bmatrix}-u_s'^2\int_s^R ml_{cg}\sin(\bar{\theta})\mathrm{d}\rho & -ml_{cg}v_su_s'\cos(\bar{\theta}) & 0\\ & -l_{pi}'u_s'\int_s^R mv_s\mathrm{d}\rho & \\ 0 & -ml_{cg}v_sv_s'\sin(\bar{\theta})\mathrm{d}\rho & 0\\ & -v_s'^2\int_r^R ml_{cg}\sin(\bar{\theta})\mathrm{d}\rho & \\ 0 & 0 & 0\end{bmatrix}\mathrm{d}s$$

$$\mathbf{F}_{g,1,s}=\int_r^R\begin{bmatrix}0 & 0 & 0\\ 0 & ml_{cg}v_s'^2\sin(\bar{\theta}) & 0\\ 0 & 0 & ml_{cg}\theta_s^2\sin(\bar{\theta})\end{bmatrix}\mathrm{d}s$$

$$\mathbf{F}_{g,1,c}=\int_r^R\begin{bmatrix}-ml_{cg}u_s'^2\cos(\bar{\theta}) & -ml_{cg}u_s'u_s'\sin(\bar{\theta}) & 0\\ -ml_{cg}v_s'u_s'\sin(\bar{\theta}) & 0 & 0\\ 0 & 0 & -ml_{cg}\theta_s^2\cos(\bar{\theta})\end{bmatrix}\mathrm{d}s$$

$$\mathbf{F}_{g,2}=\int_r^R\begin{bmatrix}-u_s'^2\int_s^R m\mathrm{d}\rho & 0 & -ml_{cg}\theta_su_s'\sin(\bar{\theta})\\ 0 & -v_s'^2\int_s^R m\mathrm{d}\rho & ml_{cg}\theta_sv_s'\cos(\bar{\theta})\\ -ml_{cg}\theta_su_s'\sin(\bar{\theta}) & ml_{cg}\theta_sv_s'\cos(\bar{\theta}) & 0\end{bmatrix}\mathrm{d}s$$

$$\mathbf{D}_{\phi,s}=\int_r^R\begin{bmatrix}0 & -l_{pi}'u_s'\int_s^R mv_s\mathrm{d}\rho & 0\\ 0 & 0 & 0\\ 0 & 0 & 0\end{bmatrix}\mathrm{d}s,\quad \mathbf{D}_{\phi,c}=\int_r^R\begin{bmatrix}l_{pi}'u_s'\int_s^R mu_s\mathrm{d}\rho & 0 & 0\\ 0 & 0 & 0\\ 0 & 0 & 0\end{bmatrix}\mathrm{d}s$$

$$\mathbf{K}=\int_r^R\begin{bmatrix}0 & 0 & 0\\ 0 & 0 & 0\\ EI_{\eta\eta\xi}\bar{\theta}'\theta_s'u_s''\sin(\bar{\theta})-EI_{\eta\xi\xi}\bar{\theta}'\theta_s'u_s''\cos(\bar{\theta}) & -EI_{\eta\eta\xi}\bar{\theta}'\theta_s'u_s''\cos(\tilde{\theta})-EI_{\eta\xi\xi}\bar{\theta}'\theta_s'v_s''\sin(\tilde{\theta}) & 0\end{bmatrix}\mathrm{d}s$$

and for constants for the nonlinear terms:

$$\mathbf{F}_1=\int_r^R\begin{bmatrix}-E(I_\xi-I_\eta)u_s''u_s'\theta_s\sin(2\tilde{\theta}) & E(I_\xi-I_\eta)v_s''u_s'\theta_s\cos(2\tilde{\theta}) & 0\\ E(I_\xi-I_\eta)u_s''v_s'\theta_s\cos(2\tilde{\theta}) & E(I_\xi-I_\eta)v_s''v_s'\theta_s\sin(2\tilde{\theta}) & 0\\ \theta_s'^2u_s''E(I_{\eta\eta\xi}\sin(\bar{\theta})-EI_{\eta\xi\xi}\cos(\bar{\theta})) & -\theta_s'^2v_s''E(I_{\eta\eta\xi}\cos(\tilde{\theta})+I_{\eta\xi\xi}\sin(\tilde{\theta})) & 0\end{bmatrix}\mathrm{d}s$$

DOI: 10.1002/we

$$\mathbf{F}_2 = \int_r^R \begin{bmatrix} 0 & 0 & 0 \\ 0 & 0 & 0 \\ -E(I_\xi - I_\eta)\theta_s u_s'' u_s'' \cos(\tilde{\theta})\sin(\tilde{\theta}) & E(I_\xi - I_\eta)\theta_s v_s'' v_s'' \cos(\tilde{\theta})\sin(\tilde{\theta}) & 0 \end{bmatrix} \mathrm{d}s$$

$$\mathbf{F}_{3,s} = \int_r^R \begin{bmatrix} 0 & -u_s'^2 \int_s^R m v_s \mathrm{d}\rho & 0 \\ 0 & -v_s'^2 \int_s^R m v_s \mathrm{d}\rho & 0 \\ 0 & 0 & 0 \end{bmatrix} \mathrm{d}s, \quad \mathbf{F}_{3,c} = \int_r^R \begin{bmatrix} u_s'^2 \int_s^R m u_s \mathrm{d}\rho & 0 & 0 \\ v_s'^2 \int_s^R m u_s \mathrm{d}\rho & 0 & 0 \\ 0 & 0 & 0 \end{bmatrix} \mathrm{d}s$$

$$\mathbf{F}_{4,s} = \int_r^R \begin{bmatrix} -u_s'^2 \int_s^R m u_s \mathrm{d}\rho & 0 & 0 \\ -v_s'^2 \int_s^R m u_s \mathrm{d}\rho & 0 & 0 \\ 0 & 0 & 0 \end{bmatrix} \mathrm{d}s, \quad \mathbf{F}_{4,c} = \int_r^R \begin{bmatrix} 0 & -u_s'^2 \int_s^R m v_s \mathrm{d}\rho & 0 \\ 0 & -v_s'^2 \int_s^R m v_s \mathrm{d}\rho & 0 \\ 0 & 0 & 0 \end{bmatrix} \mathrm{d}s$$

$$\mathbf{f}_5 = \int_r^R \begin{bmatrix} 0 & 0 & E(I_\xi - I_\eta)u_s'' v_s'' \cos(2\tilde{\theta}) \end{bmatrix}^{\mathrm{T}} \mathrm{d}s$$

and for the forcing terms:

$$\mathbf{F}_{\beta,0} = \int_r^R \begin{bmatrix} m l_{cg} u_s \sin(\bar{\theta}) & m(l_{pi} + l_{cg}\cos(\bar{\theta}))u_s \\ -m(l_{pi} + l_{cg}\cos(\bar{\theta}))v_s & m l_{cg} v_s \sin(\bar{\theta}) \\ -(I_{cg} + m l_{cg}^2)\theta_s & -m l_{cg} l_{pi} \theta_s \sin(\bar{\theta}) \end{bmatrix} \mathrm{d}s$$

$$\mathbf{f}_{\beta\phi,s} = \int_r^R \begin{bmatrix} m l_{cg}(l_{pi} + l_{cg}\cos(\bar{\theta}))u_s' \cos(\bar{\theta}) + l_{pi}' u_s' \int_s^R m(l_{pi} + l_{cg}\cos(\bar{\theta}))\mathrm{d}\rho \\ m l_{cg}(l_{pi} + l_{cg}\cos(\bar{\theta}))v_s' \sin(\bar{\theta}) \\ 0 \end{bmatrix} \mathrm{d}s$$

$$\mathbf{f}_{\beta\phi,c} = \int_r^R \begin{bmatrix} m l_{cg} l_{cg} \cos(\beta)\sin(\bar{\theta})u_s' \cos(\bar{\theta}) + l_{pi}' u_s' \int_s^R m l_{cg} \sin(\bar{\theta})\mathrm{d}\rho \\ m l_{cg} l_{cg} \sin^2(\bar{\theta})v_s' \\ 0 \end{bmatrix} \mathrm{d}s$$

$$\mathbf{F}_{\phi,0} = \int_r^R \begin{bmatrix} 0 & -m l_{cg} w_0 u_s' \cos(\bar{\theta}) \\ 0 & -m l_{cg} w_0 v_s' \sin(\bar{\theta}) \\ 0 & -m l_{cg} l_{pi}' w_0 \theta_s \sin(\bar{\theta}) \end{bmatrix} \mathrm{d}s$$

$$\mathbf{F}_{\phi,s} = \int_r^R \begin{bmatrix} 0 & 0 \\ m w_0 u_s & 0 \\ m w_0 l_{cg} \theta_s \cos(\bar{\theta}) & 0 \end{bmatrix} \mathrm{d}s, \quad \mathbf{F}_{\phi,c} = \int_r^R \begin{bmatrix} -m w_0 u_s & 0 \\ 0 & 0 \\ m w_0 l_{cg} \theta_s \sin(\bar{\theta}) & 0 \end{bmatrix} \mathrm{d}s$$

$$\mathbf{F}_{\phi,ss} = \int_r^R \begin{bmatrix} 0 & 0 \\ 0 & m l_{cg} \sin(\bar{\theta})v_s \\ 0 & m l_{cg} l_{cg} \sin(\bar{\theta})\theta_s \cos(\bar{\theta}) \end{bmatrix} \mathrm{d}s$$

$$\mathbf{F}_{\phi,cc} = \int_r^R \begin{bmatrix} 0 & m(l_{pi} + l_{cg}\cos(\bar{\theta}))u_s \\ 0 & 0 \\ 0 & -m l_{cg}(l_{pi} + l_{cg}\cos(\bar{\theta}))\theta_s \sin(\bar{\theta}) \end{bmatrix} \mathrm{d}s$$

DOI: 10.1002/we

$$\mathbf{F}_{\phi,sc} = \int_r^R \begin{bmatrix} 0 & -ml_{cg}\sin(\bar{\theta})u_s \\ 0 & -m(l_{pi}+l_{cg}\cos(\bar{\theta}))v_s \\ 0 & -ml_{cg}(l_{pi}\cos(\theta)+l_{cg}\cos(\bar{\theta})-l_{cg}\sin^2(\bar{\theta}))\theta_s \end{bmatrix} \mathrm{d}s$$

$$\mathbf{F}_{g,0} = \int_r^R \begin{bmatrix} 0 & -ml_{cg}u_s'\cos(\bar{\theta}) - l_{pi}'u_s'\int_s^R m\mathrm{d}\rho \\ 0 & -ml_{cg}v_s'\sin(\bar{\theta}) \\ 0 & ml_{cg}l_{pi}'\theta_s\sin(\bar{\theta}) \end{bmatrix} \mathrm{d}s$$

$$\mathbf{F}_{g,s}(\beta) = \int_r^R \begin{bmatrix} 0 & 0 \\ mv_s 0 & 0 \\ ml_{cg}\theta_s\cos(\bar{\theta}) & 0 \end{bmatrix} \mathrm{d}s, \quad \mathbf{F}_{g,c}(\beta) = \int_r^R \begin{bmatrix} -mu_s + ml_{cg}l_{pi}'u_s'\cos(\bar{\theta}) & 0 \\ ml_{cg}l_{pi}'v_s'\sin(\bar{\theta}) & 0 \\ ml_{cg}\theta_s\sin(\bar{\theta}) & 0 \end{bmatrix} \mathrm{d}s$$

$$\mathbf{f}_{\phi} = \int_r^R \begin{bmatrix} -l_{pi}'u_s'\int_s^R mw_0\mathrm{d}\rho & 0 & 0 \end{bmatrix}^{\mathrm{T}} \mathrm{d}s$$

$$\mathbf{F}_{ext,0} = \int_r^R \begin{bmatrix} f_{u,s}u_s & 0 & -l_{pi}'u_s'\int_s^R f_{w,s}\mathrm{d}\rho & 0 \\ 0 & f_{v,s}v_s & 0 & 0 \\ 0 & 0 & 0 & M_s\theta_s \end{bmatrix}^{\mathrm{T}} \mathrm{d}s$$

$$\mathbf{F}_{ext,1} = \int_r^R \begin{bmatrix} u_s'^2\int_s^R f_{w,s}\mathrm{d}\rho & 0 & 0 \\ 0 & u_s'^2\int_s^R f_{w,s}\mathrm{d}\rho & 0 \\ 0 & 0 & 0 \end{bmatrix}^{\mathrm{T}} \mathrm{d}s$$

Pitch Model

The individual terms in the assumed mode approximated pitch model (equation (40)) are

$$\begin{aligned}
I_{\beta,1}(\mathbf{q}) &= \mathbf{I}_{\beta,1}\mathbf{q} + \mathbf{I}_{\beta,2}\left[u_t^2 v_t^2\right]^{\mathrm{T}} \\
D_{\beta}(\dot{\mathbf{q}},\mathbf{q}) &= 2\mathbf{f}_{\beta,\mathbf{q}}\dot{\mathbf{q}} + 2\mathbf{I}_{\beta,2}\left[\dot{u}_t u_t \; \dot{v}_t v_t\right]^{\mathrm{T}} \\
f_{\beta,\ddot{\mathbf{q}}}(\ddot{\mathbf{q}},\mathbf{q}) &= m_{uv}(\ddot{u}_t v_t - \ddot{v}_t u_t) \\
f_{\beta,\phi}(\ddot{\phi},\dot{\phi},\mathbf{q}) &= \ddot{\phi}(f_{\beta,\ddot{\phi},s}u_t\sin(\beta) + f_{\beta,\ddot{\phi},c}V_t\cos(\beta) + I_{\beta,\phi,s}\sin(\beta) + I_{\beta,\phi,c}\cos(\beta)) \\
&\quad - 2\dot{\phi}^2(f_{\beta,\phi,s}\sin(2\beta) + f_{\beta,\phi,c}\cos(2\beta) + (\mathbf{f}_{\beta,\phi,s}\sin(2\beta) + f_{\beta,\phi,c}\cos(2\beta))\mathbf{q} \\
&\quad + \sin(2\beta)\mathbf{f}_{\beta,\phi,2}\left[u_t^2 v_t^2\right]^{\mathrm{T}} + \cos(2\beta)f_{\beta,\phi,2}u_t v_t\Big) \\
f_{\beta,grav}(\mathbf{q}) &= -g((\mathbf{f}_{\beta,g,2,s}\sin(\beta) + \mathbf{f}_{\beta,g,2,c}\cos(\beta))\mathbf{q} + f_{\beta,g,s}\sin(\beta) + f_{\beta,g,c}\cos(\beta)))
\end{aligned} \tag{51}$$

where the constants are

$$I_{\beta,0} = \int_r^R (l_{cg} + m(l_{cg}^2 + l_{pi}^2 + 2l_{pi}l_{cg}\cos(\bar{\theta})))\mathrm{d}s, \quad \mathbf{I}_{\beta,1} = \int_r^R [2m(l_{pi}+l_{cg}\cos(\theta)) \quad 2ml_{cg}\sin(\bar{\theta}) \quad 0]\mathrm{d}s$$

$$\mathbf{I}_{\beta,2} = \int_r^R [mu_s^2 \quad mv_s^2]\mathrm{d}s, \quad \mathbf{I}_{\beta,\mathbf{q}} = \int_r^R [mu_s l_{cg}\sin(\bar{\theta}) \quad -mv_s(l_{pi}+l_{cg}\sin(\bar{\theta})) \quad -I_{cg} - ml_{cg}^2]\mathrm{d}s$$

$$I_{\beta,\phi,s} = \int_r^R mw_0(l_{pi}+l_{cg}\cos(\bar{\theta}))\mathrm{d}s, \quad I_{\beta,\phi,c} = \int_r^R mw_0 l_{cg}\sin(\bar{\theta})\mathrm{d}s, \quad m_{uv} = \int_r^R mu_s v_s \mathrm{d}s$$

$$\mathbf{f}_{\beta,\mathbf{q}} = \int_r^R [mu_s(l_{pi}+l_{cg}\cos(\bar{\theta})) \quad mv_s l_{cg}\sin(\bar{\theta}) \quad 0]\mathrm{d}s, \quad f_{\beta,\ddot{\phi},s} = \int_r^R mu_s w_0 \mathrm{d}s, \quad f_{\beta,\ddot{\phi},c} = \int_r^R mv_s w_0 \mathrm{d}s$$

DOI: 10.1002/we

$$\mathbf{M}_{ext,0} = \int_r^R [0 \quad l_{pi} f_{v,s} \quad M_s] \mathrm{d}s, \quad \mathbf{M}_{ext,1} = \int_r^R \begin{bmatrix} 0 & u_s f_{v,s} & 0 \\ -v_s f_{u,s} & 0 & 0 \\ 0 & 0 & 0 \end{bmatrix} \mathrm{d}s$$

$$f_{\beta,\phi,s} = \int_r^R m\left(\frac{1}{2}(l_{pi}^2 - l_{cg}^2) + l_{cg}^2 \cos^2(\bar{\theta}) + l_{cg} l_{pi} \cos(\bar{\theta})\right) \mathrm{d}s$$

$$f_{\beta,\phi,c} = \int_r^R m(l_{cg}^2 \cos(\bar{\theta}) \sin(\bar{\theta}) + l_{cg} l_{pi} \sin(\bar{\theta})) \mathrm{d}s$$

$$\mathbf{f}_{\beta,\phi,s} = \int_r^R \begin{bmatrix} m u_s (l_{pi} + l_{cg} \cos(\bar{\theta})) \\ -m v_s l_{cg} \sin(\bar{\theta}) \\ 0 \end{bmatrix}^{\mathrm{T}} \mathrm{d}s, \quad \mathbf{f}_{\beta,\phi,c} = \int_r^R \begin{bmatrix} m u_s l_{cg} \sin(\bar{\theta}) \\ m v_s (l_{pi} + l_{cg} \cos(\bar{\theta})) \\ 0 \end{bmatrix}^{\mathrm{T}} \mathrm{d}s$$

$$\mathbf{f}_{\beta,\phi,2} = \int_r^R \begin{bmatrix} 1/2 m u_s^2 \\ -1/2 m v_s^2 \end{bmatrix}^{\mathrm{T}} \mathrm{d}s, \quad \mathbf{f}_{\beta,g,2,s} = \int_r^R \begin{bmatrix} m u_s \\ 0 \\ -m\theta_s l_{cg} \sin(\bar{\theta}) \end{bmatrix}^{\mathrm{T}} \mathrm{d}s, \quad \mathbf{f}_{\beta,g,2,\mathrm{c}} = \int_r^R \begin{bmatrix} 0 \\ m v_s \\ m\theta_s l_{cg} \cos(\bar{\theta}) \end{bmatrix}^{\mathrm{T}} \mathrm{d}s$$

$$f_{\beta,\phi,2} = \int_r^R m u_s v_s \mathrm{d}s, \quad f_{\beta,g,s} = \int_r^R m(l_{pi} + l_{cg} \cos(\bar{\theta})) \mathrm{d}s, \quad f_{\beta,g,c} = \int_r^R m l_{cg} \sin(\bar{\theta}) \mathrm{d}s$$

Rotor Speed Model

The individual terms in the assumed mode approximated pitch model (equation (41)) are

$$\begin{aligned}
f_{\phi,g}(\phi, \beta, \mathbf{q}) &= f_{\phi,g,0} \sin(\phi) + (f_{\phi,g,u,0} \cos(\beta) - f_{\phi,g,v,0} \sin(\beta) \\
&\quad + f_{\phi,g,u,1} u_t \cos(\beta) - f_{\phi,g,v,1} v_t \sin(\beta)) \cos(\phi) \\
I_{\phi,\beta}(\mathbf{q}, \beta) &= I_{\phi,u,0} \sin(\beta) + I_{\phi,v,0} \cos(\beta) + I_{\phi,u,1} u_t \sin(\beta) + I_{\phi,v,1} v_t \cos(\beta) \\
f_{\phi,\mathbf{q}}(\ddot{\mathbf{q}}, \beta) &= I_{\phi,u,1} \ddot{u}_t \cos(\beta) - I_{\phi,v,1} \ddot{v}_t \sin(\beta) \\
f_{\phi,\beta}\left(\dot{\beta}, \dot{\mathbf{q}}, \beta, \mathbf{q}\right) &= (I_{\phi,u,0} \cos(\beta) - I_{\phi,v,0} \sin(\beta) + I_{\phi,u,1} u_t \cos(\beta) - I_{\phi,v,1} v_t \sin(\beta)) \dot{\beta}^2 \\
&\quad + 2\dot{\beta}(I_{\phi,u,1} \dot{u}_t \sin(\beta) + I_{\phi,v,1} \dot{u}_t \cos(\beta)) \\
\mathbf{f}_{ext,0}(\beta) &= \mathbf{f}_{ext,0,s} \cos(\beta) + \mathbf{f}_{ext,0,c} \sin(\beta) \\
\mathbf{f}_{ext,1}(\mathbf{q}, \beta) &= f_{ext,1,v} v_t \sin(\beta) - f_{ext,1,u} u_t \cos(\beta)
\end{aligned} \tag{52}$$

where the constants are

$$I_\phi = \int_r^R m w_0^2, \quad I_{\phi,u,0} = \int_r^R m w_0 (l_{pi} + l_{cg} \cos(\bar{\theta})) \mathrm{d}s, \quad I_{\phi,v,0} = \int_r^R m w_0 l_{cg} \sin(\bar{\theta}) \mathrm{d}s$$

$$I_{\phi,u,1} = \int_r^R m w_0 u_s \mathrm{d}s, \quad I_{\phi,v,1} = \int_r^R m w_0 v_s \mathrm{d}s, \quad f_{\phi,g,u,1} = \int_r^R g m u_s \mathrm{d}s, \quad f_{\phi,g,v,1} = \int_r^R g m v_s \mathrm{d}s$$

$$f_{\phi,g,0} = \int_r^R g m w_0 \mathrm{d}s, \quad f_{\phi,g,u,0} = \int_r^R g m (l_{pi} + l_{cg} \cos(\bar{\theta})) \mathrm{d}s, \quad f_{\phi,g,v,0} = \int_r^R g m l_{cg} \sin(\bar{\theta}) \mathrm{d}s$$

$$f_{ext,0,s} = \int_r^R [w_0 f_{u,s} \quad 0 \quad -l_{pi} f_{w,s}] \mathrm{d}s, \quad f_{ext,0,c} = \int_r^R [0 \quad -w_0 f_{v,s} \quad 0] \mathrm{d}s$$

$$f_{ext,1,u} = \int_r^R u_s f_{w,s} \mathrm{d}s, \quad f_{ext,1,v} = \int_r^R u_s f_{w,s} ds, \quad f_{ext,1,u} = \int_r^R u_s f_{w,s} \mathrm{d}s, \quad f_{ext,1,v} = \int_r^R v_s f_{w,s} \mathrm{d}s$$

DOI: 10.1002/we

References

1. Chaviaropoulos PK, Soerensen NN, Hansen MOL, Nikolaou IG, Aggelis KA, Johansen J, Gaunaa M, Hambraus T, von Geyr HF, Hirsch C, Shun K, Voutsinas SG, Tzabiras G, Perivolaris Y, Dyrmose SZ. Viscous and aeroelastic effects on wind turbine blades. The viscel project. part II: Aeroelastic stability investigations. *Wind Energy* 2003; **6**: 387–404.
2. Block JJ, Strganac TW. Applied active control for a nonlinear aeroelastic structure. *Journal of Guidance, Control, and Dynamics* 1998; **21**: 838–845.
3. Hodges DH, Dowell EH. Nonlinear equations of motion for the elastic bending and torsion of twisted nonuniform rotor blades. *Technical Report* TN D-7818, NASA, December 1974.
4. Wendell J. Aeroelastic stability of wind turbine rotor blades. *Technical Report* E(11·1)-4131, U.S. Department of Energy, September 1978.
5. Larsen TJ, Hansen A, Buhl T. Aeroelastic effects of large blade deflections for wind turbines. *Proceedings of the special topic conference 'The Science of making Torque from Wind'*, Delft, The Netherlands, 2004; 238–246.
6. Larsen TJ, Madsen HA, Hansen AM, Thomsen K. Investigations of stability effects of an offshore wind turbine using the new aeroelastic code HAWC2. *Proceedings of the conference 'Copenhagen Offshore Wind 2005'*, Copenhagen, 2005; 25–28.
7. Johnson W. Rotorcraft aeromechanics applications of a comprehensive analysis. *AHS International Meeting on Advanced Rotorcraft Technology and Disaster Relief*, Japan, 1998; S5–1 to S5–14.
8. Cesnik CES, Hodges DH, Sutyrin VG. Cross-sectional analysis of composite beams including large initial twist and curvature effects. *AIAA Journal* 1996; **34**: 1913–1920.
9. Wenbin Y, Hodges DH, Volovoi V, Cesnik CES. On timoshenko-like modeling of initially curved and twisted composite beams. *International Journal of Solids and Structures* 2002; **39:** 5101–5121.
10. Wenbin Y, Volovoi V, Hodges DH, Hong X. Validation of the variational asymptotic beam sectional analysis. *AIAA Journal* 2002; **40:** 2105–2112.
11. Thomsen JJ. *Vibrations and Stability: Advanced Theory, Analysis, and Tools*. Springer-Verlag: Berlin-Heidelberg-New York, 2003.
12. Jonkman J. Nreloffshrbsline5mw. *Technical report*, NREL/NWTC, 1617 Cole Boulevard; Golden, CO 80401-3393, USA, 2005.
13. Hansen MH. Aeroelastic stability analysis of wind turbines using an eigenvalue approach. *Wind Energy* 2004; 7: 133–143.
14. Meirovitvh L. *Computational Methods in Structural Dynamics*. Sijthoff & Noordhoff: Alphen aan den Rijn, The Netherlands, 1980.

DOI: 10.1002/we

DANISH CENTER FOR APPLIED MATHEMATICS AND MECHANICS

Scientific Council

Secretary

Ole Sigmund, Professor, dr. techn.
Department of Mechanical Engineering, Solid Mechanics
Nils Koppels Allé, Building 404
Technical University of Denmark
DK-2800 Kgs. Lyngby
Denmark